Analysis and Control of Interfacial Processes of Zn Negative Electrodes for Large-Scale Battery

大規模蓄電池への応用に向けた亜鉛負極の

界面反応プロセスの解析と制御

February, 2019

Tomohiro OTANI

大谷　智博

Analysis and Control of Interfacial Processes of Zn Negative Electrodes for Large-Scale Battery

大規模蓄電池への応用に向けた亜鉛負極の

界面反応プロセスの解析と制御

February, 2019

Waseda University

Graduate School of Advanced Science and Engineering

Department of Advanced Science and Engineering

Research on Applied Chemistry A

Tomohiro OTANI

大谷　智博

Contents

Chapter 1:
General Introduction

Chapter 2:
Growth Behavior of Electrodeposited Zn during Charging of Zn Negative Electrode

Chapter 3:
Controlling Zn Electrodeposition Process toward Applications in Large-scale Battery

Chapter 1:

General Introduction

1.1 Battery for Power Distribution System

1.1.1 Issues in power distribution systems upon introduction of renewable energy

Toward the energy supply system less reliant on fossil fuels and reducing CO_2 emission, the renewable energy (solar and wind power) is widely introduced to the power distribution systems today. In Japan, the installed capacity of photovoltaic cell was less than 10 GW in 2012, but it increased to *c.a.* 40 GW in 2016 [1]. Averaged increase per year during this period is about 26%. Japanese government sets the target value to introduce the renewable energy in "Strategic Energy Plan" (July, 2018); 22-24% of the power supply will be provided by the renewable energy in 2030, and it should be major power source in 2050 [2].

Despite such strong motivations, several problems arise in power distribution system. Since solar and wind power potential is unstable depending on time and weather conditions, the voltage of supplied electricity is frequently fluctuated [3-5]. Furthermore, the intermittent characteristics of the renewable energy makes the electricity supply and demand unbalanced. It induces the variations in the frequency of the supplied electricity in the electricity network. Excess energy is supplied in sunny day in Spring and Autumn. This situation introduces a fatal problem in power distribution system because it can cause damage in electricity equipment in demand side and suspension in power output in supply side [6]. Actually, Kyushu electric power company shut out the electricity supply from PV cells in October, 2018 [7]. In addition, the conventional power distribution system is designed assuming electricity flow only from the supply side (power plant) to the demand side (households and factories). However, the renewable energy can be supplied from demand side, too. This energy flow from the opposite direction (the reverse power flow) increases the voltage of the supplied electricity [8, 9]. Fig. 1.1 represents several issues upon introduction of the renewable energy.

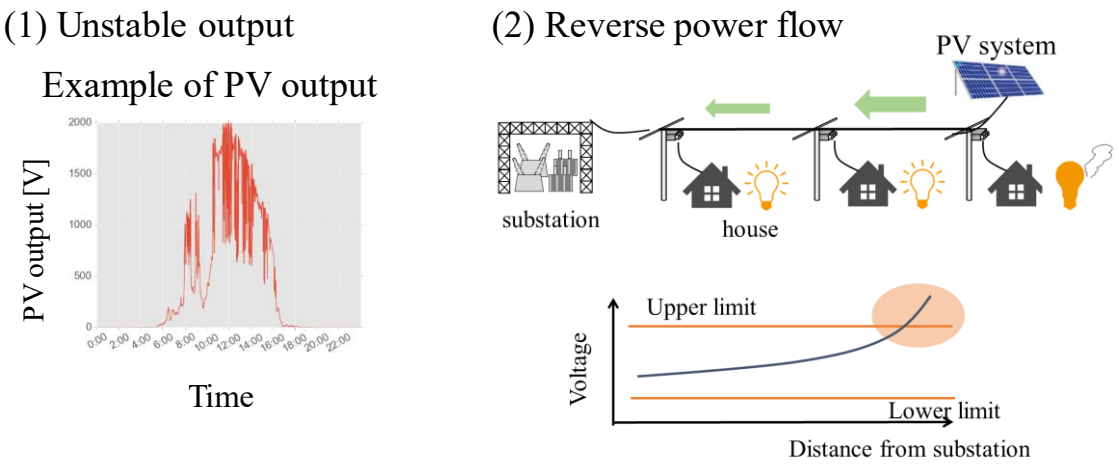

Fig 1.1 Issues in power distribution system upon introduction of renewable energy

1.1.2 Roles of large-scale battery in the power distribution system

To solve these issues, it is necessary to introduce energy storage system in power distribution system. By storing excess energy (releasing energy upon shortage), unbalanced power supply and demand can be controlled. Hydro-pumped energy storage is one option. Excess energy is stored by pumping up water, and energy is released by flowing stored water to power generator [10, 11]. However, this system requires the water reservoir sites and construction periods. Thus, it is unrealistic to control power supply and demand by this system alone.

Batteries can provide an alternative solution. Excess electricity supply is stored as chemical energy by charging, and it can be released again by discharge operation. Furthermore, the batteries are more diversely applied than that of hydro-pumped energy storage because of rapid response and easiness to install. For example, after starting the hydropower generation, only 20-30% of the rated output is attained within 1 min. This value is several % in the case of thermal power generation [6]. On the other hand, battery can charge or discharge electricity at maximum input/output within a second. In power distribution systems, battery is used for (1) stabilizing power output of renewable energy, (2) peak shaving and load leveling, (3) voltage control in power distribution system [3-6, 8, 9, 12, 13].

In the first role, the battery is used with the renewable energy source (photovoltaic cell or wind power plant). By performing charge-discharge operations corresponding to power output of the renewable energy, the supplied electricity is stabilized [3-5]. This operation is beneficial for maintaining the quality (frequency and voltage) of supplied electricity and determining total energy supply in power distribution

system.

In the second role, it can store and release the energy corresponding to the balance of electricity supply and demand. “Peak shaving” and “load leveling” refer to the battery operation balancing the energy supply and demand; by releasing the energy when the demand rises or storing energy at excess supply, the unbalanced value is controlled [14]. This operation requires the longer charge-discharge operation and higher capacity than those in the first role. It can be achieved either by centralized battery connected with the power distribution system (large scale battery, MWh to GWh scale) or batteries used in consumers (several 100 kWh) [15]. The latter battery also requires high energy density because it is placed even in the household.

In the third role, battery in substation controls the voltage of the supplied electricity (solve the issue caused by reverse power flow) [3-6, 8, 9]. Currently, the voltage is controlled by tap changer and step-voltage regulator, but its capability for controlling rapid voltage variations is limited [16]. Battery is an alternative to this controlling method. By charge-discharge operations, the fluctuations in voltage of supplied electricity are stabilized to maintain the voltage within the admissible range for consumers.

1.1.3 Types of battery and requirements in the power distribution system

Several types of batteries are used in the power distribution systems. For the battery in household and substation, the battery with high energy density is required because the placing location is limited. Li-ion battery is often used for such an application based on high energy density and efficiency [8, 9]. For a battery used for stabilizing the renewable energy output, or controlling the electricity demand, high energy density is not necessarily primary requirement because large construction area can be selected. On the other hand, the scalability to MWh capacity is important. For such an application, sodium-sulfur battery and vanadium redox flow battery attracts attention [3, 13]. Table 1.1 summarizes the characteristics of various batteries [5, 20].

Table 1.1 Several types of batteries used in power distribution system

	Li-ion	NaS	Vanadium Flow	Nickel-Hydride	Lead-acid
Theoretical Energy Density / Wh kg^{-1}	～585	786	100	225	167
Efficiencies / %	85-95	80-85	70-85	85-95	75-85
Durability	>3500 cycles	4500 cycles	>20 years	>3500 cycles	4500 cycles
Cost / USD kWh^{-1}	1200-4000	1000-3000	600-1500	-	300-600
Electrolyte	Organic	Ceramics	Aqueous	Aqueous	Aqueous

Although many verification tests for battery in power distribution system are ongoing over the world, one of the common issues is its high cost [8, 9, 19]. Since the electricity price increases by introducing the batteries, their cost must be minimized. However, the cost of battery is generally higher than 600 US$/kWh [20]. This value is considerably higher than that of hydro-pumped energy storage (200 US$/kWh), and the introduction of the battery in the electricity network is not economically feasible [10, 11]. Additionally, wide spread use of Li-ion batteries in electric vehicles and power distribution systems lead to the serious concern over the resources for the battery components (as discussed in 1.2.1). Furthermore, the care must be taken with respect to flammability of the battery component; *e.g.* organic electrolyte in Li-ion and sodium anode in NaS battery.

Considering these situations in battery for power distribution systems, Zn batteries (Zn-Ni, Zn-Air and flow-assisted battery) have been recognized as potential candidates for the energy storage system in the electricity network based on several aspects. First, due to abundant resources and low price of raw materials, Zn battery can be fabricated at a cost feasible for grid application [21]. Secondly, Zn negative electrode is advantageous both in high energy density and scalability. Theoretical capacity of Zn is 658 mAh/g. This is much higher than that of graphite anode in Li-ion battery (372 mAh/g) [22]. Furthermore, Zn can be electrodeposited from aqueous solutions, which makes it possible to operate charge-discharge cycles of large-scale battery simply by electrodeposition and anodic dissolution on large-sized current collector. Based on these advantages, Zn batteries featuring high energy density (*e.g.* Zn-air battery) and large scale (*e.g*. flow-assisted battery) have been suggested. Thirdly, the aqueous solution electrolyte gets rid of concern over safety issue by fire. Characteristics of Zn negative electrodes are described in detail in section 1.2.

1.2 Zn Negative Electrode

1.2.1 General features of Zn negative electrodes

History and electrochemical reactions

In 1800, Volta developed voltaic pile comprising of Zn anode, Al or Cu cathode in sulfuric acid, which is considered as an initiation of research and development of batteries in human history [23, 24]. Since then, Zn electrodes have been utilized as an anode material in primary batteries. Laclanché developed the battery with zinc anode, MnO_2/carbon cathode in ammonium chloride solution in 1865, which widened the market of primary batteries [25]. Alkaline Zn battery was commercialized in 1950s, and has been

a major primary battery until now. There are several reasons for using Zn as an anode material [26-29]. First, the redox potential of Zn is negative (−0.76 V vs. SHE) among the electrode materials usable in the aqueous solution. The discharge reactions is written as (1.1).

$$Zn \rightarrow Zn^{2+} + 2e^{-} \quad (E=-0.76\ V\ vs.\ SHE) \tag{1.1}$$

In addition, both discharging and charging of Zn anode are characterized by low overpotential and small Tafel slope [27]. It means a small kinetic barrier for electrochemical reactions. These features are advantageous to attain high discharge output. Secondly, it possesses high theoretical discharge capacity (658 mAh/g) which enables large energy density in small sized battery [26]. Thirdly, its commercial application is not restricted by limitations in the resources and cost as described below. Also, Zn anode is compatible with wide variety of aqueous solutions (*e.g.* sulfate, chloride and alkaline). It can be combined with many types of cathodes.

The attempts to develop the rechargeable Zn batteries have been made from 19th century. Zn-Ag was developed in the middle of 20th century [24]. It is mostly used in the military equipment as well as the spacecraft featuring high specific energy and safety. However, applications of rechargeable Zn batteries are limited due to the lack of long-term cyclability as described in the last part of this section. In 1970s and 1980s, many researches were carried out to develop the rechargeable Zn-Ni and Zn-air batteries. However, Li-ion battery achieved a great success in the rechargeable battery market in 1990s. In the 21st century, Zn batteries attract the attention again because of lower cost because of abundant natural resources. Especially, the rapid introduction of renewable energy motivates researchers and companies to develop the rechargeable Zn-Air, Zn-Ni batteries to cope with both high energy density and low cost [26-29]. For large scale applications, Zn flow-assisted battery is recognized to be potentially advantageous for the scale-up [30-32].

Resources and cost

For the battery applied in grid-scale energy storage, the abundant resources as well as low fabrication costs must be guaranteed. The cost reduction of Li-ion battery and its scale-up are major interests in the battery industry [33, 34]. These issues are inherently challenging because Li-ion battery uses rare metals in its battery components. For example, Co is often used in the cathode materials ($LiCoO_2$) and its increased demand raised the price of raw materials. During 2017, the price of Co resources was doubled

compared to the beginning of the year [35]. The price of Li resources was also increased by more than 30%-50% [35]. This situation motivates the developments of batteries composed of abundant and inexpensive materials. Zn batteries meet these requirements.

The production of Zn was 13 million ton/year in 2017 at price of *c.a* 3000 US$/ton (London Metal Exchange, LME price) [36]; *c.f.* Li was 35 thousand ton/year in 2016 at *c.a.* 8200 US$/ton ($LiCO_3$ based value, imported price to Japan) [37]. Furthermore, its production area is world-widely diverse. Fig. 1.2 shows the reserves area of Zn and Li raw materials [38, 39]. Li is maldistributed especially in Chili. Zn is produced in many areas, which is good aspect in terms of resources strategy of Japan.

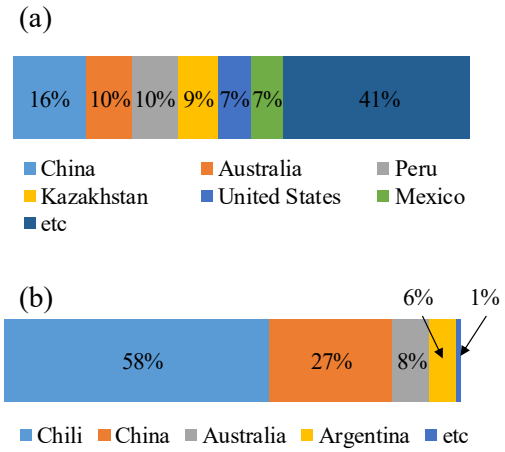

Fig. 1.2 Reserves area of (a) Zn and (b) Li resources

Based on the low price of Zn and related battery components, it is often reported that the battery can be fabricated at low cost. In particular, flow-assisted battery is advantageous to construct large-scale battery at low cost [21, 30-32, 40-42]. This is because charge-discharge reaction can be performed simply by electrodeposition/dissolution of Zn on current collector immersed in large-volume electrolyte as discussed in 1.3.3. This can simplify the fabrication process of the anode (*e.g.* kneading of active materials and pasting on the current collector). Gong *et al.* estimated the capital cost of Zn-Fe flow-assisted battery to be possibly $100/kWh [21]. This is considerably lower than the cost of currently used hydro-pumped energy storage in power distribution system (*c.a.* 200 US$/kWh) [10, 11]. The fabrication cost of Li-ion battery was around 300 US$/kWh in 2016 [33, 34].

Issue of rechargeable Zn electrode

Despite long history of Zn negative electrodes from 19th century and the potential

benefits in the secondary battery, the application of rechargeable Zn batteries are still limited. Major drawback lies in the limited cyclability of the electrode caused by morphological changes of electrodes and non-uniform distribution of active materials [43]. Unlike the graphite anode used in currently used lithium-ion battery where reactions proceed by intercalation and deintercalation of lithium ions into the stacking of graphene layer, Zn anode undergoes electrodeposition, anodic dissolution and oxide formation. In former case, the structure of the active materials can be maintained through cycling because graphite provides the "container" for Li ions. In contrast, Zn anode itself is involved in the electrochemical reactions. This makes it difficult to maintain compact morphologies over long term cycling [26-29]. Redistribution of active materials is often caused by non-uniform deposition and ZnO formation over electrode surface. It is strongly required to control such a morphological change of the electrode for the applications in the secondary batteries.

1.2.2 Reaction mechanisms of Zn negative electrodes

For the battery application, alkaline solution is mainly used as an electrolyte. This is because it exhibits high conductivity and compatibility with several positive electrodes (*e.g*. NiOOH, MnO_2, Air cathode) [43, 26-29]. Zn is dissolved as zincate ions ($Zn(OH)_4^{2-}$) in alkaline electrolyte. Charge-discharge reaction is written as (1.2).

$$Zn(OH)_4^{2-} + 2e^- \rightleftarrows Zn + 4OH^- \quad (1.2)$$

Ligands (OH^-) are successively dissociated during reduction process to Zn. Bockris *et al*. suggested several reaction steps for Zn electrodeposition and dissolution in an alkaline solution based on potentiostatic and galvanostatic measurements [46].

$$Zn(OH)_4^{2-} \rightleftarrows Zn(OH)_3^- + OH^- \quad (1.3)$$

$$Zn(OH)_3^- + e^- \rightarrow Zn(OH)_2^- + OH^- \text{ (rds)} \quad (1.4)$$

$$Zn(OH)_2^- \rightleftarrows ZnOH + OH^- \quad (1.5)$$

$$ZnOH + e^- \rightleftarrows Zn + OH^- \quad (1.6)$$

An electron transfer occurs to $Zn(OH)_3^-$ and ZnOH species, and the former process is rate-determining step for the reaction.

Standard deposition potential of Zn is −0.74 V vs. SHE. This means hydrogen evolution reaction (HER) is thermodynamically favored than Zn electrodeposition in acidic electrolyte. Therefore, alkaline solution is used to suppress HER. In this case, HER

occurs by decomposition of water molecule by two-electron reaction.

$$2H_2O + 2e^- \rightarrow H_2 + 2OH^- \quad (1.7)$$

However, Zn possesses a fairly large overpotential for HER. This results in reasonably high coulombic efficiency during Zn electrodeposition (charging).

1.2.3 Electrodeposition behavior of Zn during charging

Morphological variations of Zn electrodeposits

During electrodeposition of Zn (charging of the anode), one of the major interests lies in morphology and texture evolution of Zn crystals. This is because an appearance(brightness) and a corrosion resistance of electrodeposited film are determined by microstructures of Zn, which are practically important issues [47]. In the battery operation, morphological variations of Zn are important because they are related to self-discharge and battery failure as discussed above.

From 1960s, morphological variations of electrodeposited Zn have been widely studied under various conditions. In 1968, Naybour utilized scanning electron microscope (SEM) and transmission electron microscope (TEM) for analyzing morphological variations of Zn formed at constant current densities (−4.0 - −100 mA cm^{-2}) [48]. They found that morphologies of electrodeposited Zn varied from dendrite to layer or granular shapes, then to mossy structures by decreasing the deposition current. (Typical shapes of these structures are shown in chapter 2, Fig 2.6.) Formation of dendrite and mossy structures result in rough surface, which should be suppressed during the battery operation. At this moment, detailed shapes of mossy structures were not revealed. They were thought to be consisted of large numbers of small sized crystals. He ascribed the reason for this deposition behavior to the absorption of hydrogen at low current densities. They observed the morphological variations induced by electrolyte flow and described "phase diagram" showing morphological changes to current density and rate of electrolyte flow. Dendrites formed at higher current density were suppressed by electrolyte flow [49]. Systematic comparisons were further carried out by Wang *et al.* by galvanostatic electrodeposition and SEM analysis in 2006 [50]. They showed the morphological map describing the effects of current density, deposition time, zincate concentration, KOH concentration, and temperatures. However, the mechanisms behind morphological variations were not fully clarified. In short, the dendrite formation is enhanced under the conditions where Zn electrodeposition was performed under diffusion-limited condition of zincate ions, *i.e.*, high current density, low zincate

concentration, and low temperature. Mossy structures were observed at the opposite conditions to that of dendrite formation.

Nucleation & growth behavior behind morphological variations

In order to understand morphological variations of Zn electrodeposits, nucleation & growth behavior of Zn is often discussed. In this section, nucleation & growth behavior behind morphological variations are qualitatively discussed focusing on compact Zn electrodeposits (layer and boulder), dendrites and mossy structures.

At intermediate current densities or overpotentials between those for mossy structure and dendrite formation, layer-like structures and boulder structures are formed. They are thought to be formed by epitaxially grown Zn on substrate (2D nucleation) and 3D nucleation, respectively. At low overpotential, well-defined facets and stacking of layer-like structures (microsteps) are observed due to "bunching" of epitaxially grown film or 2D nuclei. Bunching refers to the formation behavior of microsteps. In principle, 2D nucleation is a periodic process of formation of 2D metal island with one atomic height and its growth toward lateral direction. Budevski *et al.* analyzed 2D nucleation of Ag during potentiostatic electrodeposition by preparing single crystal Ag without screw-dislocation [51-53]. After applying the potential, periodic current pulses were observed. Notably, coulombic charge of each pulse corresponded to the charge needed for depositing one atomic layer. These phenomena were interpreted as formation of an island with one atomic layer height, and following deposition occurred until atomically flat Ag layer was obtained. This situation is schematically shown in Fig. 1.3.

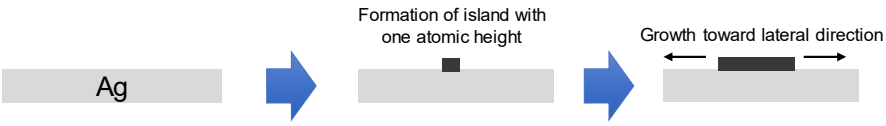

Fig. 1.3 2D nucleation of Ag

According to this explanation, only atomically flat surface is obtained after electrodeposition. However, this is hardly observed in practical situations. Instead, steps with several nm height (layer-like structures, microsteps) are often observed. This is formed by growth of some atomic layers at the same time due to limited mobility of atomic step in real case; the growth rate of another atomic layer on top of existing layer becomes same, then they are grown at the same time [54-56]. This is thought to be caused by the presence of impurities on the surface and adsorbate in the electrochemical environments. This situation is shown in Fig. 1.4.

Fig. 1.4 Microsteps formation during 2D nucleation

In Zn electrodeposition, this growth behavior results in formation of layer-like structures and ridge structures [57-59]. The different orientation of microsteps have been observed dependent on texture of underlying substrates [60, 61]. Bunching via surface diffusion of adatoms is preferentially occurs during Zn electrodeposition because an activation energy of surface diffusion of adatom was lower than that of direct deposition to kinks, steps and terrace sites [62-64].

When deposition potential (current density) is increased, boulder structures (three-dimensional particulate structures) are formed. This is thought to be formed by 3D nucleation. Rate dependence of 2D nucleation and 3D nucleation on deposition overpotential is given by eq. (1.8) and (1.9) [63-65].

$$J_n = K_1 exp\left(\frac{-K_2}{\eta_K}\right) \tag{1.8}$$

$$J_n = K'_1 exp\left(\frac{-K'_2}{\eta_K{}^2}\right) \tag{1.9}$$

J_n denotes nucleation rate, K is constant, and η is deposition overpotential. 2D nucleation rate exponentially increases with η_K but 3D nucleation is dependent on square of η_K. Therefore, 3D nucleation becomes dominant over 2D nucleation at higher overpotential.

Further increase in the deposition potential results in formation of dendrites. In general, the dendrite is formed under diffusion limited conditions of ions. Diggle *et al*. analyzed the dependence of growth rate of Zn dendrite on overpotential, concentration and temperature [66]. They confirmed that the growth rate of dendrite increased at higher overpotential. Initiation time of dendrite was defined as the time when spherical diffusion at a tip on surface was attained. Transition from linear diffusion to spherical diffusion at dendrite tip occurred as follows [64, 67]. When the rough surface is schematically drawn in Fig. 1.5, the surface becomes roughened by following deposition at the presence of protrusion with smaller radius of curvature (Fig. 1.5(b)).

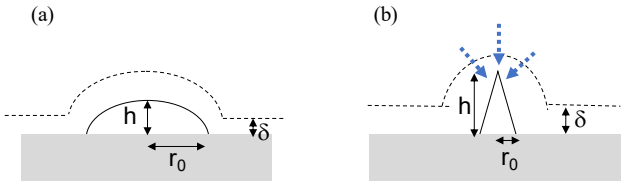

Fig. 1.5 Relation between radius of curvature in protrusion and diffusion condition (a) $r_0>\delta$, (b) $r_0<\delta$

Grey rectangular shape denotes a substrate, black solid line represents deposits shape, black dashed line is diffusion layer, and blue dashed line is diffusion flux. In the case of large radius of the curvature, linear diffusion occurs over entire surface, which maintains the initial morphologies during electrodeposition. When the radius is smaller than the diffusion layer thickness, spherical diffusion is established on the tip front (Fig. 1.5 (b)) whereas linear diffusion on bottom (flat) part. This results in locally continuous deposition on tip and increase in the length. Thus, mass transfer condition has critical roles in the dendrite formation. In the case of Zn dendrite, growth direction of the tip is reported to be (110) and (100), while compact deposits (layer-like structures) tend to expose (001) surface [68, 69]. This is in consistent with Pangarov's theory, which assumes the work required for 2D nucleation becomes minimum in the order of (001) < (110) < (100) by increasing the overpotential. Preferential growth direction is qualitatively follows this trend by changing the deposition overpotential [70, 71].

Formation of mossy structures at the overpotential below layer-structure formation is different from general understandings of electrodeposition. At low overpotential (low degree of supersaturation), epitaxial growth or 2D nucleation is favored as discussed above, which forms 2D electrodeposits. Despite this, very rough aggregates are formed at low current density region in Zn electrodeposition. Formation of mossy structures is recognized at early studies of Zn electrodeposition [48, 57, 72-74]. Several attempts have been made to explain the formation of mossy structures. It is often postulated that codeposited hydrogen and oxide layer on Zn surface causes an irregular deposition behavior [48, 73, 75-79]. Wiart *et al*. carried out successive studies with electrochemical impedance spectroscopy (EIS) on Zn electrodeposition process, and proposed the electrodeposition mechanisms in acidic and alkaline solutions. In acidic media, reaction steps like (1.10) is thought to induce mossy structures by locally continuous deposition by auto-catalytic manner [75-77]. Zn* expresses catalytically active sites for following Zn deposition (self-propagating kink).

$$Zn(I)_{ads} + e^- \rightarrow Zn^* \qquad (1.10)$$

$$H_{ads} + Zn(I)_{ads} \rightarrow Zn^* + H^+ \quad (1.11)$$

$$Zn^* + Zn(II) + 2e^- \rightarrow Zn + Zn^* \quad (1.12)$$

In alkaline solution, Zn deposition is thought to occur through surface layer comprising ZnO at low cathodic overpotential. Localized deposition is explained by this layer [77-79]. However, nucleation & growth process during mossy structure formation is still unclear. Wang *et al*. carried out SEM and TEM analysis on mossy structures [80]. They reported that the diameter of filament was in the range of 50 to 200 nm. Preferential growth direction of the filament is (001) direction, which is in accordance with Pangarov's theory at low overpotential. As a whole, general understandings of nucleation & growth behavior during mossy structure formation is still missing.

Analogy to Li electrodeposition in non-aqueous solutions

Morphological variation of electrodeposits are major interests in the researches and developments of Li metal anode, too. Li metal anode is potential alternative superior to graphite-based anode currently used in Li-ion batteries featuring very high energy density and high voltage [26, 81]. Charge-discharge reactions are electrodeposition and anodic dissolution of metal Li in organic solvent or ionic liquid.

$$Li^+ + e^- \rightleftarrows Li \quad (1.13)$$

Li metal anode also suffers from short-life time mainly due to morphological changes of Li. When Li dendrite is formed during charging, it irreversibly dissolved during discharging and residual Li tends to be isolated from current collector by dissolution of Li filaments from its root as shown in Fig. 1.6. This remaining Li is called "dead" Li [82-83].

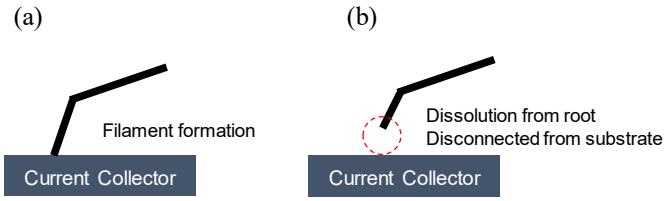

Fig. 1.6 Formation of dead Li

As is the case of Zn electrodeposition, the morphologies of Li vary dependent on the deposition conditions. Irregular shaped deposits are formed both at high and low current density regions [84, 85].

Different mechanisms were suggested for formation of irregular shaped deposits at high and low current density regions. At high current density, dendrite formation is governed by concentrations of Li ions near the surface [86]. From *in situ* observation by optical microscope, the initiation of dendrite could be correlated with "Sand" time measured from chronopotentiograms [86]. Sand time corresponds to the time when the surface concentrations of reactant becomes zero as described by eq. (1.14).

$$t_{Sand} = \pi D_{app} \frac{(z_0 c_0 F)^2}{4(J t_a)^2} \tag{1.14}$$

D is diffusion coefficient, z_0 is the chare of the cation (1 in Li^+), F is Faraday's constant, J is the current density, c_0 is concentration in bulk. t_a is the transference numbers of lithium cations and related anions. Direct measurements of Li^+ concentrations were performed by *in situ* ^{7}Li MRI analysis by Grey *et al* [87]. Li^+ depletion was confirmed at the onset of dendrite formation. In contrast, such a correlation between morphological evolution and ionic concentrations was not found at lower current density regions. Mönig *et al.* observed mossy structures were grown by incorporation of reduced Li not to growth front but to root of the deposits (root growth) [88-90]. Many researchers postulated that solid-electrolyte interface (SEI) is non-uniformly formed on the Li surface, and it induces locally concentrated deposition [86-90]. SEI is formed by reductive decomposition of electrolyte on Li surface due to more positive reduction potential of solvent than that of Li. Thus, the formation of mossy structure is thought to be initiated by localized deposition by non-uniform SEI formation. This implies that formation of mossy structures during Zn electrodeposition is also affected by non-uniform surface properties, but they are not decomposition products of electrolyte. (Unlike Li electrodeposition, aqueous solutions are used in Zn electrodeposition.)

1.2.4 Anodic dissolution of Zn and ZnO formation

According to pourbaix diagram of Zn in H_2O, various complexes are formed between Zn^{2+} and OH^- such as $Zn(OH)_2$, $Zn(OH)_3^-$, and $Zn(OH)_4^{2-}$. In the battery application, electrolyte contains more than 1.0 mol dm^{-3} KOH. At this condition (pH more than 14), $Zn(OH)_4^{2-}$ is a major complex. Therefore, discharge reaction of Zn negative electrode can be written as (1.15).

$$Zn + 4OH^- \rightleftarrows Zn(OH)_4^{2-} + 2e^- \quad (1.15)$$

During dissolution, zincate concentration increases and OH^- decreases. The zincate concentration is beyond the solubility limit [91-93]. Then, ZnO is formed by (1.16) or (1.17).

$$Zn(OH)_4^{2-} \rightleftarrows ZnO + H_2O + 2OH^- \quad (1.16)$$

$$Zn + 2OH^- \rightleftarrows ZnO + H_2O + 2e^- \quad (1.17)$$

Formation of ZnO results in passivation of the electrode; following dissolution of zinc is inhibited by the presence of ZnO layer on the electrode surface. Linear sweep voltammograms during anodic polarization generally shows active to passive transition [94, 95].

In the battery operation, ZnO layer affects the performance of the electrode. First, discharge capacity is limited not by the amount of Zn but by ZnO formation [96-98]. Second, the reactions reversibility is influenced by ZnO layer [96-98]. Third, ZnO formation induces redistribution of active materials over electrode surface [44, 45]. These aspects will be discussed in 1.3.4. In the following section, previous studies regarding chemical nature of passivated film, mechanisms of ZnO formation during discharge, structural analysis of ZnO by Raman spectroscopy, and crystal growth of ZnO are discussed.

Chemical nature of passivated film on Zn

Investigations on passivation behavior of Zn has been carried out from 1940s, and it becomes important research topics in middle of 20th century because it is recognized as important process in the battery applications [24].

Early studies on passivated film focused on the nature of passivated film (color, appearance, chemical composition). Presence of γ-$Zn(OH)_2$, ε-$Zn(OH)_2$, and ZnO were confirmed in passivated film by X-ray diffraction (XRD) [99]. $Zn(OH)_2$ are generally formed at low OH^- concentrations, while the majority of the component was ZnO at high OH^- concentration. Although the reason for this behavior is not clarified, the dehydration reaction of $Zn(OH)_2$ (1.17) may proceed under high OH^- concentration due to decreased H_2O activity [97, 101, 102]. Still, the discrepancy exists about the formation of $Zn(OH)_2$ even under similar dissolution condition. (*e.g.*, *In situ* Raman analysis shown below did

not detect $Zn(OH)_2$ even at low KOH concentrations.)

$$Zn(OH)_2 \rightarrow ZnO + H_2O \quad (1.18)$$

In 1969, Power and Breiter classified passivation films into type I and type II based on color and its appearance [103]. Type I is white, loose, and flocculent films formed at the absence of convection. Type II was compact and appears to form directly at the surface. Its color is light grey to black. They were formed under stirred electrolyte, and positive anodic potential in quiescent electrolyte. Based on temporal changes in color and appearance in optical microscope during potential sweeping, they claimed that passivated films have duplex character in quiescent electrolyte; type I films covered the type II film. Formation of type II film was recognized as an active to passive transition (Dissolution of Zn was still possible after forming type I film due to the porous structures of the film, but it is suppressed by dense type II film). However, they did not provide any structural information about each type.

Mechanisms for ZnO formation during anodic dissolution

As a mechanism for ZnO formation during anodic dissolution, two mechanisms are proposed. One is dissolution-precipitation mechanisms and the other is solid-state reaction [94, 95, 99]. In former process, ZnO is precipitated in supersaturation zone with zincate species near the surface. In the latter process, ZnO is directly formed from Zn substrate by reaction (1.17) by attacking of OH^- to Zn. Dissolution-precipitation mechanisms are recognized as a major process because the properties of passivated films are in consistent with this process [93, 99, 104]. First, a passivated layer comprises of not monolayer but 3D structures sometimes having several μm thickness. Formation of such a film may not occur in solid-state reaction where Zn surface is spontaneously passivated by film formation. Second, the precipitation of ZnO is coupled with changes in ionic concentrations of zincate and OH^- concentrations as discussed below [91-93].

In 1979, Szpak performed SEM analysis on discharge products on Zn electrode in KOH solution [104]. They confirmed various morphologies like thistle-like structure, carpet-like growth and boulder-type growth. These morphologies were caused by different nucleation and growth behavior of ZnO in the supersaturated solution near the surface. Duplex nature observed in the study of Power and Breiter was thought to originate from densification of precipitated ZnO on the surface. However, the resolution power of SEM images was insufficient to identify micro/nanostructures of ZnO.

Liu *et al.* assumed changes in the growth mechanisms of ZnO during

galvanostatic dissolution based on chronopotentiometry and the modeling of mass transfer [105]. At initial stages of dissolution, only zincate formation occurs because it did not reach the solubility limit. Then, the formation of type-I film starts by dissolution-precipitation mechanisms in supersaturation zone near the surface. After forming porous and flocculent films on the surface, OH^- diffuses through this layer during Zn dissolution. Finally, solid-state reaction occurs by depletion of OH^- at the surface. At this point, potential plateau was observed in chronopotentiograms. This solid-state reaction accounts for the formation of type-II films and duplex nature of the passivated film.

Although conclusive information is still missing about the duplex nature of the passivated film, it is evident that nucleation & growth process of ZnO is coupled with dynamic changes in the concentration of zincate and OH^- at the surface. Arise *et al*. carried out successive studies on this aspect by using horizontally upward faced electrode to demonstrate the battery operation [91-93]. In 2006, they utilized holographic interferometry to measure the ionic mass-transfer rates of ionic species ($Zn(OH)_4^{2-}$, K^+ and OH^-) during anodic dissolution of Zn [91]. They constructed a transient diffusion model to simulate the concentration changes at the surface, which was agreed with the interferometric results. At this moment, the formation of ZnO is not considered. In 2010, similar techniques were applied to numerically simulate the potential transients during anodic dissolution [92]. By applying Butler-Volmer equations based on calculated transients of ionic concentrations at the surface, the overpotential was determined. This value was in good agreement with the experimentally measured value at low current density region. However, the deviations were clearly observed at higher current density region because of ZnO precipitation by higher degree of zincate supersaturation than that at low current density. Qualitative correlations between surface concentration of ions and ZnO crystal growth were found by SEM, too [93].

In summary, dissolution-precipitation mechanism is recognized as a major process governing ZnO precipitation during anodic dissolution of Zn. Since this process is strongly dependent on the degree of zincate supersaturation in electrolyte (near the electrode surface), the properties of electrolyte remarkably affect the ZnO formation behavior, which motivated many researchers to investigate effects of solution condition on the battery performance as discussed in 1.3.4. However, it is still not fully understood how such a process affect crystal structures and morphologies of precipitated ZnO as demonstrated in studies by Szpak and Arise [93, 104]. These aspects are important for maintaining the reversibility of the negative electrode [106, 107].

In situ Raman analysis

In order to obtain information about the structure of discharge products, Raman spectroscopy is often used. Advantages of Raman scattering are (1) capable of revealing crystal structures of ZnO at an atomic scale (*e.g.* the presence of crystal defects and strain can be revealed by observed vibration mode and peak shift), (2) no need for vacuum condition and capability of *in situ* measurements in the electrolyte, (3) fast data acquisition time compared to X-ray diffraction. Based on these advantages, some attempted to analyze the structure of discharge products during charge-discharge cycles by *in situ* Raman measurements.

In 1989, Wiart performed the analysis during potentiostatic polarization [108]. At rest potential, the presence of the native oxide layer was confirmed, which was thought to be related with irregular deposition behavior at low overpotential (the formation of mossy structure). This oxide layer could be eliminated by applying cathodic overpotential. During anodic polarization, ZnO was formed, and no signal corresponding to $Zn(OH)_2$ was observed. Different peaks were evolved depending on dissolution conditions; major peak was located at 560 cm^{-1} during early stages of dissolution, or after passivation at positive potential. Prolonged polarization resulted in evolution of another peak at 440 cm^{-1}. Different peaks originate from the various lattice vibrations of ZnO like Fig. 1.7 [109, 110].

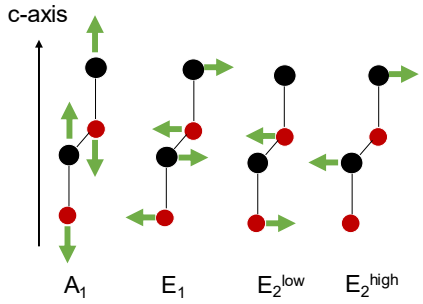

Fig1.7 Lattice vibration of wurtzite ZnO and corresponding Raman scattering

Former peak is assigned to E_1 longitudinal optical (LO) phonon mode and latter peak is E_2 mode of lattice vibrations of ZnO. E_1 (LO) mode is evolved when crystal defects are introduced to the lattice. When excess Zn is introduced in the interstitial sites of wurtzite ZnO, which induces the resonant Raman scattering from E_1 (LO) mode [111]. E_2 mode is generally observed for crystalline wurtzite ZnO [109, 110].

D. Scherson analyzed ZnO formation during discharging of Zn negative electrode by *in situ* Raman spectroscopy. During discharging of the commercial primary Zn/MnO_2 battery, they confirmed the formation of crystalline ZnO near the last stages of

discharging. They did not find any signals originating from $Zn(OH)_2$ [112]. In 2003, the analysis was further carried out under various discharging conditions, *e.g*. different concentration of KOH, discharge time, applied potential [113, 114]. In addition to crystalline ZnO (characterized by evolution of E_2 mode of ZnO), the formation of ZnO with crystal defects (Zn excess in interstitial sites, characterized by evolution of E_1(LO) mode) was notable. This is the case especially at early stages of dissolution and at positive oxidation potential though the formation process of ZnO underlying these changes are not clarified.

Crystal growth of ZnO in chemical synthesis technique

In the field outside the battery, ZnO attracts attention as a functional material having semiconductive properties. Its wide band gap, transparency and non-toxicity are appealing points in several application fields like photovoltaic cell, thermoelectric device and so on [115-118]. For such applications, ZnO films and nano-particles are prepared by sputtering, chemical or physical vapor deposition, hydrothermal synthesis and electrodeposition [119-122].

In chemical synthesis of ZnO in aqueous solution (*e.g*. hydrothermal synthesis and electrodeposition), ZnO is basically formed by supersaturation of zincate ions in alkaline solution. Several similarities are expected in its growth behavior during anodic dissolution of Zn. Under hydrothermal growth of ZnO, Li *et al*. assumed nucleation of ZnO took place via dehydration reactions of zincate species like (1.19) [123].

$$Zn(OH)_4^{2-} + Zn(OH)_4^{2-} \rightarrow Zn_2O(OH)_6^{4-} + H_2O \quad (1.19)$$

Each nucleus grows by incorporation of zincate ion (growth unit) into crystals.

$$Zn_xO_y(OH)_z^{(z+2y-2x)-} + Zn(OH)_4^{2-} \rightarrow Zn_{x+1}O_{y+1}(OH)_{z+2}^{(z+2y-2x+2)-} + H_2O \quad (1.20)$$

The reaction order to zincate ions are known vary depending on the precipitation condition of ZnO. At the presence of ZnO seed layer (existing ZnO nuclei), the reaction follows the first order reaction on zincate ion. However, at the presence of silicate or Li^+ in the solution, the reaction order was reported to be changd [101, 124]. Such a change is ascribed to alteration to the rate determining step (r.d.s) for ZnO formation; by the presence of adsorbate and dopant on/in the crystal, r.d.s may change from decomposition at the surface to nucleation (dehydration reactions between zincate species) because of an inhibition on the former reaction [124].

Similar discussion was applied for anodic dissolution, too. Dirkse thought polymeric zincate species like Fig 1.8 are formed in supersaturated zincate solutions though these structures have not been clarified and identified in the solution yet [100]. Szpak also claimed that nucleation & growth is governed by the formation of zincate polymeric species and its growth by addition of $Zn(OH)_3^-$ [104]. However, less attempts have been made to explain morphology and crystal structures of precipitated ZnO based on this concept.

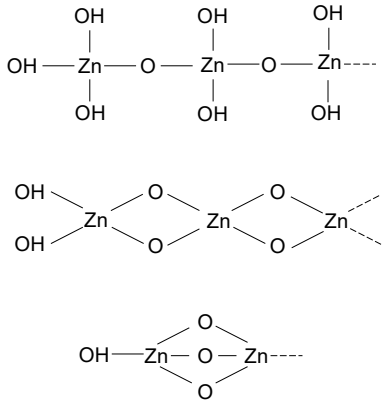

Fig. 1.8 Structure of polymeric zincate species

1.3 Research and Development of Zn Batteries

1.3.1 Controlling methods for Zn negative electrode

Until now, several controlling methods has been invented to overcome the issue of morphological changes and redistribution of active materials. Here, these methods are briefly introduced. An emphasis is placed on explaining the role of each controlling method in interfacial phenomena.

Additive / Composition of electrolyte

By adding chemical species altering the electrochemical behaviors of Zn negative electrode in the electrode or electrolyte, the cyclability can be improved. McLarnon and Cairns listed several additive candidates for Zn negative electrode [43]. Since organic species are often used in electrodeposition industry, their effects are also considered in battery operation, too. Following roles have been suggested; (1) suppressing the formation of dendrite by modifying the surface reaction by adsorption on the surface [125-127], (2) Changing the formation behavior of discharge products by interactions with oxide species [128-130], (3) promoting ZnO formation by altering the properties of electrolyte (water and OH^- activity) [97]. Although some of them are

beneficial for improving the cyclability of the electrode, addition of organic species sometimes causes an increase in the solution resistance (decrease in ionic conductivity), and there is a concern over decomposition of organic species during electrochemical reactions [97, 131]. Therefore, the care must be taken with respect to battery performance and stability of additive species during long term cycling.

Inorganic additives (ionic species and metal) also attract attention. During electrodeposition, it has been recognized that addition of metal species in electrolyte or electrode can alter the morphological evolution of electrodeposited Zn [43, 132]. Especially, lead addition is known to suppress dendrite and mossy structures [133-136]. This aspect will be discussed in detail in 1.3.2. During discharge, a composite electrode like calcium-zincate can improve the cyclability mainly by decreasing the solubility of discharge products and suppressing the redistribution of active materials (described in 1.3.4) [137, 138]. A drawback of this methods is a decrease in the specific capacity by introduction of elements which does not contribute to the electrochemical reactions [137]. Types of anion in Zn salt or supporting electrolyte also has influences on charge-discharge behavior. For example, nitrate ions are known to induce the formation of mossy structures [139, 140]. Such a change originates from the reaction of anionic species itself (reductive decomposition) or specific adsorption on the electrode surface, and following changes in nucleation & growth behavior of Zn [141-143]. Similarly, the cationic species also alters the electrochemical behaviors by forming surface alloy or changing the double layer structures [144, 145]. ZnO formation behavior is known to be affected by ionic species (acetate, nitrate, alkali cations) in hydrothermal synthesis or electrodeposition, but this aspect is rarely examined during anodic dissolution of Zn [115, 118, 123, 124].

Shape of active materials

In addition to electrolyte composition and electrode materials (Zn, ZnO, conductive supporting agents, binder and additives), the shapes of active materials are known to influence the cyclability of the electrode. In general, smaller particles with large surface area are preferred because active surface area can be maximized, and substantial current density can be decreased [26-29]. For example, Wen *et al*. tried to synthesize ZnO with various morphologies and use them as active materials for Zn electrodes. They found that “hollow-fusiform” ZnO exhibited better electrochemical activity and cyclability than conventional ZnO powder and hexagonal pyramid-like structures [106, 107].

However, unlike the graphite anode in lithium-ion batteries, initial morphologies of Zn active materials are no longer maintained after several cycle numbers. This is because metal Zn is dissolved into electrolyte and ZnO precipitation occurs with

supersaturation of zincate. In other words, it is required to control Zn and ZnO morphologies not only at initial state but also during electrochemical reactions.

Electrolyte flow

In electrodeposition process, electrolyte flow is often introduced to decrease the concentration overpotential by enhancing mass transfer of ionic species near the electrode surface. This is achieved by thinning diffusion layer thickness on the electrode.

Introduction of electrolyte flow is advantageous for the battery operation as well in terms of increasing the voltaic efficiency, suppressing the dendrite, and avoiding the supersaturation and ZnO precipitation (materials redistribution). For Zn batteries, a battery using electrolyte flow is called "flow-assisted battery". (In conventional flow battery like vanadium redox-flow battery, ionic species are converted each other during charge-discharge cycles, but the active materials are converted between metal Zn and Zn^{2+} in "flow-assisted" battery.) Since electrodeposition (charging) can be directly performed on a current collector, a large-scale battery can be fabricated much easier than the conventional batteries using pasted electrode [30-32, 40, 41]. Details and previous studies regarding flow-assisted battery is described in 1.3.3.

Current collector (Substrate)

In flow-assisted battery, the charge-discharge reactions are performed directly by electrodeposition and anodic dissolution of Zn on current collector. In this case, current collector is analogous to a substrate for Zn electrodeposition. In general, the electrodeposition behavior is affected by substrate properties. McBreen *et al*. investigated effects of various substrates on Zn electrodeposition behavior, and found that morphologies and texture of electrodeposited Zn were influenced by types of substrate. Alloy formation with substrate, and misfit between the Zn basal plane and the lattice of underlying metal is the reasons for various growth behaviors [146, 147]. Banerjee *et al*. compared charge-discharge behaviors of Zn on various substrates [148]. Coulombic efficiency was dependent on the substrate metals, and Sn exhibited the best performance due to compact Zn electrodeposition on this substrate. However, they concluded that use of Sn was unrealistic because Sn itself was severely corroded in alkaline electrolyte. Also, the choice of current collector is restricted by cost, too. Therefore, application of this idea is limited due to the durability and cost of substrates metals although electrodeposition behavior can be controlled by choosing appropriate current collector,.

Separator

In general, the role of separator in the Zn battery is separating the electrolyte to cathode and anode sides, but to maintain hydroxide ions permeable through the membrane. Polyethylene (PE), polypropylene (PP), polyvinyl alcohol (PVA), and polyamide are often used as materials for the membrane of separators [27, 28]. One of the problems regarding the separator is that zinc ionic species are sometimes migrate through the open structures (pores) of the membrane, which increases the concentration polarization and decreases the cycle efficiencies. Several approaches have been invented to solve this problem. Kiros *et al*. introduced $Mn(OH)_2$ particles to the membrane and avoided zincate migration [149]. Sulfonation of microporous membrane resulted in high anionic transport numbers and better cyclability [150]. Sometimes, separators are useful to retard the dendritic growth by physically blocking the tip of dendrites [151].

For the application in the flow-assisted battery, however, it is sometimes claimed that separator can be eliminated because of enhanced mass transfer and direct electrodeposition/dissolution on current collector, which is advantageous for reducing the total cost of the battery [40, 42].

Some of these controlling methods are proved to be beneficial for improving the cyclability of Zn negative electrodes. However, there are sometimes compromise between the cyclability and other battery performances (*e.g.* specific capacity, conductivity, voltaic efficiency). Knowledge in the electrodeposition process of Zn is valuable even for the battery application because its reaction corresponds to the charging reaction. Nevertheless, there are several differences between electrodeposition and charging operation of the battery. First, electrodeposition is performed at a certain fixed current density or applied potential. It means suitable current can be selected based on coulombic efficiency and morphologies. In contrast, the battery operation requires wide range of charging currents. The cyclability and performance should be maintained under these conditions. Second, the maintenance in electrodeposition conditions (*e.g.* composition of electrolyte) is performed occasionally to sustain the quality of electrodeposits, but battery requires long term cyclability without such an maintenance [152, 153]. Third, not only electrodeposition but also anodic dissolution is performed in the battery operation. This requires that the charging products (electrodeposited Zn) can be reversibly oxidized to Zn ions or ZnO again. Among these methods, effects of metal additive, electrolyte flow, and solubility of zincate are further discussed below.

1.3.2 Metal additives for controlling Zn electrodeposition

Effects of metal species in the electrolyte on Zn electrodeposition behaviors have been important topics in the electrowinning process, and several papers were published regarding this matter [154-158]. In this case, metal species are not additives but impurities in the solution. For example, Mackinnon *et al*. summarized the effects of several metal impurities [154]. Their effects have been mainly discussed with respect to deposition potential of Zn, coulombic efficiency, morphology and texture evolution (crystal orientation). Especially, the coulombic efficiency during Zn electrodeposition is significantly influenced by impurity metals. For example, In and Tl improved the coulombic efficiency, but Sn and Ge decreased the efficiency. Interestingly, the current efficiency periodically changed depending on the atomic number of additive metals. These trends were explained by periodic changes in exchange current for hydrogen evolution reaction (HER) of metals; at the presence of impurities with high overpotential (low exchange current) for HER, the coulombic efficiency improves. Thus, the changes in the electrodeposition behavior is thought to originate from codeposited metal species. However, morphological changes by impurities are not explained.

Among several impurities effect, Pb is often analyzed because Pb is one of the major impurities contained in the mineral resources of Zn (smithsonite) [159, 160]. Pb improves the coulombic efficiency probably due to higher overpotential for HER than that of Zn. Additionally, it increases the overpotential for Zn electrodeposition, and induces morphological changes. Wiart *et al*. carried out electrochemical impedance spectroscopy (EIS) on Zn electrodeposition with Pb impurities in sulfate electrolyte focusing on changes in the elementary steps for Zn electrodeposition [161, 162]. They concluded that rate constant of some elementary steps for Zn electrodeposition like (1.21) and HER were decreased by the presence of Pb_{ad}, but charge transfer reactions involved in Zn electrodeposition were not modified by Pb [161, 162, 167]. Similar effects were elucidated even in alkaline solution by Mao *et al*. with the polarization analysis [133]. The changes in morphological features (suppression of dendrites and mossy structures) are also ascribed to these changes in elementary steps for Zn electrodeposition.

$$ZnH_{ad}^{+} + H^{+} + e^{-} \rightarrow Zn + H_2 \quad (1.21)$$

Similarly, positive influences of metal additives have been recognized from 1970s during the development of Zn negative electrode. For primary batteries, it is beneficial for avoiding self-discharge by suppressing HER [163-165]. Furthermore, their potential effects in compact Zn electrodeposition motivated many researchers to shed

light on additive effects in secondary Zn batteries [43, 26-29, 50, 132, 166-172]. However, the use of Pb in Zn battery is unrealistic because of its toxicity; RoHS regulation limits the commercialization of electric devices containing Pb in the components [173, 174]. Thus, alternative additive species are required. From above described effects of additive metals, general requirements for additive species are (1) having more positive deposition potential than Zn (codeposition with Zn), (2) having high overpotential for HER (avoiding loss of the coulombic efficiency), (3) soluble in alkaline electrolyte, and (4) no toxicity. Based on these requirements, Bi, Sn and In are potential candidates for obtaining compact Zn electrodeposition [31, 50, 168, 172, 175]. However, there are several questions unanswered. First, less attention has been paid to the mechanisms behind the morphological changes by these species. Although correlations between morphological change and suppressed HER is postulated, there is no direct evidence. Moser *et al*. carried out *in situ* XRD analysis on Zn electrodes with Bi additives, and found that Bi was reduced prior to the Zn electrodeposition [168]. They thought Bi provided the conductive path for active materials of the negative electrode. However, Y. S. Meng *et al.* claimed that an improved cyclability could not be explained only by the increased conductivity [175]. Furthermore, there is no systematic comparisons between the different additive species on compact Zn electrodeposition and the battery characteristics. Quantitative criteria for the use of additive metals in Zn batteries is still missing.

1.3.3 Flow-assisted Zn battery

In the conventional battery design, active materials of Zn (powder of metallic Zn and ZnO) are pasted on the current collector and tightly assembled in the battery. Aim of this architecture is to achieve high energy density by densely packed active materials in the battery. On the other hand, a different architecture has been suggested for attaining scalability of the battery; charge-discharge reactions are performed directly on the current collector in flowing electrolyte containing Zn^{2+} ions [30-32, 40, 41]. In other words, the power unit (electrodes) and the energy storage unit (electrolyte tank) are separated [40]. Such a battery is called flow-assisted Zn battery. Fig. 1.9 shows a schematic image of the flow-assisted battery.

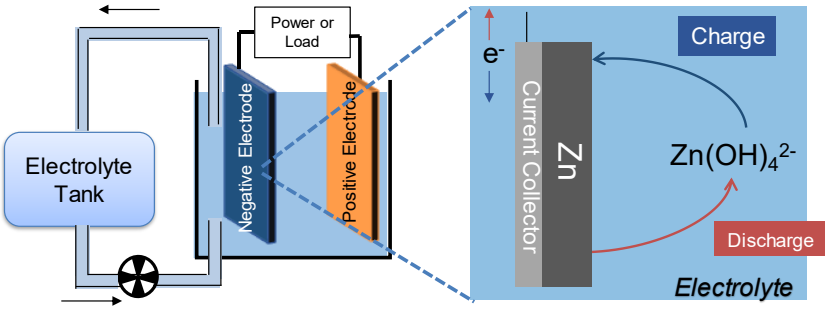

Fig. 1.9Schematic image of flow-assisted battery

There are several advantages of flow-assisted battery. First, simple structures make it possible to fabricate large-scale batteries at low cost. Scale-up is easily achieved by just enlarging the electrode size and electrolyte volume. Second, concentration overpotential during the charge-discharge reaction can be minimized by thinning diffusion layer by introduction of an electrolyte flow. This is beneficial for increasing the voltaic efficiency, mitigating the dendrite growth of Zn, and avoiding side reactions (HER on negative electrode and oxygen evolution reaction, OER on positive electrode). Formation of ZnO during the discharge is suppressed under electrolyte flow because the supersaturation of zincate is not attained at the surface. It means charge-discharge reactions can be performed simply by deposition and dissolution of metal Zn on current collector.

Some attempts were made from 1970s to fabricate Zn flow-assisted battery [176, 177]. However, it attracts major attention after 2010s, when the needs for the grid-scale energy storage system grows; it is recognized that large-scale battery can be developed with considerably lower cost than that of Li-ion batteries [21, 30-34, 41, 42]. Better cyclability of the flow-assisted battery than that of pasted electrode was confirmed. However, it is also recognized that short-circuiting tends to happen even under electrolyte flow [42, 178].

The group in the City University of New York carried out successive studies on the Zn flow-assisted batteries. In 2010, they observed the growth behavior of Zn electrodeposits inside the microfluidic device [178]. Short-circuiting occurs by the formation of porous electrodeposits. Such an analysis is further performed by fabricating the battery [179]. They concluded that electrolyte flow itself was beneficial for improving the performance and suppressing the dendrite formation. However, the reconditioning (dissolution at low discharge rate) is required at certain numbers of cycles to attain better cyclability because electrodeposited Zn tends to be inactive and remain on the electrode after discharge. Furthermore, they investigated morphologies of electrodeposited Zn under various charging conditions (current density, electrolyte flow rate and zincate

concentrations) by SEM, and constructed the “map” showing the relation between the electrodeposition condition and the morphologies [180]. They found that mossy structures preferentially formed at low current density and high zincate concentrations which are opposite conditions to that of dendrite formation. The influences of such a morphological change on charge-discharge behavior, and mechanism behind the variations were further analyzed by using rotating disk electrode (RDE) [181]. Current efficiency during the charge-discharge reactions decrease when dendrites and mossy structures were formed, and the value suddenly decreased after several 10 cycling. Formation of compact Zn electrodeposits is beneficial to maintain the high current efficiency. Introduction of electrolyte flow (rotating the electrode) improves the current efficiency at higher charging rate (dendrite growth), but it has no positive influences on the value at low current density. In other words, mossy structure formation is less influenced by mass transfer of Zn species than that for dendrite formation. They also developed bench-scale battery (25 kWh), and it exhibited more than 1000 cycles at cost of *c.a.* 400$/kWh. However, it still suffers from short-circuiting by the formation of mossy structures [42].

In summary, although flow-assisted batteries are promising candidates for the applications in large-scale energy storage, morphological changes of Zn negative electrode are still problematic issues. Especially, the formation of mossy structures at lower current density region is problematic because it seems difficult to suppress the formation of this structure only by varying the electrolyte flowing rate. Therefore, it is strongly required to obtain compact Zn electrodeposits over wide range of charging currents. Profound understanding of nucleation & growth behavior of electrodeposited Zn provides a basis for such a control.

1.3.4 Controlling methods based on low zincate solubility

For achieving high energy density (*e.g.* in Zn-air battery), conventional pasted electrode where active materials (Zn and ZnO particles) are pasted on the current collector is used. In this case, ZnO is inevitably formed on the electrode during discharge due to lack of electrolyte flow and rapid charge-discharge rates [26-29]. Therefore, in addition to electrodeposition process during charging, ZnO formation during discharge is often considered as a major target for controlling electrode reactions. Among many attempts to control discharging behavior, one of the major strategies is to form insoluble discharge products on the electrode surface. In general, the formation of zincate is favored in alkaline zincate solution, and the precipitation of ZnO occurs only when supersaturation condition is attained. Soluble zincate formation in the electrolyte is recognized as a cause

of the battery failure based on two reasons. First, Zn dendrite is easily deposited upon charging process because concentration of zincate ions near the surface is depleted during electrodeposition [97, 98]. Second, by the concentration gradients over the electrode surface due to natural convection, the amount of ZnO precipitates varies depending on the position of the electrode [44, 45], which induces redistribution of active materials over the surface. To overcome these issues, many researchers tried not to form soluble zincate but to fix the discharge products on the electrode surface; when the discharge products (solid) is fixed on the electrode, the charging can be performed without a depletion of reactant species, and redistribution is mitigated by suppressing the concentration variations. This charge-discharge cycles are analogous to Pb-acid battery where Pb and $PbSO_4$ were reversibly converted during the cycles [97, 182]. These situations are schematically drawn in Fig. 1.10.

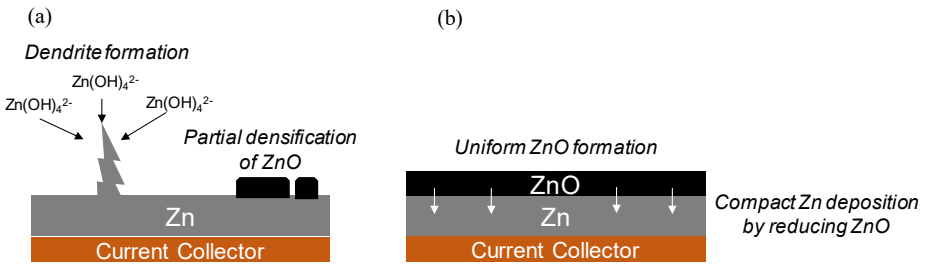

Fig. 1.10 Schematic images during charging (a) after forming soluble zincate during discharge and (b) after forming insoluble discharge products.

Several methods have been developed to fix the discharge products on the electrode surface. One is decreasing the solubility of zincate in the electrolyte by modifying the composition, or by introducing additive species [97, 183, 184]. For example, Nakata *et al*. added propylene carbonate (PC) to decrease H_2O activity, which promoted ZnO formation immediately after the dissolution started [97]. By adding PC, the cyclability improved via suppression on dendrite formation during charging. Calcium addition in the electrode is known to alter the chemical nature of the discharge products; the product became not ZnO but calcium-zincate, and its solubility in alkaline solution is very low [137], which contributed to the reversible conversion between Zn and the discharge product. Another method is physically fixing ZnO on the surface by coating the electrode by an ionomer or introducing separator not permeable to zincate ions [185]. Since zincate ions cannot diffuse away from the electrode, the supersaturation is easily attained in these conditions.

These methods are beneficial for improving the cyclability of the electrode, *i.e.*

maintaining the high coulombic efficiency, avoiding the capacity fading and suppressing the dendrite. However, there are some drawbacks. First, discharge capacity is sometimes limited by lowering zincate solubility because once Zn electrode is totally covered by ZnO, following dissolution reaction becomes impossible. For example, in the case of PC addition mentioned above, the passivation capacity decreased in the order of magnitude [97]. Second, KOH solution generally possesses high conductivity, but this advantage may be sacrificed by modifying the composition, which results in the loss of the voltaic efficiency [97, 128-130]. Furthermore, the electrode still suffers from sudden drop in the discharge capacity and the coulombic efficiencies during cycling. Although dendritic growth is sometimes considered as a cause of such a battery failure, there is no detailed analysis regarding the failure conditions of Zn negative electrode. Some researchers mentioned that there is concern over irreversible reduction of ZnO to Zn, and hydrogen evolution reaction (HER) on ZnO layer [186]. They cause capacity fading and low coulombic efficiencies.

1.4 Scope and Strategy of This Thesis

As described above, many researches have been performed for controlling charge-discharge cycles of Zn negative electrodes. For the application in flow-assisted battery, introduction of electrolyte flow is effective to suppress the formation of dendrite, and actual testing of the energy storage system is also carried out to exhibit better cyclability than that of the conventional pasted electrodes. However, these batteries still suffer from morphological changes of the electrode; highly filamentous mossy structures are often observed upon charging under low current density or under electrolyte flowing conditions.

Towards achieving high energy density and rapid charge-discharge cycles, ZnO formation is inevitable. Some studies recognized that the acceleration of ZnO formation is beneficial to improve the battery reversibility by suppressing dendrite and redistribution of active materials, but less attempts were made to understand nucleation & growth process of ZnO. In other words, although macroscopic effects of ZnO formation (whether it is precipitated or not) has been discussed, the strategies to control microstructure of ZnO and its influence on electrode reaction is lacking.

Based on these backgrounds, the scope and strategies of this thesis is described as follows.

1.4.1 Zn electrodeposition during charging

For controlling charging behavior of Zn negative electrode especially for Zn flow-assisted batteries, it is required to understand and control the morphological evolution of mossy structures. Although there were some studies regarding the mechanisms of mossy structures formation, nucleation & growth process behind this irregular deposition behavior is not fully understood. Therefore, in chapter 2, deposition behavior of mossy structures is investigated in detail. First, its growth behavior is compared to dendrite formed at high current density region via *in-situ* optical microscope analysis. Based on macroscopic growth behavior of the structure, its characteristic growth process is discussed. Then, by focusing on early stages of morphological evolution by SEM and TEM, nucleation & growth process behind mossy structure formation is elucidated. Mechanisms of mossy structure formation is discussed in this context.

Towards retarding formation of mossy structure during operation of the battery, the effects of metal additives are thoughtfully investigated in chapter 3. By investigating electrochemical behaviors of Zn and its crystal growth in additive containing solution, the involvements of additive species in Zn electrodeposition process are elucidated. In order to demonstrate the applicability of metal additives, their effects are investigated in Zn-Ni flow-assisted battery under conditions close to the practical battery operation. Through these investigations, a guiding principle to use metal additives in flow-assisted battery is established.

1.4.2 ZnO formation during discharge

Based on its characteristic formation process (precipitation via supersaturation in the solution near the electrode), nucleation & growth process behind ZnO formation is investigated in chapter 4. Especially, the effects of electrolyte composition and microstructures of Zn electrode on ZnO formation are analyzed by electrochemical measurements, SEM and XRD. *In situ* Raman spectroscopy was also performed to shed light on dynamic changes of the crystal growth of ZnO during discharge. Importance of ZnO formation in charge-discharge cycles of the electrode is pursued based on the electrochemical behavior of passivated electrode (*e.g.* re-charging after ZnO formation).

Chapter 5 focuses on controlling methods for Zn dissolution and ZnO formation. Especially, the effects of Li^+ on discharge behavior is analyzed. Although Li^+ is often used as an additive in chemical synthesis (hydrothermal growth) of ZnO or electrolyte for the battery, their involvements in discharge reaction is not fully understood. Furthermore, charging behavior after passivation reveals the beneficial effects of Li^+ to suppress surface roughening of the electrode. They are why Li^+ effects are investigated in this chapter.

Through comparative study to chapter 4, the involvements of Li^+ in dissolution of Zn and ZnO formation are revealed. From these studies, it is clarified that what factors should be controlled toward achieving high energy density and rapid charge-discharge cycles.

Reference

[1] Agency for Natural Resources and Energy, http://www.enecho.meti.go.jp/about/special/tokushu/saiene/saienecost.html, (Accessed on November 29th, 2018).

[2] Agency for Natural Resources and Energy, 5th Strategic Energy Plan, http://www.enecho.meti.go.jp/en/category/others/basic_plan/5th/pdf/strategic_energy_plan.pdf, (Accessed on November 29th, 2018).

[3] T. Shibata, T. Kumamoto, Y. Nagaoka, K. Kawase, K. Yano, Redox Flow Batteries for the Stable Supply of Renewable Energy, *SEI Technical Review*, **76** (2013) 14-22.

[4] Y. Kojima, Battery Control Technology for Renewable Energy Penetration, *J. Soc. Instrument and Control Engineers*, **55** (2016) 609.

[5] A. Ishigame, Introduction of Investigating R&D Committee on Battery Energy Storage Technology for Power System, *National Convention record I.E.E. Jpn*. **6** (2016) S8(1).

[6] A. Koyama, Expectations for the Battery Energy Storage in Power System, *National Convention record I.E.E. Jpn.* **6** (2016) S8(3).

[7] The Mainichi, Kyushu electric gorws ahead with 1st solar power production halt request, https://mainichi.jp/english/articles/20181013/p2a/00m/0na/017000c, (Accessed on November 29th, 2018).

[8] Y. Kojima, Battery Control Technology for Power System Stable Operation (Part 2: Voltage and transient stability), *National Convention record I.E.E. Jpn*. **6** (2016) S8(15).

[9] T. Matsushita, Demonstration Projects of Battery Control Technology in Japan, *National Convention record I.E.E. Jpn.* **6** (2016) S8(19).

[10] Ministry of Economy, Trade and Industry, http://www.enecho.meti.go.jp/committee/council/basic_problem_committee/028/pdf/28sankou2-2.pdf (Accessed on November 30th, 2018).

[11] Mitsubishi Research Institute, Inc., http://www.meti.go.jp/meti_lib/report/2016fy/000300.pdf (Accessed on November 30th, 2018).

[12] M. Resch, J. Bühler, M. Klausen, A. Sumper, Impact of operation strategies of large scale battery systems on distribution grid planning in Germany, *Renew. Sust. Energ. Rev.* **74** (2017) 1042.

[13] A. Poullikkas, A comparative overview of large-scale battery systems for electricity storage, *Renew. Sust. Energ. Rev.* **27** (2013) 778.

[14] M. Hosseina, S. M. T. Bathaee, Optimal scheduling for distribution network with Redox flow battery storage, *Energy Convers. Manag*. **121** (2016) 145.

[15] A. Zeh, M. Rau, R. Witzmann, Comparison of decentralized and centralized grid-compatible battery storage systems in distribution grids with high PV penetration, *Prog. Photovolt: Res. Appl.* **24** (2016) 496.

[16] S. Akagi, S. Yoshizawa, J. Yoshinaga, M. Ito, Y. Fujimoto, Y. Hayashi, T. Yano, H. Nakahata, T. Hisada, X. M. Tran, Capacity determination of a battery energy storage system based on the control performance of load leveling and voltage control, *J. Int. Counc. Electr. Eng*. **6** (2016) 94.

[17] T. Kobayashi, Battery Energy Storage Technology (Typical Batteries and Features), *National Convention record I.E.E. Jpn*. **6** (2016) S8(7).

[18] Development of Containerized Energy Storage System with Lithium-ion Batteries, *Mitsubishi Heavy Industries Tech. Rev.* **50** (2013) 56.

[19] Y. Sasaki, The Current Perspective of Oversea Storage battery Technologies, *National Convention record I.E.E. Jpn.* **6** (2016) S8(23).

[20] C. Zhang, Y. -L. Wei, P. -F. Cao, M. -C. Lin, Energy storage system: Current studies on batteries and power condition system, *Renew. Sust. Energ. Rev.* **82** (2018) 778.

[21] K. Gong, X. Ma, K.M. Conforti, K.J. Kuttler, J.B. Grunewald, K.L. Yeager, M.Z. Bazant, S. Gu, Y. Yan, A zinc-iron redox-flow battery under $100 per kW h of system capital cost, *Energy Environ. Sci.* **8** (2015) 2941.

[22] M. Hayashi, T. Shodai, *Electrochemistry* **78** (2010) 529.

[23] A. Volta, On the electricity excited by the more contact of conducting substances of different kinds, *Phil. Trans. R. Soc. Lond*. **90** (1800) 403.

[24] G. X. Zhang, Zinc as an Energy Carrier for Energy Conversion and Storage, *Electrochem. Soc. Trans.* **16** (2009) 47.

[25] S. A. Saunder, On the variations of the electromotive force of a new form of Leclanch é's cell, *Nature* **12** (1875) 564.

[26] J. -S. Lee, S. T. Kim, R. Cao, N. -S. Choi, M. Liu, K. T. Lee, J. Cho, Metal Air Batteries with High Energy Density: Li-Air versus Zn-Air, *Adv. Energy Mater.* **1** (2011) 34.

[27] Y. Li, H. Dai, Recent advances in zinc-air batteries, *Chem. Soc. Rev*. **43** (2014) 5257.

[28] P. Pei, K. Wang, Z. Ma, Technologies for extending zinc-air battery's cyclelife: A review, Appl. Energy **128** (2014) 315.

[29] M. Xu, D. G. Ivey, Z. Xie, W. Qu, Rechargeable Zn-air batteries: Progress in electrolyte development and cell configuration advancement, *J. Power Sources* **283** (2015) 358.

[30] C. P. Léon, A. F. Ferrer, J. G. García, D. A. Szánto, F. C. Walsh, Redox flow cells for energy conversion, *J. Power Sources* **160** (2006) 716.

[31] A. Khor, P. Leung, M. R. Mohamed, C. Flox, Q. Xu, L. An, R. G. A. Wills, J. R. Morante, A. A.

Shah, Review on zinc-based hybrid flow batteries: From fundamentals to applications. *Mater. Today Energy* **8** (2018) 80.

[32] D. E. Turney, J. W. Gallaway, G. G. Yadav, R. Ramirez, M. Nyce, S. Banerjee, Y. -c. K. C. -Wiegart, J. Wang, M. J. D'Ambrose, S. Kolhekar, J. Huang, X. Wei, Rechargeable Zinc Alkaline Anodes for Long-Cycle Energy Storage, *Chem. Mater.* **29** (2017) 4819.

[33] Secondary Battery System: Quantitative Technology Scenarios, and Science and Technology Roadmap based on Elemental Technology Structure, Japan Science and Technology Agency, https://www.jst.go.jp/lcs/pdf/fy2013-pp-03.pdf, (Accessed on November 30th, 2018).

[34] New Energy and Industrial Technology Development Organization, http://www.nedo.go.jp/content/100873514.pdf, (Accessed on November 30th, 2018).

[35] Y. Kita, Y. Arai, JPGMEC Current Topics No. 18-13 (2018) 1-8, http://mric.jogmec.go.jp/reports/current/20180611/86983/, (Accessed on November 29th, 2018).

[36] A. Unei, Metal Resources Report (JOGMEC), 48 (2018) 1-15., http://mric.jogmec.go.jp/reports/mr/20180802/88354/, (Accessed on November 29th, 2018).

[37] Japan Oil, Gas and Metals National Corporation, "Mining resources material flow 2017 8. Lithium",
http://mric.jogmec.go.jp/wp-content/uploads/2018/03/material_flow2017_Li.pdf, (Accessed on November 29th, 2018).

[38] M. Watanabe, Metal Resources Report (JOGMEC), 40 (2010) 159., http://mric.jogmec.go.jp/wp-content/old_uploads/reports/resources-report/2010-11/MRv40n4-10.pdf, (Accessed on November 29th, 2018).

[39] K. Yonemura, Metal Resources Report (JOGMEC), 45 (2015) 57., http://mric.jogmec.go.jp/wp-content/old_uploads/reports/resources-report/2015-09/vol45_No3_03.pdf, (Accessed on November 29th, 2018).

[40] J. Cheng, L. Zhang, Y.-S. Yang, Y.-H. Wen, G.-P. Cao, X.-D. Wang, Preliminary study of single flow zinc-nickel battery, *Electrochem. Commun*. **9** (2007) 2639.

[41] P. K. Leung, C. Ponce-de-León, C. T. J. Low, A. A. Shah, F. C. Walsh, Characterization of a zinc-cerium flow battery, *J. Power Sources* **196** (2011) 5174.

[42] D. E. Turney, M. Shmukler, K. Galloway, M. Klein, Y. Ito, T. Sholklapper, J. W. Gallaway, M. Nyce, S. Banerjee, Development and testing of an economic grid-scale flow-assisted zinc/nickel-hydroxide alkaline battery, *J. Power Sources* **264** (2014) 49.

[43] F. R. McLarnon, E. J. Cairns, The Secondary Alkaline Zinc Electrode, *J. Electrochem. Soc.* **138** (1991) 645.

[44] R. E. F. Einerhand, W. Vsscher, Zinc Electrode Shape Change, I. In Situ Monitoring, *J. Electrochem. Soc*. **138** (1991) 1.

[45] R. E. F. Einerhand, W. Vsscher, Zinc Electrode Shape Change, II. Process and Mechanism, *J.*

Electrochem. Soc. **138** (1991) 7.

[46] J. O' M. Bockris, Z. Nagy, A. Damjanovic, On the Deposition and Dissolution of Zinc in Alkaline Solutions, *J. Electrochem. Soc*. **119** (1972) 285.

[47] J. Gong, G. Zangari, Electrodeposition and Characterization of Manganese Coatings, *J. Electrochem. Soc*. **149** (2002) C209.

[48] R. D. Naybour, Morphologies of zinc electrodeposited from zinc-saturated aqueous alkaline solution, Electrochim. Acta **13** (1968) 763.

[49] R. D. Naybour, The Effect of Electrolyte Flow on the Morphology of Zinc Electrodeposited from Aqueous Alkaline Solution Containing Zincate Ions, *J. Electrochem. Soc*. **116** (1969) 520.

[50] R. Y. Wang, D. W. Kirk, G. X. Zhang, Effects of Deposition Conditions on the Morphology of Zinc Deposits from Alkaline Zincate Solutions, *J. Electrochem. Soc.* **153** (2006) C357.

[51] E. Budevski, W. Bostanoff, T. Witanoff, Z. Stoinoff, A. Kotzewa, R. Kaischew, Kembildungserscheinungen an veretzungsfreien (100)-flächen von sibereinkristallen, *Electrochim. Acta* **11** (1966) 1697.

[52] R. Kaischew, E. Budevski, Surface Processes in Electrocrystallization, Contemp. Phys. 8 (1967) 489.

[53] V. Bostanov, W. Obretenov, G. Staikov, D. K. Roe, E. Budevski, *J. Crys. Growth* **52** (1981) 761.

[54] J. M. Keen, J. P. G. Farr, The growth of electrodeposits, *J. Electrochem. Soc*. **109** (1962) 668.

[55] H. J. Pick, G. G. Storey, T. B. Vaughan, The structure of electrodeposited copper-I An experimental study of the growth of copper during electrodeposition, *Electrochim. Acta* **2** (1960) 165.

[56] T. B. Vaughan, H. J. Pick, The structure of electrodeposited copper-II The nucleation of copper electrodeposits on copper substrates, *Electrochim. Acta* **2** (1960) 179.

[57] K. Raeissi, A. Saatchi, M. A. Golozar, Effect of nucleation mode on the morphology and texture of electrodeposited zinc, *J. Appl. Electrochem.* **33** (2003) 635.

[58] J. McBreen, E. Gannon, Kinetics of Zinc Deposition on Zinc Sigle Crystals, *J. Electrochem. Soc*. **133** (1986) 2048.

[59] J. O'M. Bockris, Z. Nagy, D. Drazic, On the Morphology of Zinc Electrodeposition from Alkaline Solutions, *J. Electrochem. Soc*. **120** (1973) 30.

[60] A. Tanaka, T. Nakamura, Y. Ueda, F. Noguchi, Observation of the Electrodeposition of Zinc from Sulfuric Acid Bath, *J. Jpn. Inst. Metals.* **44** (1980) 741.

[61] S. Itoh, N. Yamazoe, T. Seiyama, Electrocrystallization of various metals onto copper single crystal substrates, *Surf. Technol.* **5** (1977) 27.

[62] S. Haruyama, Electrochemistry 31 (1963) 478.

[63] T. Ishiyama, K. Suzuki, K. Hashimoto, On the Processes in Metal Electrocrystallization, *Proceedings of the Institute of Natural Sciences, Nihon Univ.*, **5** (1970) 1-36.

[64] S. Haruyama, Hyomen Gijutusha no Tameno Denkikagaku, Vol. 2, Maruzen (2005).

[65] E. Budevski, G. Staikov, W. Lorenz, Electrochemical phase formation and growth, Wiley-VCH, Weinheim, 1996.

[66] J. W. Diggle, A. R. Despic, J. O'M. Bockris, The Mechanism of the Dendritic Electrocrystallization of Zinc, *J. Electrochem. Soc.* **116** (1969) 1503.

[67] K. I. Popov, P. M. Živković, N. D. Nikolić, Electrochemical aspects of formation of dendrites, *Zastita Materijala* **57** (2016) 55.

[68] I. N. Justinijanoić, A. R. Despić, Some observations on the properties of zinc electrodeposited from alkaline zincate solutions, *Electrochim. Acta* **18** (1973) 709.

[69] A. R. Despić, M. M. Purenović, Critical Overpotential and Induction Time of Dendritic Growth, *J. Electrochem. Soc.* **121** (1974) 329.

[70] N. A. Pangarov, The crystal orientation of electrodeposited metals, *Electrochim. Acta* **7** (1962) 139.

[71] N. A. Pangarov, On the crystal orientation of electrodeposited metals, *Electrochim. Acta* **9** (1964) 721.

[72] M. M. Jakšić, Impurity effects on the micromorphology of electrodeposited zinc I: Theoretical considerations and a review of existing knowledge, *Surf. Coatings Technol.* **24** (1985) 193.

[73] M. M. Jakšić, Impurity effects on the micromorphology of electrodeposited zinc II: Causes, appearances and consequences of spongy zinc growth, *Surf. Coatings Technol.* **28** (1985) 113.

[74] M. M. Jakšić, Impurity effects on the micromorphology of electrodeposited zinc III: Potential sweep analysis, *Surf. Coatings Technol.* **28** (1985) 113.

[75] I. Epselboin, M. Ksouri, R. Wiart, On a Model for the Electrocrstallization of Zinc Involving an Autocatalytic Step, *J. Electrochem. Soc.* **122** (1975) 1206.

[76] J. Bressan, R. Wiart, Inhibited zinc electrodeposition: electrode kinetics and deposit morphology, *J. Appl. Electrochem.* **9** (1979) 43.

[77] C. Cahet, B. Saïdani, R. Wiart, The kinetics of zinc deposition at low overpotentials in alkaline electrolytes, *Electrochim. Acta* **33** (1988) 405.

[78] C. Cahet, B. Saïdani, R. Wiart, A model for zinc deposition in alkaline electrolytes: Inhibition layer and activation mechanism, *Electrochim. Acta* **34** (1989) 1249.

[79] C. Cahet, B. Saïdani, R. Wiart, The behavior of zinc electrode in alkaline electrolytes I. A Kinetic analysis of cathodic deposition, *J. Electrochem. Soc*. **138** (1991) 678.

[80] R. Y. Wang, D. W. Kirk, G. X. Zhang, Characterization and Growth Mechanism of Filamentous Zinc Electrodeposits, *Electrochem. Soc. Trans*. **2** (2007) 19.

[81] W. Xu, J. Wang, F. Ding, X. Chen, E. Nasybulin, Y. Zhang, J. -G. Zhang, Lithium metal anodes for rechargeable batteries, *Energy Envrion. Sci*. **7** (2014) 513.

[82] J. Yamaki, S. Tobishima, K. Hayashi, K. Saito, Y. Nemoto, M. Arakawa, A consideration of the morphology of electrochemically deposited lithium in an organic electrolyte, *J. Power Sources* **74**

(1998) 219.
[83] K. N. Wood, E. Kazyak, A. F. Chadwick, K. -H. Chen, J. -G. Zhang, K. Thornton, N. P. Dasgupta, Dendrites and Pits: Untangling the Complex Behavior of Lithium Metal Anodes through Operando Video Microscopy, *ACS Cent. Sci*. **2** (2016) 790.
[84] T. Nishida, K. Nishikawa, M. Rosso, Y. Fukunaka, Optical observation of Li dendrite growth in ionic liquid, *Electrochim. Acta* **100** (2013) 333.
[85] K. Nishikawa, T. Mori, T. Nishida, Y. Fukunaka, M. Rosso, T. Homma, In Situ Observation of Dendrite Growth of Electrodeposited Li Metal, *J. Electrochem. Soc*. **157** (2010) A1212.
[86] P. Bai, J. Li, F. R. Brushett, M. Z. Bazant, Transition of lithium growth mechanism in liquid electrolytes, *Energy Environ. Sci.* **9** (2016) 3221.
[87] H. J. Chang, A. J. Ilott, N. M. Trease, M. Mohammadi, A. Jerschow, C. P. Grey, Correlating Microstructural Lithium Metal Growth with Electrolyte Salt Depletion in Lithium Batteries Using ^{7}Li MRI, *J. Am. Chem. Soc.* **137** (2015) 15209.
[88] J. Steiger, D. Kramer, R. Mönig, Microscopic observations of the formation, growth and shrinkage of lithium moss during electrodeposition and dissolution, *Electrochim. Acta* **136** (2014) 529.
[89] J. Steiger, D. Kramer, R. Mönig, J. Power Sources, Mechanisms of dendritic growth investigated by in situ light microscopy during electrodeposition and dissolution of lithium, *J. Power Sources* **261** (2014) 112.
[90] A. Kushima, K. P. So, C. Su, P. Bai, N. Kuriyama, T. Maebashi, Y. Fujiwara, M. Z. Bazant, J. Li, Liquid cell transmission electron microscopy observation of lithium metal growth and dissolution: Root growth, dead lithium and lithium flotsams, *Nano Energy* **32** (2017) 271.
[91] I. Arise, Y. Fukunaka, F. R. McLarnon, Ionic Mass Transfer Accompanying Anodic Dissolution of Zinc in Alkaline Solution, *J. Electrochem. Soc*. **153** (2006) A69.
[92] I. Arise, S. Kawai, Y. Fukunaka, F. R. McLarnon, Numerical Calculation of Ionic Mass-Transfer Rates Accompanying Anodic Zinc Dissolution in Alkaline Solution, *J. Electrochem. Soc.* **157** (2010) A171.
[93] I. Arise, S. Kawai, Y. Fukunaka, F. R. McLarnon, Coupling Phenomena Between Zinc Surface Morphological Variations and Ionic Mass Transfer Rate in Alkaline Solution, *J. Electrochem. Soc.* **160** (2013) D66-D74.
[94] L. M. Bauch, A. Higginson, Passivation of zinc in concentrated alkaline solution – I. Characteristic of active dissolution prior to passivation, *Electrochim. Acta* **30** (1985) 1163-1172.
[95] L. M. Bauch, A. R. Baikie, Passivation of zinc in concentrated alkaline solution – II. Role of various experimental factors and the distinction between the solid-state and dissolution-precipitation mechanisms, *Electrochim. Acta* **30** (1985) 1173.
[96] A. Nakata, H. Murayama, K. Fukuda, T. Yamane, H. Arai, T. Hirai, Y. Uchimoto, J. Yamaki, Z. Ogumi, Transformation of Leaf-like Zinc Dendrite in Oxidation and Reduction Cycle, *Electrochim.*

Acta **166** (2015) 82.

[97] A. Nakata, H. Arai, T. Yamane, T. Hirai, Z. Ogumi, Preserving Zinc Electrode Morphology in Aqueous Alkaline Electrolytes Mixed with Highly Concentrated Organic Solvent, *J. Electrochem. Soc.* **163** (2016) A50.

[98] H. -I. Kim, E. -J. Kim, S. -J. Kim, H. -C. Shin, Influence of ZnO precipitation on the cycling stability of rechargeable Zn-air batteries, *J. Appl. Electrochem.* **45** (2015) 335-342.

[99] M. Bockelmann, L. Reining, U. Kunz, T. Turek, Electrochemical characterization and mathematical modeling of zinc passivation in alkaline solutions; A review, *Electrochim. Acta* **237** (2017) 276.

[100] C. D. Chouvy, J. Vedel, M. C. B. Funel, R. Cortes, Supersaturated zincate solutions: A Structural Study, *J. Electrochem. Soc*. **142** (1995) 1359.

[101] C. D. Chouvy, J. Vedel, Supersaturated zincate solutions: A study of the decomposition kinetics, *J. Electrochem. Soc.* **138** (1991) 2538.

[102] T. Corridoni, A. Sodo, F. Bruni, M. A. Ricci, M. Nardone, Probing water dynamics with OH^-, *Chem. Phys.* **336** (2007) 183.

[103] R. W. Powers, M. W. Breiter, The anodic dissolution and passivation of zinc in concentrated potassium hydroxide solutions, *J. Electrochem. Soc*. **116** (1969) 719.

[104] S. Szpak, C. J. Gabriel, The Zn-KOH System: The Solution-Precipitation Path for Anodic ZnO Formation, *J. Electrochem. Soc*. **126** (1979) 1914.

[105] M. Liu, G. M. Cook, N. P. Yao, Passivation of Zinc Anodes in KOH Electrolytes, *J. Electrochem. Soc*. **128** (1981) 1664.

[106] R. Wen, Z. Yang, X. Fan, Z. Tan, B. Yang, Electrochemical performances of ZnO with different morphology as anodic materials for Ni/Zn secondary batteries, *Electrochim. Acta* **83** (2012) 376.

[107] Y. F. Yuan, J. P. Tu, H. M. Wu, Y. Z. Yang, D. Q. Shi, X. B. Zhao, Electrochemical perofmance and morphology evolution of nanosized ZnO as anode material of Ni-Zn batteris, *Electrochim. Acta* **51** (2006) 3632.

[108] A. H. Goff, S. Joiret, B. Saïdani, R. Wiart, In-situ Raman spectroscopy applied to the study of the deposition and passivation of zinc in alkaline electrolytes, *J. Electroanal. Chem*. **263** (1989) 127.

[109] T. C. Damen, S. P. S. Porto, B. Tell, Raman Effect in Zinc Oxide, *Phys. Rev*. **142** (1966) 570.

[110] C. V. Manzano, O. Caballero-Calero, S. Hormeño, M. Penedo, M. Luna, M. S. Martín-González, ZnO morphology control by pulsed electrodeposition, *J. Phys. Chem. C* **117** (2013) 1502.

[111] J. M. Calleja, M. Cardona, Resonant Raman scattering in ZnO, *Phys. Rev. B* **16** (1977) 3753.

[112] W. B. Cai, Q. Shi, M. F. Mansuetto, D. A. Scherson, In situ Raman spectroscopy on an operating AA Zn-MnO_2 battery under high discharge currents, *Electrochem. Solid-State Lett.* **3** (2000) 319.

[113] Q. Shi, L. J. Rendek, W. -B. Cai, D. A. Scherson, In situ Raman spectroscopy of single particle microelectrodes: zinc passivation in alkaline electrolytes, *Electrochem. Solid-State Lett.* **6** (2003) E35.

[114] W. -B. Cai, D. A. Scherson, In situ Raman spectroscopy of zinc electrodes in alkaline solutions, *J. Electrochem. Soc.* **150** (2003) B217.

[115] Z. L. Wang, Zinc oxide nanostructures: growth, properties and applications, *J. Phys.: Codens. Matter* **16** (2004) R829.

[116] G. Hua, Y. Zhang, C. Ye, M. Wang, L. Zhang, Controllable growth of ZnO nanoarrays in aqueous solution and their optical properties, *Nanotechnology* **18** (2007) 145605.

[117] K. Ogata, H. Dobashi, K. Koike, S. Sasa, M. Inoue, M. Yano, Growth of Zinc Oxide Nanorods Via Aqueous Solution Process and Their Application for Biosensors, *J. Soc. Mater. Sci. Jpn*. **60** (2011) 976.

[118] H. Matsuo, K. Yoshitoku, M. Saito, H. Takahashi, I. Terasaki, T. Homma, Fabrication of ZnO-Based Thermoelectric Micro-Devices by Electrodeposition, *J. Electrochem. Soc.* **165** (2018) D417.

[119] G. J. Exarhos, S. K. Sharma, Influence of processing variables on the structure and properties of ZnO films, *Thin Solid Films* **270** (1995) 27.

[120] M. Haseman, P. Saadatkia, D. J. Winarski, F. A. Selim, K. D. Leedy, S. Tetlak, D. C. Look, W. Anwand, A. Wagner, Effects of Substrate and Post-Growth Treatments on the Microstructure and Properties of ZnO Thin Films Prepared by Atomic Layer Deposition, *J. Electronic Mater.* **45** (2016) 6337.

[121] X. Liu, X. Wu, H. Cao, R. P. H. Chang, Growth mechanism and properties of ZnO nanorods synthesized by plasma-enhanced chamical vapor deposition, *J. Appl. Phys*. **95** (2004) 3141.

[122] T. Sekiguchi, S. Miyashita, K. Obara, T. Shishido, N. Sakagami, Hydrothermal growth of ZnO single crystals and their optical characterization, *J. Cryst. Growth* **214/215** (2000) 72.

[123] W. -J. Li, E. -W. Shi, W. -Z. Zhong, Z. -W. Yin, Growth mechanism and growth habit of oxide crystals, *J. Cryst. Growth* **203** (1999) 186.

[124] N. Uekawa, R. Yamashita, Y. J. Wu, K. Kakegawa, Effect of alkali metal hydroxide on formation processes of zinc oxide crystallites from aqueous solutions containing $Zn(OH)_4^{2-}$ ions, *Phys. Chem. Chem. Phys*. **6** (2004) 442.

[125] S. J. Banik, R. Akolkar, Suppressing Dendrite Growth during Zinc Electrodeposition by PEG-200 Additive, *J. Electrochem. Soc.* **160** (2013) D519.

[126] S.J. Banik, R. Akolkar, Suppressing Dendrite Growth during Alkaline Zinc Electrodeposition using Polyethyleneimine Additive, *Electrochim. Acta*. **179** (2015) 475.

[127] C. Yang, Z. Zhang, Z. Tian, K. Zhang, J. Li, Y. Lai, Effects of Carboxymethyl Cellulose on the Electrochemical Characteristics and Dendrite Growth of Zinc in Alkaline Solution, *J. Electrochem. Soc*. **163** (2016) A1836.

[128] H. Yang, Y. Cao, X. Ai, L. Xiao, Improved discharge capacity and suppressed surface passivation of zinc anode in dilute alkaline solution using surfactant additives, *J. Power Sources* **128** (2004) 97.

[129] R. K. Ghavami, Z. Rafiei, Performance improvements of alkaline batteries by studying the

effects of different kinds of surfactant and different derivatives of benzene on the electrochemical properties of electrolytic zinc, *J. Power. Sources* **162** (2006) 893.

[130] J. Lee, B. Hwang, M. Part, K. Kim, Improved reversibility of Zn anodes for rechargeable Zn-air batteries by using alkoxide and acetate ions, *Electrochim. Acta* **199** (2016) 164.

[131] O. Berkh, L. Burstein, Y. S. Diamand, E. Gileadi, The Chemical and Electrochemical Activity of Citrate on Pt Electrodes, *J. Electrochem. Soc.* **158** (2011) F85.

[132] J. McBreen, Nickel/zinc batteries, *J. Power Sources* **51** (1994) 37.

[133] Z. Mao, S. Srinivasan, A. J. Appleby, Effect of PbO on zinc electrodeposition from zincate solutions, *J. Appl. Electrochem.* **22** (1992) 693.

[134] J. W. Diggle, A. Damjanovic, The Inhibition of the Dendritic Electrocrystallization of Zinc from Doped Alkaline Zincate Solutions, *J. Electrochem. Soc.* **119** (1972) 1650.

[135] Y.-H. Wen, J. Cheng, L. Zhang, X. Yan, Y.-S. Yang, The inhibition of the spongy electrocrystallization of zinc from doped flowing alkaline zincate solutions, *J. Power Sources* **193** (2009) 890.

[136] Y. Wen, T. Wang, J. Cheng, J. Pan, G. Cao, Y. Yang, Lead ion and tetrabutylammonium bromide as inhibitors of the growth of spongy zinc in single flow zinc/nickel batteries, *Electrochim. Acta* **59** (2012) 64.

[137] X-M. Zhu, H-X. Yang, X-P. Ai, J-X. Yu, Y -L. Cao, Structural and electrochemical characterization of mechanochemically synthesized calcium zincate as rechargeable anodic materials, *J. Appl. Electrochem.* **33** (2003) 607.

[138] Y. Liu, Z. Yang, J. Yan, Zinc hydroxystannate as high cycle performance negative electrode material for Zn/Ni secondary battery, *J. Electrochem. Soc.* **163** (2016) A3146.

[139] G. P. Rajarathnam, M. Schneider, X. Sun, A. M. Vassallo, The influence of supporting electrolyte on zinc half-cell performance in zinc/bromine flow batteries, *J. Electrochem. Soc*. **163** (2016) A5112.

[140] A. J. Gay, F. Bergsma, The influence of nitrate ion on the morphology of zinc electrodeposits, *Electrochim. Acta* **23** (1978) 1067.

[141] N. Vasailjevic, M. Wood, P. J. Heard, W. Schwarzacher, The Influence of Specific Anion Adsorption on the Surface Roughness of Electrodeposited Polycrsytalline Cu Films, *J. Electrochem. Soc.* **157** (2010) D193.

[142] S. Khorsand, K. Raeissi, M.A. Golozar, Effect of Oxalate Anions on Zinc Electrodeposition from an Acidic Sulphate Bath, *J. Electrochem. Soc.* **158** (2011) D377 [143] D. S. Baik, D. J. Fray, Electrodeposition of zinc from high acid zinc chloride solutions, *J. Appl. Electrochem.* **31** (2001) 1141.

[143] O. M. Magnussen, Ordered Adlayers on Metal Electrode Surfaces, *Chem. Rev*. **102** (2002) 679.

[144] M. Nakamura, Y. Nakajima, N. Hoshi, H. Tajiri, O. Sakata, Effect of Non-Specifically Adsorbed Ions on the Surface Oxidation of Pt (111), *Chem. Phys. Chem*. **14** (2013) 2426.

[145] M. R. Vogt, A. Lachwnwitzer, O. M. Magnussen, R. J. Behm, In-situ STM study of the initial

stages of corrosion of Cu(100) electrodes in sulfuric and hydrochloric acid solution, *Surf. Sci.* **399** (1998) 46.

[146] M.G. Chu, J. McBreen, G. Adzic, Substrate Effects on Zinc Deposition from Zincate Solutions I. Deposition on Cu, Au, Cd and Zn, *J. Electrochem. Soc*. **128** (1981) 2281

[147] J. McBreen, M.G. Chu, G. Adzic, Substrate Effects on Zinc Deposition from Zincate Solutions II. Deposition on Pb, Tl, Sn and In, *J. Electrochem. Soc*. **128** (1981) 2287.

[148] X. Wei, D. Desai, G. G. Yadav, D. E. Turney, A. Couzis, S. Banerjee, Impact of anode substrate on electrodeposited zinc over cycling in zinc-anode rechargeable alkaline batteries, *Electrochim. Acta* **212** (2016) 603.

[149] Y. Kiros, Separation and permeability of zincate ions through membranes, *J. Power Sources* **62** (1996) 117.

[150] G. M. Wu, S. J. Lin, J. H. You, C. C. Yang, Study of high-anionic conducting sulfonated microporous membranes for zinc-air electrochemical cells, *Mater. Chem. Phys*. **112** (2008) 798.

[151] C. Chakkaravarthy, A. K. A. Waheed, H. V. K. Udupa, Zinc-air alkaline batteries – a review, *J. Power Sources* **6** (1981) 203.

[152] S. Ishimaru, Auto-Chemical Controller and Analysis of Precious Metal Solution, *J. Surf. Finish. Soc. Jpn.,* **67** (2016) 572.

[153] K. Ito, Automatic Analytical Instruments for Additives in Plating Bath, *J. Surf. Finish. Soc. Jpn.,* **67** (2016) 585.

[154] D. J. Mackinnon, J. M. Brannen, P. L. Fenn, Characterization of impurity effects in zinc electrowinning from industrial acid sulphate electrolyte, *J. Appl. Electrochem*. **17** (1987) 1129.

[155] D. J. Mackinnon, J. M. Brannen, The effect of lead on zinc deposit structures obtained from high purity synthetic and industrial acid sulphate electrolytes, *J. Appl. Electrochem.* **9** (1979) 55.

[156] D. J. Mackinnon, P. L. Fenn, The effect of tin on zinc electrowinning from industrial acid sulphate electrolyte, *J. Appl. Electrochem.* **14** (1984) 701.

[157] H. Nakano, S. Oue, S. Hisano, S. Kobayashi, H. Fukushima, Codeposition Behavior of Impurities during Electrogalvanization in Sulfate Baths in the Presence of Fe Ions, *ISIJ Int.* **47** (2007) 1029.

[158] T. Greul, J. Gerdenitsch, A. W. Hassel, The influence of tin ions on the electrodeposition of zinc, *Mater. Corros.* **65** (2014) 410.

[159] M. Boni, N. Mondillo, The "Calamines" and "Others": The great family of supergene nonsulfide zinc ores, *Ore Geology Rev*. **67** (2015) 208.

[160] E. Abkhoshk, E. Jorjani, M. S. Al-Harahsheh, F. Rashchi, M. Naazeri, Review on the hydrometallurgical processing of non-sulfide zinc ores, *Hydrometallurgy* **149** (2014) 153.

[161] R. Ichino, C. Cachet, R. Wiart, Influence of Ge^{4+} and Pb^{2+} ions on the kinetics of zinc electrodeposition in acidic sulphate electrolyte, *J. Appl. Electrochem*. **25** (1995) 556.

[162] R. Ichino, C. Cachet, R. Wiart, Mechanism of zinc electrodeposition in acidic sulfate electrolytes containing Pb^{2+} ions, *Electrochim. Acta* **41** (1996) 1031.

[163] L. M. Bauch, F. L. Tye, N. C. White, Corrosion and polarization characteristics of zinc in battery electrolyte analogous and the effect of amalgamation, *J. Appl. Electrochem*. **13** (1983) 623.

[164] M. Paramasivam, M. Jayachandran, S. V. Iyer, Influence of alloying additives on the performance of commercial grade aluminium as galvanic anode in alkaline zincate solution for use in primary alkaline batteries, *J. Appl. Electrochem.* **33** (2003) 303.

[165] Y. Sato, M. Takahashi, H. Asakura, T. Yoshida, K. Tada, K. Kobayakawa, Gas evolution behavior of Zn alloy powder in KOH solution, *J. Power Sources* **38** (1992) 317.

[166] F. Mansfeld, S. Gilman, The Effect of Lead Ions on the Dissolution and Deposition Characteristics of a Zinc Single Crystal in 6N KOH, *J. Electrochem. Soc*. **117** (1970) 588.

[167] J. Bressan, R. Wiart, Use of impedance measurements for the control of the dendritic growth of zinc electrodeposits, *J. Appl. Electrochem.* **7** (1977) 505.

[168] F. Moser, F. Fourgeot, R. Rouget, O. Crosnier, T. Brousse, In situ X-ray diffraction investigation of zinc based electrode in Ni-Zn secondary batteries, *Electrochim. Acta* **109** (2013) 110.

[169] J. W. Gallaway, A. M. Gaikwad, B. Hertzberg, C. K. Erdonmez, Y.-C. K. C.-Wiegart, L. A. Sviridov, K. E.-Lutterodt, J. Wang, S. Banerjee, D. A. Steingart, An In Situ Synchrotron Study of Zinc Anode Planarization by a Bismuth Additive, *J. Electrochem. Soc*. **161** (2014) A275.

[170] M. Mansfeld, S. Gilman, The Effect of Several Electrode and Electrolyte Additives on the Corrosion and Polarization Behavior of the Alkaline Zinc Electrode, *J. Electrochem. Soc*. **117** (1970) 1328.

[171] F. Mansfeld, S. Gilman, The Effect of Tin and Tetraethylammonium Ions on the Characteristics of Zinc Deposition on a Zinc Single Crystal in Aqueous KOH, *J. Electrochem. Soc*. **117** (1970) 1154.

[172] H.-I. Kim, H.-C. Shin, SnO additive for dendritic growth suppression of electrolytic zinc, *J. Alloys Compd.* **645** (2015) 7.

[173] S. Kemmlein, D. Herzke, R. J. Law, Brominated flame retardants in the European chemicals policy of REACH – Regulation and determination in materials, *J. Chromatgraphy A* **1216** (2009) 320.

[174] W. Scharnhorst, Life Cycle Assessment in the Telecommunication Industry: A Review, *Int. J. LCA.* **13** (2008) 75.

[175] J. W. Shin, J. -M. You, J. Z. Lee, R. Kumar, L. Yin, J. Wang, Y. S. Meng, Phys., Deposition of ZnO on bismuth species towards a rechargeable Zn-based aqueous battery, *Chem. Chem. Phys.* **18** (2016) 26376.

[176] J. Jorne, J. T. Kim, D. Kralik, The zinc-chlorine battery: half-cell overpotential measurements, *J. Appl. Electrochem*. **9** (1979) 573.

[177] J. McBreen, Rechargeable zinc batteries, *J. Electroanal. Chem.* **168** (1984) 415.

[178] J. W. Gallaway, D. Desai, A. Gaikwad, C. Corredor, S. Banerjee, D. Steingart, A Lateral

Microfluidic Cell for Imaging Electrodeposited Zinc near the Shorting Condition, *J. Electrochem. Soc*. **157** (2010) A1279.

[179] Y. Ito, M. Nyce, R. Plivelich, M. Klein, D. Steingart, S. Banerjee, Zinc morphology in zinc-nickel flow assisted batteries and impact on performance, *J. Power Sources* **196** (2011) 2340.

[180] Y. Ito, X. Wei, D. Desai, D. Steingart, S. Banerjee, An indicator of zinc morphology transition in flowing alkaline electrolyte, *J. Power Sources* **211** (2012) 119.

[181] D. Desai, X. Wei, D. A. Steingart, S. Banerjee, Electrodeposition of preferentially oriented zinc for flow-assisted alkaline batteries, *J. Power Sources* **256** (2014) 145.

[182] C. P. Zhang, S. M. Sharkh, X. Li, F. C. Walsh, C. N. Zhang, J. C. Jiang, The performance of a soluble-lead-acid flow battery and its comparison to a static lead-acid battery, *Energy Convers. Manag.* **52** (2011) 3391.

[183] T. C. Adler, F. R. McLarnon, E. J. Cairns, Low-Zinc-Solubility Electrolytes for Use in Zinc/Nickel Oxide Cells, *J. Electrochem. Soc*. **140** (1993) 289.

[184] D. Schröder, N. N. S. Borker, M. König, U. Krewer, Performance of zinc air batteries with added K_2CO_3 in the alkaline electrolyte, *J. Appl. Electrochem*. **42** (2015) 427.

[185] K. Miyazaki, 3. Zn-Air secondary batteries, *Electrochemistry* **82** (2014) 181.

[186] I. Sanghi, M. Fleishcmann, Some potentiostatic studies on zinc, *Electrochim. Acta* **1** (1959) 161.

Chapter 2:

Growth Behavior of Electrodeposited Zn during Charging of Zn Negative Electrode

2.1 Introduction

During the charging of Zn negative electrode, Zn is electrodeposited on the electrode by reaction (2.1).

$$Zn(OH)_4^{2-} + 2e^- \rightarrow Zn + 4OH^- \quad (2.1)$$

Unlike the currently used graphite anode for Li-ion battery in which Li ion is intercalated into the graphite structures, metallic phase of active material is directly formed on the electrode. Accordingly, the shape of the electrode tends to vary during charge-discharge cycles by forming various morphologies of Zn crystals. In the conventional pasted electrode for Zn-Ni and Zn-air battery, the formation of dendritic Zn (leaf-like or fractal structures of Zn crystals) is often considered as a cause of the battery failures [1, 2]. By continuous deposition of dendrites, they penetrate the separator between the negative and positive electrodes, and cause the short-circuiting by reaching the positive electrode. Dendrite is known to be formed under the diffusion limited condition of Zn ions; when Zn^{2+} is depleted near the electrode surface, deposition is localized on protrusion structures by forming a spherical diffusion layer around the structure [3, 4]. In the case of flow-assisted battery in which Zn electrodeposition is performed under electrolyte flow, dendrite formation can be suppressed by enhanced mass transfer of Zn ions.

Despite this fact, flow-assisted batteries also suffer from severe morphological changes of the electrode during reactions. Turney *et al.* performed charge-discharge cycles of the Zn-Ni flow-assisted battery, and found that highly filamentous, mossy structures are formed upon the battery failure [5, 6]. Evolution of mossy structures is also problematic for the battery because it can cause the short-circuiting, plugging of the electrolyte flow path, and loss of coulombic efficiency by detachment of the structure from a current collector. Ito *et al*. investigated morphological variations of Zn electrodeposits in the Zn-Ni flow-assisted battery in various conditions (zincate concentration, electrolyte flow rate, and current density), and mossy structures are formed even under electrolyte flowing conditions [6]. The most characteristic point of mossy structure formation is that it is preferentially formed at charging at low current density. Accordingly, the formation of mossy structure is governed by a different factor

other than mass transfer of Zn^{2+}.

The formation of mossy structures in Zn electrodeposition has been recognized from early studies in Zn electrodeposition or Zn negative electrode. The correlations between electrodeposition conditions and mossy structure formation is investigated [7, 8]. Many researchers tried to explain the mechanism for this irregular deposition behavior. A common argument is that mossy structure is caused by the uneven chemical or physical state of the electrode surface. For example, a screw-dislocation on the Zn crystals is considered to induce continuous deposition on this site [9, 10]. Side-reactions like hydrogen adsorption and oxide formation are often correlated with mossy structure formation [7, 11, 12]. Among several explanations, the possibility of oxide formation on Zn surface gains the most of attentions for this moment. Wiart *et al*. analyzed electrodeposition behavior at low overpotential by electrochemical impedance spectroscopy (EIS), and established the model describing Zn electrodeposition occurring under oxide layer on the surface [13-16]. However, less attention has been paid to the dynamic growth behavior of mossy structures and the nucleation & growth process behind the irregular deposition. And, it has not been clarified how non-uniformity in the surface state or the reaction mechanism affect the nucleation & growth behavior.

Objective of this chapter is to elucidate the nucleation & growth behavior of Zn behind the mossy structure formation at low overpotential. For this purpose, an evolution of mossy structures was *in situ* analyzed by an optical microscope, and its deposition behavior was compared with dendrite. By focusing on an early stages of mossy structure formation, a characteristic nucleation & growth process of Zn at electrodeposition at low overpotential was revealed. Electrodeposition mechanisms behind such a process are discussed.

2.2 Methodology

2.2.1 Analysis on the polarization behavior and morphological variations of Zn

The polarization behavior and morphological variations during Zn electrodeposition were analyzed by performing Zn electrodeposition on Zn or Cu substrates. Zn substrate is mechanically polished Zn plate (>99.5%, 0.30 mm thickness, Nilaco). Mechanical polishing was performed by a mechanical lapping polishing machine

(MA-400D, Musashino Denshi Co., Ltd.) with a colloidal silica slurry (Semi-Sperse 25, Cabot Microelectronics Corp.). After that, surface was slightly etched in the mixture of 1.0 mL of 35% hydrochloric acid + 100 mL pure water. Cu electrodes were Cu plate (>99.9%, 0.30 mm thickness, Nilaco) or Cu layer on Si wafer (Cu (100 nm)/Cr (10 nm) on Si(111)) prepared by electron beam evaporation (EBX-6D, ULVAC). Mechanical polishing was performed on Cu plate as carried out for Zn plate. Cu electrode was immersed in 45 mL pure water + 5.0 mL 96% sulfuric acid for 30 s before electrochemical measurements. A counter electrode was Zn plate (>99.5%, 0.30 mm thickness, Nilaco), and a reference electrode was Hg/HgO (Inter Chemie. Inc.). A counter electrode was immersed in 45 mL pure water + 5.0 mL 96% sulfuric acid for 30 s before measurements. Potential shown below will be described vs. Hg/HgO. The working electrode and the counter electrode were vertically placed in an electrochemical cell facing each other. The reference electrode was placed between the electrodes. The surface of the working electrode was confined to 0.50 cm^2 by an electrode holder. Schematic image of the cell and the photograph of the holder are shown in Fig. 2.1.

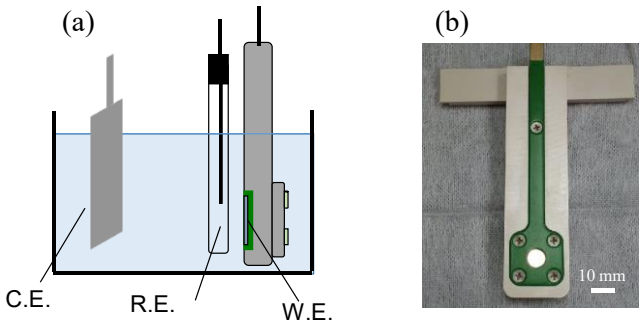

Fig. 2.1 Electrochemical cell and an electrode holder for the working electrode.

Electrolytes for Zn electrodeposition were 6.0 mol dm^{-3} KOH + 0.10 – 0.50 mol dm^{-3} zincate. For preparing the electrolyte, 48wt% KOH (UGR grade, Kanto Chemical) was first diluted to 6.0 mol dm^{-3} by pure water. Then, ZnO (reagent grade, Kanto Chemical) was dissolved in this solution to obtain desire concentration of zincate ions. The electrolyte was deaerated by nitrogen bubble for 10 min before the measurements. For analyzing effects of cation species in the electrolyte, ZnO was dissolved in 50wt% CsOH (99%, Sigma-Aldrich) to yield 5.7 mol dm^{-3} CsOH + desired concentration of zincate. Li containing solution was prepared by dissolving $LiOH \cdot H_2O$ (reagent grade, Kanto Chemical) in pure water, and mixing it with KOH to yield 5.0 mol dm^{-3} KOH + 1.0 mol dm^{-3} LiOH. Electrochemical measurements were carried out by using the electrochemical measurement system (HZ-7000, Hokuto Denko). Linear sweep

voltammetry (LSV) of Cu electrode in 6.0 mol dm^{-3} KOH + 0.50 mol dm^{-3} zincate was measured by sweeping the potential from rest potential to −2.0 V. Electrodeposition was performed both by potentiostatic and galvanostatic conditions. Deposited amount of Zn (thickness of electrodeposited Zn film) was controlled by stopping the deposition at certain passed charge for deposition. Electrodeposition was mainly performed at room temperature (24℃). Rotating disk electrode (RDE) was also used for analyzing Zn electrodeposition behavior under electrolyte flow. In this case, Cu plate was used as a working electrode (confined surface area = 0.50 cm^2), and it was horizontally downward faced to a Zn counter electrode.

Electrochemical impedance spectroscopy (EIS) of Zn electrode in a different alkaline solution was performed by using HZ-7000 equipped with a frequency response analyzer (FRA). A working electrode was Zn wire embedded in epoxy resin with mirror-finished surface (shown in Fig. 2.2, surface area = 1.96×10^{-3} cm^2). This electrode was horizontally upward faced to counter electrode (Pt mesh, Nilaco) and reference electrode (Hg/HgO). Alternating current was superimposed at frequency ranging from 100 kHz to 100 mHz at $\Delta I = \pm 100$ μA cm^{-2} =196 nA at REST potential. Measurements points were 5 points / decades. Prior to EIS measurements, the electrode was polarized at −1500 mV for 3 min to eliminate native oxide layer on Zn surface, then holding at REST potential for another 3 min. Curve fittings of the impedance data to an equivalent circuit were carried out by using a software provided by Hokuto Denko (EIS version 1.0.23).

Surface morphology after electrodeposition was analyzed by optical microscope equipped with CCD camera (VC-3000, Omron) and scanning electron microscopy (SEM, S-5500 or SU-8240, Hitachi). Laser scanning confocal microscope (LSCM, VK-9510, Keyence) was also used for analyzing the surface morphology and evaluate surface roughness. Transmission electron microscopy (TEM, JEM-2010, JEOL) was performed by preparing the TEM samples by focused ion beam etching (FIB, JIB-4000, JEOL) on electrodeposited film on Zn plate. Coulombic efficiency during electrodeposition was evaluated by anodic dissolution at potentiostatic condition (−1.37 V) immediately after electrodeposition at −1.42 V, −1.46 V, and −1.48 V in 6.0 mol dm^{-3} KOH + 0.50 mol dm^{-3} ZnO. The efficiencies were calculated by comparing passed charge during anodic dissolution to that during electrodeposition. Anodic dissolution was stopped after the anodic current dropped to 0 mA. In addition, the efficiency was calculated from the deposited amount of Zn evaluated by inductively coupled plasma emission spectroscopy (ICP-AES, 5500x, Agilent). This analysis was performed after dissolving the electrodeposited Zn on evaporated Cu in 5.0 mL nitric acid. Analyte was diluted to 100 mL before the measurements.

2.2.2 *In situ* analysis by optical microscope

Cross-sectional view

Growth behavior of Zn dendrites and mossy structures were *in situ* observed by an optical microscope equipped with CCD camera (3R-MSUSB601, 3R system). A working electrode was Zn wire (>99.99%, 0.50 mmϕ, Nilaco) embedded in an epoxy resin; edge of the Zn wire was polished, and electrodeposition was performed on this surface. This electrode was prepared by following scheme. First, zinc wire was inserted into a pipette tip, and epoxy resin (Epohold Resin-Quart, Aqra) and curing agent (Epohold Hardener, Aqra) were poured in it. After solidification of the resin (*c.a.* 12 hours), the pipette tip was removed, and the electrode surface was polished by abrasive papers up to #1200. Finally, the mirror-like surface was obtained by the mechanical lapping polishing machine as described above. After the polishing, the electrode was immersed into 1.0 mL 35% hydrochloric acid + 100 mL pure water for 10 s.

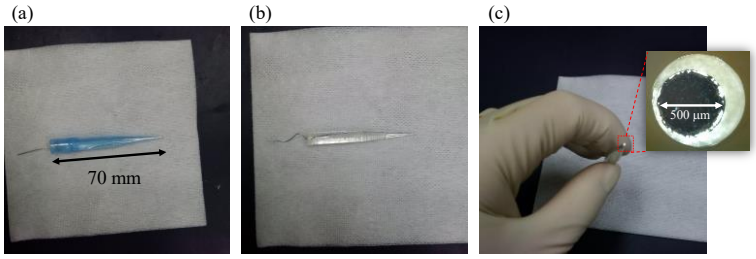

Fig. 2.2 Preparation of the working electrode for *in situ* analysis; (a) Zn wire in a pipette tip, (b) Zn wire embedded in a epoxy resin, and (c) Zn wire after polishing the surface.

After the polishing, the electrode was immersed into 1.0 mL 35% hydrochloric acid + 100 mL pure water for 10 s. This electrode was fixed in a polystyrene case and Zn wires (>99.99%, 0.50 mmϕ, Nilaco) were also introduced as a counter and a quasi-reference electrode. The Photograph of an electrochemical cell is shown in Fig. 2.3.

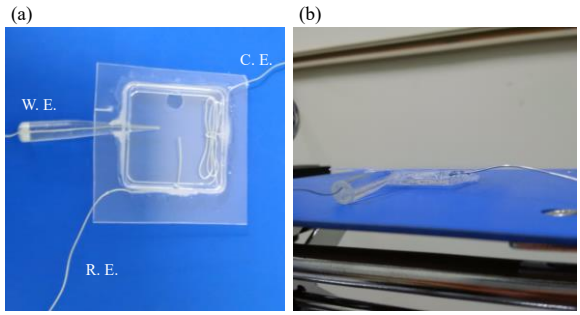

Fig. 2.3 Photograph of an electrochemical cell used in *in situ* analysis; from (a) top of the cell and (b) cross-sectional direction of the cell.

Zn electrodeposition was performed in 6.0 mol dm^{-3} KOH + 0.25 mol dm^{-3} zincate at galvanostatic condition at −10 mA cm^{-2} and −80 mA cm^{-2}. The working electrode was placed vertically in downward or upward faced to the counter electrode during the measurements. Morphological evolution was observed by the CCD camera from the cross-sectional direction of the electrode (corresponding to the viewpoint of Fig. 2.3 (a)). Surface morphology after the electrodeposition was also investigated by SEM (VE-7800, Keyence or SU-8240, Hitachi). For this analysis, electrodeposits formed at −10 mA cm^{-2} were detached from the electrode and pasted on carbon tape.

Top view

Surface morphologies were analyzed from top of the electrode, too. For this analysis, Zn plate was placed on polystyrene case, and the surface area was confined to 0.28 cm^2 (6.0 mmϕ) by polytetrafluoroethylene (PTFE) tape. A Zn wire was placed around the working electrode. Electrodeposition was performed at galvanostatic condition in two-electrode configuration in 6.0 mol dm^{-3} KOH + 0.25 mol dm^{-3} zincate. Prior to the *in situ* observation, Zn electrodeposition was performed at −20 mA cm^{-2} for 500 s. This initial deposition was introduced in order to monitor the morphological changes from initially deposited conditions (layer-like structures). Surface morphology during electrodeposition was observed by optical microscope (DZ2 Zoom Microscope, Union Optical Co., Ltd.) equipped with a CCD camera (ARTCAM-130, ARTRAY Co., Ltd.). Zn electrodeposition was performed at −5.0 mA cm^{-2} and −20 mA cm^{-2}. The schematic image of an electrochemical cell is shows in Fig. 2.4.

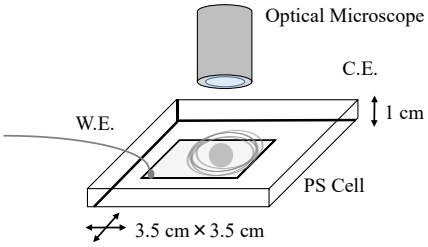

Fig. 2.4 Schematic image of *in situ* observation during electrodeposition from top of the deposits

2.2.3 Pulsed electrodeposition at different current densities

Effects of pulsed electrodeposition on Zn electrodeposition behaviors were investigated by comparing potential profiles, morphological evolution and coulombic efficiencies. Zn electrodeposition was performed on an electron beam evaporated copper

plate as described in 2.2.1. An electrolyte for electrodeposition was 6.0 mol dm^{-3} KOH + 0.50 mol dm^{-3} zincate. Four deposition conditions were set; (1) galvanostatic electrodeposition at −5.0 mA cm^{-2} for 600 s, (2) pulsed electrodeposition at −5.0 mA cm^{-2} for 1 s and 0 mA cm^{-2} for 1 s (600 cycles), (3) galvanostatic electrodeposition at −50 mA cm^{-2} for 60 s, and (4) pulsed electrodeposition at −50 mA cm^{-2} for 1 s and 0 mA cm^{-2} for 1 s (60 cycles). Total passed charge in each condition was set to 3.0 C cm^{-2}. Surface morphology after electrodeposition was investigated by an optical microscope and SEM as performed in the analysis on the early stages of electrodeposition. Coulombic efficiency (η) during electrodeposition at each condition was evaluated by anodic dissolution of electrodeposited film at +10 mA cm^{-2}. By using the time (*t* sec) required for the potential becomes positive (−1320 mV), the coulombic efficiency was evaluated by (2.2).

$$\eta = \frac{-10\ mA \times t\ s}{3000\ mC} \times 100 \tag{2.2}$$

Analysis on surface morphology was performed as described in 2.2.1.

2.3 Results and Discussion

2.3.1 The polarization behavior and morphological variations at different deposition potential

First, the polarization behavior during Zn electrodeposition was analyzed by LSV. Figure 2.5 shows the current during potential sweep from REST potential to −2.0 V. A working electrode was electron beam evaporated Cu on Si wafer.

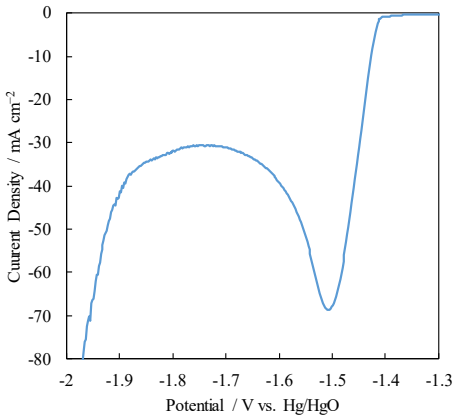

Fig. 2.5 LSV during cathodic scan in 6.0 mol dm^{-3} KOH + 0.50 mol dm^{-3} zincate at scan rate of 20 mV s^{-1}.

From −1.4 V, rapid increase in the current is observed. This corresponds to the electrodeposition reaction of Zn from zincate ion [17-19].

$$Zn(OH)_4^{2-} + 2e^- = Zn + 4OH^- \quad (2.3)$$

The current exhibits a peak around −1.5 V, then it decreases until potential reaches about −1.8 V. This indicates that Zn electrodeposition is under diffusion limited controlled below −1.5 V. At this potential region, thickness of the diffusion layer on the Zn surface increases, which decreases the current for Zn electrodeposition. The current increases again below −1.8 V. Bubbles evolves on the surface at this region. It corresponds to hydrogen evolution reactions (HER) by the decomposition of water molecule.

$$H_2O + 2e^- = H_2 + 2OH^- \quad (2.4)$$

Since HER decreases the coulombic efficiency during the charge-discharge cycles,

charging (Zn electrodeposition) should be performed at the potential above −1.8 V [20].

Morphological variations of the electrodeposited Zn at different deposition potentials were analyzed by potentiostatic deposition of Zn from 6.0 mol dm^{-3} KOH + 0.50 mol dm^{-3} zincate on Zn substrate. Prior to electrodeposition at each potential, Zn was electrodeposited at −1460 mV for 60 s. This process was introduced to avoid influence of native state (*e.g.* native oxide) of Zn substrate on electrodeposition. Based on the potential shown in LSV, electrodeposition was performed at −1420, −1460, −1520, −1620 and −1720 mV. Electrodeposition was stopped at passed charge of 5.0 C cm^{-2}. Fig. 2.6 shows SEM images of the electrodeposits at each deposition potential.

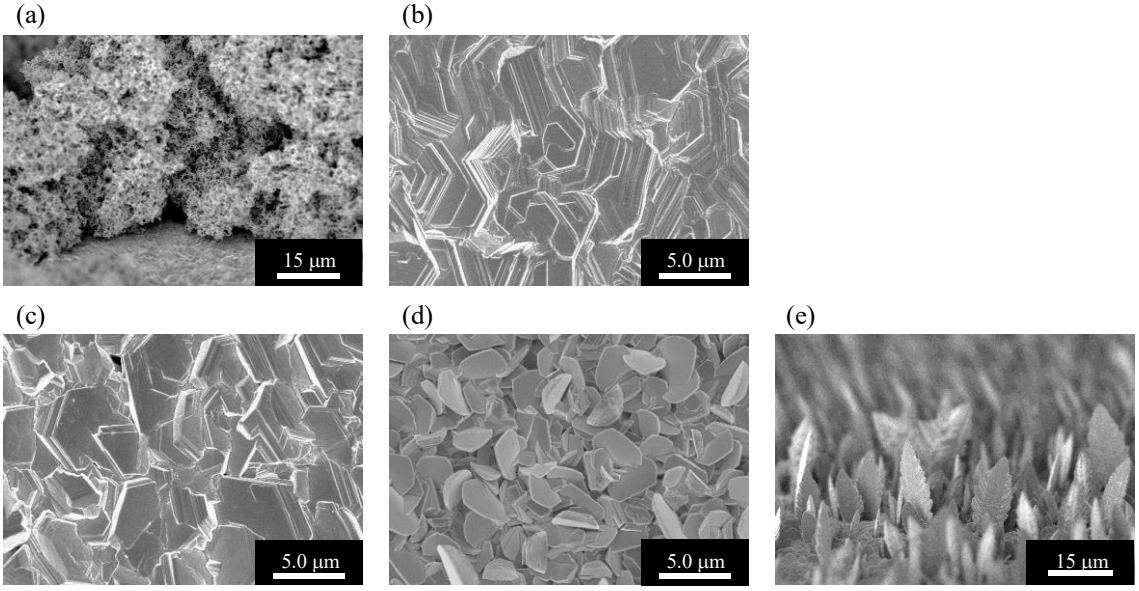

Fig. 2.6 SEM images of Zn electrodeposits formed at (a) −1420, (b) −1460, (c) −1520, (d) −1620 and (e) −1720 mV. Passed charge for deposition is 5.0 C cm^{-2}. (a) and (e) are images taken from cross-sectional direction of the electrode.

At −1460 and −1520 mV, compact deposits comprising stacking of layer-like structures are obtained. Grain boundaries between the particle is less defined at −1460 than that at −1520 mV. These morphologies corresponded to layer-like structures (−1460 mV) and boulders (−1520 mV) as described in the previous paper [7, 8]. At negative deposition potential, defined particles rather than continuous layers are formed due to the transition from two-dimensional (2D) nucleation to three-dimensional (3D) nucleation at high overpotential [4, 21]. At more negative potential below the current reaches the peak value in LSV, rough deposits appear. At −1620 mV; plate-like structures are oriented vertical to the substrate. Leaf-like structures with many branches are formed at −1720 mV. They are

dendrites formed under the diffusion limited condition of zincate ions. In addition, very rough deposits are formed at −1420 mV. Fig. 2.7 shows enlarged image of these structures.

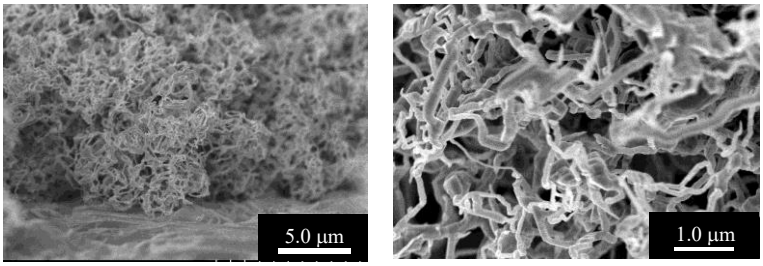

Fig. 2.7 SEM images of Zn electrodeposits formed at −1420 mV.

These rough deposits comprise filamentous deposits. This structure is called mossy structures, a characteristic morphology to Zn electrodeposits formed at low overpotential [7, 8, 22]. In electrodeposition at low overpotential, the deposited film generally exhibits low surface roughness because electrodeposition at low overpotential prefers the deposits with minimum product of surface area and surface free energy (an equilibrium shape of the crystal) [23, 24]. The formation of mossy structure is unique because it enlarges the electrode surface area. Practically, mossy structure formation is problematic especially for the flow-assisted battery [6]. Rough deposits are easily detached from the current collector, which decreases the coulombic efficiency and causes a plugging of electrolyte flow path. Furthermore, it is difficult to control the evolution of mossy structures only by electrolyte flow unlike the dendrite formed at higher overpotential [6, 8]. Actually, the battery failure of the flow-assisted battery often occurs by the evolution of mossy structures [5, 6].

2.3.2 *In situ* analysis on morphological evolution of Zn electrodeposits

Cross-sectional view

In order to monitor the dynamic growth behavior of mossy structures and Zn dendrites, Zn electrodeposition was performed on edge of Zn wire (500 μmϕ) embedded in an epoxy resin, and the morphological evolution was *in situ* observed by an optical microscope equipped with CCD camera. Electrodeposition was performed by galvanostatic conditions at −80 mA cm^{-2} to deposit dendrites and −10 mA cm^{-2} to observe the formation of mossy structures in 6.0 mol dm^{-3} KOH + 0.25 mol dm^{-3} zincate. Fig. 2.8 shows the potential profiles at each current density and the electrode configuration.

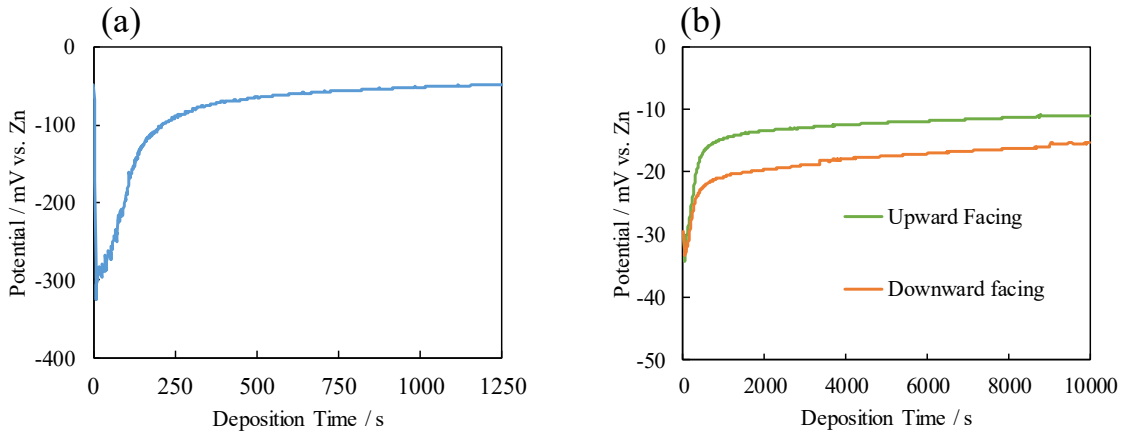

Fig. 2.8 Potential profiles during galvanostatic electrodeposition of Zn on Zn electrode (500 μmϕ) at (a) −80 mA cm^{-2} and (b) −10 mA cm^{-2}. Electrodeposition at −10 mA cm^{-2} was performed in upward faced and downward faced working electrode.

CCD images during electrodepositions are shows in Fig. 2.9 to Fig. 2.11.

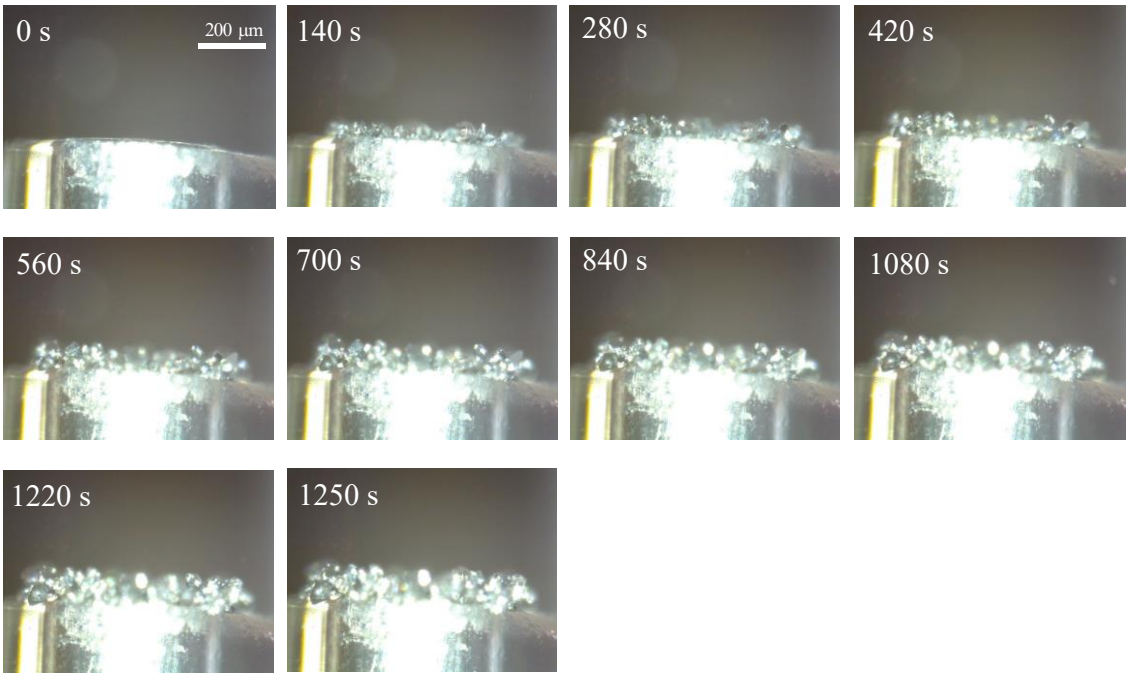

Fig. 2.9 *In situ* CCD images during electrodeposition of Zn at −80 mA cm^{-2} (cross-sectional view).

Fig. 2.10 *In situ* CCD images during electrodeposition of Zn at −10 mA cm^{-2} in upward faced electrode (cross-sectional view).

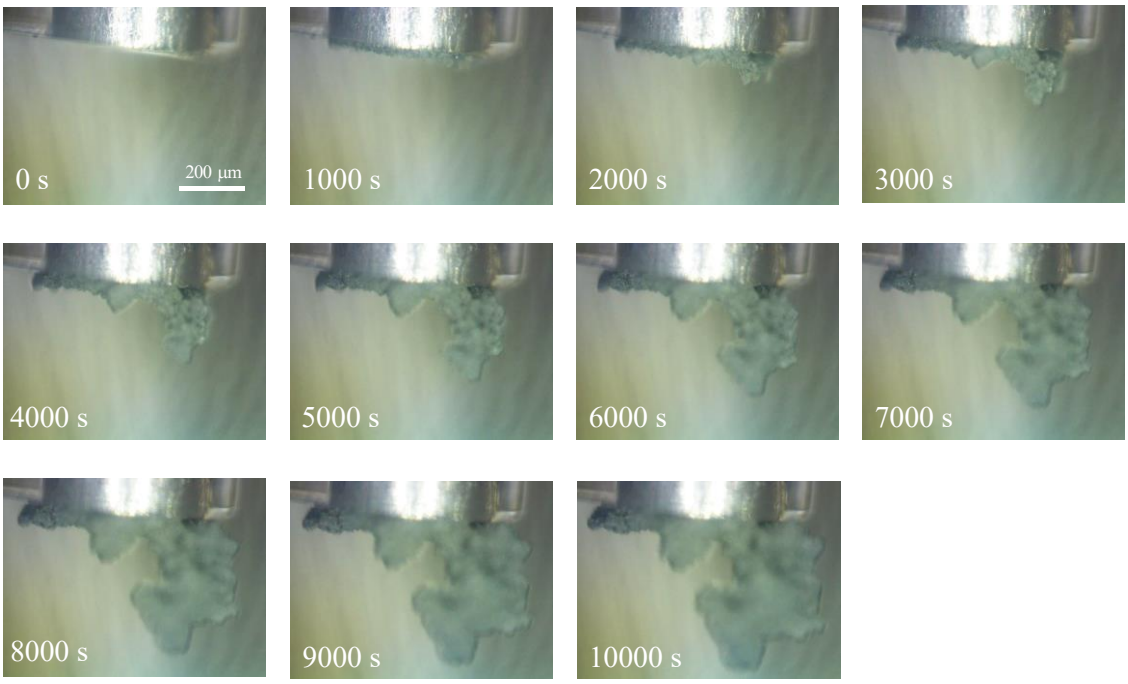

Fig. 2.11 *In situ* CCD images during electrodeposition of Zn at −10 mA cm^{-2} in downward faced electrode (cross-sectional view).

Length of the rough deposits were measured by measuring the vertical length from the

surface of working electrode to the top of the electrodeposit as demonstrated in Fig. 2.12. They are plotted versus deposition time in Fig. 2.13.

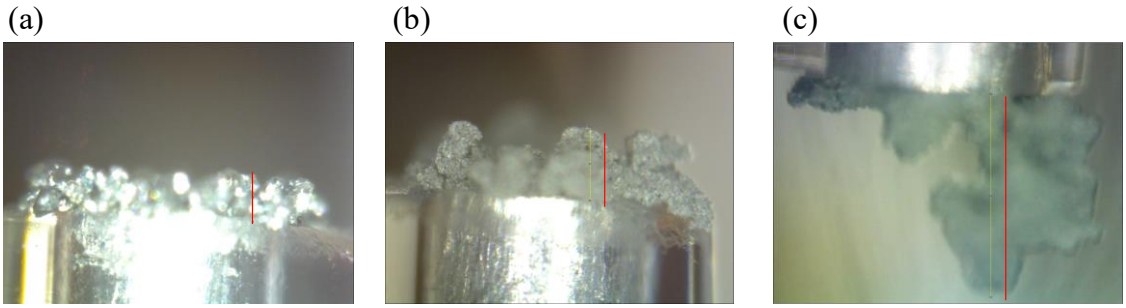

Fig. 2.12 Measurements of the length of rough electrodeposits

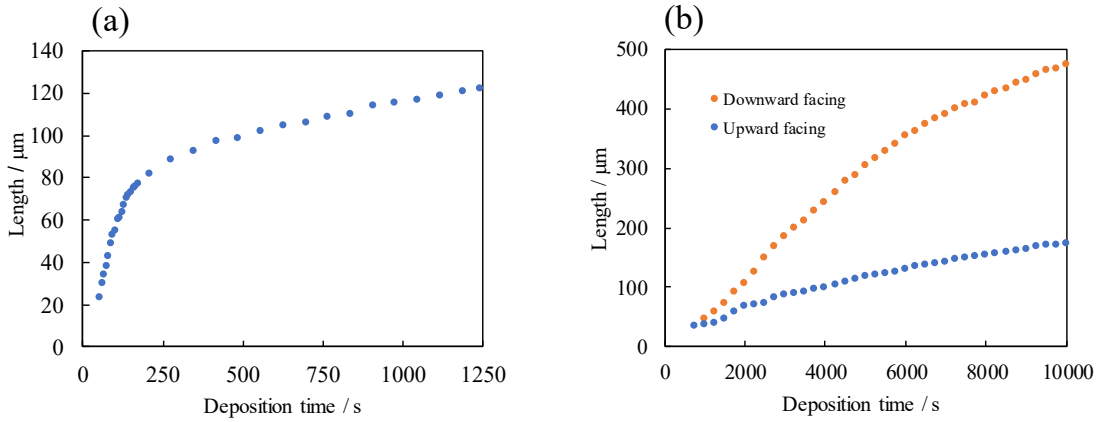

Fig. 2.13 Length of rough electrodeposits at −80 mA cm^{-2} and −10 mA cm^{-2}.

SEM images of the electrodeposits after the measurements are shown in Fig. 2.14. The electrodeposits formed at −10 mA cm^{-2} (upward faced) were detached from the electrode and transferred on a carbon tape for SEM observation.

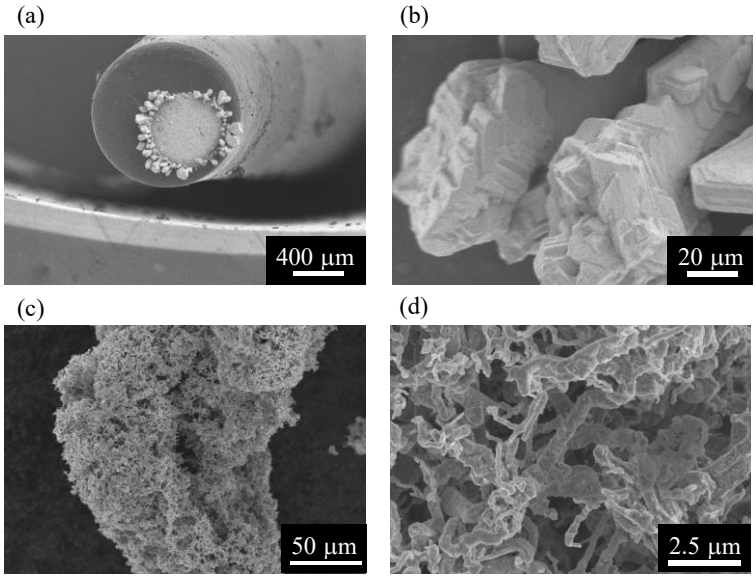

Fig 2.14 SEM images of electrodeposited Zn after *in situ* measurements at (a), (b) −80 mA cm^{-2} and (c), (d) −10 mA cm^{-2} in upward faced electrode. (b) and (d) are higher magnification images than (a) and (c).

When electrodeposition is performed at −80 mA cm^{-2}, the potential immediately dropped below −300 mV and potential oscillation is observed. Such a potential oscillation indicates the dendritic growth of electrodeposited Zn; periodicity was observed upon the formation of stacking of plate-like structures like Fig. 2.6 (d)) [25]. This study expected oxidation and deposition were partially and periodically occurred on the plate-like structures, and the potential was thought to oscillate by variations in the local current density. From CCD images and the length of the rough deposits, the irregular deposits rapidly grow at initial stages of deposition where the potential stays at negative value and oscillates. This corresponds to the rapid growth of dendrite structures under the diffusion limited condition; the current is concentrated on the tip of dendrites because the shape of the diffusion layer is hemispherical at the tip, while it is planner on a compact part [3, 4, 26]. However, after increasing the surface area by forming dendrites, the potential becomes positive and the growth rate slows down due to a decrease in the substantial current density. These behaviors result in similar potential profiles (Fig. 2.8 (a)) and the plots of the dendrite length (Fig. 2.13 (a)).

In the case of −10 mA cm^{-2}, the potential stays in positive value corresponding to before reaching the diffusion limited condition in LSV. The rough deposits continuously grow during the entire measurements. From SEM images, these deposits are composed of filamentous structures. These deposits are mossy structures formed at low

current density region. There are two characteristic points during the mossy structure formation. First, the growth rate does not decrease even after forming the rough deposits. This means an increased surface area by mossy structure does not contribute to the following electrochemical reactions. Second, morphological features at the outer surface are maintained during the deposition as shown in Fig. 2.15; the front shape of the electrodeposits is unchanged during the electrodeposition. This indicates that the electrodeposition does not occur on the outer surface of mossy structure but inside the structures, which is in stark contrast with the dendrite growth where deposition occurs on the tip of the structures. Thus, the growth of mossy structures occurs by non-uniform Zn electrodeposition in the certain growth sites inside the structures. Similar electrodeposition behavior is observed during Li electrodeposition in organic solvent; filamentous structures of electrodeposited Li is reported to grow not by deposition on the tip but by incorporation of Li atom to the root of the filament [27, 28]. This case was explained by the formation of solid electrolyte interface (SEI) on electrodeposited Li; non-uniform SEI layer resulted in variations in the local current density and localized deposition on the root of the filaments [29]. In current case, it is noteworthy that the localized deposition inside the mossy structures occurs even in an aqueous electrolyte where SEI formation never occurs. From SEM images of mossy structures like Fig. 2.14, it is difficult to identify such a certain growth sites inside the filamentous deposits. In order to shed light on a non-uniform growth of the filament, early stages of the filament formation will be analyzed in detail in section 2.3.3, below.

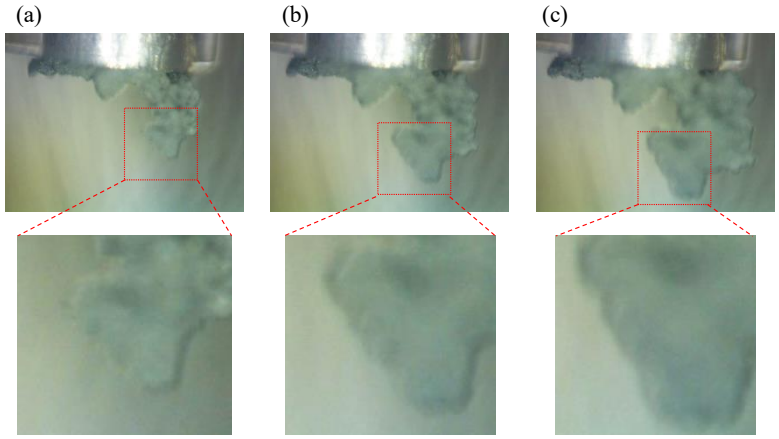

Fig. 2.15 Morphological features of the outer surface of mossy structures during deposition.

Top view

For discussing the non-uniform electrodeposition behavior, mossy structure formation behavior was *in situ* analyzed from top view, too. The images taken at −5.0 mA cm^{-2} and −20 mA cm^{-2} are shown in Fig. 2.16 and Fig 2.17, respectively. At higher current density below that for the dendrite formation, suppression or delay in the mossy structure formation was expected. Fig 2.18 shows enlarged images of the area shown in the red square (the surface corresponding to compact deposit) at 480 s in Fig. 2.16.

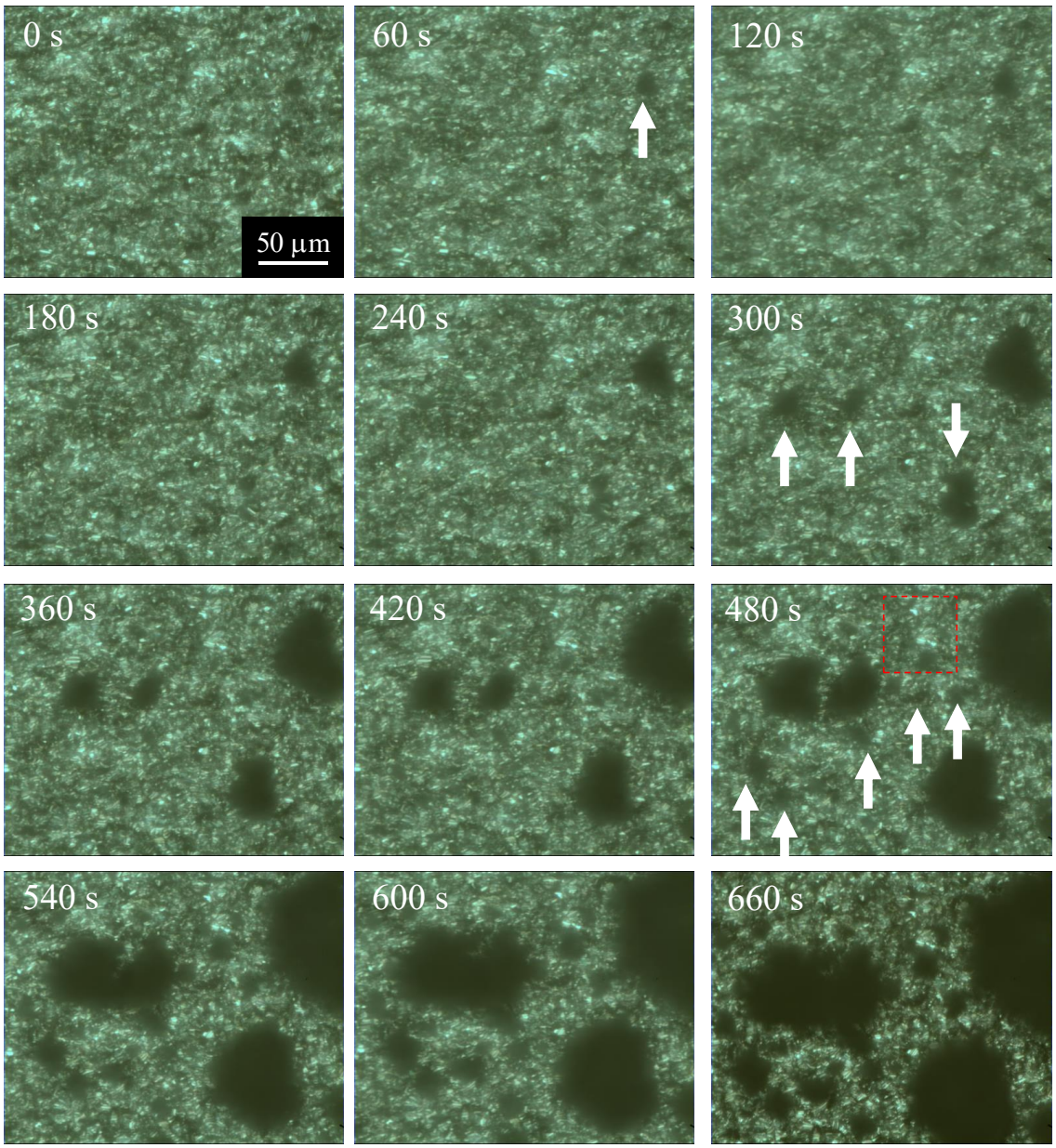

Fig. 2.16 *In situ* CCD images during electrodeposition at −5.0 mA cm^{-2} (top view). White arrows indicate the formation of mossy structures. A red square at 480 s corresponds to an enlarged area in Fig. 2.18.

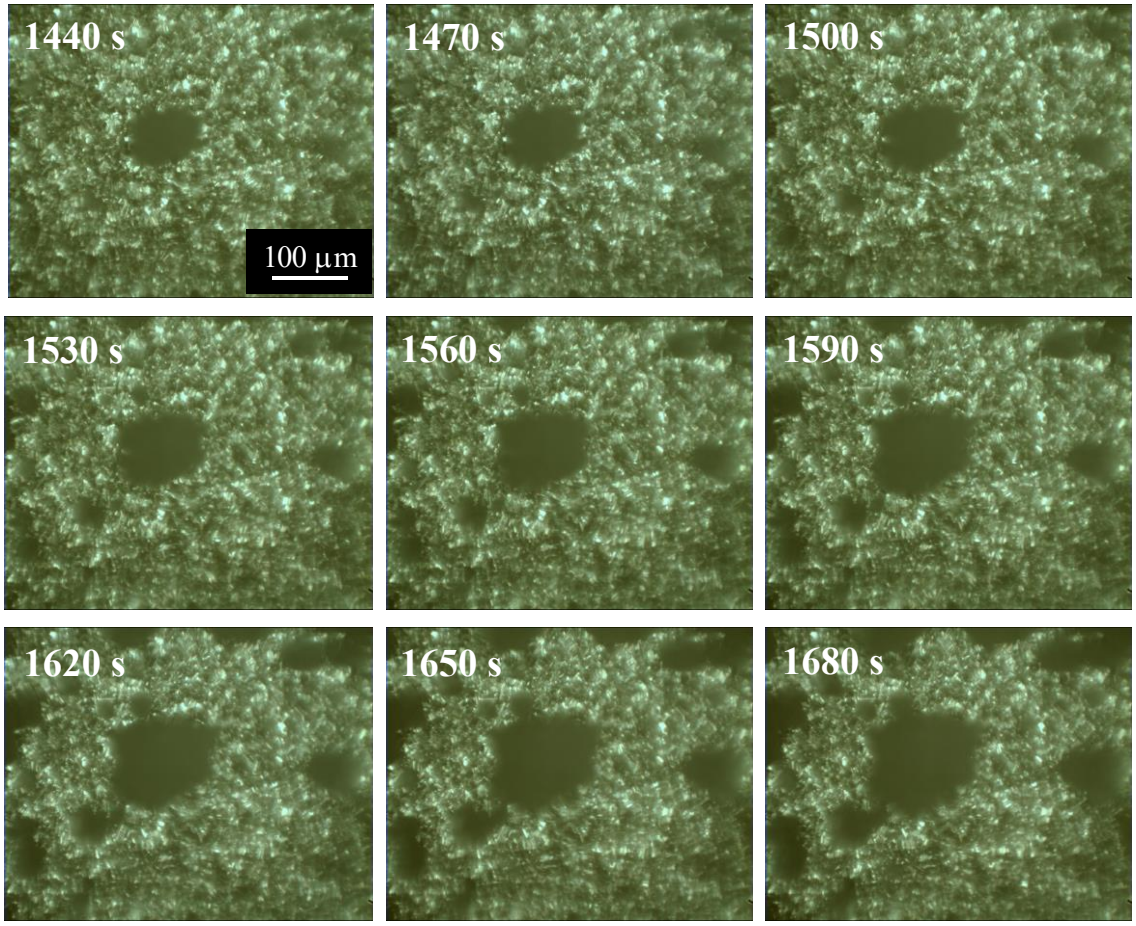

Fig. 2.17 *in situ* CCD images during electrodeposition at −20 mA cm^{-2} (top view)

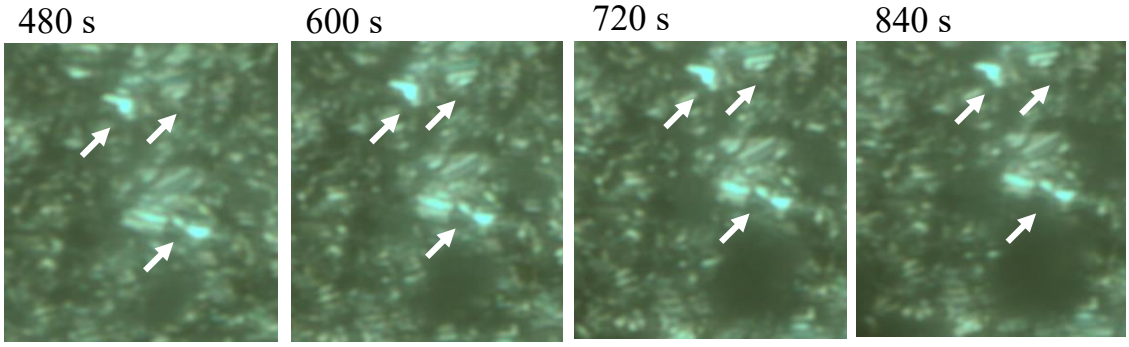

Fig. 2.18 Enlarged images of the surface corresponding to compact deposit at −5.0 mA cm^{-2}. White arrows indicate characteristic structures maintained during electrodeposition.

At −5.0 mA cm^{-2}, mossy structures are observed immediately after starting the electrodeposition (60 s, white arrows). Three other structures were formed from compact electrodeposits around 300 s. The density is further increased around 480 s. Thus, mossy

structures are successively formed during the observation. Upon such a successive formation of mossy structures, there are minor variations in the surface morphological features at compact deposits (Fig. 2.18). This means the deposition locally occurs on mossy structures, and local current density outside the mossy structure becomes low. At -20 mA cm^{-2}, initiation of mossy structure is delayed, and density of the structure is lower than that at -5.0 mA cm^{-2}. However, once it is formed, it continuously increases in the size. Also, other mossy structures are formed at later stages of deposition. Accordingly, mossy structures covered the surface at longer duration of electrodeposition even at relatively higher current density. Continuous electrodeposition in mossy structures indicates variations in the local current density, which possibly induces the successive formation of mossy structures as shown in Fig. 2.19; after decreasing the current outside the existing mossy structure, new structures are successively formed.

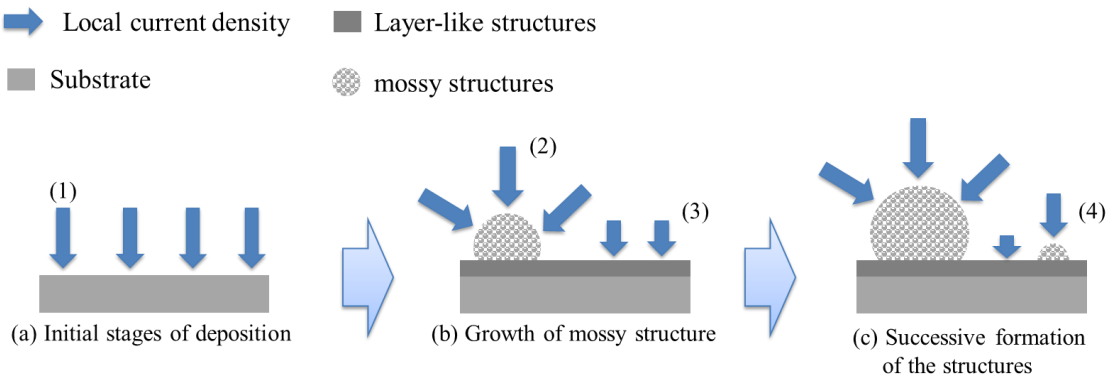

Fig. 2.19 Schematic image of the successive formation of mossy structures by variations in the local current density

2.3.3Analysis on early stages of the mossy structure formation

Morphological evolution of mossy structures at initial stages of electrodeposition

From *in situ* analysis shown above, the mossy structure formation was characterized by the non-uniform electrodeposition at low current density. Once mossy structures were formed, it induced variations in the local current density, and mossy structures were successively deposited. Although an increase in the current was effective to delay the formation of mossy structures, it was difficult to maintain the compact Zn electrodeposits for long duration. In order to understand the nucleation & growth behavior behind the mossy structure formation, early stages of deposition where mossy structure was initiated from compact electrodeposit were investigated. Morphological evolution at -5.0 mA cm^{-2} and -10 mA cm^{-2} were compared in 6.0 mol dm^{-3} KOH + 0.25 mol dm^{-3}

zincate. Lower concentration of zincate than in the above study was used to avoid a faster transition from compact deposits to mossy structures at higher zincate concentration [8]. Fig. 2.20 shows the potential profile during the electrodeposition. Fig. 2.21 shows optical microscope images of electrodeposits at passed charge for deposition of 5.0 C cm^{-2}.

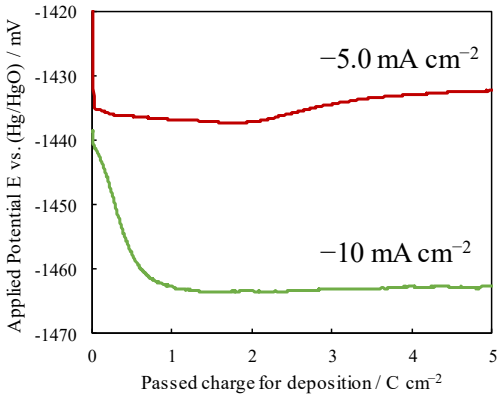

Fig. 2.20 The potential profile during the galvanostatic electrodeposition at −5.0 mA cm^{-2} and −10 mA cm^{-2}.

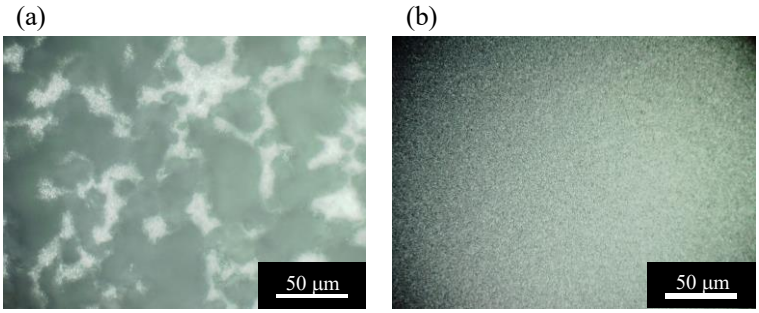

Fig. 2.21 Optical microscope images of Zn electrodeposits at (a) −5.0 mA cm^{-2} and (b) −10 mA cm^{-2} at 5.0 C cm^{-2}.

At −5.0 mA cm^{-2}, dark colored deposits corresponding to mossy structures cover the electrode surface, while bright colored compact deposits are formed at −10 mA cm^{-2}. RMS roughness of each deposit is 7.3 and 0.4 μm. Cross-sectional SEM images of these deposits are shown in Fig. 2.22.

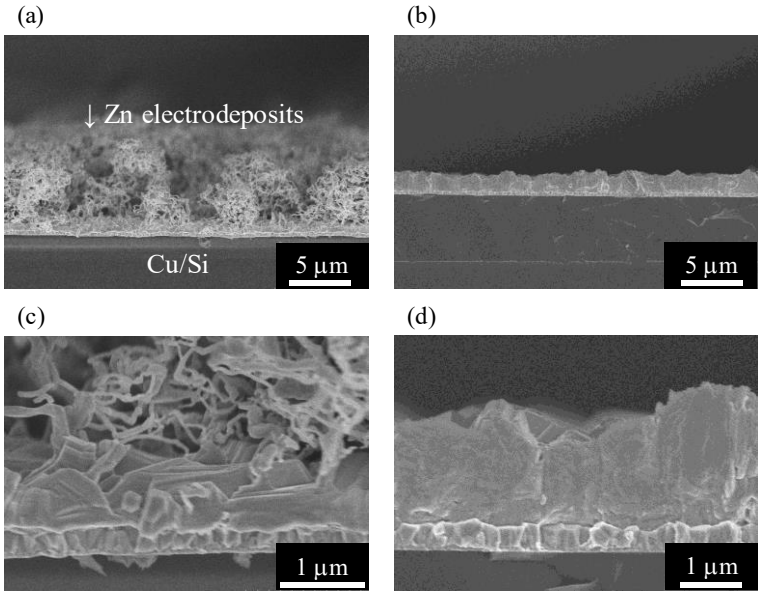

Fig. 2.22 Cross-sectional SEM images of Zn electrodeposits at (a), (c) −5.0 mA cm^{-2} and (b), (d) −10 mA cm^{-2} at 5.0 C cm^{-2}. (c) and (d) are higher magnification images of (a) and (b).

Filamentous structures are formed at −5.0 mA cm^{-2}, while compact deposits are maintained at −10 mA cm^{-2}. However, from higher magnification image, compact deposits are maintained at initial stages of deposition. Filaments are thought to transiently initiated from the compact deposits at lower current density. Such an initial stage of filament formation was further analyzed by SEM from top view in Fig. 2.23.

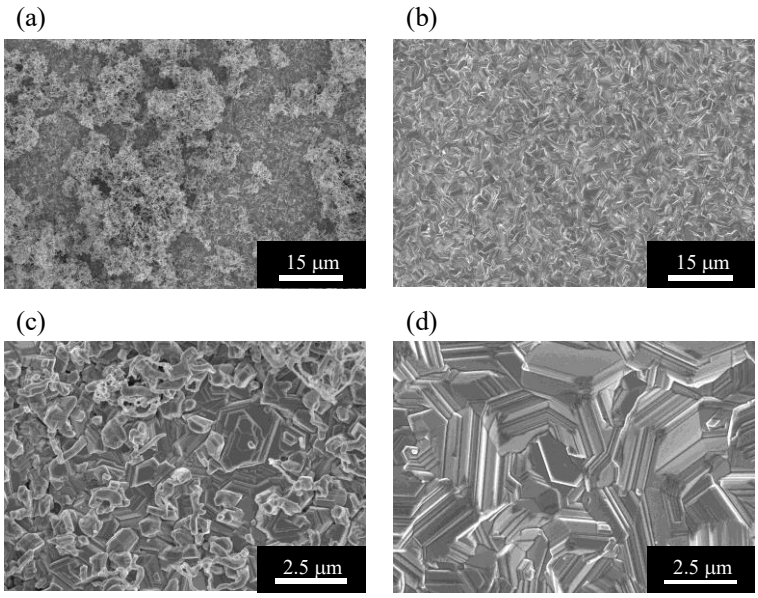

Fig. 2.23 SEM images of Zn electrodeposits at (a), (c) −5.0 mA cm^{-2} and (b), (d) −10 mA cm^{-2} at 5.0 C cm^{-2}. (c) and (d) were higher magnification images of (a) and (b).

At initial stages mossy structure formation in higher magnification images, filamentous structures are initiated from the stacking of layer-like structures (microsteps). The formation of microsteps is observed at −10 mA cm^{-2}, but the size of the terrace (the top surface of stacking of layer-like structure) is much larger than that at −5.0 mA cm^{-2}. Thus, a difference between Fig. 2.23 (c) and (d) is that the microsteps growth toward lateral direction is suppressed at lower current density. Instead, deposition occurs locally and continuously on the filamentous structures.

The above-mentioned assumption (the mossy structure formation by suppressed evolution of microsteps) is testified by changing the potential after forming mossy structures; mossy structures are formed by potentiostatic deposition at −1420 mV until passing 3.0 C cm^{-2}, then the potential was stepped to −1480 mV. After passing another 1.0 C cm^{-2} at this potential, surface morphology was analyzed by SEM.

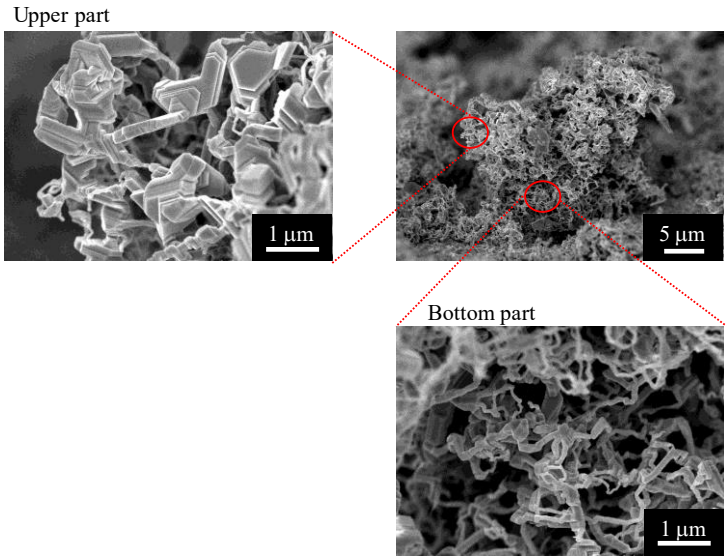

Fig. 2.24 SEM images of mossy structures after potential step from −1420 mV (3.0 C cm^{-2}) to −1480 mV(1.0 C cm^{-2}).

At the bottom part of mossy structures, filamentous structures with *c.a* 100 nm diameter are formed. However, at the top parts of the deposits corresponding to deposits formed at 2^{nd} potential step (−1480 mV), the stacking of layer-like structures appears inside the filamentous structures. This observation confirms that the filament formation is characterized by suppression on the growth of microsteps to the lateral direction and continuous deposition on the top of the microsteps.

FIB processing and TEM analysis on electrodeposits

Surface morphologies at different current densities were analyzed by TEM. For performing TEM analysis, the samples were prepared by FIB processing. Fig. 2.25 shows the surface morphology of Zn electrodeposits formed at −5.0 mA cm^{-2} and −10 mA cm^{-2} on Zn substrate during FIB processing.

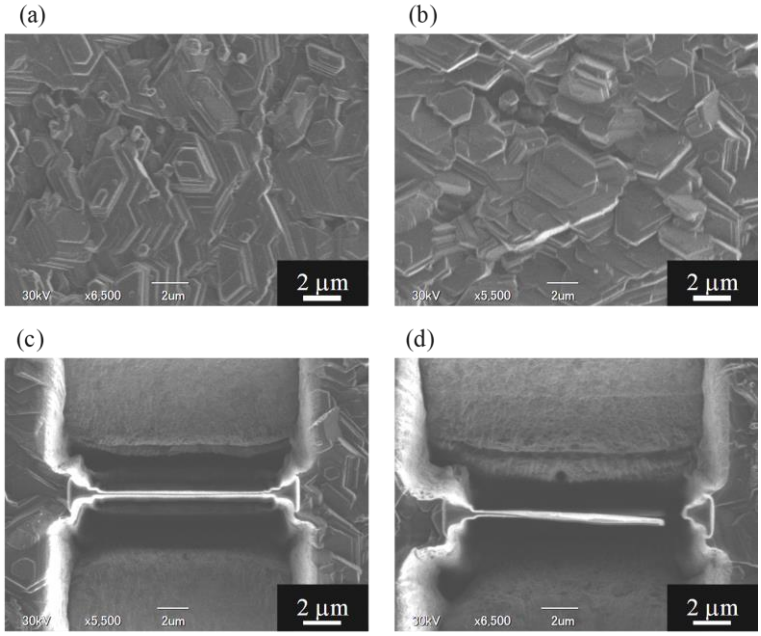

Fig. 2.25 SEM images during FIB processing of Zn electrodeposits formed at (a), (c) −5.0 mA cm^{-2} and (b), (d) −10 mA cm^{-2}. (a) and (b) are SEM images of initial morphology of the surface. (c) and (d) are SEM images after etching the surface. Thin plates at the center of images were transferred to the TEM grid.

Prepared samples were transferred to the TEM grids. Obtained TEM images are shown in Fig. 2.26.

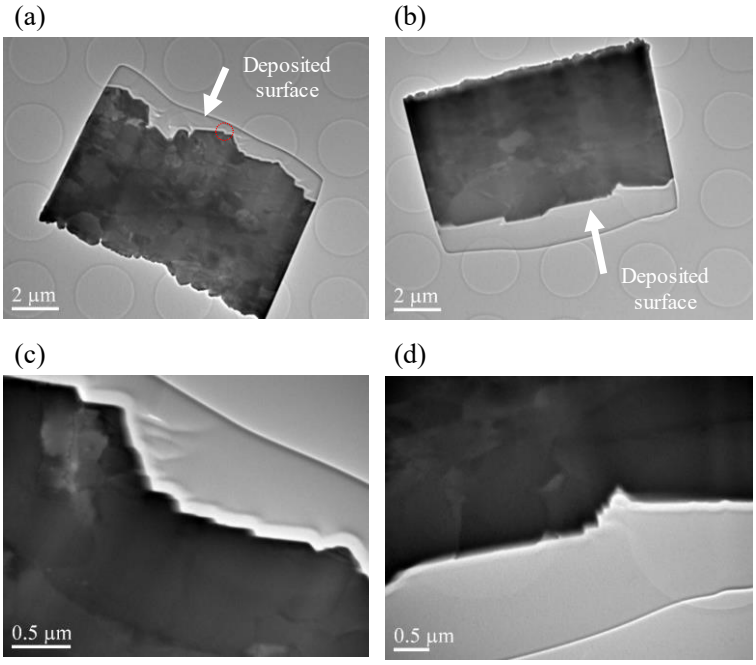

Fig. 2.26 TEM images of samples prepared by FIB on electrodeposits formed at (a), (c) −5.0 mA cm^{-2} and (b), (d) −10 mA cm^{-2}. (c) and (d) are higher magnification images of (a) and (b). White arrows denote the surface of the electrodeposits. Red circle on (a) shows a magnified area in Fig. 2.27.

As discussed in SEM analysis, the surface area of an exposed terrace on each microstep structure is smaller at −5.0 mA cm^{-2} than that at −10 mA cm^{-2}; a flat terrace is observed at the surface of the electrodeposit at −10 mA cm^{-2}, while many microsteps with a narrow terrace are formed at −5.0 mA cm^{-2}. Thus, the evolution of microsteps to the lateral direction is suppressed, and the formation of a new step structure is favored at lower current density. Atomic structure at the step (a red circle in Fig. 2.26 (a)) was analyzed by observation at higher magnification in Fig. 2.27.

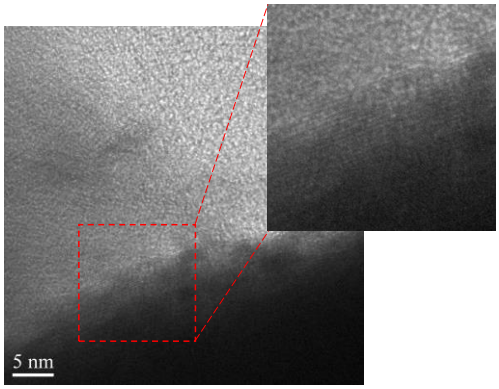

Fig. 2.27 TEM images of electrodeposited Zn at −5.0 mA cm^{-2}. An enlarged image denotes the lattice fringe in the deposit.

Although it is difficult to obtain a clear image over the entire surface, the lattice fringe is observed in the area shown by a red square. The closed packed plane of the Zn lattice is likely to be horizontally arranged to the microsteps. In other words, the terrace of microstep is basal plane of hcp-Zn, (002) plane. This is in accordance with previous predictions by optical microscope and SEM analysis [30, 31, 25]. Mossy structure itself also preferentially grows to (002) direction [22, 32, 33]. Therefore, mossy structure is initiated by continuous deposition on the terrace of microsteps, (002) surface. After describing the coulombic efficiencies during electrodeposition at different applied potential, the formation process of mossy structure via microsteps growth is discussed in 2.3.4.

Coulombic efficiency at different applied potentials

In order to discuss the mechanism behind the mossy structure formation at low overpotential, the coulombic efficiency was evaluated after electrodeposition at different applied potential. Initially, Zn electrodeposition was performed at −1420, −1460 and −1480 mV until reaching 5.0 C cm^{-2}. Then, the electrodeposited film was anodically dissolved at −1.37 V in a same solution. Additionally, amount of Zn species in electrodeposited film prepared by the same conditions were measured by ICP-AES. Fig. 2.28 shows LSCM images of the samples for ICP-AES analysis.

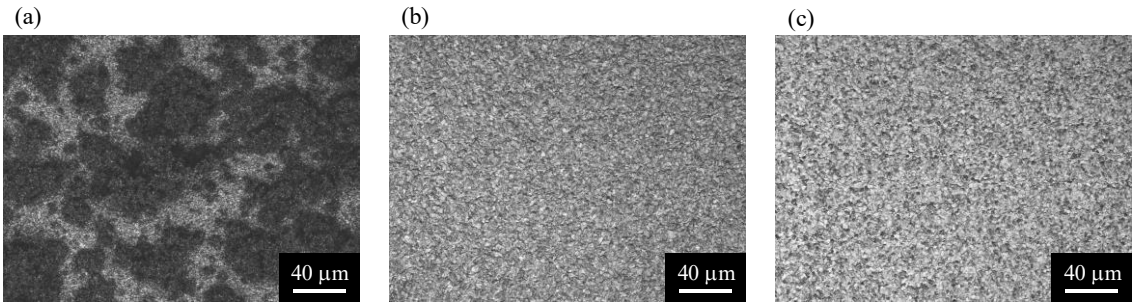

Fig. 2.28 LSCM images of surface morphologies of the electrodeposited Zn on Cu at (a) −1420 mV, (b) −1460 mV and (c) −1480 mV at 5.0 C cm^{-2}.

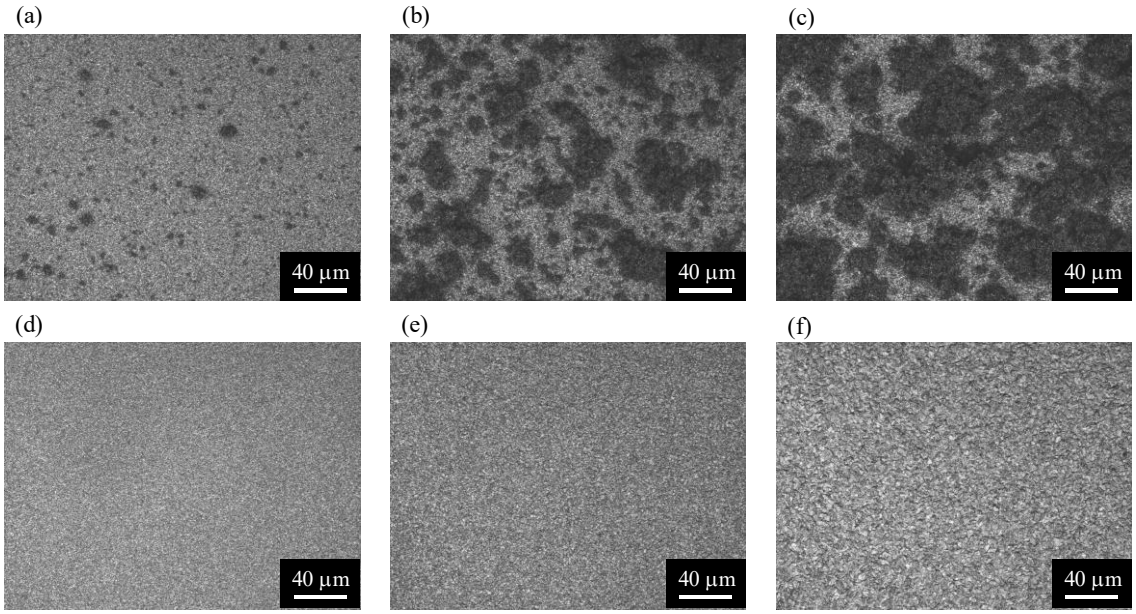

Fig. 2.29 LSCM images of surface morphologies of the electrodeposited Zn on Cu at (a) −1420 mV, 1.5 C cm^{-2}, (b) −1420 mV, 3.0 C cm^{-2}, (c) −1420 mV, 5.0 C cm^{-2}, (d) −1460 mV, 1.5 C cm^{-2}, (e) −1460 mV, 3.0 C cm^{-2}, and (f) −1460 mV, 5.0 C cm^{-2}.

Fig. 2.30 shows the current profiles during the anodic dissolution

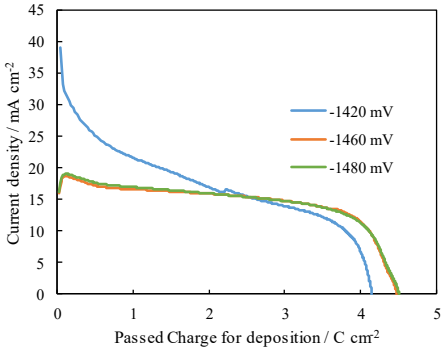

Fig. 2.30 Current profile during the anodic dissolution of electrodeposited film at different applied potential with passed charge for deposition of 5.0 C cm^{-2}.

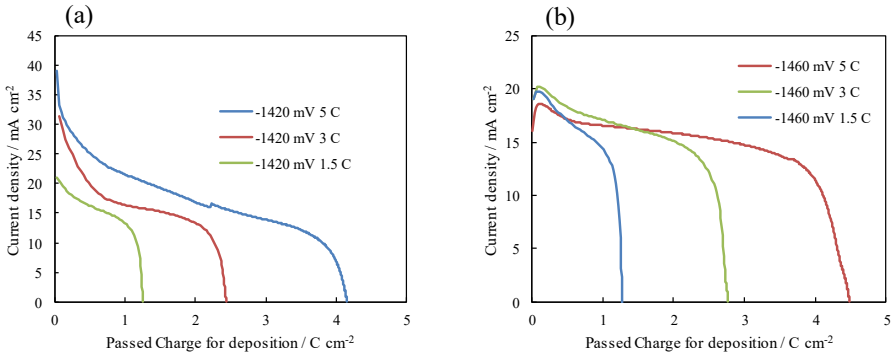

Fig. 2.31 Current profile during the anodic dissolution of electrodeposited film at at (a) −1420 mV and (b) −1460 mV with various passed charge for deposition.

The calculated current efficiencies are summarized in Table 2.1.

Table 2.1 Current efficiencies evaluated by anodic dissolution and ICP-AES

Potential / mV	Passed charge / C cm^{-2}	$\eta_{\text{anodic dissolution}}$ / %	$\eta_{\text{ICP-AES}}$ / %
−1420	1.5	84	90
−1420	3.0	82	88
−1420	5.0	83	91
−1460	1.5	85	96
−1460	3.0	92	95
−1460	5.0	90	95
−1480	5.0	91	95

At each condition, the coulombic efficiency does not reach 100%. Several reasons are expected for the loss of the coulombic efficiency; (1) side reactions (hydrogen evolution) occurs during Zn electrodeposition, (2) electrodeposited Zn became electrochemically inactive during the anodic dissolution, (3) deposited Zn is re-dissolved again. To discuss these possibilities, following things are notable. First, the coulombic efficiency is low at the conditions mossy structures are formed (−1420 mV). In previous study, the large surface area of mossy structure can be considered to be a cause of corrosion of Zn, which may induce a dissolution of Zn or oxide formation (corresponding to (2) and (3) in the above possibilities). However, the coulombic efficiencies are less dependent on the passed charge for deposition. This means the efficiency is low even before forming mossy structures. Accordingly, decrease in the coulombic efficiency is caused not only by the corrosion of electrodeposited Zn but also by inherent factors affecting Zn

electrodeposition. Furthermore, in all deposition conditions, the value calculated by ICP-AES is higher than that evaluated by the anodic dissolution. This suggests electrodeposited Zn becomes partially inactive during the anodic dissolution. In other words, although Zn species exists in the deposits, it cannot react during the anodic dissolution. This situation can happen when ZnO is formed during electrodeposition or by corrosion immediately after electrodeposition.

From these results, it is likely that the decrease in the coulombic efficiency occurs due to factors (1) or/and (2). First possibility is that hydrogen is codeposited during Zn electrodeposition. However, increased efficiency in ICP-AES compared to anodic dissolution cannot be explained by HER only. Another possibility is that ZnO is formed at electrodeposition at low overpotential. Actually, previous study suggested that ZnO can be formed by the disproportionation reaction between reaction intermediates for Zn electrodeposition like (2.5).

$$2ZnOH \rightarrow Zn + ZnO + H_2O \quad (2.5)$$

These factors can be considered as causes of irregular deposition behavior at low overpotential as discussed in 2.3.4.

Effects of cation speceis and concentration of zincate ion on mossy structure formation

As described above, the effects of current density or deposition overpotential on mossy structure formation is evident; mossy structure is preferentially formed at low overpotential. However, less attention has been paid to effects of zincate concentration in the electrolyte on mossy structure formation, while it is well known that dendrite is suppressed at high zincate concentration. Some studies expected that mossy structure is suppressed at low zincate concentration region [6, 8]. However, influence of zincate concentrations on the deposition process at low overpotential region is not clarified. To understand this, galvanostatic electrodeposition was performed at different concentration of zincate ions. First, Zn electrodeposition was performed at -5.0 mA cm^{-2} in the vertically faced electrode (Fig. 2.1). Fig. 2.32 shows the potential profiles during electrodeposition at different current density, and Fig. 2.33 shows SEM images after electrodeposition.

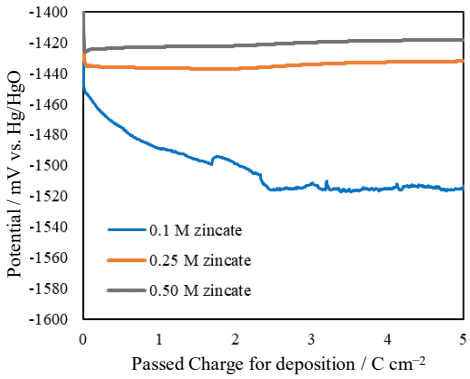

Fig. 2.32 Potential profiles during the galvanostatic electrodeposition of Zn at −5.0 mA cm^{-2} for 1000 s in a static electrolyte at various concentrations of zincate.

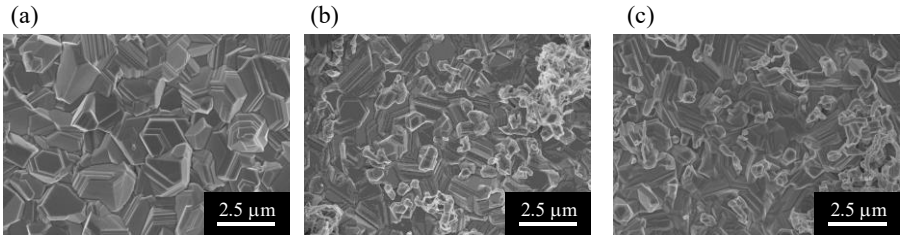

Fig. 2.33 Surface morphologies of electrodeposited Zn at −5.0 mA cm^{-2} for 1000 s in 6.0 mol dm^{-3} KOH + (a) 0.1 mol dm^{-3} zincate, (b) 0.25 mol dm^{-3} zincate, (c) 0.50 mol dm^{-3} zincate.

As previously discussed, mossy structures formation is suppressed at lower concentration (0.10 mol dm^{-3}). From chronopotentiograms, the potential negatively shifts during electrodeposition in 0.10 mol dm^{-3} zincate solution, which indicates an increase in the concentration overpotential; zincate concentration is depleted at the surface. These trends were further analyzed by using RDE for various concentrations of zincate. Advantages of RDE is a higher diffusion limited current by the forced convection. In other words, surface concentration can be maintained higher than that in a static electrolyte. Fig 2.34 shows the potential profiles during the electrodeposition using RDE in 6.0 mol dm^{-3} KOH + zincate, and corresponding SEM images are shown in Fig. 2.35 (low magnification images) and Fig. 2.36 (high magnification images).

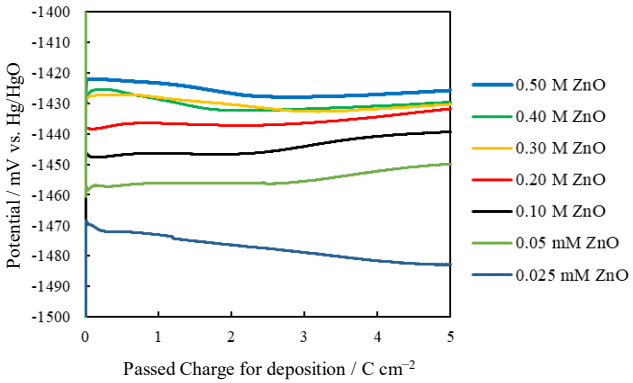

Fig. 2.34 Potential profiles during the galvanostatic electrodeposition of Zn at −5.0 mA cm^{-2} for 1000 s under electrode rotation at 600 rpm with various concentrations of zincate.

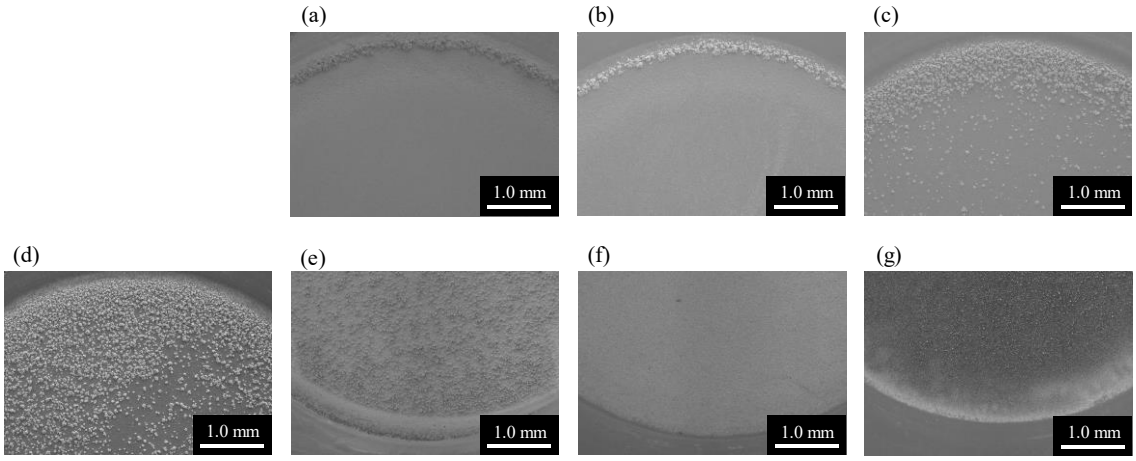

Fig. 2.35 SEM images (low magnification) of electrodeposited Zn at −5.0 mA cm^{-2} for 1000 s under electrode rotation at 600 rpm in (a) 0.40, (b) 0.30, (c) 0.20, (d) 0.10, (e) 0.050, (f) 0.025 mol dm^{-3}, and (g) 0.010 mol dm^{-3} zincate solutions.

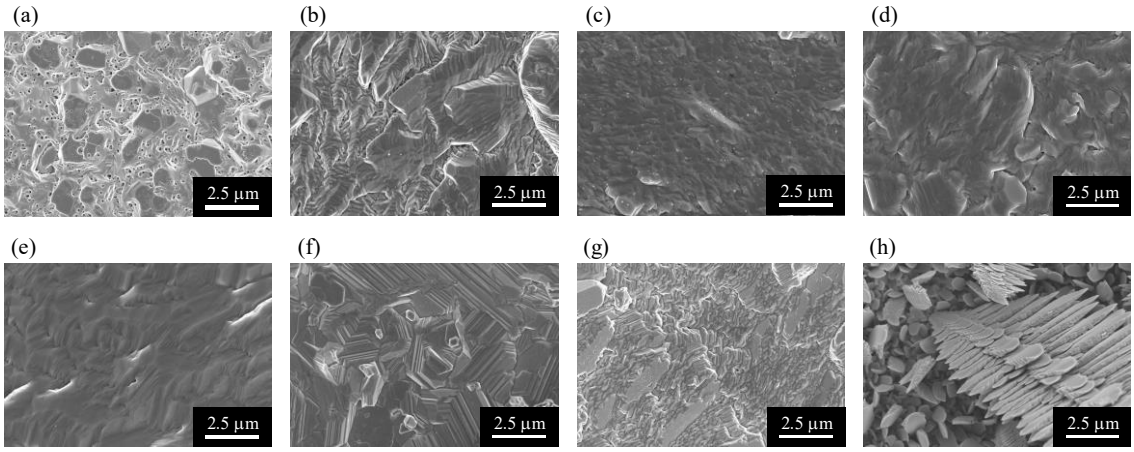

Fig. 2.36 SEM images (high magnification) of electrodeposited Zn at −5.0 mA cm^{-2} for 1000 s under electrode rotation at 600 rpm in (a) 0.50, (b) 0.40, (c) 0.30, (d) 0.20, (e) 0.10, (f) 0.050, (g) 0.025 mol dm^{-3}, and (h) 0.010 mol dm^{-3} zincate solutions.

From 0.10 to 0.025 mol dm^{-3} in Fig. 2.35, the trend is similar to that in a static electrolyte; mossy structures evolve at higher concentrations of zincate. Compact deposits are obtained at 0.025 mol dm^{-3}, then dendrites are formed at 0.010 mol dm^{-3}. However, at concentration more than 0.20 mol dm^{-3}, the formation of mossy structure is suppressed on center part of the electrode. Furthermore, microsteps becomes less defined than that at 0.050 mol dm^{-3}, this trend is not observed in a static electrolyte. Accordingly, mossy structures are suppressed either by continuous growth of microsteps (as discussed in SEM and TEM analysis above in a static electrolyte) or by the formation of less defined Zn facets.

From fundamental understandings of nucleation & growth of electrodeposited metals, morphological changes from compact to dendrite is interpreted in term of changes in surface concentration of zincate species near the electrode surface as discussed in section 1.2.3. When zincate ions are depleted, Zn deposition proceeds under diffusion-limited condition. However, at lower current density region or high concentration region, their effects on mossy structure formation has not been explained reasonably; although concentration of adatoms may alter the deposition behaviors (nucleation density), its value may not be changed under the galvanostatic condition at low current density region where diffusion-limited condition is not attained. From analysis on the growth behavior of mossy structures described above, the formation process of mossy structure seems governed by non-uniform surface properties of Zn electrode rather than mass transfer of ionic species in the electrolyte. This is analogous to Li electrodeposition under the presence of SEI [28, 29]. Furthermore, it is difficult to explain the inconsistent (non-

linear) dependence of mossy structure formation on Zn concentration under forced convection.

These findings suggest that the formation of microsteps and non-uniform surface reaction are influenced by ionic species in the electrolyte. For example, Wiart *et al.* claimed that the formation of mossy structures were promoted under the presence of anodically dissolved zincate species (ADZ), which was supposed to induce the formation of surface layer on Zn electrode [13-16]. Here, different explanation is attempted by focusing on the charge of ionic species. Based on the fact that the concentration dependence is non-linear, and microsteps formation is altered at different concentration region, I assume it is not reasonable to explain the mossy structure formation only by zincate concentration alone. Since $Zn(OH)_3^-$ and $Zn(OH)_2^-$ as well as zincate are negatively charged (chapter 1, eq. (1.3) to (1.6)), deposition behavior may be altered by surface charge, too. To testify this assumption, Zn electrodeposition was carried out in 5.7 mol dm^{-3} CsOH + 0.044 mol dm^{-3} or 0.10 mol dm^{-3} zincate by using a RDE at −5.0 mA cm^{-2} for 1000 s. Since Cs^+ has larger ionic radius (lower charge density) than that of K^+, its interaction with electrode surface in outer Helmholtz plane may be weaker than that of K^+ or Li^+. Fig. 2.37 shows the potential profiles during electrodeposition and Fig. 2.38 shows SEM images after electrodeposition.

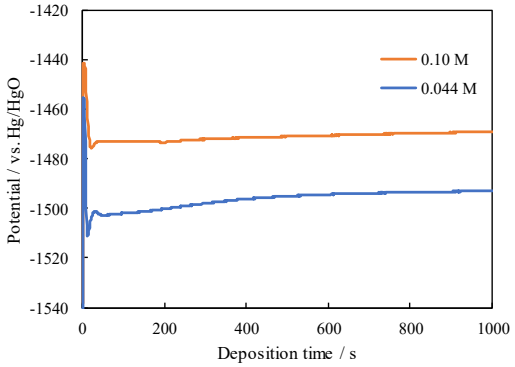

Fig. 2.37 Potential profiles during the galvanostatic electrodeposition of Zn at −5.0 mA cm^{-2} for 1000 s under electrode rotation at 600 rpm in 5.7 mol dm^{-3} CsOH + 0.044 mol dm^{-3} or 0.10 mol dm^{-3} zincate.

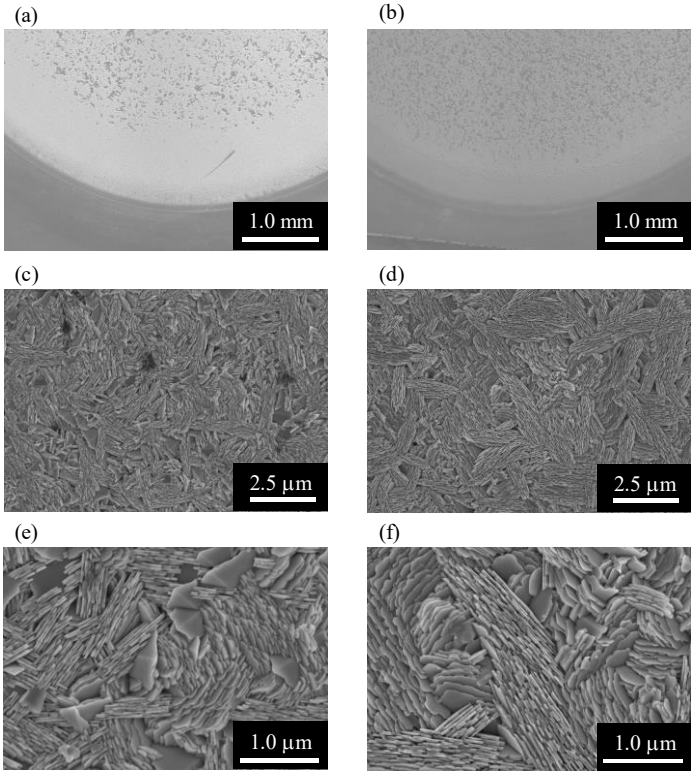

Fig. 2.38 SEM images of electrodeposited Zn at −5.0 mA cm^{-2} for 1000 s under electrode rotation at 600 rpm in 5.7 mol dm^{-3} CsOH + (a), (c), (e) 0.044 mol dm^{-3} or (b), (d), (f) 0.10 mol dm^{-3} zincate. (c), (e) and (d), (f) are higher magnification images than that of (a) and (b), respectively.

Influences of cations species in Zn electrodeposition process are evident from following things. First, deposition potential is negatively (*c.a.* 20 mV) shifted after changing the cation species from K^+ to Cs^+. From SEM images, compact Zn surface is obtained by using CsOH solution. The formation of microsteps and mossy structures are totally changed; stacking of horizontally aligned microsteps are no longer observed, and plate-like structures are vertically deposited on the surface.

EIS analysis in different alkaline solutions

In order to shed light on the effects of cation species in the Zn electrochemical behavior, EIS was measured on Zn electrodes in different alkaline solutions (without zincate ions) at REST potential. A Zn wire embedded in a epoxy resin was used as a working electrode because a clear capacitive loop was not observed in the electrode configuration shown in Fig 2.1 or RDE. EIS was successively measured in the different electrolyte by using the same electrochemical cell and replacing the electrolyte. Two sets

of experiments were carried out because there was a concern over the reproducibility by using Zn wires for EIS measurements; variations in surface conditions (*e.g.* scratches formed during polishing) easily altered the impedance. First set of experiments were performed by changing the alkaline solution from 6.0 mol dm^{-3} KOH, 1.0 mol dm^{-3} LiOH + 5.0 mol dm^{-3} KOH, then to 5.7 mol dm^{-3} CsOH solutions. Another set of experiments were performed in the opposite order; CsOH, KOH + LiOH, then to KOH. Nyquist plots obtained at frequency range 10 kHz to 1 Hz are shown in Fig. 2.39.

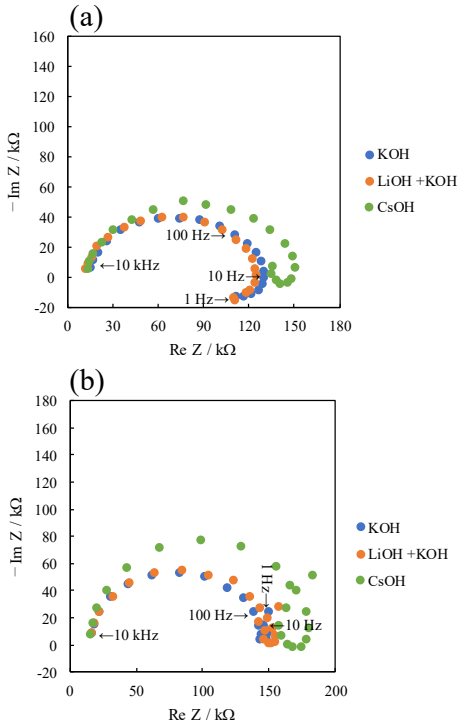

Fig. 2.39 Nyquist plots measured for Zn electrodes in the different alkaline solution

Obtained Nyquist plots exhibits a typical capacitive semicircle and inductive features at low frequency region. The latter inductive feature is often observed for Zn electrode in alkaline solution, which is caused by the potential dependent changes in the coverage of reaction intermediates (*e.g.* $ZnOH_{ad}$) during electrodeposition or dissolution of Zn [34, 35]. Shape and size of a capacitive semicircle vary between each experimental set possibly due to different surface conditions of the employed working electrode. Therefore, quantitative comparison is difficult from this result, and only qualitative trend is discussed. When same surface condition is assumed in each experimental set, it is notable that charge transfer resistance (intersection points of the plots at lower frequency to dashed line (−Im Z=0) corresponds to sum of the solution resistance R_s and charge-transfer resistance R_{ct})

increases in CsOH solution, while the difference in the solution resistance is less remarkable. This indicates that the elementary steps for electrodeposition or anodic dissolution of Zn are suppressed in CsOH solution. This trend is in consistent with increased overpotential for Zn electrodeposition. Also, in chapter 5, enhanced anodic dissolution by Li^+ addition will be discussed. Therefore, electrochemical reactions of Zn are facilitated by the presence of Li^+ or K^+ at the surface. This is possibly due to significant interactions of reaction intermediates of Zn (*e.g.* $Zn(OH)_2^-$) with cation having large charge density (charge density is in the order; $Li^+ > K^+ > Cs^+$), which may facilitate the certain elementary step. Similar trend was observed in Pt oxidation in alkaline solution; the stability of the reaction intermediates of Pt changed by interaction with Li^+ on the surface [36]. Therefore, cation species also affect the non-uniform deposition behavior through interacting with negatively charged reaction intermediates, and localized deposition is possibly induced by non-uniform distribution of cation (Li^+ or K^+) species on the surface. Furthermore, the inductive features at low frequency region is considerably different in CsOH solution; inductive semi-circle more clearly appears than that in KOH or LiOH solution. Since the inductive features at this region originate from potential dependence of coverage of Zn intermediates, its potential dependence may be varied by different interactions with cation species.

At this moment, it is difficult to quantitatively carry out the fitting to obtained Nyquist plots due to lack of understandings on the inductive features at low frequency region and variations by surface conditions of Zn electrodes. For qualitative comparison of the capacitive feature, fitting is performed for the frequency range 10 kHz – 10 Hz based on the equivalent circuit shown in Fig. 2.40. To simplify the response, solution resistance (R_s) connected to parallel constant phase element (CPE) and charge-transfer resistance (R_2) are considered [37].

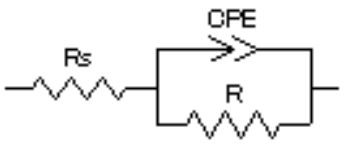

Fig. 2.40 Equivalent circuit composed of R_s, R_2 and CPE

CPE is introduced instead of capacitor to consider the different surface conditions (*e.g.* roughness) of the electrode. Since obtained capacitive semicircles in Fig. 2.39 are distorted from perfect semicircles, it is impossible to fit the curve to the equivalent circuit with general capacitor. Fitted curves are shown in Fig. 2.41. Values for R_s, R_2 CPE

constant (T_{CPE}) and CPE exponent (p) are summarized in Tables 2.2. Apparent capacitance, C can be calculated from CPE constant and exponent from (2.6) and surface area = 1.96×10^{-3} cm^2 [37].

$$C = {T_{CPE}}^{1/p} \, R^{(1-p)/p} \tag{2.6}$$

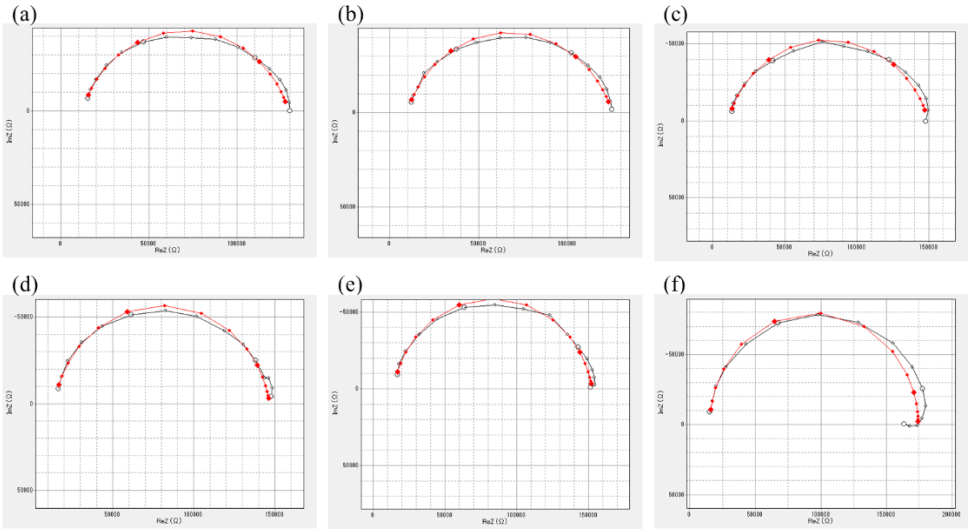

Fig. 2.41 Fitted curves to Nyquist plots obtained in various alkaline solutions for (a)-(c) first experiment and (d)-(f) second experiment. (a), (d) KOH, (b), (e) KOH + LiOH, (c), (f) CsOH solutions.

Table 2.2 Value of resistance and CPE in the fitted curve to Fig. 2.39(a)

	KOH	KOH + LiOH	CsOH
R_s / kΩ	12.2	9.72	10.3
T_{CPE} / F s^{p-1}	1.40×10^{-8}	1.69×10^{-8}	1.28×10^{-8}
p / -	0.8076	0.8118	0.8239
R_2 / kΩ	117	115	139
Calculated C / μF cm^{-2}	1.55	2.03	1.69

Table 2.3 Value of resistance and CPE in the fitted curve to Fig. 2.39(b)

	KOH	KOH + LiOH	CsOH
R_s / kΩ	14.0	14.1	15.3
T_{CPE} / F s^{p-1}	4.23×10^{-9}	4.37×10^{-9}	1.49×10^{-9}
p / -	0.9000	0.8940	1
R_2 / kΩ	133	139	159
Calculated C / μF cm^{-2}	0.939	0.925	0.758

The calculated values vary depending on experiments. Especially p value is different in Table 2.2 and 2.3 possibly due to the different surface state (*e.g.* roughness is expected to be low in 2nd experiment based on the p value close to 1). This limits the applicability of the analysis, and the order of some values are not in consistent between two experiments. Therefore, it is difficult to discuss the trends other than charge-transfer resistance mentioned above; R_2 increases in CsOH solution in both experiments. Since cation species are known to alter the capacitance value, it is noteworthy to discuss different capacitance value in each solution [38]. Qualitatively, the capacitance increases in the Li^+ containing solution than that in Cs^+ containing solution despite large hydration radius of Li^+. This implies that cation with large charge density can considerably interact with Zn surface, which results in higher capacitance. But, conclusive results are still missing due to a different order in the first and second experiment (KOH solution exhibits 2nd highest value in first experiment and the highest value in second experiment.). For future research, it would be valuable to analyze the EIS spectra quantitatively by focusing on capacitance and inductive features. Especially, the latter is closely related to elementary steps for Zn electrodeposition as previously pointed out [34, 35]. Although it is still difficult to conclude effects of cation species in electrochemical behaviors and surface morphologies, its effects (including the concentration dependence) are rationalized in 2.3.4.

2.3.4 Mechanisms of the mossy structure formation

From *in situ* optical microscope analysis on the formation behavior of mossy structure, it was characterized by non-uniform electrodeposition of Zn at low overpotential region. Despite increase in the surface area of electrodeposits, the deposition locally and continuously occurred inside the structure. At microscopic level, SEM and TEM investigations on the early stages of mossy structure formation revealed that filamentous structure was initiated from microsteps. The growth of microsteps toward the lateral direction is suppressed at low overpotential. This situation is

schematically shown in Fig. 2.42.

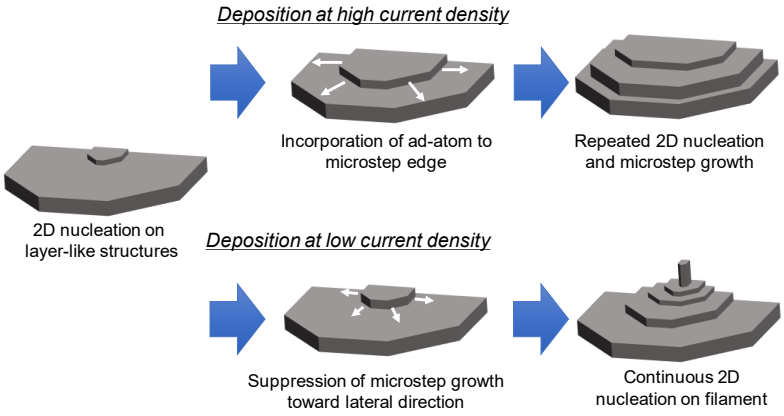

Fig. 2.42 Formation process of mossy structures from microsteps

From fundamental understandings of metal electrodeposition, the suppression of microsteps growth at low overpotential is unique because electrodeposition at low overpotential generally favors two-dimensional structures with low surface roughness (minimum product of surface free energy and surface area) [4, 23]. Since Zn basal plane, (002) plane is the close packed surface, it has the lowest surface energy among Zn crystal facets. This means Zn is electrodeposited in a manner exposing the rough surface with higher surface free energy than that of basal plane. This is the opposite to the trend mentioned above.

This growth process is interpreted as locally continuous deposition on the terrace sites of microsteps. Mitsuhashi *et al*. claimed that continuous 2D nucleation tends to occur on basal plane because this plane has larger terrace than other plane, and the ad-atom mobility on this surface is low [32]. However, this explanation does not clarify why it is favored under low overpotential. There must be factors which induce localized depositions on microsteps structures.

From previous studies, some researches assumed that Zn surface in alkaline solution was covered by oxide layer, and Zn electrodeposition occurs through this layer [13-16]. The oxide formation from reaction intermediate of Zn electrodeposition/dissolution is considered like (2.4). Also, hydrogen adsorption is often considered as a cause for the irregular deposition behavior especially in acidic media as discussed in (1.11) [39, 40]. In current study, it was confirmed that the coulombic efficiency during Zn electrodeposition was low even at initial stages of deposition where mossy structure did not sufficiently evolve, which was not explained by the corrosion of mossy structure. This indicates that the side-reactions (hydrogen adsorption or oxide

formation from reaction intermediates) are considerable factors affecting nucleation & growth behavior; by forming H_{ad} on terrace sites or partial passivation of steps by ZnO, nucleation is favored at the terrace of microsteps.

Additionally, comparison between effects of K^+ and Cs^+ poses a new viewpoint from interfacial structure of Zn electrodes. Since deposition potential of Zn is negatively shifted (charge-transfer resistance is increased in EIS) and microsteps formation is altered (uniform nucleation is promoted) by Cs^+, Zn deposition process is considerably influenced by interactions between negatively charged Zn intermediates like $Zn(OH)^{2-}$, $Zn(OH)^{3-}$ and cation species. When K^+ is used, it interacts with zincate species by high charge density (small ionic radius). This facilitated the reaction and higher mobility of intermediate species at the surface where K^+ is adsorbed (this refers to non-specifically adsorbed cation, or cation in outer Helmholtz plane) [36]. Well-defined facets with large terrace formed in KOH solution may originate from such an interaction. Upon formation of mossy structure, there is possibly non-uniformity in the distribution of cationic species over the electrode surface (facet selective adsorption of K^+). Limited mobility of Zn intermediate may result in localized deposition. Such an interaction may be diminished in CsOH solution because of low charge density (large ionic radius) of Cs^+. Deposition of large, well-defined facet is suppressed due to limited mobility of intermediate species. Instead, deposition is forced to occur through large number of nucleation event, which requires the higher degree of supersaturation of ad-atoms (higher deposition overpotential.) As a similar effect to Cs^+, tetra-alkyl-ammonium cation (TAA^+) is known to possess the suppression effects on dendrite [41]. It was reported that the suppression effects were enhanced by long alkyl chain (suppression effects were in the order of methyl<ethyl<propyl group). The reason was ascribed to physical adsorption of TAA^+ on Zn surface via alkyl chain, and the physical covering in active sites for Zn electrodeposition. Considering that Cs^+ possesses similar effects on compact Zn electrodeposition, not only physical blocking but also an electrostatic interaction of Zn intermediate species in the electrical double layer is responsible for different electrodeposition behavior; such an interaction is also expected to be weak with TAA^+ because of the bulky structures.

The concentration dependence of mossy structure formation is rationalized from the interactions between cations and reaction intermediates. At low concentration (but higher than that for dendrite initiation), compact Zn electrodeposits with microsteps structures are formed (Fig. 2.36(g)). Here, K^+ can considerably interact with intermediate species on the surface because K^+ is not sufficiently surrounded by negatively charged zincate in the solution. Then, reaction intermediates possess high mobility to form well-

defined facet. At intermediate concentration range (*e.g.* Fig. 2.36(f)), interaction between K^+ and surface becomes partially weak due to increase in the negatively charged zincate in electrolyte. In this case, Zn species may accumulate on the surface which can interact with K^+. Then, deposition is localized on this facet. Further increase in the zincate concentration shields cation species in the solution, and it results in suppression in the interaction between cation and the surface. In this case, deposition occurs regardless of non-specifically adsorbed cation, which induces a deposition of less-defined microsteps.

2.3.5 Morphological changes during pulsed electrodeposition

Pulsed electrodeposition is one of the effective methods to suppress the irregular electrodeposits. By periodically setting the electrodeposition and halt of reactions at rest potential, the depletion of ionic concentrations during the deposition is recovered at rest potential. Which may suppress the formation of dendrites under diffusion limited conditions. However, the morphological changes of mossy structures by pulsed electrodeposition are not understood. Here, electrodeposition behaviors of dendrites and mossy structures under pulsed electrodeposition and galvanostatic conditions are compared.

Figure 2.43 shows potential profile during galvanostatic electrodeposition at −5.0 mA cm^{-2} and −50 mA cm^{-2} in 6.0 mol dm^{-3} KOH + 0.50 mol dm^{-3} zincate. Passed charge for deposition was set to 3.0 C cm^{-2}.

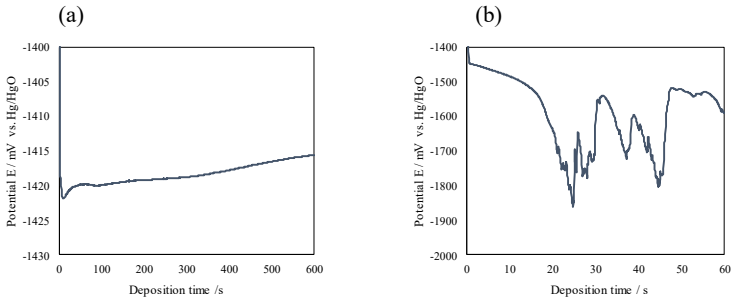

Fig 2.43 Potential profiles during the galvanostatic electrodeposition in 6.0 mol dm^{-3} KOH + 0.50 mol dm^{-3} zincate at (a) −5.0 mA cm^{-2} and (b) −50 mA cm^{-2}.

At −5.0 mA cm^{-2}, the deposition potential is slightly shifted to the positive value. On the other hand, the potential drops to the negative value around 20 s and oscillates at −50 mA cm^{-2}. Since the deposition potential reaches below −1800 mV, hydrogen evolution occurs and Zn electrodeposition may proceed under the diffusion-limited condition. This trend indicates the evolution of dendrites as discussed in Fig. 2.8. Pulsed cycle is introduced at each current density. The potential profile is shown in Figs. 2.44 and 2.45.

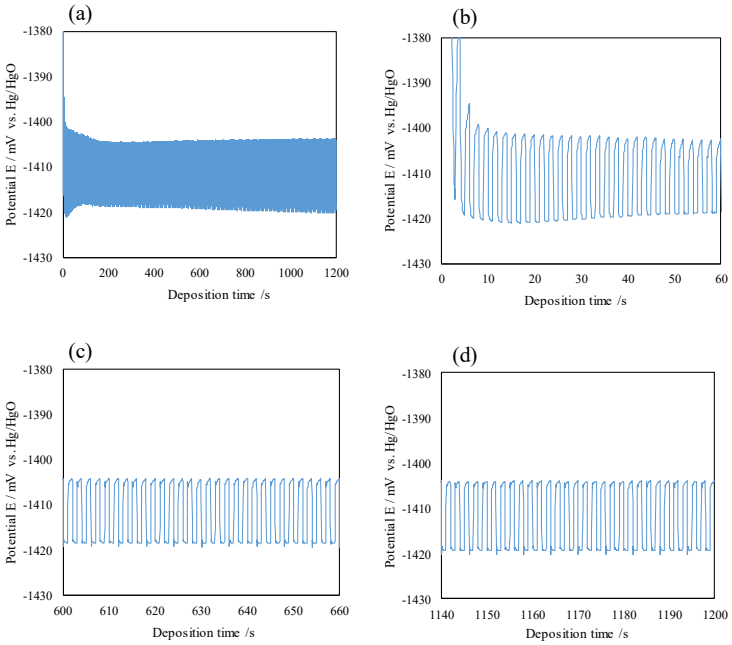

Fig. 2.44 Potential profiles during the pulsed electrodeposition at −5.0 mA cm^{-2} for 1 s and 0 mA cm^{-2} for 1 s; (a) entire profiles, profiles, enlarged profile at (b) 0 s – 60 s, (c) 600 s- 660 s, and (d) 1140 s – 1200 s.

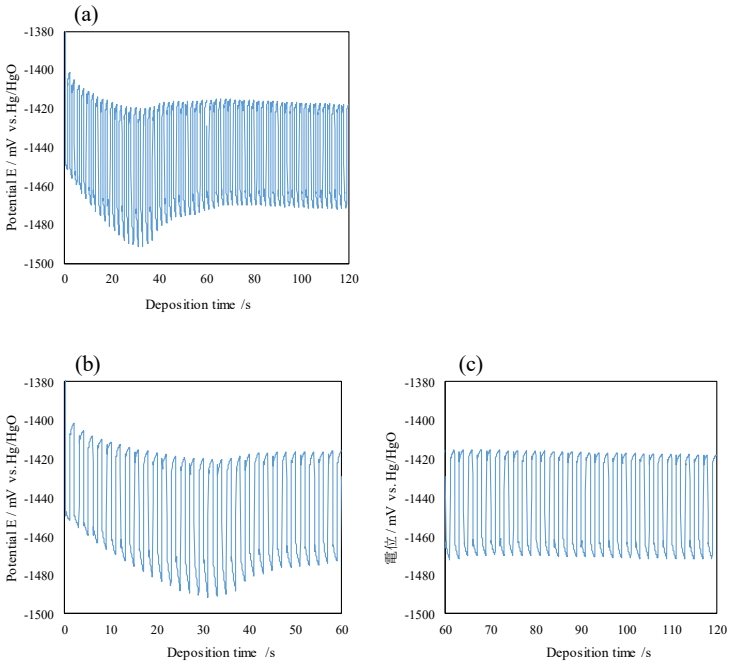

Fig 2.45 Potential profiles during the pulsed electrodeposition at −50 mA cm^{-2} for 1 s and 0 mA cm^{-2} for 1 s; (a) entire profile, enlarged profile at (b) 0 s – 60 s, and (c) 60 s – 120 s.

In the case of lower current density, the potential value stays in the similar value to that at constant current, *c.a.* −1420 mV. On the other hand, at high current density, deposition potential becomes much positive than that at constant current. Since the most negative value during deposition is *c.a.* −1500 mV around 30 s, zinc electrodeposition proceeds before reaching the diffusion-limited condition. This means the surface concentration of zincate is recovered during REST period.

Morphological variations were analyzed by an optical microscope and SEM after the galvanostatic electrodeposition and pulsed electrodeposition. Results are shown in Figs. 2.46 and 2.47, respectively.

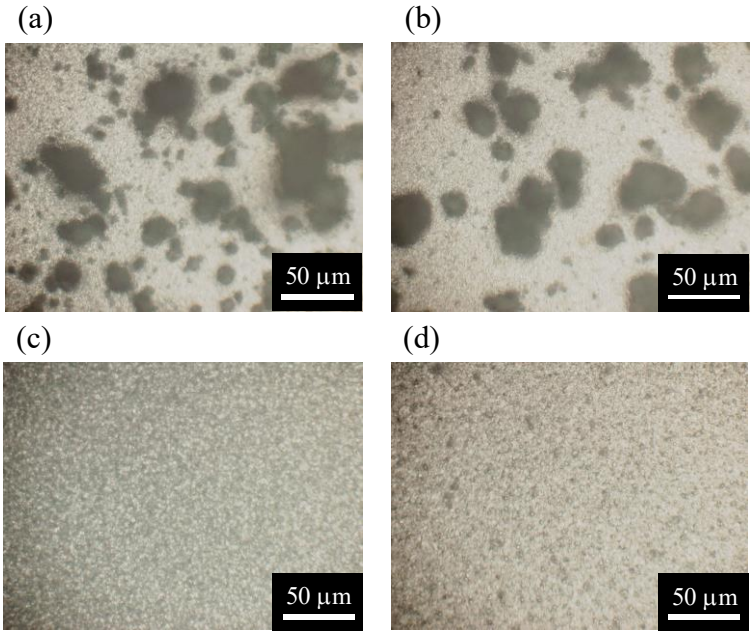

Fig 2.46 Optical microscope images of Zn electrodeposits formed after (a) galvanostatic electrodeposition at −5.0 mA cm^{-2}, (b) pulsed electrodeposition at −5.0 mA cm^{-2}, (c) galvanostatic electrodeposition at −50 mA cm^{-2}, and (d) pulsed electrodeposition at −50 mA cm^{-2}.

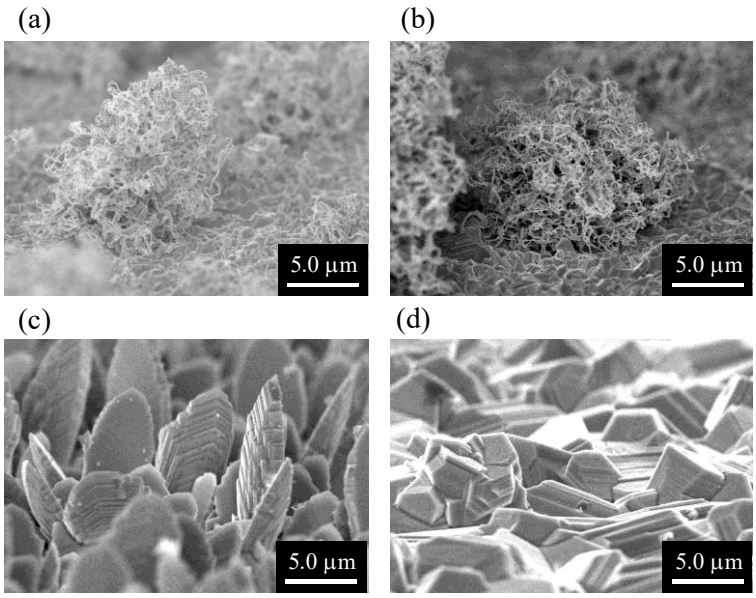

Fig. 2.47 SEM images of Zn electrodeposits formed after (a) galvanostatic electrodeposition at −5.0 mA cm^{-2}, (b) pulsed electrodeposition at −5.0 mA cm^{-2}, (c) galvanostatic electrodeposition at −50 mA cm^{-2}, and (d) pulsed electrodeposition at −50 mA cm^{-2}.

At lower current density, the evolution of mossy structure is evident from the dark colored deposits in an optical microscope image. Although the density of the structures decreases by introducing the pulsed cycle, its elimination is impossible. Furthermore, this decrease in the density may be caused by partial dissolutions of the structures during REST potential as discussed below. In contrast, pulsed electrodeposition is effective to suppress the formation of dendrite at higher current density region (Figs. 2.47 (c) and (d)). This is because electrodeposition under the diffusion-limited condition can be avoided by introducing the pulsed cycle as discussed in the potential profiles.

The Coulombic efficiency during each electrodeposition is evaluated by performing galvanostatic dissolution at +10 mA cm^{-2} after electrodeposition in each condition. Fig. 2.48 shows the potential profiles during the dissolution.

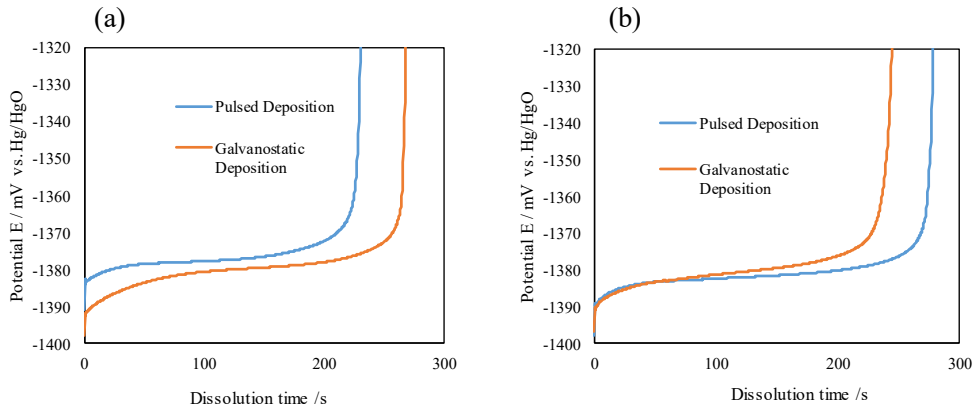

Fig. 2.48 Potential profiles during the galvanostatic dissolution of electrodeposited Zn formed by galvanostatic electrodeposition and pulsed electrodeposition at (a) −5.0 mA cm^{-2} and (b) −50 mA cm^{-2}.

The Coulombic efficiency, η is evaluated by the time required for potential increase (*t* sec) to the positive value, (2.2). Table 2.4 shows the calculated value.

Table 2.4 Coulombic efficiency during the galvanostatic and pulsed electrodeposition

Deposition Condition	Coulombic Efficiency / %
Constant Current (−5 mA cm^{-2})	89
Pulsed Deposition(−5 mA cm^{-2})	77
Constant Current (−50 mA cm^{-2})	80
Pulsed Deposition (−50 mA cm^{-2})	92

At high current density, the coulombic efficiency is improved by the pulsed electrodeposition. This is because hydrogen evolution is suppressed by avoiding the diffusion-limited conditions of zincate. On the other hand, the coulombic efficiency is worsened by the pulse during mossy structure formation. This indicates that partial dissolutions occur on mossy structures due to a large surface area by the filamentous electrodeposits.

Thus, although pulsed electrodeposition is effective to suppress the formation of dendrite at high current density by enhancing the mass transfer of zincate ions, it has the negative influence on the Coulombic efficiency at low current density region. This is because the filamentous structures are corroded upon introduction of REST potential. This demonstrates that different strategies other than controlling mass transfer are required for suppressing the mossy structure formed at low current density region.

Conclusion

Evolution of mossy structures during electrodeposition of Zn at low overpotential or current density was investigated to elucidate nucleation & growth process behind the irregular deposition behavior. From *in situ* optical microscope observation, a continuous increase in the surface area was observed during the mossy structures formation under the galvanostatic condition. In other words, the growth rate didn't decrease even after forming the rough deposits. This was in contrast with dendritic growth at higher current densities where an increase in surface area resulted in decreased growth rates. This result indicated that the formation of mossy structures was characterized by a non-uniform current distribution in the structures; not all surface contributed to the reaction, but an electrodeposition locally and continuously occurred in certain sites inside the structures. At initial stages of the electrodeposition, mossy structures were initiated from the stacking of layer-like structures (microsteps). SEM and TEM analysis revealed that the growth of microsteps towards lateral directions were suppressed at low overpotential, and an electrodeposition continuously occurred on the terrace sites of microsteps. Thus, mossy structures are thought to be initiated by non-uniform evolution of microsteps. Such a deposition behavior was coupled with the low Coulombic efficiencies during electrodeposition, which suggested that the non-uniform deposition behavior was caused by hydrogen adsorption or oxide formation on microsteps. Furthermore, cation species in the electrolyte are thought to interact with the reaction intermediates of Zn deposition; cation with large charge density can facilitate the electrodeposition and dissolution reactions. This affects the crystal growth behavior (microsteps evolution) of electrodeposited Zn.

Reference

[1] F. R. McLarnon, E. J. Cairns, The Secondary Alkaline Zinc Electrode, *J. Electrochem. Soc.* **138** (1991) 645.

[2] A. Nakata, H. Murayama, K. Fukuda, T. Yamane, H. Arai, T. Hirai, Y. Uchimoto, J. Yamaki, Z. Ogumi, Transformation of Leaf-like Zinc Dendrite in Oxidation and Reduction Cycle, *Electrochim. Acta* **166** (2015) 82.

[3] J. W. Diggle, A. R. Despic, J. O'M. Bockris, The Mechanism of the Dendritic Electrocrystallization of Zinc, *J. Electrochem. Soc.* **116** (1969) 1503.

[4] S. Haruyama, Hyomen Gijutsu shanotameno Denkikagaku, Vol. 2, Maruzen (2005).

[5] D. E. Turney, M. Shmukler, K. Galloway, M. Klein, Y. Ito, T. Sholklapper, J. W. Gallaway, M. Nyce, S. Banerjee, Development and testing of an economic grid-scale flow-assisted zinc/nickel-hydroxide alkaline battery, *J. Power Sources* **264** (2014) 49.

[6] J. W. Gallaway, D. Desai, A. Gaikwad, C. Corredor, S. Banerjee, D. Steingart, A Lateral Microfluidic Cell for Imaging Electrodeposited Zinc near the Shorting Condition, J. Electrochem. Soc. 157 (2010) A1279.

[7] R. D. Naybour, Morphologies of zinc electrodeposited from zinc-saturated aqueous alkaline solution, Electrochim. Acta **13** (1968) 763.

[8] R. Y. Wang, D. W. Kirk, G. X. Zhang, Effects of Deposition Conditions on the Morphology of Zinc Deposits from Alkaline Zincate Solutions, *J. Electrochem. Soc.* **153** (2006) C357.

[9] S. Nageswar, Crystal growth at the cathode, *Electrodepos. Surf. Treat.* **3** (1975) 417.

[10] I. N. Justinijanoić, A. R. Despić, Some observations on the properties of zinc electrodeposited from alkaline zincate solutions, *Electrochim. Acta* **18** (1973) 709.

[11] M. M. Jakšić, Impurity effects on the micromorphology of electrodeposited zinc I: Theoretical considerations and a review of existing knowledge, *Surf. Coatings Technol.* **24** (1985) 193.

[12] M. M. Jakšić, Impurity effects on the micromorphology of electrodeposited zinc II: Causes, appearances and consequences of spongy zinc growth, *Surf. Coatings Technol.* **28** (1985) 113.

[13] J. Bressan, R. Wiart, Inhibited zinc electrodeposition: electrode kinetics and deposit morphology, *J. Appl. Electrochem.* **9** (1979) 43.

[14] C. Cahet, B. Saïdani, R. Wiart, The kinetics of zinc deposition at low overpotentials in alkaline electrolytes, *Electrochim. Acta* **33** (1988) 405.

[15] C. Cahet, B. Saïdani, R. Wiart, A model for zinc deposition in alkaline electrolytes: Inhibition layer and activation mechanism, *Electrochim. Acta* **34** (1989) 1249.

[16] C. Cahet, B. Saïdani, R. Wiart, The behavior of zinc electrode in alkaline electrolytes I. A Kinetic analysis of cathodic deposition, *J. Electrochem. Soc*. **138** (1991) 678.

[17] Z. Mao, S. Srinivasan, A. J. Appleby, Effect of PbO on zinc electrodeposition from zincate

solutions, *J. Appl. Electrochem.* **22** (1992) 693.

[18] M. Cai, S. Park, Spectroelectrochemical Studies on Dissolution and Passivation of Zinc Electrodes in Alkaline Solutions, *J. Electrochem. Soc*. **143** (1996) 2125.

[19] C. Mele, B. Bozzini, Spectroelectrochemical investigation of anodic cathodic behavior of zinc in 5.3 M KOH, *J. Appl. Electrochem.* **45** (2015) 43.

[20] D. Desai, X. Wei, D. A. Steingart, S. Banerjee, Electrodeposition of preferentially oriented zinc for flow-assisted alkaline batteries, *J. Power Sources* **256** (2014) 145.

[21] J. O'M. Bockris, Z. Nagy, D. Drazic, On the Morphology of Zinc Electrodeposition from Alkaline Solutions, *J. Electrochem. Soc*. **120** (1973) 30.

[22] R. Y. Wang, D. W. Kirk, G. X. Zhang, Characterization and Growth Mechanism of Filamentous Zinc Electrodeposits, *Electrochem. Soc. Trans*. **2** (2007) 19.

[23] The Metal Finishing Society of Japan, Kinzoku Hyomen Gijutsu Kouza 2, Kinzoku Hyomen Kagaku II, Asakura Syoten (1970).

[24] C. M. López, K. S. Choi, Electrochemical Synthesis of Dendritic Zinc Films Composed of Systematically Varying Motif Crystals, *Langmuir* **22** (2006) 10625.

[25] K. Fukami, S. Nakanishi, T. Tada, H. Yamasaki, S. Sakai, S. Fukushima, Y. Nakato, Self-Organized Periodic Growth of Stacked Hexeagonal Wafers in Synchronization with a Potential Oscillation in Zinc Electrodeposition, *J. Electrochem. Soc.* **152** (2004) C493.

[26] K. I. Popov, P. M. Živković, N. D. Nikolić, Electrochemical aspects of formation of dendrites, *Zastita Materijala* **57** (2016) 55.

[27] J. Yamaki, S. Tobishima, K. Hayashi, K. Saito, Y. Nemoto, M. Arakawa, A consideration of the morphology of electrochemically deposited lithium in an organic electrolyte, *J. Power Sources* **74** (1998) 219.

[28] K. N. Wood, E. Kazyak, A. F. Chadwick, K. -H. Chen, J. -G. Zhang, K. Thornton, N. P. Dasgupta, Dendrites and Pits: Untangling the Complex Behavior of Lithium Metal Anodes through Operando Video Microscopy, *ACS Cent. Sci*. **2** (2016) 790.

[29] H. J. Chang, A. J. Ilott, N. M. Trease, M. Mohammadi, A. Jerschow, C. P. Grey, Correlating Microstructural Lithium Metal Growth with Electrolyte Salt Depletion in Lithium Batteries Using ^{7}Li MRI, *J. Am. Chem. Soc.* **137** (2015) 15209.

[30] A. Tanaka, T. Nakamura, Y. Ueda, F. Noguchi, Observation of the Electrodeposition of Zinc from Sulfuric Acid Bath, J. Jpn. Inst. Metals. 44 (1980) 741.

[31] S. Itoh, N. Yamazoe, T. Seiyama, Electrocrystallization of various metals onto copper single crystal substrates, Surf. Technol. 5 (1977) 27.

[32] T. Mitsuhashi, Y. Ito, Y. Takeuchi, S. Harada, T. Ujihara, Non-uniform electrodeposition of zinc on the (0001) plane, *Thin Solid Films*, **590** (2015) 207.

[33] G. P. Rajarathnam, M. Schneider, X. Sun, A. M. Vassallo, The influence of supporting electrolyte

on zinc half-cell performance in zinc/bromine flow batteries, *J. Electrochem. Soc*. **163** (2016) A5112.
[34] T. Yamashita, S. Toshima, The Electrode Reactions of Deposition and Dissolution of Zinc, *J. Chem. Soc. Jpn.* **12** (1980) 1824.
[35] C. Cachet, Z. Chami, R. Wiart, Electrode kinetics connected to deposit growth for zinc electrodeposition: influence of surfactants, Electrochim. Acta **32** (1987) 465.
[36] M. Nakamura, Y. Nakajima, N. Hoshi, H. Tajiri, O. Sakata, Effect of Non-Specifically Adsorbed Ions on the Surface Oxidation of Pt (111), *Chem. Phys. Chem*. **14** (2013) 2426.
[37] M. Itagaki, Denki Kagaku Impedance Hou, 2nd edition, Maruzen (2011).
[38] J. C. Icaza, R. K. Guduru, Effect of ion charges on the electrical double layer capacitance of activated carbon in aqueous electrolyte systems, *J. Power Sources* **336** (2016) 360.
[39] I. Epselboin, M. Ksouri, R. Wiart, On a Model for the Electrocrstallization of Zinc Involving an Autocatalytic Step, *J. Electrochem. Soc.* **122** (1975) 1206.
[40] J. Bressan, R. Wiart, Inhibited zinc electrodeposition: electrode kinetics and deposit morphology, *J. Appl. Electrochem*. **9** (1979) 43.
[41] C. J. Lan, C. Y. Lee, T. S. Chin, Tetra-aklyl ammonium hydroxides as inhibitors of Zn dendrite in Zn-based secondary batteries, *Electrochim. Acta* **52** (2007) 5407.

Chapter 3:

Controlling Zn Electrodeposition Process toward Applications in Large-scale Battery

3.1 Introduction

As demonstrated in chapter 2, one of the major drawbacks of Zn flow-assisted battery is the evolution of mossy structures during charging. Controlling methods are required to suppress the formation of mossy structures and maintain the compact deposits during the charge-discharge cycles. Although a control of electrolyte flow is one of the possible methods, it is difficult to maintain the compact deposits at thicker Zn film (corresponding to the deep depth of charge) [1-4]. One of the major methods for controlling morphological evolution of electrodeposits is using an additive. For example, the addition of polyethylene glycol (PEG) or polyethylenimine (PE) exhibited the suppression effects on the formation of dendrites [5, 6]. However, the use of organic species in the battery is sometimes unrealistic because they can be decomposed during the reaction and cannot tolerate the long-term cycling. Furthermore, they often decreased the conductivity of the electrolyte and increased the overpotential for electrodeposition, which are disadvantages to gain high voltaic efficiencies [5, 6].

As an alternative method for the organic additives, metal additives often attract attention for controlling the morphological evolution of Zn negative electrode [7-9]. For example, by adding Pb ion in the electrolyte, the formation of mossy structures is suppressed [10-13]. In general, these effects are ascribed to codeposition of additive metal with Zn; after deposition of additive species with Zn, electrodeposition behavior of Zn is altered depending on the chemical property of the codeposited metal [14-17]. However, several aspects need to be further clarified. First, there are a lot of uncertainties about the substantial involvements of the additive species in Zn electrodeposition. For example, although the suppressed hydrogen evolution by additive species is often correlated with a compact electrodeposition, its validity is not clear [11, 15, 16, 18]. Second, despite several additive species reported before, there are no comparable studies between additive species. In addition to their effects on a compact electrodeposition, an influence on charge-discharge characteristics is also important for practical use.

Based on these backgrounds, aim of this chapter is to clarify the effects of metal additives (Pb, Sn and In) in the Zn electrodeposition process, and establish the systematic basis to apply the metal additives for the practical battery operation. For first purpose, electrodeposition behavior of Zn with additive species were thoughtfully investigated in

three-electrode configuration by focusing on the electrochemical behavior during electrodeposition, morphology, texture and composition of the electrodeposits. Latter aspects were discussed based on the analysis of the additive effects under the conditions close to the practical operation (*e.g.* wide-range of current densities, deep depth of charge, introducing electrolyte flow, performing charge-discharge cycles) of the Zn-Ni flow-assisted battery.

3.2 Methodology

3.2.1 Analysis on effects of metal additives on morphological evolution of Zn

Effects of the additive species were analyzed by using the electrochemical cell used in chapter 2; the working electrode and the counter electrode were vertically faced each other. The working electrode was electron beam evaporated Cu on silicon wafer. A mechanically polished Zn (99.5%, 0.30 mm thickness, Nilaco) or Sn plate (99.9%, 0.50 mm thickness, Nilaco) with mirror-finished surface was also used as a working electrode for linear sweep voltammetry (LSV) and comparing morphological evolution. Electrode surface area was 0.50 cm^2 confined by the electrode holder.

The electrolyte containing additive species (Pb, Sn or In) were prepared as follows. Basically, metal sources without a foreign counter anion (*e.g.* Cl^- or NO_3^-) are used in order to investigate the effects derived only from the cation species. An exception was indium; since the solubility of $In(OH)_3$ and In_2O_3 is limited in alkaline solutions, $InCl_3 \cdot 4H_2O$ was used as a In source. For Pb containing solution, 5.0 mmol dm^{-3} PbO (reagent grade, Kanto chemical) was first dissolved in 48wt% KOH (UGR grade, Kanto chemical). This solution was diluted by pure water to obtain 6.0 mol dm^{-3} KOH + 0.010, 0.10, 1.0 mmol dm^{-3} PbO. Sn containing solution was prepared by first dissolving 0.10 mol dm^{-3} $K_2SnO_3 \cdot 3H_2O$ (99.9%, Sigma-Aldrich) in pure water, then this solution was mixed with 48wt% KOH to yield 6.0 mol dm^{-3} KOH + 5, 10, 25, 50 mmol dm^{-3} $K_2SnO_3 \cdot 3H_2O$. For In additive, 5.0 mmol dm^{-3} $InCl_3 \cdot 4H_2O$ (97%, Sigma-Aldrich) was directly dissolved in 6.0 mol dm^{-3} KOH and this solution was diluted to yield 6.0 dm^{-3} KOH + 0.10, 1.0 mmol dm^{-3} $InCl_3 \cdot 4H_2O$. To investigate the effects of types of In salts, $In(OH)_3$ (99.99%, Sigma-Aldrich) was also directly dissolved in 6.0 mol dm^{-3} KOH to yield 1.0 mmol dm^{-3} $In(OH)_3$ solution. For each solution, 0.25 mol dm^{-3} ZnO (reagent grade,

Kanto chemical) was dissolved in the final step to form zincate ions. The solution without additive was 6.0 mol dm^{-3} KOH + 0.25 mol dm^{-3} zincate. The composition of electrolytes are summarized in Table 3.1.

Table 3.1 Composition of the electrolyte

	Concentration / mol dm^{-3}
KOH	6.0
ZnO	0.25
PbO	0 - 1.0×10^{-3}
$K_2SnO_3 \cdot 3H_2O$	0 - 50×10^{-3}
$InCl_3 \cdot 4H_2O$	0 - 5.0×10^{-3}
$In(OH)_3$	0, 1.0×10^{-3}

Electrochemical measurements were performed by using an electrochemical measurements system (HZ-7000, Hokuto Denko). LSV was performed by sweeping the electrode potential from REST potential to −2.0 V at scan rate of 20 mV s^{-1}. Zn electrodeposition was performed by galvanostatic condition at −5.0 mA cm^{-2} for 1000 s.

Surface morphologies of electrodeposited Zn was analyzed by an optical microscope equipped with Charge Coupled Device (CCD) camera (VC-3000, Omron) and SEM (SU-8240 and S-5500, Hitachi). Surface roughness of the electrodeposited Zn was evaluated by a laser scanning confocal microscope (VK-9510, Keyence). Crystal structures of the deposits were analyzed by X-ray diffraction (XRD, Rint-Ultima III, Rigaku). The content of Pb and Sn in the deposit was analyzed by inductively coupled plasma atomic emission spectroscopy (ICP-AES, 5500x, Agilent) after dissolving the Zn electrodeposits in nitric acid solution. The depth profile of the deposits composition was analyzed by glow discharge optical emission spectroscopy (GDS, GDA750, Rigaku). The chemical state of In in the film was analyzed by X-ray photoelectron spectroscopy (XPS, JPS-9010TR, JEOL).

3.2.2 Controlling charging behavior of Zn-Ni flow-assisted battery by In and Sn additives

The effects of In and Sn additives were investigated under the conditions close to the practical operations of Zn-Ni flow-assisted batteries. This analysis was performed in R&D Center Kagoshima, Kyocera Corporation during the internship work. As a current collector for the negative electrode (a substrate for Zn electrodeposition), a copper plate (0.30 mm thickness, Taiho Trading Co., Ltd.) was used. A positive electrode was $Ni(OH)_2$ on a Ni current collector. An electrode surface area of each electrode was defined to 50 cm^2 by the channel plate and the rubber covers shown in Fig. 3.1(a). The distance between the electrodes were 2.2 mm. The capacity of the positive electrode was 2160 mAh (equivalent charge = 155.5 C cm^{-2}). The capacity and charge-discharge rates mentioned in this section were based on this value; *i.e.* 1C rate means 2160 mA = 43.2 mA cm^{-2}. A membrane separator between negative and positive electrode was not introduced in this study, which was analogous to previous studies of the Zn-Ni flow-assisted battery [18, 19]. Such a cell configuration was possible because the concentration polarization was not increased even without separator under electrolyte flow though an influence of intermixing of reactant and byproducts was inevitable as discussed in the results section [9]. An electrolyte for the analysis was 6.5 mol dm^{-3} KOH + 0.60 mol dm^{-3} zincate solution. This solution was prepared by first dissolving ZnO (reagent grade, >99.0%, Kanto chemical) in deionized water at 80 °C. Desired concentrations were obtained by adding KOH (reagent grade, >86.0%, Kanto chemical) and deionized water. Higher KOH concentration than section 3.2.1 was chosen because it exhibited higher conductivity. Also, zincate concentration was increased to suppress the formation of dendrite during charging. As an additive, $K_2SnO_3 \cdot 3H_2O$ or $InCl_3 \cdot 4H_2O$ was added to the electrolyte. Initial concentration of the additive species was 50 mmol dm^{-3}, and this solution was diluted to obtain desired concentrations of additives. Electrolyte flow was introduced by a cassette tube pump (SMP-21AS, As-one) from the inlet located at the bottom of the cell to the outlet at the top. For the analysis on the morphological variations at several charging rates, the electrolyte was not circulated but flown from the reservoir to the bottle for the wasted electrolyte to avoid a decrease in the zincate concentrations of the electrolyte. During charge-discharge cycles, the electrolyte was circulated between the cell and the reservoir.

After reactions, deionized water was circulated for 10 min before disassembling the cell. Then, Zn negative electrode was rinsed with deionized water again and dried in air. The charge-discharge conditions of the cell is shown in Table 3.2.

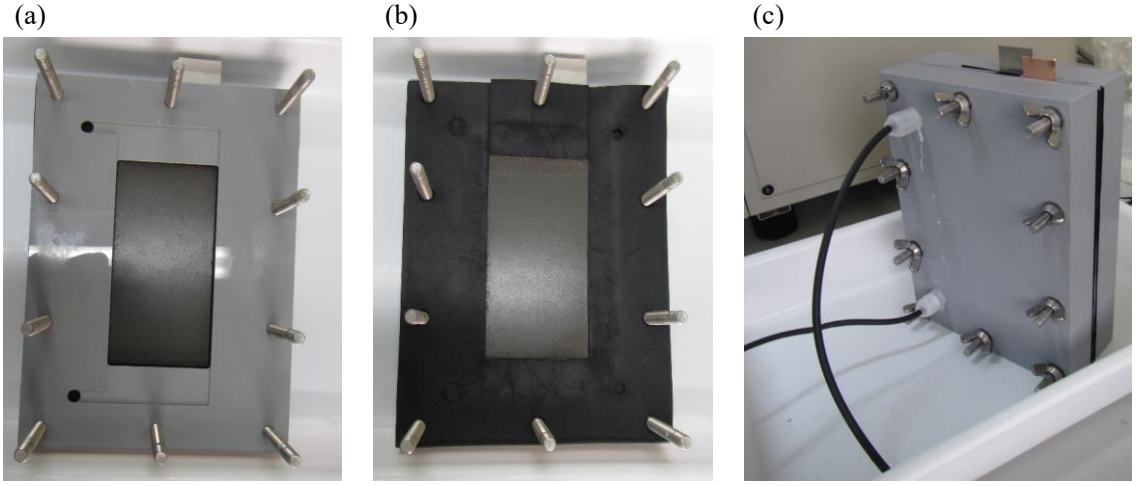

Fig. 3.1 Electrochemical cell for analysis of Zn-Ni flow-assisted battery. (a) Channel plate inside the cell, (b) rubber plate defining the electrode surface area and the distance between the electrodes, (c) outer appearance of the cell.

Table 3.2 Charge-discharge conditions of Zn-Ni flow-assisted battery

Depth of charge	540 mAh / 2160 mAh
Charging rate	C/20 – 1C rate
Flow rate	0.2, 1.0, 2.0 mL/sec
Temp.	R.T. (24-25 ˚C)

Charge-discharge operations were performed by the battery cycler (Bio-Logic, BCS-815). For analyzing the morphological variations after charging and charge-discharge cycles, the capacity was mainly limited to 540 mAh in order to avoid the degradation on the positive electrode at deep depth of charge. Surface morphologies of the negative electrode after reactions were investigated by a digital camera, an ptical microscope (SMZ445, Nikon) equipped with a CCD camera (Dino-Eye Premier M, Thanko). SEM (6700 F, JEOL) was also used for analyzing the microstructures of Zn electrodeposits. Composition of Zn, Sn and In were analyzed by ICP-AES (ICPS-8100, Shimazu). The analyte was prepared by dissolving the electrode in nitric acid solution.

3.3 Results and Discussion

3.3.1 Effects of metal additives on morphological evolution of Zn

Effects on the polarization behavior during Zn electrodeposition

Based on previous researches regarding the additive effects on Zn negative electrode, additive species are supposed to meet following requirements. These criteria is qualitatively inferred from previous researches and its validity and underlying mechanism are investigated through this chapter. First, additive metals should be codeposited with Zn. For example, Moser confirmed Bi electrodeposition prior to Zn deposition, which was thought to provide a conductive path for the active materials (Zn powders) [20]. Second, the overpotential of deposited additive for HER is sufficiently high to avoid self-discharge (decrease in Coulombic efficiency) [7, 9, 18, 21, 22]. Since the electrochemical reactions (Zn electrodeposition and water decomposition) can occur on codeposited metal, HER is also promoted depending on the additive metals. HER during charging is sometimes correlated with the mossy structure formation, too. Accordingly, metal with low melting point is often used as an additive for Zn battery because they have higher overpotential for HER. In this chapter, I attempt to understand another underlying reason why the metal with low melting point is beneficial for Zn negative electrode. Third, additive species should be soluble in an alkaline solution as ion though some previous studies used additives as powders (oxide particles) [8, 11, 20]. This feature is advantageous for the application in flow-assisted battery in terms of the scalability and cost; it is possible to control the charge-discharge cycles simply by introducing additive species in the electrolyte.

Based on these criteria, effects of Pb, Sn and In were investigated as additives to suppress the formation of mossy structures. As and Tl are also expected to have high overpotential for HER, but they have a toxicity [23]. There is some literature about Bi addition effects [19, 24], but it is relatively expensive [25]. Pb is well-known additive to obtain compact Zn electrodeposits previously [10-13]. However, effects of Sn and In on the formation of mossy structure are not well elucidated, yet. Furthermore, toxicity of Pb is unfavorable for the battery application to meet the regulations like RoHS. Following additive salts were basically used otherwise noted; PbO, $K_2SnO_3 \cdot 3H_2O$, and $InCl_4 \cdot 4H_2O$. Latter two sources were selected because they were more soluble than oxide or hydroxide species.

First, the effects of three additives on the polarization behavior during Zn electrodeposition was analyzed. Fig. 3.2 compares LSV of Cu electrodes in the solution containing various concentrations of Pb, Sn and In additives.

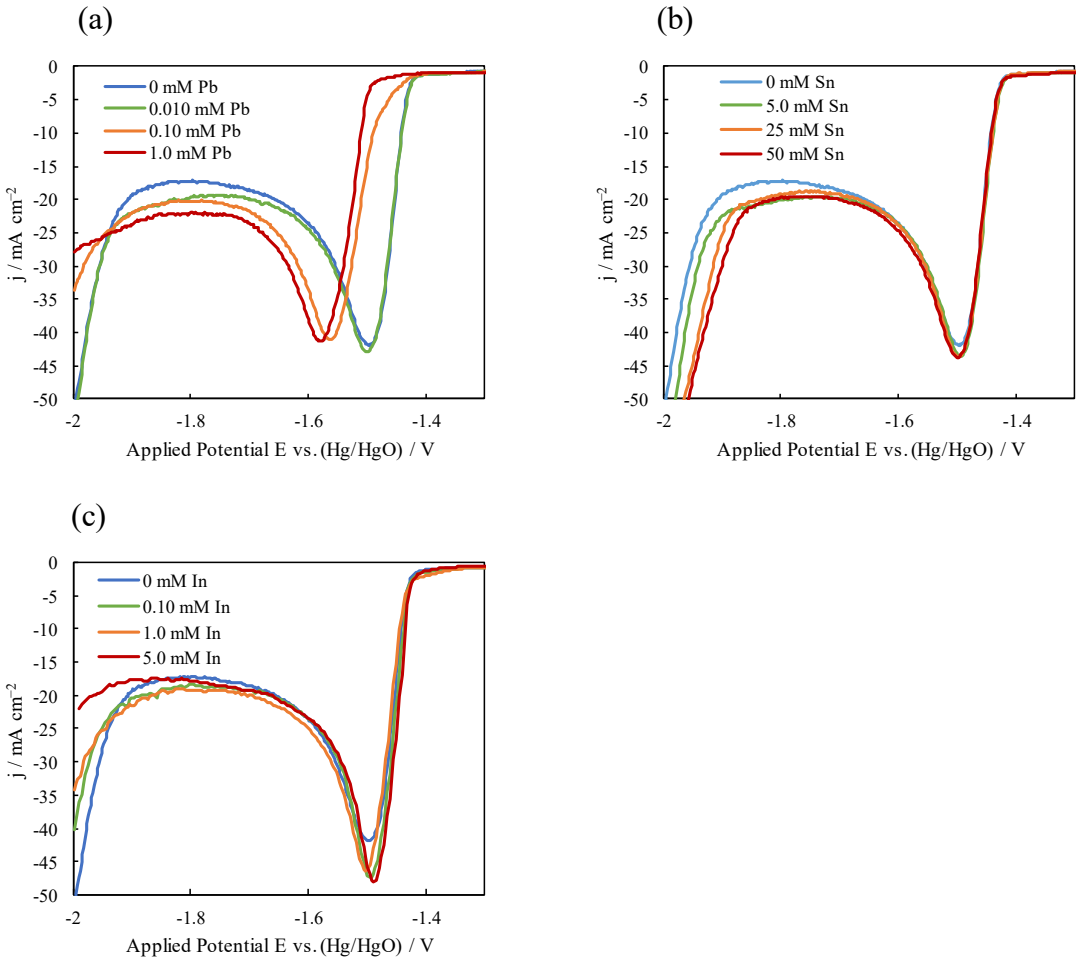

Fig 3.2 Linear sweep voltammograms of Cu electrodes in 6.0 mol dm^{-3} KOH + 0.25 mol dm^{-3} zincate +; (a) 0.010 – 1.0 mmol dm^{-3} Pb, (b) 1 – 50 mmol dm^{-3} Sn and (c) 0.10 – 5.0 mmol dm^{-3} In.

The peak around –1.4 V is due to Zn electrodeposition and current increase around –1.9 V is caused by hydrogen evolution by the decomposition of water as discussed in chapter 2. By adding the additive species, there are two distinctive changes in the voltammograms. First, the deposition potential is shifted to the negative value by adding Pb. Second, HER is promoted or suppressed depending on the additive species. Pb and In decreases the current for HER at −2.0 V, while the onset of HER becomes positive by adding Sn.

Former changes suggest that a larger overpotential is required for Zn electrodeposition at the presence of Pb. In other words, the deposition reaction of Zn is suppressed by the presence of Pb. The elementary steps for Zn electrodeposition were written as following equations [11].

$$2H_2O + e^- \rightarrow H_{ad} + OH^- \quad (3.1)$$

$$Zn(OH)_4^{2-} \rightleftharpoons Zn(OH)_2 + 2OH^- \quad (3.2)$$

$$Zn(OH)_2 + e^- \rightarrow Zn(OH)_{ad} + OH^- \quad (3.3)$$

$$Zn(OH)_{ad} + H_{ad} \rightarrow Zn + H_2O \quad (3.4)$$

$$Zn(OH)_{ad} + e^- \rightarrow Zn + OH^- \quad (3.5)$$

At the presence of Pb, the elementary step (3.1) and (3.4) were thought to be suppressed due to high overpotential of Pb for HER. This is also thought to be beneficial for obtaining compact electrodeposits. However, such a suppression effect is not expected in the case of In and Sn addition because of no negative shift in the potential in Fig. 3.2. Also, this trend is better than that of Pb because an increased overpotential results in loss of the voltaic efficiency.

The latter effect was in accordance with the overpotential for HER of each additive metal. Pb and In have higher overpotential for HER, while Sn has slightly lower overpotential for HER [23, 26] than that of Zn. Retarded HER is advantageous for suppressing the corrosion of Zn (self-discharge) [7, 9, 18, 22].

The effects of metal species on Zn electrodeposition reaction are apparent from the discussion above. However, it is difficult to distinguish the reduction current for additive species in Fig. 3.2. To confirm the deposition of the additive metals, LSV of Zn electrode was measured in the solution containing only 6.0 mol dm^{-3} KOH + 50 mmol dm^{-3} Sn or 5.0 mmol dm^{-3} In. Zn working electrode was used to demonstrate the additives deposition on Zn surface. The results are shown Fig. 3.3.

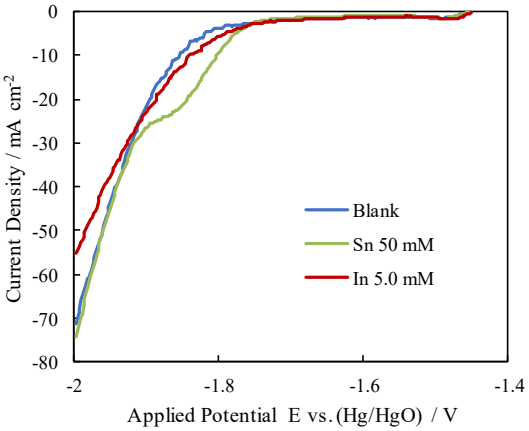

Fig 3.3 Linear sweep voltammograms of Zn electrodes in 6.0 mol dm^{-3} KOH (blue), 6.0 mol dm^{-3} KOH + 50 mmol dm^{-3} Sn (green), and 6.0 mol dm^{-3} KOH + 5.0 mmol dm^{-3} In (red).

In the Sn containing solution, there is a shoulder-like peak around −1.8 V. This is caused by the reduction of Sn(IV) to Sn(II). The polarization behavior at HER region is almost same to that without additive. In the case of In addition, there is no remarkable peak though the current slightly increases around −1.8 V. But, indium deposition is inferred again from suppressed HER at −2.0 V. These results indicate that the additive species are deposited with Zn though the reduced amount is much smaller than that of Zn, which is in accordance with the composition analysis shown below.

Morphological variations of electrodeposited Zn at various additive concentrations

Zn electrodeposition was performed by galvanostatic conditions at −5.0 mA cm^{-2} for 1000 s to investigate the effects of the additive species on the morphological evolution. Fig. 3.4 represents the potential transients during the deposition at various concentrations of additive species.

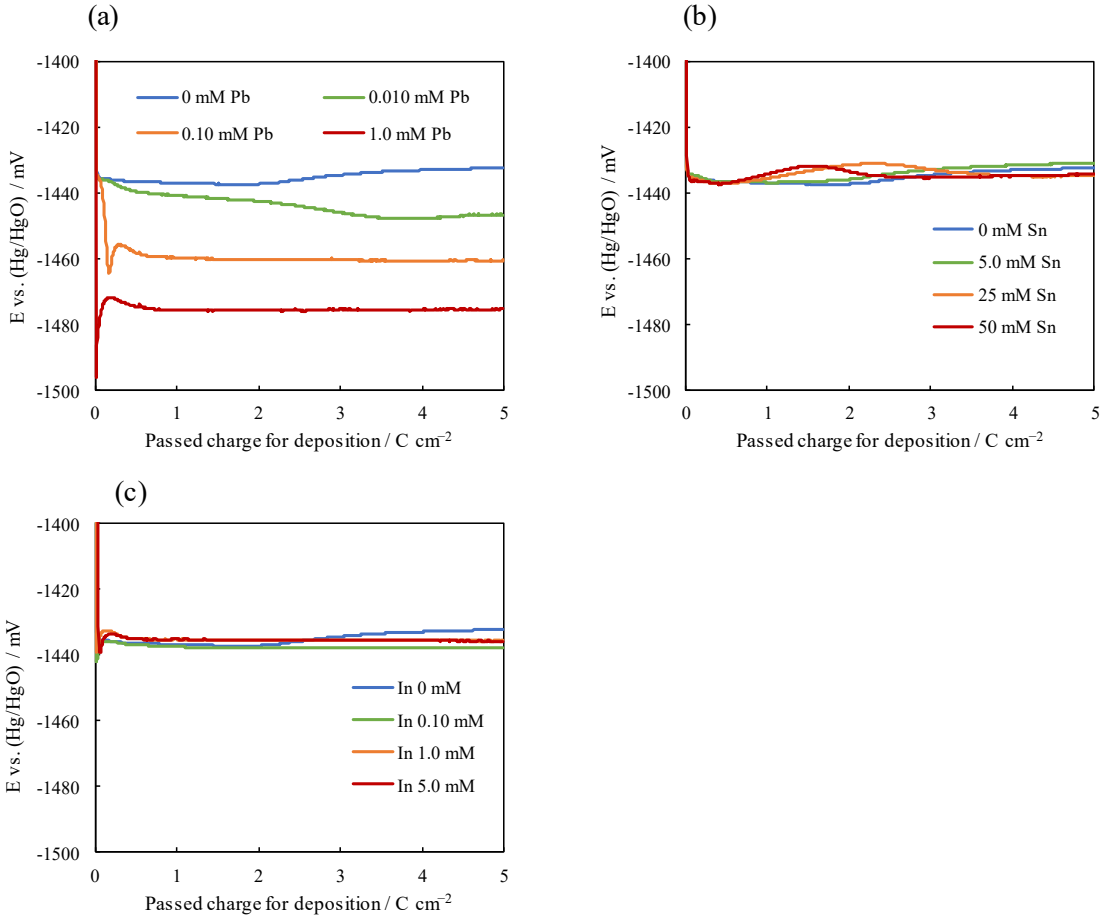

Fig 3.4 Chronopotentiograms during Zn electrodeposition at −5.0 mA cm^{-2} in 6.0 mol dm^{-3} KOH + 0.25 mol dm^{-3} zincate + (a) 0.010 – 1.0 mmol dm^{-3} Pb, (b) 1 – 50 mmol dm^{-3} Sn and (c) 0.10 – 5.0 mmol dm^{-3} In.

The deposition potential is negatively shifted by Pb additive, while the potential stays in a similar region in the case of Sn and In addition. This trend is in accordance with LSV measurements (Fig. 3.2). In addition, there is a potential maximum in 0.10, 1.0 mmol dm^{-3} Pb, 1.0 and 5.0 mmol dm^{-3} In addition. Such a peak is often observed during the metal deposition on a foreign substrate [27]. It possibly originates from Pb / In deposition on Cu surface or Zn electrodeposition on additive metals (*e.g.* Gallaway *et al* confirmed that Bi additive was electrodeposited prior to Zn electrodeposition, and the they termed the Bi effects to "substrate effects" [24]). After electrodeposition, surface morphologies of representative condition were investigated by an optical microscope.

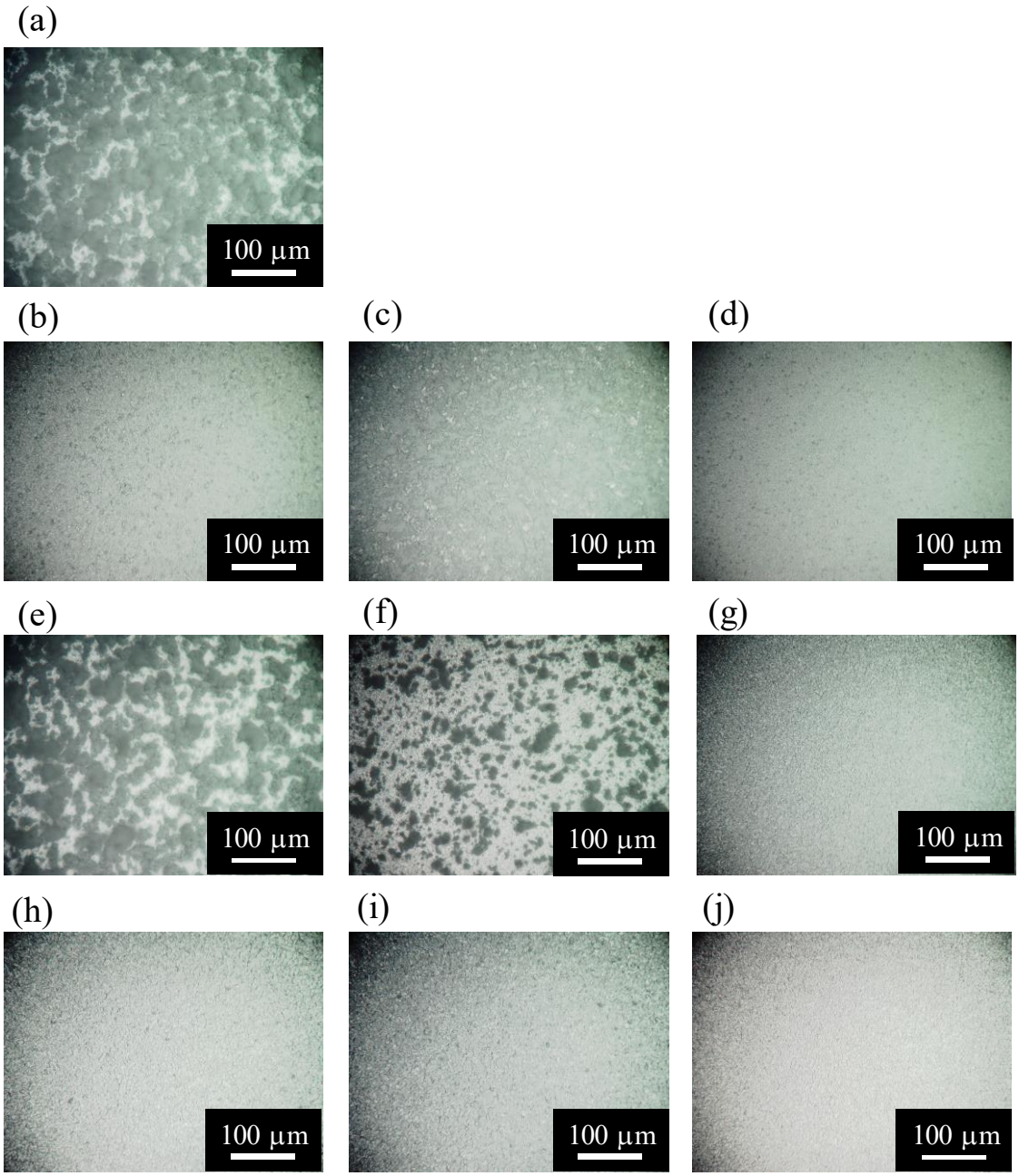

Fig. 3.5 Optical microscope images of surface morphologies of Zn electrodes after electrodeposition; (a) without additive, (b) 0.010 mmol dm^{-3} Pb, (c) 0.10 mmol dm^{-3} Pb, (d) 1.0 mmol dm^{-3} Pb, (e) 5.0 mmol dm^{-3} Sn, (f) 10 mmol dm^{-3} Sn, (g) 50 mmol dm^{-3} Sn, (h) 0.10 mmol dm^{-3} In, (i) 1.0 mmol dm^{-3} In and (j) 5.0 mmol dm^{-3} In.

The RMS roughness was evaluated by laser scanning confocal microscopy. Table 3.3 shows the average ± S.D. value.

Table 3.3 RMS roughness of Zn electrodeposits at various additive concentrations

Additive	Concentration / mmol dm^{-3}	RMS roughness / mm
No additive	-	7.29 ± 0.05
Pb	0.010	0.82 ± 0.01
Pb	0.10	1.19 ± 0.03
Pb	1.0	0.21 ± 0.01
Sn	5.0	6.07 ± 0.48
Sn	10	3.71 ± 0.05
Sn	25	0.45 ± 0.01
Sn	50	0.57 ± 0.00
In	0.10	0.52 ± 0.02
In	1.0	0.41 ± 0.02
In	5.0	0.44 ± 0.01

By adding the additive species, the formation of mossy structures is suppressed, and compact deposits (white color) is obtained. However, its concentration dependence is considerably different each other. In the case of Pb and In, less than 0.10 mmol dm^{-3} addition is effective to suppress the structure, while more than 25 mmol dm^{-3} is required for Sn addition. This concentration dependence is caused by variation in deposited amount with Zn; From composition analysis by ICP-AES (Table 3.4 and 3.5), the content of Sn is much smaller than that of Pb. (The value shown in red color in the table is less than the detection limit.) Thus, the suppression of mossy structure is possible when sufficient amount of additive species are reduced with Zn. This corresponds to the first criteria mentioned in the beginning of the results section, and is first report that describes correlations between additive performance and its contents in Zn electrodeposits. The compositional variations of additive species are further discussed in the analysis of the Zn-Ni flow-assisted battery.

Table 3.4 Content of Pb in Zn electrodeposits

Pb concentration / mmol dm^{-3}	Zn / ppm	Pb / ppm	Zn / at%	Pb / at%
0.010	6.92	0.003	99.99	0.01
0.10	7.00	0.018	99.92	0.08
1.0	6.31	0.212	98.95	1.05

Table 3.5 Content of Sn in Zn electrodeposits

Sn concentration / mmol dm^{-3}	Zn / ppm	Sn / ppm	Zn / at%	Sn / at%
5	7.13	0.002	99.99	0.01
10	7.29	0.006	99.95	0.05
25	7.11	0.012	99.90	0.09
50	7.19	0.010	99.92	0.08

Effects of additive species on morphologies and texture evolution of electrodeposited Zn

In order to discuss the mechanisms behind morphological changes, morphologies and crystal structure (texture evolution) of the Zn electrodeposits were further investigated. Fig. 3.6 shows SEM images of electrodeposited Zn at the representative concentrations.

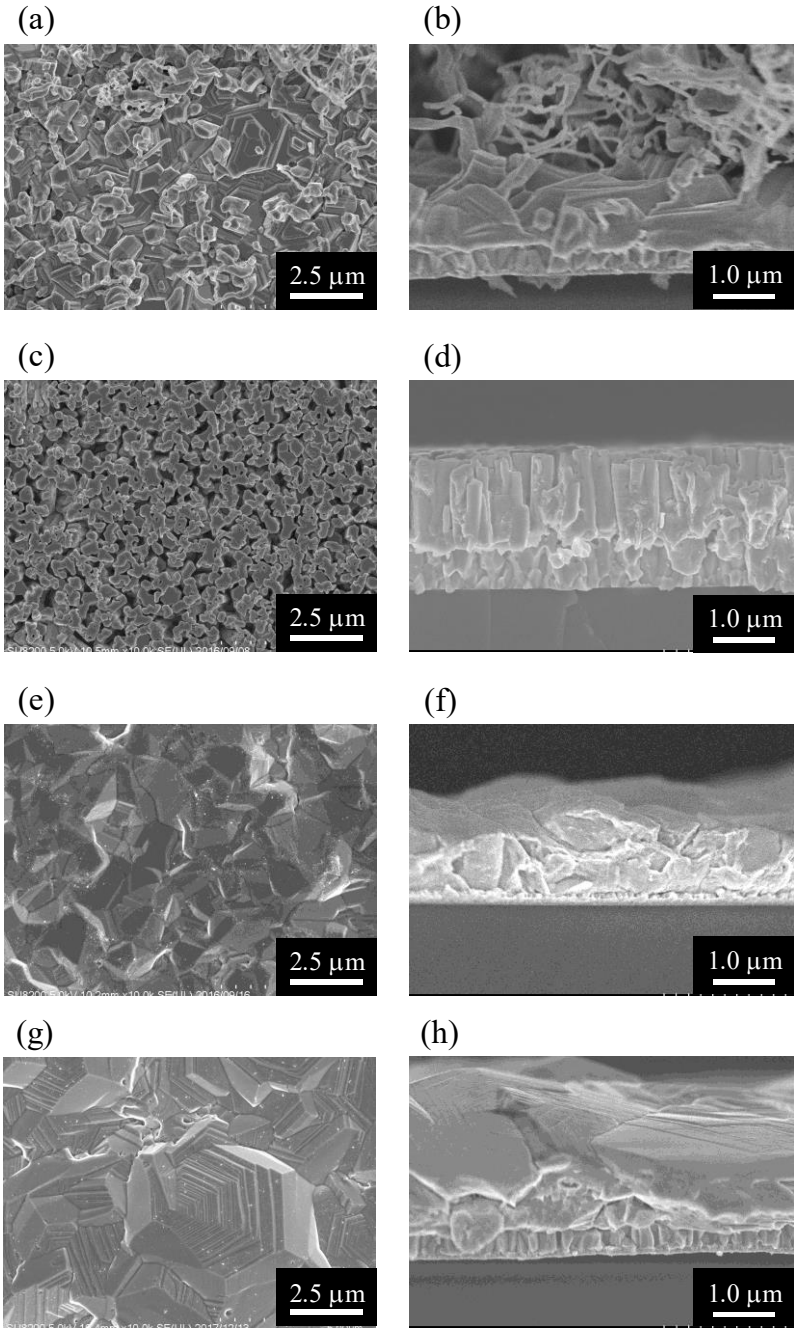

Fig. 3.6 SEM images of galvanostatically electrodeposited Zn at −5.0 mA cm^{-2} for 1000 s; (a), (b) without additive, with (c), (d) 1.0 mmol dm^{-3} Pb, (e), (f) 50 mmol dm^{-3} Sn and (g), (h) 1.0 mmol dm^{-3} In. (a), (c), (e) and (g) are top-view and (b), (d), (f) and (h) are cross-sectional images.

By adding Pb, very fine nuclei with several 100 nm diameter are uniformly formed over the entire surface. From cross-sectional images, they have columnar structures oriented perpendicular to the substrate. When Sn is added, the formation of

microsteps structures (stacking of layer-like structures) is suppressed. On the other hand, microstep structures are formed, but following evolution of filamentous structure is suppressed by In additive. Such a continuous deposition of microsteps is similar to the deposition behavior observed at deposition with a higher current density region in Chapter 2.

Texture evolution of Zn deposits at early stages of deposition at 200 and 400 s (passed charge for deposition = 1.0, 2.0 C cm^{-2}) was analyzed by XRD. Early stages of deposition were purposely analyzed because the texture becomes random in a thick film.

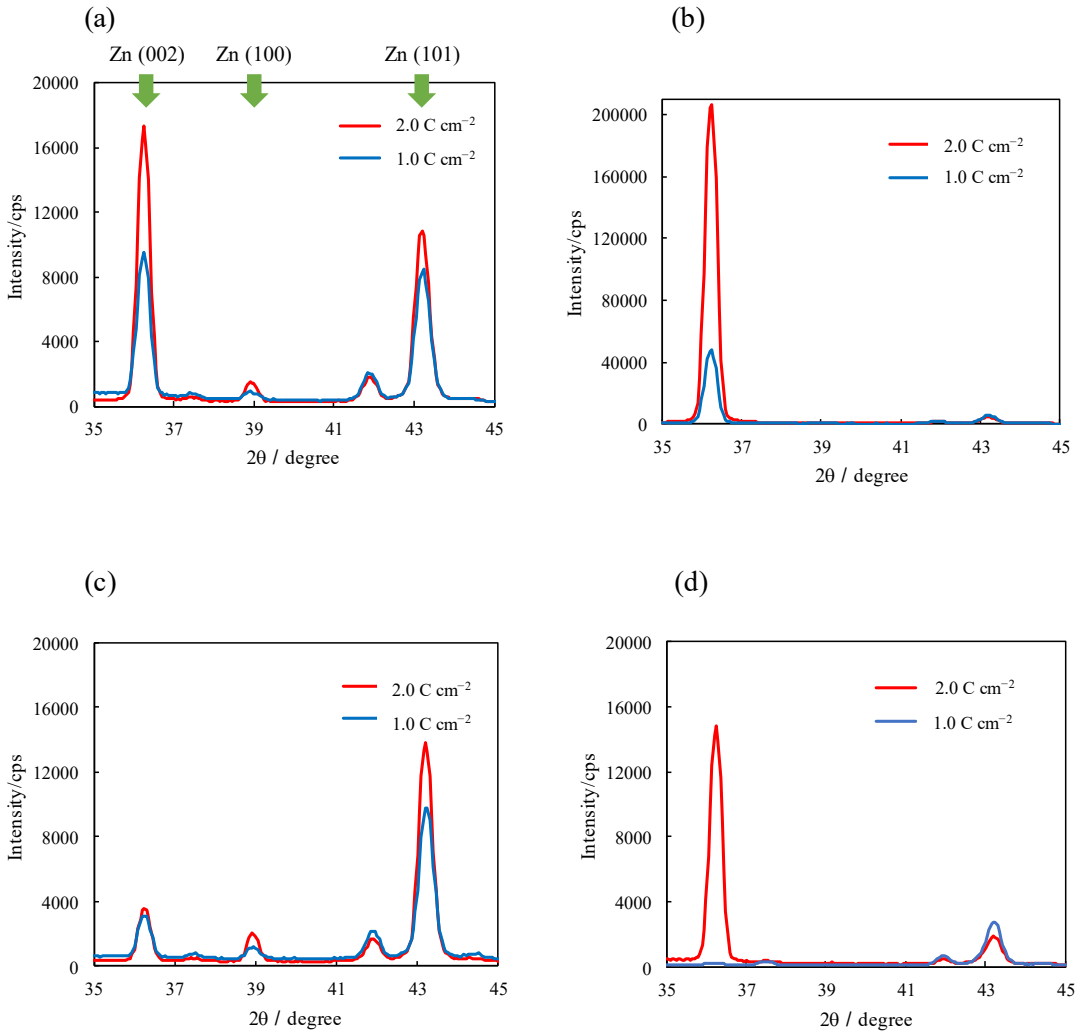

Fig. 3.7 XRD patterns of galvanostatically electrodeposited Zn at −5.0 mA cm^{-2} for 1000 s; (a) without additive, with (b) 1.0 mmol dm^{-3} Pb, (c) 50 mmol dm^{-3} Sn and (d) 1.0 mmol dm^{-3} In.

The deposits without additive species exhibit relatively strong (002) orientation.

It is generally reported that electrodeposition of hcp metals at low overpotential yields the deposits with (002) orientation [28, 29]. Also, the microsteps structures shown in Fig. 3.6 (a) exposes the terrace of (002) surface. Similarly, electrodeposits with In additive also show (002) orientation. Upon the addition of Pb, peak intensity of (002) becomes 10 times stronger than that without additive. This means a columnar structure formed by Pb additive is oriented to (002) direction. In the case of the deposits without microsteps formed by Sn additive, the texture evolution to (002) is suppressed. In short, the texture evolution is in accordance with the morphological variations; When microsteps are formed, the electrodeposits exhibit relatively strong (002) orientation. Furthermore, the columnar structures formed by Pb shows very strong (002) orientation.

Additionally, it is notable that the suppressing effects of Sn on microsteps formation is similar to that observed in Zn electrodeposition on Sn substrate without an additive. Fig. 3.8 shows surface the morphology of Zn electrodeposits on Sn substrate without additive at 5.0 C cm^{-2}.

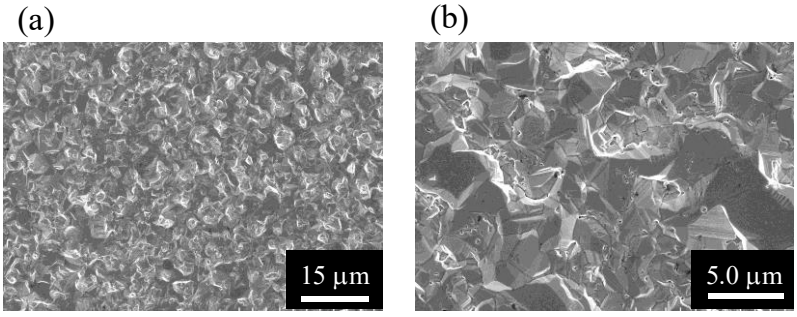

Fig 3.8 SEM images of Zn electrodeposit on Sn substrate. (b) is higher magnification image of (a).

It was previously reported that the irregular deposits can be suppressed by selecting a proper current collector [25]. However, the use of Sn substrate is limited due to the corrosion in the alkaline solution. Also, the substrate effects disappear at thicker deposited film like 20 C cm^{-2}. On the other hand, the additive metals may continuously enable the compact Zn electrodeposition. This explains why compact electrodeposits can be obtained even without increase in the overpotential for Zn electrodeposition in Sn and In. The mechanism of compact Zn deposition by additive species will be discussed in the last part of this section. Also, the applicability of In and Sn additives in Zn-Ni flow-assisted battery is investigated in section 3.3.2.

Influence of anion species in Zn electrodeposition

In the analysis discussed above, $InCl_3 \cdot 4H_2O$ was used as additive salt for In addition. This salt was selected because it was more soluble than $In(OH)_3$ or In_2O_3 in the alkaline solution. However, Cl^- has sometimes influences on electrode reactions. (A stable form of In^{3+} in alkaline solutions is InO_2^-, and Cl^- is thought to dissociate from In^{3+} [30].) Here, the effects of Cl^- on Zn electrodeposition was investigated by performing electrodeposition with KCl or $In(OH)_3$.

Fig 3.9 compares the potential transients during Zn electrodeposition with 1.0 mmol dm^{-3} KCl, $InCl_3 \cdot 4H_2O$ and $In(OH)_3$.

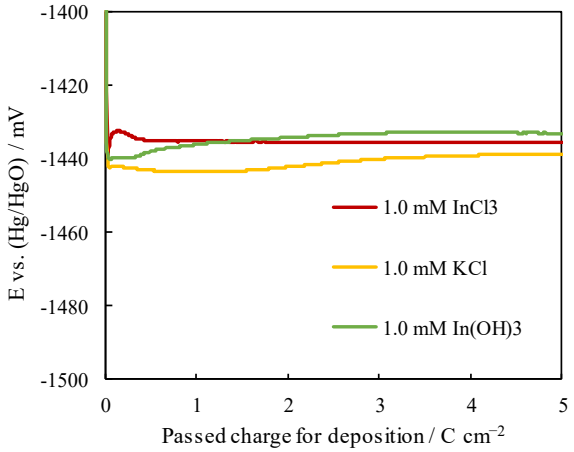

Fig 3.9 Chronopotentiograms during Zn electrodeposition at −5.0 mA cm^{-2} in 6.0 mol dm^{-3} KOH + 0.25 mol dm^{-3} zincate + 1.0 mmol dm^{-3} $InCl_3 \cdot 4H_2O$ (red), KCl (yellow) and $In(OH)_3$ (green).

Although the changes in the potential value itself are not remarkable, the shape of the potential transients are different each other. When KCl is added, the potential first shifted to the negative value, then it becomes positive again around 2.0 C cm^{-2}. This trend is similar to that without an additive; potential change to the negative value is caused by an increase in concentration overpotential and positive shift originates from increase in the surface area due to the mossy structure formation. In the case of $In(OH)_3$ and $InCl_3 \cdot 4H_2O$ addition, the potential value becomes stable before passing 1.0 C cm^{-2}. Surface morphologies of each electrodeposit were further analyzed by an optical microscope (Fig. 3.10) and SEM (Fig. 3.11).

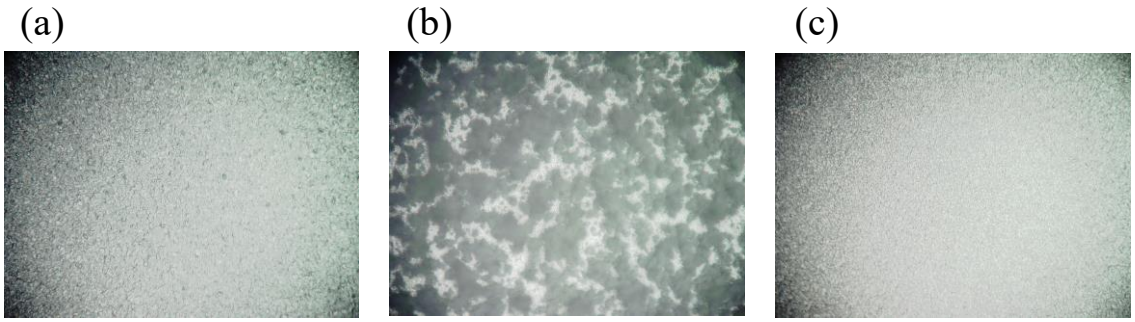

Fig 3.10 Optical microscope images of Zn electrodeposits formed at −5.0 mA cm^{-2} in 6.0 mol dm^{-3} KOH + 0.25 mol dm^{-3} zincate + (a) 1.0 mmol dm^{-3} $InCl_3 \cdot 4H_2O$, (b) KCl and (c) $In(OH)_3$.

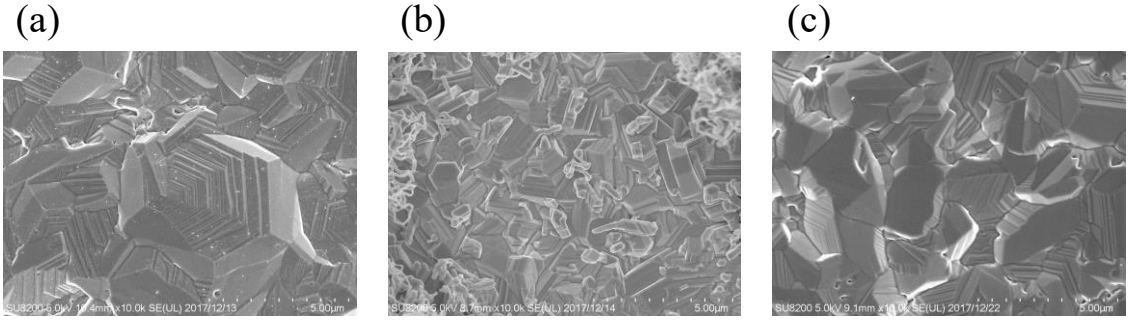

Fig 3.11 SEM images of Zn electrodeposits formed at −5.0 mA cm^{-2} in 6.0 mol dm^{-3} KOH + 0.25 mol dm^{-3} zincate + (a) 1.0 mmol dm^{-3} $InCl_3 \cdot 4H_2O$, (b) KCl and (c) $In(OH)_3$.

The images clearly indicate that the formation of mossy structure is suppressed not by Cl^- but by In. In the case of KCl containing solution, mossy structure is initiated from microsteps as is the case for the solution without additive. Both $InCl_3 \cdot 4H_2O$ and $In(OH)_3$ are effective to suppress the formation of mossy structures. However, Zn microstructures formed by each additive are different; in the case of $In(OH)_3$, the formation of microsteps is less dominant than in the Cl^- containing solution. To further discuss these morphological changes, XRD was also measured on the electrodeposits with 1.0 mmol dm^{-3} $In(OH)_3$.

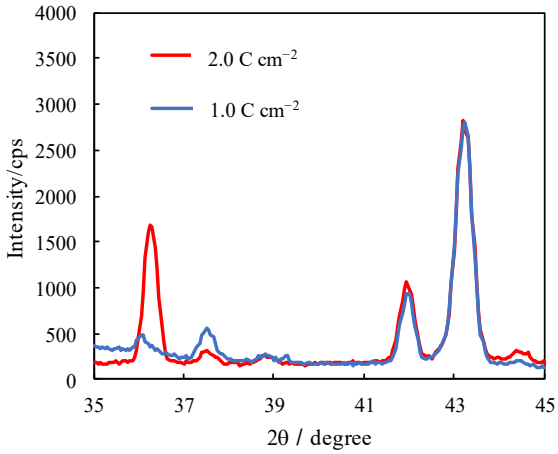

Fig 3.12 XRD patterns of electrodeposited Zn with 1.0 mmol dm^{-3} $In(OH)_3$.

Please note that the absolute diffraction intensities are not comparable to the above described XRD results due to changes in the detector condition. However, it is noticeable that the relative intensity of Zn (002) is weaker than that of (101). Thus, the texture evolution to (002) is suppressed in the case of $In(OH)_3$. This means In itself have the suppression effects on the texture evolution to (002) (microstep formation), but this texture is maintained by the presence of Cl^-. Such a change in the texture by anion species has been often observed during electrodeposition. For example, NO_3^- was known to induce (002) texture evolution and the mossy structure formation in acidic media for Zn electrodeposition [31, 32]. As a mechanism for such a change, two possibilities could be considered. First, an adsorbed anion sometimes alters the diffusivity of adatom on the surface [33, 34]. Since the formation of microsteps is a repeated process of 2D nucleation and its growth toward lateral direction, the diffusivity of adatom may affect the microsteps evolution. Another possibility is the alteration to the charge transfer reaction by an adsorbed anion. It is expected that the texture is altered when the rate balance between the atomic steps formation and the charge transfer to Zn species is changed [35].

Depth profile of additive species in deposits and its chemical state

In order to discuss the mechanism behind the morphological change by additive species, it is important to understand how metal species exists in the deposit. In the case of Pb, alteration to reaction steps of Zn electrodeposition might suppress the formation of mossy structures as discussed above. However, in the case of Sn and In, such an effect was not expected because there was a minor difference in the polarization behavior during Zn electrodeposition. Although deposition of In or Sn in Zn deposits was evident from

LSV and ICP-AES analysis, its compositional variations in the depth and the chemical state were not clear. XRD analysis showed no peaks corresponding to additive species due to the low amount of additive metals in the deposit. Therefore, GDS and XPS analysis were performed for Zn electrodeposits formed with In.

Fig 3.13 shows the depth profile of In composition in electrodeposited Zn with 1.0 mmol dm^{-3} $InCl_3 \cdot 4H_2O$ additive or Pb composition with 1.0 mmol dm^{-3} PbO additive analyzed by GDS. Passed charge for the deposition was 5.0 C cm^{-2}. The profile shows the relative intensity of emission from each element, not actual composition of the deposits.

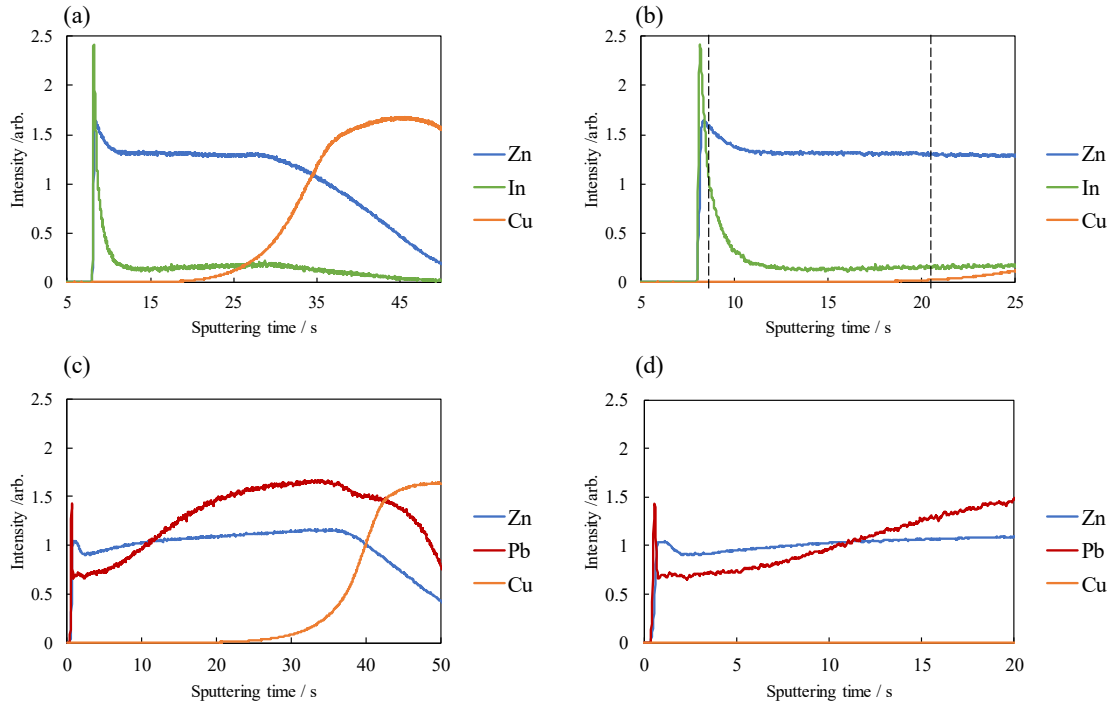

Fig 3.13 Depth profile of the composition of Zn, In and Cu; (a) entire profile, (b) enlarged profile near the surface and Zn, Pb and Cu; (c) entire profile, (d) enlarged profile near the surface . Dashed lines in (b) shows the time at which the ratio is compared in the text.

The ratio of the intensity at a dashed line in Fig. 3.13 (b) is In/Zn=1.25 at 8.3 s and In/Zn=0.15 at 20 s. This indicates the content of In is high near the surface compared to that in the bulk..

To analyze the absolute composition of In at the surface and inside the deposits including its chemical state, XPS analysis was performed. Fig 3.14 shows the result of

wide scan and Fig. 3.15 shows the spectra of narrow scan corresponds to peaks of In 3d 5/2. To analyze the composition beneath the surface, Ar sputtering (30 s) was performed to etch the deposit. About 100 nm Zn layer was etched by this procedure (total thickness is *c.a.* 500 nm at 1.0 C cm^{-2}).

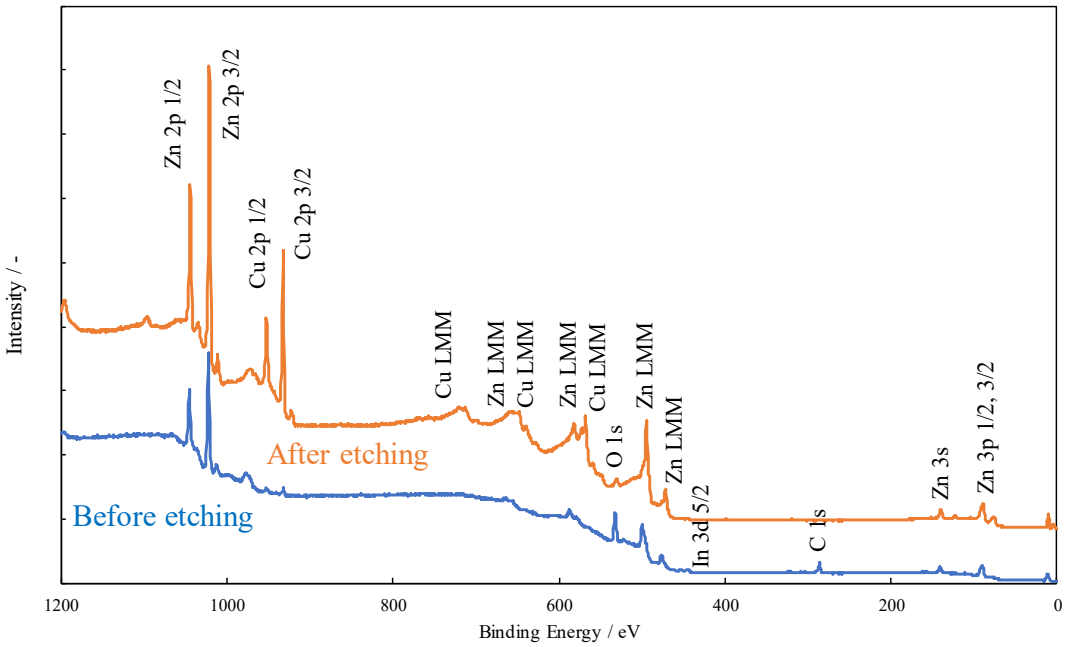

Fig. 3.14 XPS spectra of Zn electrodeposits with In additive (wide scan)

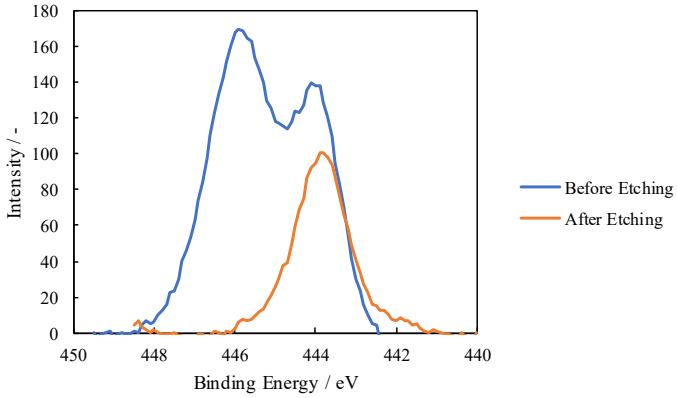

Fig. 3.15 XPS spectra of Zn electrodeposits with In additive (In 3d 5/2)

Peaks are observed at 444 eV and 445.8 eV in the narrow scan. A former peak is assigned to metal In and a latter peak originates from In_2O_3 or $In(OH)_3$. The composition of In compared to Zn + In is 2.4 at% before etching and 0.4 at% after etching. From the wide

scan, there is no detectable peak other than Zn, Cu, In, O and C. This means an incorporation of Cl to the deposits is negligible.

Before the etching, a peak corresponding to In_2O_3 or $In(OH)_3$ is stronger than that corresponding to metal In. After etching, this peak disappears, and only a peak from metal In remains. This result indicates that In is deposited as metal, but it undergoes oxidation during air exposure. As is the case for GDS analysis, content of In is 6 times higher near the surface than in the bulk.

In Zn electrodeposition with Pb additive, the composition ratio of Pb decreases from bottom of the deposits to the surface. This is ascribed to preferential deposition of metal with positive deposition potential at the initial stage, and following decrease in the reduction rate by reaching the diffusion-limited condition of deposited metal [36, 11]. A peak is observed at the surface. High content of Pb at the surface may originate from the replacement deposition of Pb by Zn dissolution after stopping the electrodeposition though electrode was immediately taken out from the solution. (Zn is dissolved as Zn^{2+} and Pb^{2+} is deposited as Pb.) Similar trend is observed in In additive, too. In fact, REST potential of Zn electrodes (measured immediately after immersing in the electrolyte before LSV measurements shown in Fig. 3.3) varies in the additive containing solution; 6.0 mol dm^{-3} KOH is −1453 mV, 6.0 mol dm^{-3} KOH + 5.0 mmol dm^{-3} $InCl_3 \cdot 4H_2O$ is −1450 mV, and 6.0 mol dm^{-3} KOH + 5.0 mmol dm^{-3} $K_2SnO_3 \cdot 3H_2O$ is −1449 mV. This implies that the REST potential is shifted to the positive value in the additive containing solution due to coupling between the anodic dissolution of Zn and the additive deposition. The current increase by this positive shift is roughly estimated from the polarization behavior; according to LSV during anodic dissolution (shown in Fig. 5.1), the current increase by 3 mV shift to the positive potential is *c.a.* 181 μA. This is much higher than an estimated partial current from In composition from Fig. 3.15. Partial current density can be calculated from Zn 99.6at% and In 0.4at% with two and three electron transfer reactions, respectively at −5.0 mA cm^{-2}. This yields the partial current density = 30 μA for In electrodeposition. Since above mentioned positive shift corresponds to the value without zincate ions in electrolyte, an actual replacement reaction is thought to be much slower than 181 μA (because it is coupled with Zn electrodeposition reaction, too), but it may have considerable effect on composition after stopping the reaction.

Although an increase in In content at the surface may be explained by replacement electrodeposition, the trend observed in In added deposits is different from that observed in Pb containing deposits; the compositional profile is stable inside the bulk and high content regions continues over several seconds. (In the case of Pb containing deposit, only a spike is observed at the outermost surface.) Since the replacement reaction

is limited only to the surface, increase in In content over broad range cannot be explained. This implies that In metal tends to aggregate at the surface even before stopping the deposition reaction.

Such an aggregation of codeposited metal at the surface was observed in Ni electrodeposition with Pb additive [37]. Since Pb had lower surface free energy than that of Ni, it aggregated on the surface of the electrodeposit during Ni electrodeposition, which also suppressed the surface roughening of Ni electrodeposits by behaving as a "surfactant". Pb does not form an alloy with Ni as is the case for Zn-Pb, Zn-Sn and Zn-In systems [38].

Since the substrates for Zn electrodeposition also possess the suppression effects on mossy structures formation, deposited additive metal may provide the surface enabling compact deposition. This is possible by higher content of additive metals at the surface. When Sn and In are codeposited with Zn, they exist as a separate phase to metal Zn. Then, by lower surface free energies than that of Zn [39], they aggregate at the surface of Zn electrodeposits. Also, the electrode surface which has the high surface energy is active area for electrodeposition. (Electrodeposition at low overpotential generally yields the surface with lowest surface free energy.) Thus, the compact electrodeposition by additive metal is possible through the codeposition with Zn and the aggregation on the surface.

The mechanisms for mossy structure suppression

From analysis on Pb, Sn and In addition effects on morphological evolution of electrodeposited Zn, the mechanisms for mossy structure suppression by additive species were elucidated as follows.

In the case of Pb addition, a significant increase in the deposition potential is notable. This is ascribed to previously suggested suppressed effects on the elementary steps for Zn electrodeposition. Especially, Mao *et al*. assumed the reaction step like (3.6) is suppressed by the presence of Pb [11]. Such suppression effects may totally alter the nucleation and growth behavior of Zn from initial stages of deposition. The evolution of microsteps via 2D nucleation and bunching (an incorporation of adatom to a step or kink sites) itself is suppressed. This is similar to the effects of organic additives used in electrodeposition. They are thought to diminish the active growth sites on the electrode surface via adsorption, then induce the nucleation of fine particles [40-42].

In contrast, Sn and In don't increase the deposition potential. This means the compact deposition originates from the different mechanisms other than the suppression on the elementary steps for Zn electrodeposition. Also, the compact Zn electrodeposition is not explained only by suppressed HER because an onset of HER becomes positive by

adding Sn in Fig. 3.3. From XRD and SEM of electrodeposits, the texture evolution to (002) direction and the formation of microstep are not observed by Sn and In additives (without Cl^-). This trend is similar to that on the electrodeposits on Sn and In substrate (Fig. 3.8) [43, 44]. These changes are thought to be caused by a large misfit between the substrate metal and Zn basal plane, (002) surface of hcp-Zn. The misfit between Zn and Sn is 13% and that between Zn and In is 22%. On the surface with large misfit value, the texture evolution to corresponding direction is suppressed [36]. Since 2D nucleation preferentially occurs on (002) surface of hcp-Zn because of a large terrace and a lower adatom mobility on this plane [45], the suppressed texture evolution to (002) may result in the crystal growth without the microsteps formation.

Although texture evolution to (002) is observed at the presence of Cl^- in the solution, compact Zn electrodeposition is still possible. This implies that the presence of metal In at the Zn surface itself is beneficial for mitigating the irregular growth sites which is supposed to have higher surface energy than other region on the surface [40-42]. Actually, In (and Pb, Sn) possesses lower surface energy than that of Zn. From GDS and XPS results, it is notable that the content of additive metal is higher at the surface than in the bulk. In addition to the possible replacement deposition of additive metals, this implies that codeposited metal tends to aggregate at the surface during electrodeposition. Actually, Zn films electrodeposited with Sn and In sometimes exhibit the surface covered by nano-particles (diameter = several 10 nm) like Fig. 3.16.

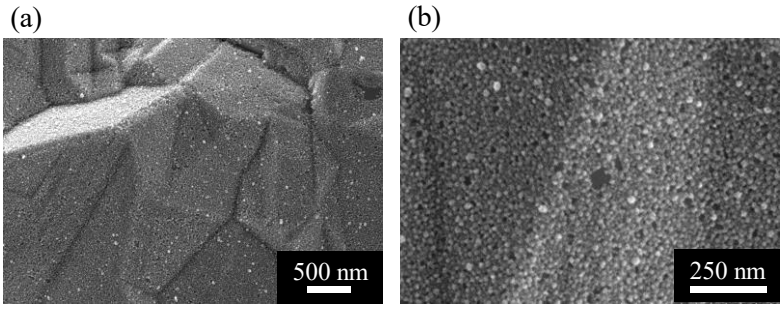

Fig. 3.16 Nano particles covering Zn surface (after electrodeposition at −5.0 mA cm^{-2}, 1000 s with 25 mmol dm^{-3} Sn).

Such an aggregation is possibly caused by no alloy formation between Sn-Zn or In-Zn system and above-mentioned lower surface energy [38, 39]. Thus, additive metals continuously provide the surface enabling the compact Zn electrodeposition through codeposition with Zn. The previously suggested correlation between suppressed HER and the compact deposition by additive species is interpreted as correlations between HER

overpotential and the surface energy; metal with low surface energy possesses lower binding energy of atoms in the crystals, which is also a general trend observed in metals having higher overpotential for HER [40].

3.3.2 Controlling charging behavior of Zn-Ni flow-assisted battery by In and Sn additives

In 3.3.1, it was clarified that the use of In and Sn is effective to obtain compact Zn electrodeposits at certain deposition conditions. However, its applicability in practical operation conditions (deep depth of charge, wide range of current density, charge-discharge cycling) of Zn flow-assisted battery is still lacking. Therefore, their performance in the Zn-Ni flow-assisted battery was analyzed.

Morphological variations without an additive

To demonstrate morphological variations of Zn electrodeposits in the Zn-Ni flow assisted battery, charging of the cell was performed at various current densities and electrolyte flow rates. Morphological variations after charging are shown in Fig. 3.17. The capacity was 540 mAh (=38.9 C cm^{-2}), which meant deposited Zn was more than 7 times thicker than that observed in section 3.3.1 (5.0 C cm^{-2}).

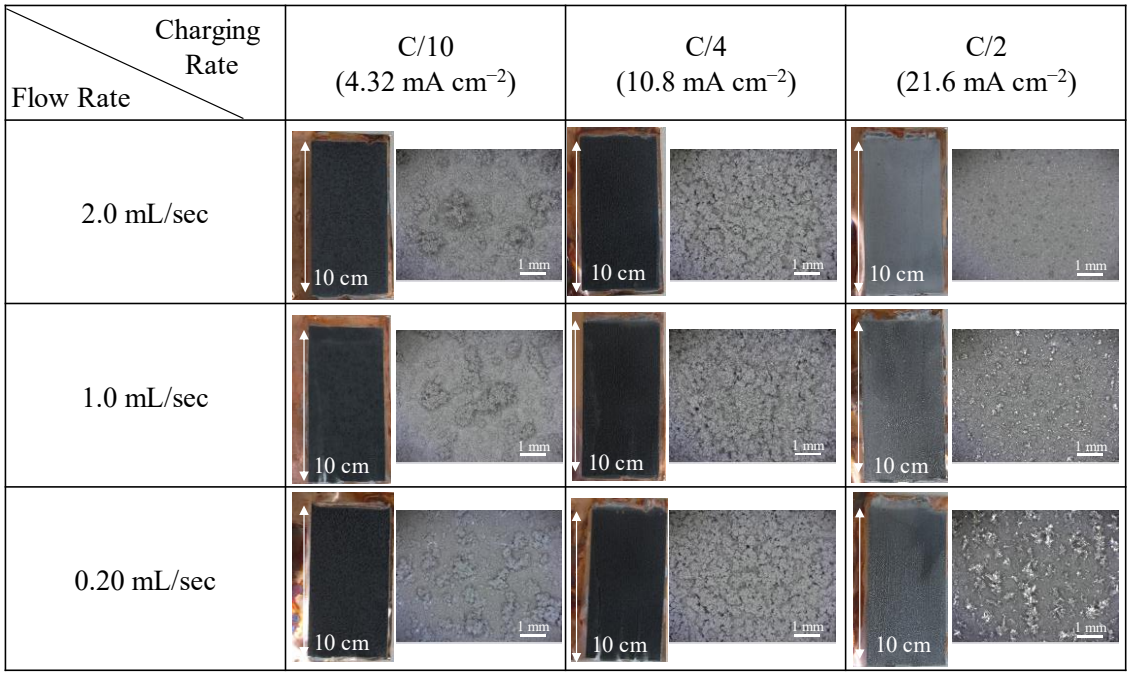

Fig 3.17 Morphological variations of Zn electrodes in the Zn-Ni flow-assisted battery at various charging rates and electrolyte flow rates with capacity of 540 mAh.

At lower current density at C/4 and C/10, dark colored deposits are formed at each flow rate. They are mossy structures and their formation is less influenced by an electrolyte flow. At C/2, the color of deposits is changed to grey, but it still exhibits rough surface. From cross-sectional SEM images of the electrode after charging at C/2 under various flowing rate (Fig. 3.18), increasing the electrolyte flow rate is effective to suppress the evolution of these rough deposits. This is a typical trend observed in dendrites formation; since a dendrite is initiated under the mass-transfer limited condition of zincate, its evolution is suppressed under electrolyte flowing conditions. Fig. 3.19 represents SEM images of Zn electrodeposits at various charging rate at fixed flow rate (1.0 mL/s). Compact electrodeposits were obtained only in the limited charging rate (C/2.4). Especially, the formation of mossy structure is problematic because its evolution cannot be controlled only by an electrolyte flow.

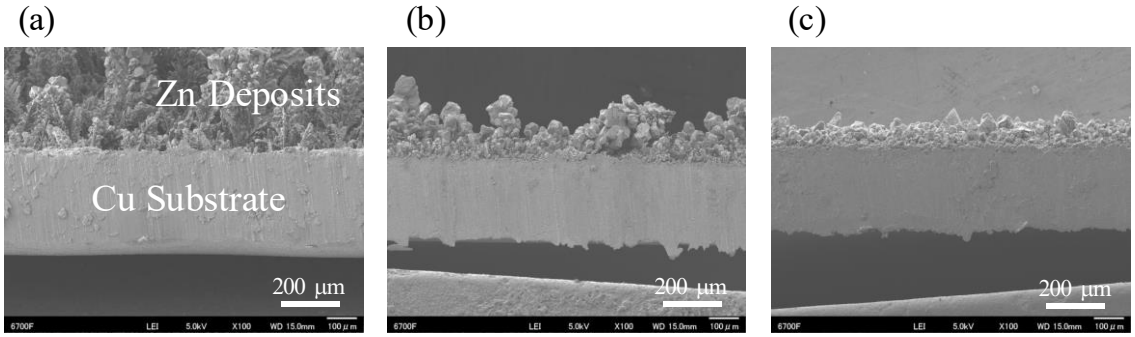

Fig. 3.18 Cross-sectional SEM images of electrodeposits at C/2 rate charging at flowing rate of (a) 0.20 mL/sec, (b) 1.0 mL/sec and (c) 2.0 mL/sec.

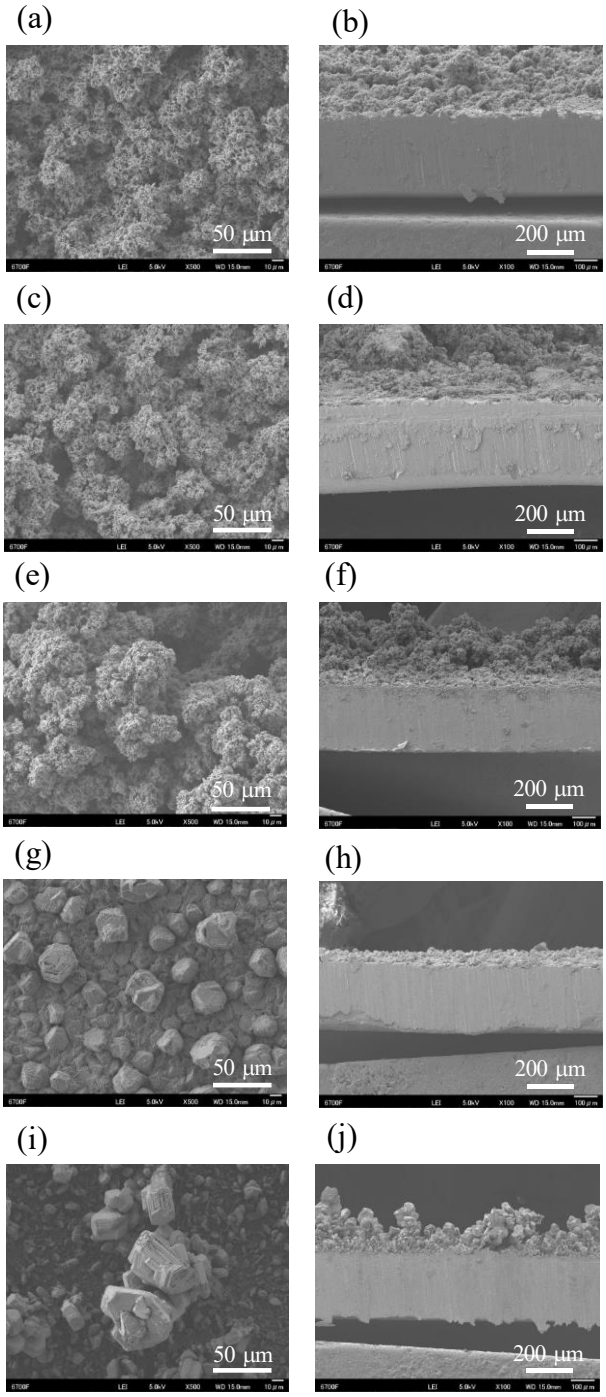

Fig 3.19 SEM images of Zn electrodeposits after charging. Charging rate is (a), (b) C/10, (c), (d) C/4, (e), (f) C/3, (g), (h) C/2.4, (i), (j) C/2. (a), (c), (e), (g) and (i) are top-view images and (b), (d), (f), (h) and (j) are cross-sectional view images.

Effects of Sn and In additives in the morphological evolution of Zn in the Zn-Ni battery

Based on the additive effects discussed in section 3.3.1, the effects of In and Sn additive were analyzed in the Zn-Ni flow-assisted battery. Fig. 3.20 shows the photographs of the electrodes taken by a digital camera after charging in the electrolyte with various concentrations of additive species. Corresponding cross-sectional SEM images are shown in Fig. 3.21. Charging rate was C/10 and capacity was 540 mAh.

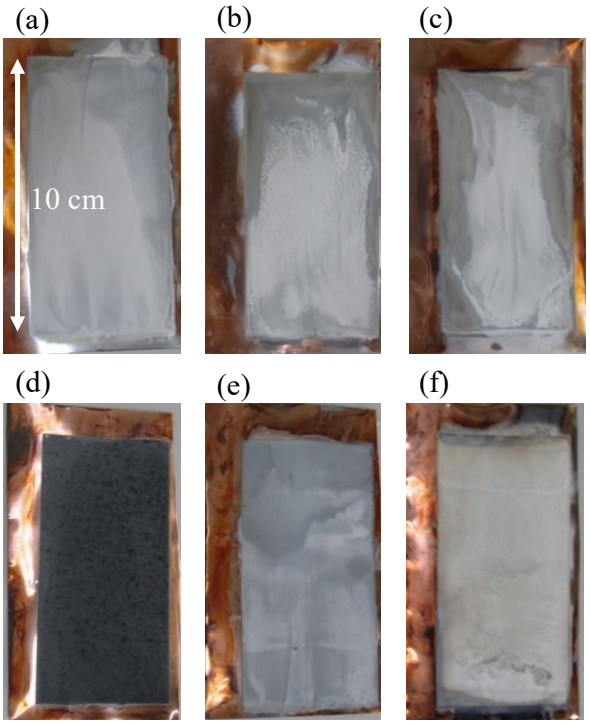

Fig. 3.20 Photographs of Zn electrodes taken by digital camera after charging with (a) 1.0 mmol dm^{-3} In, (b) 5.0 mmol dm^{-3} In, (c) 25 mmol dm^{-3} In, (d) 1.0 mmol dm^{-3} Sn, (e) 5.0 mmol dm^{-3} Sn, (f) 25 mmol dm^{-3} Sn additives.

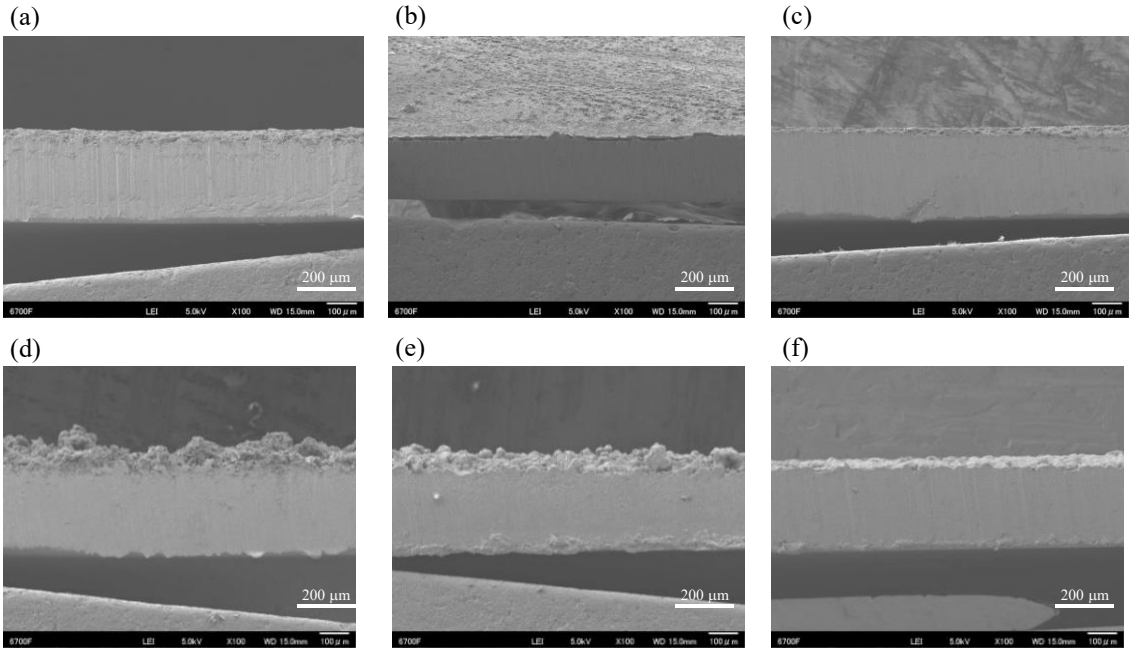

Fig. 3.21 Cross-sectional SEM images of Zn electrodeposits with (a) 1.0 mmol dm^{-3} In, (b) 5.0 mmol dm^{-3} In, (c) 25 mmol dm^{-3} In, (d) 1.0 mmol dm^{-3} Sn, (e) 5.0 mmol dm^{-3} Sn, (f) 25 mmol dm^{-3} Sn additives.

By adding In or Sn, the evolution of mossy structure is suppressed. However, more than 25 mmol dm^{-3} was required for Sn, whereas 1.0 mmol addition was effective in the case of In. This concentration dependence is in consistent with half-cell analysis shown in section 3.3.1 (Fig. 3.5). Composition analysis was performed by ICP-AES, and results are shown in Table 3.6.

Table 3.6 Composition of Zn electrodeposits at various additive concentrations

Conc. / mmol dm^{-3}	In / at%	Sn / at%
0.10	N.D.	-
1.0	0.06	N.D.
5.0	0.07	N.D.
25	0.24	N.D.

In the case of In, the content increases when the concentration of In salt in the electrolyte increases. In contrast, Sn content is less than the detection limit (*c.a.* 0.02at%) at all concentrations investigated. Therefore, the better performance of In than Sn originates from a higher reduced amount during charging. From the basis of

electrodeposition, higher content of In than that of Sn seems unreasonable due to more negative deposition potential of In than that of Sn; the standard redox potential of In^{3+}/In is −0.34 V and that of Sn^{2+}/Sn is −0.14 V [46]. As a cause of the lower reduced amount of Sn, the differences in the reduction steps are notable. In an alkaline solution, In is dissolved as InO_2^- (III), while Sn is dissolved as SnO_3^{2-}(IV). InO_2^- is reduced to In(0) in an one step, but SnO_3^{2-}(IV) requires the two-step reduction; first to $HSnO_2^-$ (II), then to Sn (0) [47, 48]. From the LSV measured on the solution without zincate (Fig. 3.3), Sn containing solution exhibits only one peak despite the presence of Sn^{4+}. This implies that the second reduction step is not sufficient during Zn electrodeposition. Thus, the formation of stable Sn(II) ions in an alkaline solution is a possible cause of the lower content in Zn electrodeposits.

Although a compact Zn electrodeposition is possible at C/10 rate, it should be maintained over a wide range of current densities in a practical operation of the battery. The effects of In addition were examined at various charging rate under electrolyte flow rate of 1.0 mL/s and the capacity of 540 mAh. Fig. 3.22 shows CCD images after charging.

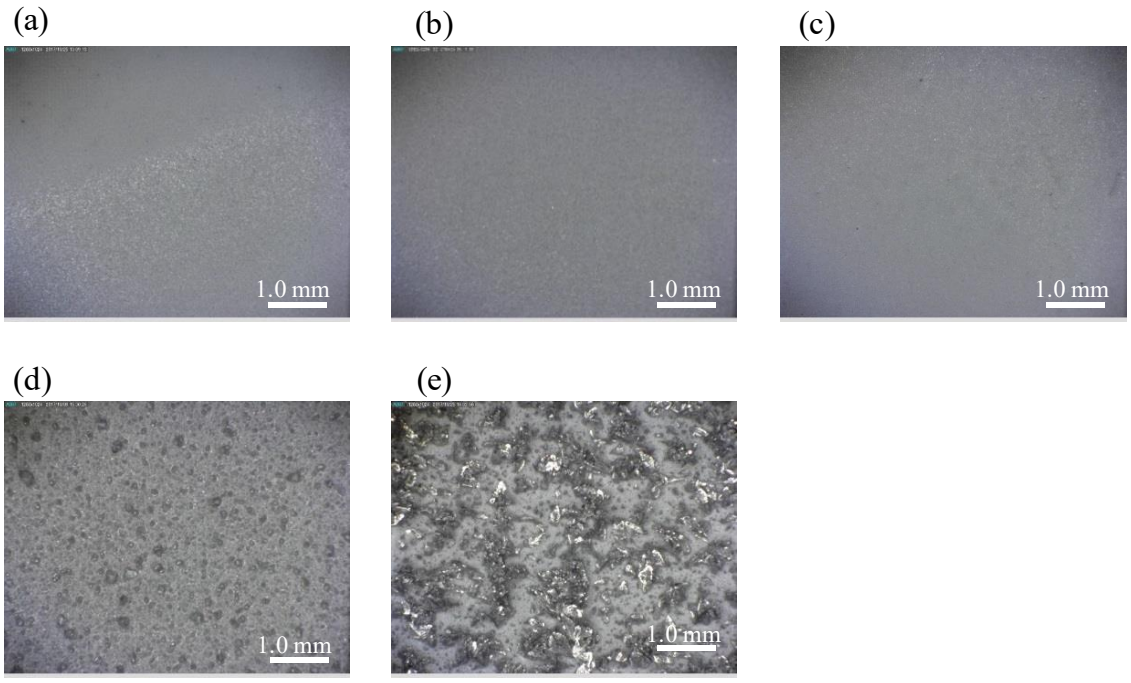

Fig. 3.22 CCD images of surface morphologies of electrodeposited Zn with 1.0 mmol dm^{-3} In at (a) C/20, (b) C/10, (c) C/4, (d) C/2 and (e) 1C rates.

At lower current densities from C/20 to C/4, the formation of mossy structures are totally suppressed. In addition, relatively smooth morphology is obtained compared to the

solution without additive even at C/2 where the dendritic growth is observed. Although it is difficult to eliminate dendrites at higher current density like 1C rate, In addition is effective to obtain compact deposits over a wide range of current densities. Table 3.7 shows the content of In in each deposit. Similar composition is maintained over a wide range of current densities, this makes it possible to obtain compact Zn deposits.

Table 3.7 Composition of Zn electrodeposits at various additive concentrations

Rate	In content/ at%
C/20	0.06
C/10	0.06
C/4	0.04
C/2	0.06
1C	0.09

Charge-discharge behavior of the Zn-Ni flow-assisted battery

In practical battery operation, the additive effects should be maintained over many charge-discharge cycles. Furthermore, they should not affect the characteristics of charge-discharge reactions (*i.e.* the voltaic efficiency and the Coulombic efficiency) negatively. To investigate these influences, the charge-discharge cycles of the cell was performed at C/10 rate and C/2 rate up to 10 cycles with cut off-voltage during discharge of +0.80 V. The capacity of the cell was limited to 540 mAh and the reaction was stopped at the end of 11th charging. Representative potential profiles during cycling are shown in Fig. 3.23. The Coulombic efficiencies and energy efficiencies during charge-discharge cycles at each cycle number is shown in Tables 3.8 and 3.9. The Coulombic efficiency, η_c is calculated by (3.6) based on the discharge capacity of each cycle. The energy efficiencies, η_E is calculated by considering the average power output (the product of the current and the voltage) during each cycle (3.7). Q is a discharge capacity (mAh), i is average current (A), E is average voltage (V), and t is reaction time (sec).

$$\eta_c = \frac{Q_{discharge}\, mAh}{540\, mAh} \tag{3.6}$$

$$\eta_E = \frac{i_{discharge}\,[A] \times E_{discharge}\,[V] \times t_{discharge}\,[sec]}{i_{charge}\,[A] \times E_{charge}\,[V] \times t_{charge}\,[sec]} \tag{3.7}$$

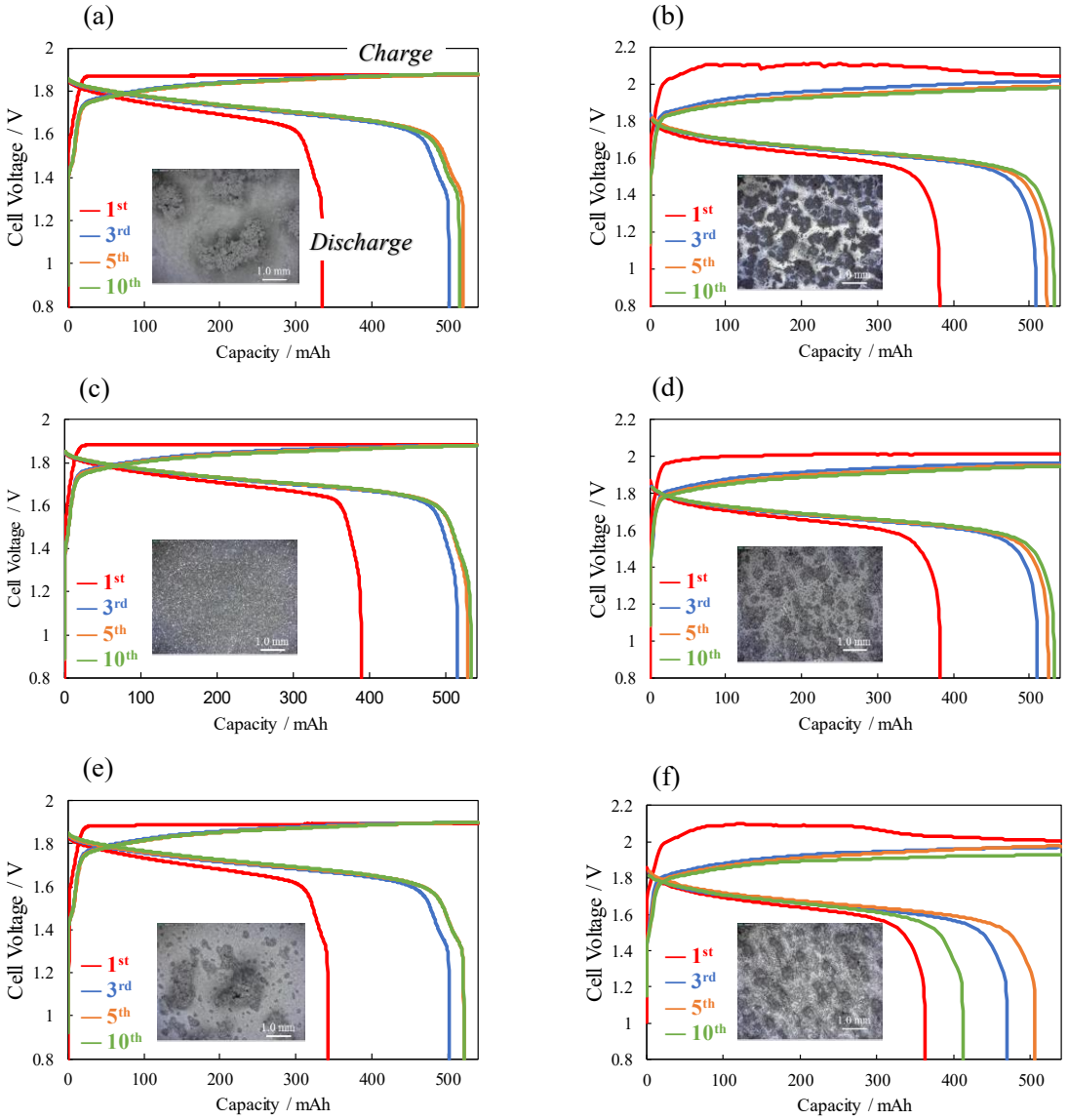

Fig. 3.23 Potential profiles during charge-discharge cycles of the Zn-Ni flow-assisted battery; (a) without additive at C/10, (b) without additive at C/2, (c) with 1.0 mmol dm^{-3} In at C/10, (d) with 1.0 mmol dm^{-3} In at C/2, (e) with 25 mmol dm^{-3} Sn at C/10 and (f) with 25 mmol dm^{-3} Sn at C/2. An inset image shown in each figure is CCD image after 11^{th} charging.

Table 3.8 Coulombic efficiencies during charge-discharge cycles

	Without Additive		In 1 mmol dm^{-3}		Sn 25 mmol dm^{-3}	
	C/10	C/2	C/10	C/2	C/10	C/2
1st	62%	71%	72%	71%	64%	67%
3rd	93%	94%	95%	95%	93%	87%
5th	96%	97%	98%	97%	96%	94%
10th	96%	99%	99%	99%	96%	76%

Table 3.9 Energy efficiencies during charge-discharge cycles

	Without Additive		In 1 mmol dm^{-3}		Sn 25 mmol dm^{-3}	
	C/10	C/2	C/10	C/2	C/10	C/2
1st	56%	55%	66%	59%	57%	53%
3rd	86%	77%	88%	82%	85%	73%
5th	89%	81%	91%	84%	87%	80%
10th	89%	83%	92%	86%	87%	64%

At C/10 rate, a compact deposition is still maintained by In additive, but rough deposits evolve in the Sn containing solution. At C/2 rate, rough deposits are observed at all conditions, but their coverage on the surface is decreased both in the In and Sn addition case. The composition of each deposit is shown in Table 3.10.

Table 3.10 The content of In and Sn in the electrode after 11th charge

Additive	Charging rate	Content / at%
1.0 mmol dm^{-3} In	C/10	0.38
1.0 mmol dm^{-3} In	C/2	0.34
25 mmol dm^{-3} Sn	C/10	0.81
25 mmol dm^{-3} Sn	C/2	0.50

The content of In and Sn increases compared to 1st charging, which indicates irreversible deposition and dissolution of additive metals. A notable point is that the content of Sn is larger than that of In despite the lower reduced amount at first charging (Table 3.6). This means that the reduced Sn during charging is not fully dissolved during the following discharging. This is possibly caused by the more positive redox potential of Sn/Sn^{2+} than

In/In^{3+} and the stable Sn(II) formation. The remained Sn amount decreases at C/2 rate than that at C/10 rate because of a sufficient anodic overpotential for Sn dissolution. Additionally, there is a concern over the formation of oxide species like SnO during cycling, which is undesirable in terms of loss of the electrode conductivity and the additive species active for a compact Zn electrodeposition. (However, characterizations of the chemical state of the additive metals after cycling is not carried out in the current study.) Thus, in addition to the sufficient reduction during charging, a reversible oxidation to ionic species upon discharge is another important requirement for additive species. In is superior than Sn in this aspect, which is beneficial for maintaining the compact Zn electrodeposits even after cycling.

From Tables 3.8, the Coulombic efficiency is far below 100% at initial cycles. This is due to the lack of "aging", the formation of conductive path for the positive electrode. At a fully discharged state, $Ni(OH)_2$ exhibits a limited electron conductivity. After performing electrochemical cycling, conductive supporting agents like $CoO/Co(OH)_2$ were oxidized to CoOOH, which provide a conductive path for the active materials [49, 50]. When the Coulombic efficiencies at 10^{th} cycle are compared, In improves the Coulombic efficiency, while the value is worsened in the case of Sn at C/2. This indicates that the side-reaction (HER) is suppressed at the presence of In in the deposit, but it is not the case for Sn addition.

In this study, a membrane separator between anode and cathode was not introduced. An influence of such a cell configuration is not evident until 10 cycles; the charging voltage decreases, and the Coulombic efficiency improves after increasing the cycling numbers even at C/2 rate. In general, the cell voltage may increase due to an increased concentration polarization by the diffusion of zincate species towards the positive electrode in a static electrolyte, which may initiate Zn dendrites, too. Therefore, an increase in the concentration polarization is effectively suppressed by an electrolyte flow in the current study. On the other hand, the energy efficiencies at initial cycles varies depending on the additive species though the low efficiencies at early cycling mainly originate from the positive electrodes as described above. This suggests that the additive species have an influence on the positive electrode, too (*e.g.* suppressing the side reaction (oxygen evolution reaction)). For the prolonged cycling, in fact, previous study on Zn-Ni flow-assisted battery (without separator) showed the formation of Zn-Ni mixed compound at the positive electrode during cycling [19]. Although chemical nature of this compound was not revealed in the paper, the influence of reactant on Zn anode could affect the cyclability through influencing the cathode, too. Therefore, a care must be taken with respect to the influences of Zn and additive species to the positive electrodes during

long-term cycling, but the characterization on the positive electrodes have not been carried out in this study.

In short, In additive is advantageous during the charge-discharge cycles in terms of compact electrodepositions after cycling and the effects on the energy efficiencies. These advantages originate from (1) a reversible dissolution to the ionic state upon discharge, (2) a minor influence on the voltage during the charge-discharge reactions (*c.f.* conventionally suggested Pb increases the voltage during charging), (3) the high overpotential for HER.

Applicability of In additive in various charging conditions

During the battery operation, variations are expected in the charge-discharge conditions (*e.g.* depth of charge, flow rates, temperature, etc). To demonstrate the applicability of In additive, charging was performed under various conditions. First, the capacity was extended from 540 mAh to 2160 mAh. Deep depth of charge is required to enable the high capacity and energy density. However, 540 mAh was basically selected to avoid the degradation of the positive electrode in the current study. Fig. 3.24 shows morphologies of Zn electrodes at deep depth of charge (2160 mAh).

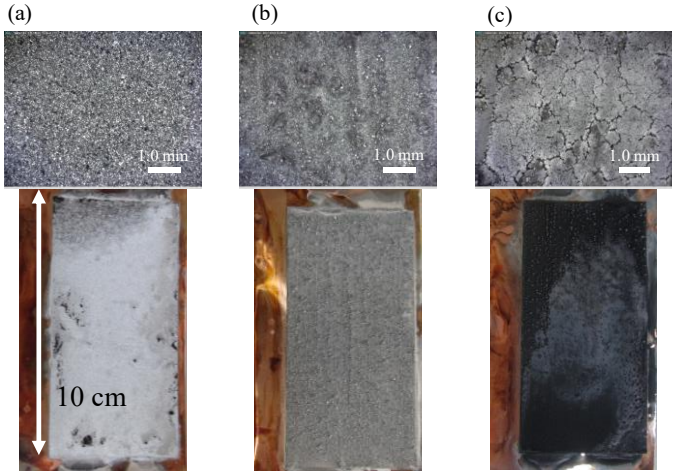

Fig. 3.24 Surface morphologies of Zn electrodes (a) with 1.0 mmol dm^{-3} In at C/10 rate, (b) with 1.0 mmol dm^{-3} In at C/2 rate and (c) without additive at C/2 rate at the capacity of 2160 mAh.

At C/10 rate (Fig. 3.24 (a)), compact deposits are still maintained. The dark part observed in a photograph originates from the collapsed positive electrode during disassembling the cell. It indicates that the morphological changes of the positive electrode are more serious

problem for attaining the deep depth of charge. At C/2 rate (Fig. 3.24(b)), relatively rough deposits evolve, but this was much smooth than that without additive (Fig. 3.24 (c)) where cracks were observed in a CCD image.

In electrodeposition, the composition of the deposit is affected by an electrolyte flow rate [51], which arises the concern over the loss of additive performance at different flow rates. To investigate this, charging is performed at various electrolyte flow rates (0, 1.0 and 2.0 mL/s). Morphologies after charging is shown in Fig. 3.25.

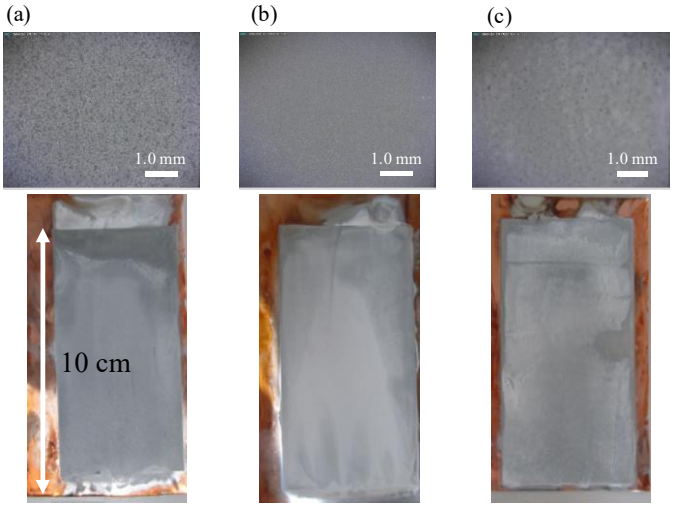

Fig. 3.25 Surface morphologies of Zn electrodes with 1.0 mmol dm^{-3} In at the capacity of 540 mAh at flow rate, (a) 0 mL/s, (b) 1.0 mL/s, (c) 2.0 mL/s.

Compact Zn electrodeposits are obtained at all flow rates investigated. It is notable that In addition was effective even under the static condition (0 mL/s). This is beneficial for reducing the cost for operating pump for the battery though the introduction of the electrolyte flow is necessary at a higher charging rate to suppress the dendritic growth as demonstrated in Fig. 3.17. When the current density is below that for the initiation of the dendrite (*e.g.* C/2 rate at flow rate of 1.0 mL/s), the indium addition is effective to obtain compact electrodeposits regardless of the electrolyte flow rates.

In this study, a Cu substrate was mainly used as a current collector for the negative electrode. In the practical operations of the battery, cost of Cu is a drawback [25]. An electrodeposited Ni on a steel substrate is one of the possible candidates for the current collector due to higher corrosion resistance of Ni in the alkaline condition. To demonstrate the applicability of In additive for various substrates, the charging was performed on Cu, Zn and Ni substrate. The results are shown in Fig. 3.26.

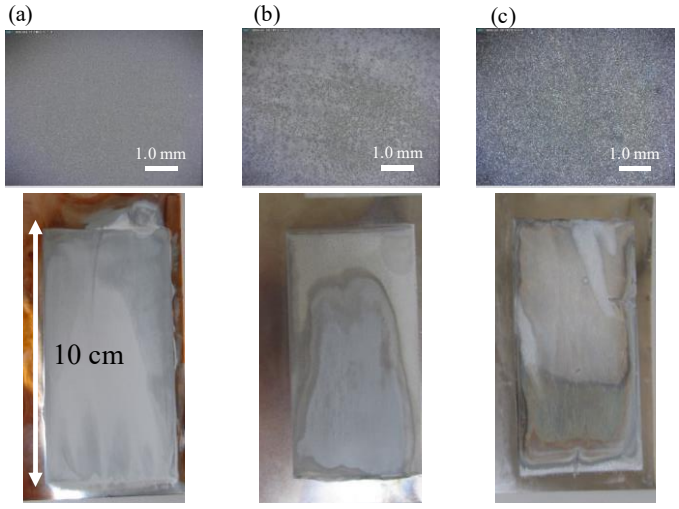

Fig. 3.26 Surface morphologies of Zn electrodes with 1.0 mmol dm^{-3} In at the capacity of 540 mAh on (a) Cu substrate, (b) Zn substrate, (c) Ni substrate.

A compact electrodeposition is maintained regardless of the substrates. This means In additive does not require certain interactions between electrodeposited Zn and substrate metal; *e.g*. underpotential deposition [52]. Instead, a co-deposition with Zn results in compact Zn electrodeposits, which can be basically applied to a wide variety of substrate metals.

During the battery operation, the temperature of the cell may be varied. Charging is performed under cold and hot conditions by holding the cell in a refrigerator and a heater. Fig 3.27 shows the surface morphologies of the electrodes after charging at −25 ˚C and 50 ˚C .

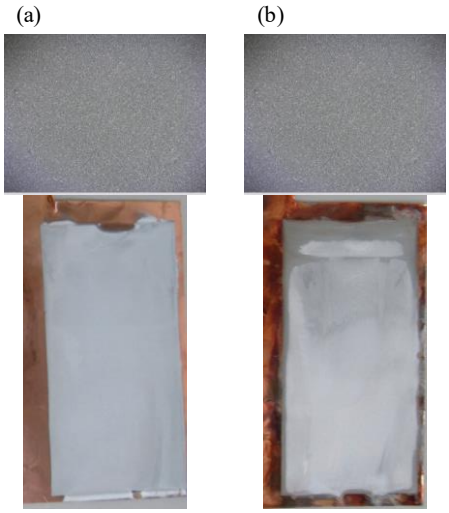

Fig. 3.27 Surface morphologies of Zn electrodes with 1.0 mmol dm^{-3} In at the capacity of 540 mAh at (a) −25 ˚C and (b) 50 ˚C.

Compact electrodeposition is still possible in both cases.

From these results, In was effective for obtaining compact Zn electrodeposits over a wide variety of charging conditions. The compositional analysis by ICP-AES shows less variable content of In in the deposits under various charging conditions. Table 3.11 – 3.13 shows the content of In at each charging condition.

Table 3.11 Content of In at different current densities at 2160 mAh

Charging rate	In content / at%
C/10	0.04
C/2	0.03

Table 3.12 Content of In in Zn electrodeposits at different electrolyte flow rates

Flow rate / mL s^{-1}	In content/ at%
0	0.05
1	0.06
2	0.05

Table 3.13 Content of In in Zn electrodeposits at different temperature

Temp./ ˚C	Rate	In content / at%
−25	C/2	0.04
−25	C/10	N. D.
R.T.	C/2	0.06
R.T.	C/10	0.06
50	C/2	0.05
50	C/10	0.07

Conclusion

Through investigating Pb, Sn and In addition effects on the Zn electrodeposition, the mechanisms behind the compact Zn electrodeposition by the additive species were analyzed. In the polarization behavior during the Zn electrodeposition, Pb increased the deposition overpotential, while the potential stayed in a similar region to that without additive in the case of Sn and In addition. This suggested the compact Zn electrodeposition by Pb additive was possibly caused by the suppressing effects of deposited Pb on the elementary steps for Zn electrodeposition. On the other hand, Sn and In suppressed the formation of mossy structures through changing the microsteps evolution behavior without increasing the overpotential, which was analogous to Zn electrodeposition on the foreign substrates. Accordingly, the additive species continuously provided the surface for compact Zn electrodeposition by codeposition with Zn. GDS and XPS analysis showed such a process was possible by an aggregation of codeposited metals at the surface of Zn electrodeposits.

Based on the results above, the applicability of Sn and In additives were investigated under the conditions close to the practical Zn-Ni flow-assisted battery operation. In exhibited a better performance in compact Zn electrodeposition than Sn because mossy structure was suppressed even at 1.0 mmol dm^{-3} In, while more than 25 mmol dm^{-3} was required in Sn. A different concentration dependence was caused by higher reduced amount of In in the electrodeposit. On the other hand, the content of Sn was higher than that of In after charge-discharge cycles, and compact Zn electrodeposit was no longer maintained. This indicates that an irreversible dissolution and an accumulation of inactive Sn like SnO. From these results, In is advantageous in terms of (1) compact electrodeposition at low concentration, (2) more reversible deposition and dissolution reaction than Sn, (3) no negative influence on the energy efficiencies.

Reference

[1] R. Y. Wang, D. W. Kirk, G. X. Zhang, Effects of Deposition Conditions on the Morphology of Zinc Deposits from Alkaline Zincate Solutions, *J. Electrochem. Soc.* **153** (2006) C357.

[2] Y. Ito, M. Nyce, R. Plivelich, M. Klein, D. Steingart, S. Banerjee, Zinc morphology in zinc-nickel flow assisted batteries and impact on performance, *J. Power Sources* **196** (2011) 2340.

[3] Y. Ito, X. Wei, D. Desai, D. Steingart, S. Banerjee, An indicator of zinc morphology transition in flowing alkaline electrolyte, *J. Power Sources* **211** (2012) 119.

[4] D. Desai, X. Wei, D. A. Steingart, S. Banerjee, Electrodeposition of preferentially oriented zinc for flow-assisted alkaline batteries, *J. Power Sources* **256** (2014) 145.

[5] S. J. Banik, R. Akolkar, Suppressing Dendrite Growth during Zinc Electrodeposition by PEG-200 Additive, *J. Electrochem. Soc.* **160** (2013) D519.

[6] S.J. Banik, R. Akolkar, Suppressing Dendrite Growth during Alkaline Zinc Electrodeposition using Polyethyleneimine Additive, *Electrochim. Acta*. **179** (2015) 475.

[7] F. R. McLarnon, E.J. Cairns, The Secondary Alkaline Zinc Electrode, *J. Electrochem. Soc*. **138** (1991) 645.

[8] J. McBreen, Nickel/zinc batteries, *J. Power Sources* **51** (1994) 37.

[9] A. Khor, P. Leung, M.R. Mohamed, C. Flox, Q. Xu, L. An, R.G.A. Wills, J.R. Morante, A.A. Shah, Review of zinc-based hybrid flow batteries: From fundamentals to applications, *Mater. Today Energy* **8** (2018) 80.

[10] F. Mansfeld, S. Gilman, The Effect of Lead Ions on the Dissolution and Deposition Characteristics of a Zinc Single Crystal in 6N KOH, *J. Electrochem. Soc.* **117** (1970) 588.

[11] Z. Mao, S. Srinivasan, A. J. Appleby, Effect of PbO on zinc electrodeposition from zincate solutions, *J. Appl. Electrochem.* **22** (1992) 693.

[12] Y.-H. Wen, J. Cheng, L. Zhang, X. Yan, Y.-S. Yang, The inhibition of the spongy electrocrystallization of zinc from doped flowing alkaline zincate solutions, *J. Power Sources* **193** (2009) 890.

[13] Y. Wen, T. Wang, J. Cheng, J. Pan, G. Cao, Y. Yang, Lead ion and tetrabutylammonium bromide as inhibitors of the growth of spongy zinc in single flow zinc/nickel batteries, *Electrochim. Acta* **59** (2012) 64.

[14] M. M. Jakšić, Impurity effects on the micromorphology of electrodeposited zinc II: Causes, appearances and consequences of spongy zinc growth, *Surf. Coatings Technol.* **28** (1985) 113.

[15] M. M. Jakšić, Impurity effects on the micromorphology of electrodeposited zinc III: Potential sweep analysis, *Surf. Coatings Technol.* **28** (1985) 113.

[16] R. Ichino, C. Cachet, R. Wiart, Influence of Ge^{4+} and Pb^{2+} ions on the kinetics of zinc electrodeposition in acidic sulphate electrolyte, *J. Appl. Electrochem*. **25** (1995) 556.

[17] R. Ichino, C. Cachet, R. Wiart, Mechanism of zinc electrodeposition in acidic sulfate electrolytes containing Pb^{2+} ions, *Electrochim. Acta* **41** (1996) 1031.

[18] J. Cheng, L. Zhang, Y.-S. Yang, Y.-H. Wen, G.-P. Cao, X.-D. Wang, Preliminary study of single flow zinc-nickel battery, *Electrochem. Commun*. **9** (2007) 2639.

[19] D. E. Turney, M. Shmukler, K. Galloway, M. Klein, Y. Ito, T. Sholklapper, J. W. Gallaway, M. Nyce, S. Banerjee, Development and testing of an economic grid-scale flow-assisted zinc/nickel-hydroxide alkaline battery, *J. Power Sources* **264** (2014) 49.

[20] M. Mansfeld, S. Gilman, The Effect of Several Electrode and Electrolyte Additives on the Corrosion and Polarization Behavior of the Alkaline Zinc Electrode, *J. Electrochem. Soc*. **117** (1970) 1328.

[21] F. Moser, F. Fourgeot, R. Rouget, O. Crosnier, T. Brousse, In situ X-ray diffraction investigation of zinc based electrode in Ni-Zn secondary batteries, *Electrochim. Acta* **109** (2013) 110.

[22] P.K. Leung, C. Ponce-de-León, F.J. Recio, P. Herrasti, F.C. Walsh, Corrosion of the zinc negative electrode of zinc-cerium hybrid redox flow batteries in methanesulfonic acid, *J. Appl. Electrochem.* **44** (2014) 1025.

[23] D.J. Mackinnon, J.M. Brannen, P.L. Fenn, Characterization of impurity effects in zinc electrowinning from industrial acid sulphate electrolyte, *J. Appl. Electrochem*. **17** (1987) 1129.

[24] J. W. Gallaway, A. M. Gaikwad, B. Hertzberg, C. K. Erdonmez, Y. K. C.-Wiegart, L. A. Sviridov, K. E. -Lutterodt, J. Wang, S. Banerjee, D. A. Steingart, An In Situ Synchrotron Study of Zinc Anode Plarization by a Bismuth Additive, *J. Electrochem. Soc.* **161** (2014) A275.

[25] X. Wei, D. Desai, G. G. Yadav, D. E. Turney, A. Couzis, S. Banerjee, Impact of anode substrate on electrodeposited zinc over cycling in zinc-anode rechargeable alkaline batteries, *Electrochim. Acta* **212** (2016) 603.

[26] D. J. Mackinnon, P. L. Fenn, The effect of tin on zinc electrowinning from industrial acid sulphate electrolyte, *J. Appl. Electrochem*. **14** (1984) 701.

[27] I. Danaee, F. Shoghi, M. D. Mobarake. M. Kameli, Electrocrystallization of palladium from $Pd(NH_3)_4Cl_2$ bath on stainless steel 316L, *J. Solid State Electrochem.* **14** (2010) 57.

[28] N. A. Pangarov, The crystal orientation of electrodeposited metals, *Electrochim. Acta* **7** (1962) 139.

[29] N. A. Pangarov, On the crystal orientation of electrodeposited metals, *Electrochim. Acta* **9** (1964) 721.

[30] E. Fahrenkrug, J. Gu, S. Maldonado, Electrochemically gated alloy formation of crystalline InAs thin films at room temperature in aqueous electrolytes, *Chem. Matter.* **26** (2014) 4535.

[31] A. J. Gay, F. Bergsma, The influence of nitrate ion on the morphology of zinc electrodeposits, *Electrochim. Acta* **23** (1978) 1067.

[32] G. P. Rajarathnam, M. Schneider, X. Sun, A. M. Vassallo, The influence of supporting electrolyte

on zinc half-cell performance in zinc/bromine flow batteries, *J. Electrochem. Soc*. **163** (2016) A5112.

[33] K. Krug, J. Stettner, O.M. Magnussen, In Situ Surface X-Ray Diffraction Studies of Homoepitaxial Electrochemical Growth on Au (100), *Phys. Rev. Lett.* **96** (2006) 246101.

[34] N. Vasailjevic, M. Wood, P.J. Heard, W. Schwarzacher, The Influence of Specific Anion Adsorption on the Surface Roughness of Electrodeposited Polycrsytalline Cu Films, *J. Electrochem. Soc.* **157** (2010) D193.

[35] D.S. Baik, D.J. Fray, Electrodeposition of zinc from high acid zinc chloride solutions, *J. Appl. Electrochem.* **31** (2001) 1141.

[36] S. Wodarz, T. Otani, H. Hagiwara, T. Homma, Characterization of electrodeposited Co-Pt Nanodot Array at Initial Deposition Stage, *Electrochem. Soc. Trans.* **64** (2015) 99.

[37] C.-L. Lin, A.-W. Wu, Y.-C. Wang, Y.-C. Tseng, J.-S. Tsay, Spin reorientation transitions and structures of electrodeposited Ni/Cu(100) ultrathin films with and without Pb additives, *Phys. Chem. Chem. Phys*. **15** (2013) 2360.

[38] S. Nagasaki, M. Hirabayashi, Nigen Goukin Joutai Zushu, Agne Gijutsu Center, Vol. 2, (2002).

[39] L. Vitos, A.V. Ruban, H.L. Skriver, J. Kollár, The surface energy of metals, *Surf. Sci*. **441** (1998) 186.

[40] S. Haruyama, Hyomen Gijutusha no Tameno Denkikagaku, Vol. 2, Maruzen (2005).

[41] H. Fischer, Aspects of inhibition in electrodeposition of compact metals I. Effects of electrochemical inhibition, *Electrodepos. Surface Treat*. **1** (1973) 239.

[42] H. Fischer, Aspects of inhibition in electrodeposition of compact metals II. Effects of morphological interface inhibition, *Electrodepos. Surface Treat*. **1** (1973) 319.

[43] M.G. Chu, J. McBreen, G. Adzic, Substrate Effects on Zinc Deposition from Zincate Solutions I. Deposition on Cu, Au, Cd and Zn, *J. Electrochem. Soc*. **128** (1981) 2281

[44] J. McBreen, M.G. Chu, G. Adzic, Substrate Effects on Zinc Deposition from Zincate Solutions II. Deposition on Pb, Tl, Sn and In, *J. Electrochem. Soc*. **128** (1981) 2287.

[45] T. Mitsuhashi, Y. Ito, Y. Takeuchi, S. Harada, T. Ujihara, Non-uniform electrodeposition of zinc on the (0001) plane, *Thin Solid Films* **590** (2015) 207.

[46] A.J. Bard, L.R. Faulkner, Electrochemical methods - Fundamentals and Applications, *John Wiley & Sons Inc.*, New York, 2000.

[47] A.G. Muñoz, S.B. Saidman, J.B. Bessone, Electrodeposition of Zn and In onto vitreous carbon, *J. Appl. Electrochem.* **29** (1999) 1297.

[48] F.C. Walsh, C.T.J. Low, A review of developments in the electrodeposition of tin, *Surf. Coat. Technol*. **288** (2016) 79.

[49] A. Motori, F. Sandrolini, Electrical properties of nickel hydroxide for alkaline cell systems, *J. Power Sources* **48** (1994) 361.

[50] S. Deabate, F. Henn, S. Devautour, J.C. Giuntini, Conductivity and Dielectric Relaxation in

Various $Ni(OH)_2$ Samples, *J. Electrochem. Soc*. **150** (2003) J23.

[51] S. Wodarz, T. Hasegawa, S. Ishio, T. Homma, Structural control of ultra-fine CoPt nanodot arrays via electrodeposition process, *J. Magn. Magn. Mater.* **430** (2017) 52.

[52] E. Budevski, G. Staikov, W. Lorenz, Electrochemical phase formation and growth, Wiley-VCH, Weinheim, 1996.

Chapter 4:

Formation Mechanism of ZnO during Discharge of Zn Negative Electrode

4.1 Introduction

During the discharge of Zn negative electrode, zincate ions ($Zn(OH)_4^{2-}$) are formed by anodic dissolution of electrodeposited Zn (formed during charging). Then, ZnO is precipitated on the electrode after the concentration of zincate reaches the solubility limit (attaining the supersaturated condition). The precipitated ZnO has influences on the electrode reactions. First, the discharge capacity of the electrode is limited not by the amount active material (Zn) but by electrode passivation by impeding the diffusion of OH^- and zincate ions by ZnO layer [1]. Second, ZnO formation causes the redistribution of active materials (Zn and ZnO) on the electrode surface [2, 3]. Since the ZnO formation during the discharge is very sensitive to the mass transfer condition in the electrolyte, the precipitated amount of ZnO varies over the electrode surface, which can cause an accumulation of active materials. Third, ZnO affects the following charging process [4-6]. When ZnO is densely formed on the electrode, it becomes difficult to reduce ZnO again to Zn [4]. These influences are especially important for achieving high energy densities (*e.g*. applications in Zn-Air battery) because the supersaturated condition is easily attained under the static electrolyte and the tightly assembled electrodes [8].

Therefore, to attain good cyclability of Zn negative electrodes, it is necessary to control the ZnO formation behavior. To clarify the viewpoint for such a control, profound understandings on nucleation & growth behavior of ZnO during anodic dissolution of Zn are necessary. In this section, morphological variations and crystal structures of ZnO are analyzed at various dissolution conditions. Then, nucleation & growth process of ZnO behind the morphological variations are discussed. In addition to the dissolution conditions (*e.g.* concentration of OH^-, current densities), effects of surface morphologies of Zn electrode on the ZnO formation process are analyzed. Even recently published review article mentioned that the little attention has been paid to the effects of Zn surface conditions to the ZnO formation despite the remarkable influence of the properties of substrates in the chemical synthesis technique of ZnO (hydrothermal growth, electrodeposition) [8-10]. I expect that the surface properties of Zn electrode have potentially important factors influencing the discharge behavior of the electrode.

4.2 Methodology

Anodic dissolution of Zn was performed in a three-electrode configuration. A configuration of the electrochemical cell was different from that used in chapters 2 and 3; a working electrode was horizontally upward faced to a Zn counter electrode (Zn wire, Nilaco, 0.50 mmϕ, 99.99%) and Hg/HgO reference electrode. A schematic image and photograph of the electrochemical cell are shown in Fig. 4.1. This configuration was used because influences of natural convection (buoyancy driven convection) could be avoided [11]. The experimental setup was constructed by cutting the bottom of a spectroscopic cell (polystyrene, 1.0 cm × 1.0 cm × 4.5 cm), and attaching it to the electrode holder used in chapter 2 (Fig. 4.1(b)). A working electrode was Zn plate (0.30 mm thickness, 99.5%, Nilaco) or electrodeposited Zn on Cu plate (0.30 mm thickness, 99.9%, Nilaco). Pretreatments of each electrode was performed as described in chapter 2. Zn electrodeposition on Cu plate was carried out by galvanostatic conditions at −40 mA cm^{-2} for 1000 s from 6.0 mol dm^{-3} KOH + 0.50 mol dm^{-3} zincate. To investigate effects of the surface morphologies of the Zn electrode on the ZnO growth behavior, 1.0 mmol dm^{-3} PbO or 50 mmol dm^{-3} $K_2SnO_3 \cdot 3H_2O$ was also added to the electrolyte as performed in chapter 3. Electrolytes for anodic dissolution were alkaline zincate solutions containing 2.0 – 6.0 mol dm^{-3} KOH + 0.050 – 0.25 mol dm^{-3} zincate. When an electrodeposition was performed prior to anodic dissolution, the electrolyte was replaced after electrodeposition. Anodic dissolution was performed by galvanostatic condition at current densities of +20 and +40 mA cm^{-2}. Dissolution was stopped at certain dissolution time or when the potential increased to the positive value (*e.g.* −0.60 V vs. R.E.). After dissolution, electrolyte was immediately removed, and the electrode surface was rinsed with pure water.

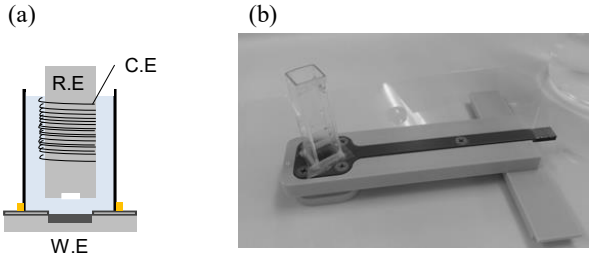

Fig. 4.1 Electrochemical cell used in anodic dissolution of Zn negative electrode; (a) schematic image of the configuration of three electrodes, (b) photographs of the electrode holder for a working electrode.

Surface morphologies of the electrode after electrochemical measurements were investigated by SEM (SU-8240 or S-5500, Hitachi). Crystal structures of the discharge products were analyzed by XRD (Rint-Ultima III, Rigaku). In order to identify the phase (presence of $Zn(OH)_2$ species) formed after the dissolution, the discharged electrode was heated by hot plate (PC-420D, Corning) at 200℃ for 1 h. Raman measurements were performed on the electrode after dissolution or during anodic dissolution (*in situ* measurements) by 3D laser Raman microspectroscopy with a confocal optical system (Nanofinder 30, Tokyo Instruments, Inc.). Measurements conditions for Raman spectroscopy are summarized in Table 4.1.

For the *in situ* Raman measurements, anodic dissolution was required to perform under the laser irradiation. Therefore, the electrochemical reactions should be performed in a small sized electrode so that thickness of electrolyte could be minimized to obtain Raman signal. To perform this analysis, the edge of Zn wire was polished by abrasive papers (#240, #400, #800 and #1200) after embedding in the epoxy resin as carried out in chapter 2. Then, an electrode surface area was confined to the edge area of the wire (*i.e.* 500 μmϕ). A Zn counter electrode (wire) was placed around the working electrode. Pt wire (Nilaco, 99.98%) was used as a quasi-reference electrode. Anodic dissolution was performed at +100 mA cm^{-2}. Higher value than that used for Zn plate was set to avoid very long dissolution time before the ZnO formation; when smaller sized electrode was used, the ZnO formation was delayed due to the enhanced diffusion of $Zn(OH)_4^{2-}$ and OH^- compared to the large sized electrode (*e.g.* spherical diffusion versus planer diffusion [12]).

Table 4.1 Raman Measurements Conditions

Wavelength of Laser	532 nm (*in situ*), 633 nm (*ex situ*)
ND	0.5
Grating	600 G /mm
Lens	× 10(*in situ*), × 50(*ex situ*)
Pinhole	50 μm
Exposure Time	10 s (*in situ*), 30 s (*ex situ*)

4.3 Results and Discussion

4.3.1 Effects of current density and electrolyte composition on the ZnO formation process

The ZnO formation during anodic dissolution has been described by the dissolution-precipitation mechanism where ZnO is precipitated from the supersaturated zincate species [13-15]. Therefore, nucleation & growth of ZnO is thought to be mainly governed by the dynamic changes in ionic concentrations near the electrode surface. Zn anodic dissolution was performed at several conditions (different OH^- concentrations and dissolution current densities). For this analysis, Zn plate was used as a working electrode.

The effects of KOH concentrations were investigated by dissolving Zn electrode in 2.0, 4.0, and 6.0 mol dm^{-3} KOH + 0.050 mol dm^{-3} zincate at +20 and +40 mA cm^{-2}. Fig. 4.2 shows potential profiles during anodic dissolution in each electrolyte. SEM images after passivation (after increase in the potential) are shown in Fig. 4.3 (+20 mA cm^{-2}) and Fig. 4.4 (+40 mA cm^{-2}). XRD patterns after passivation are shown in Fig. 4.5.

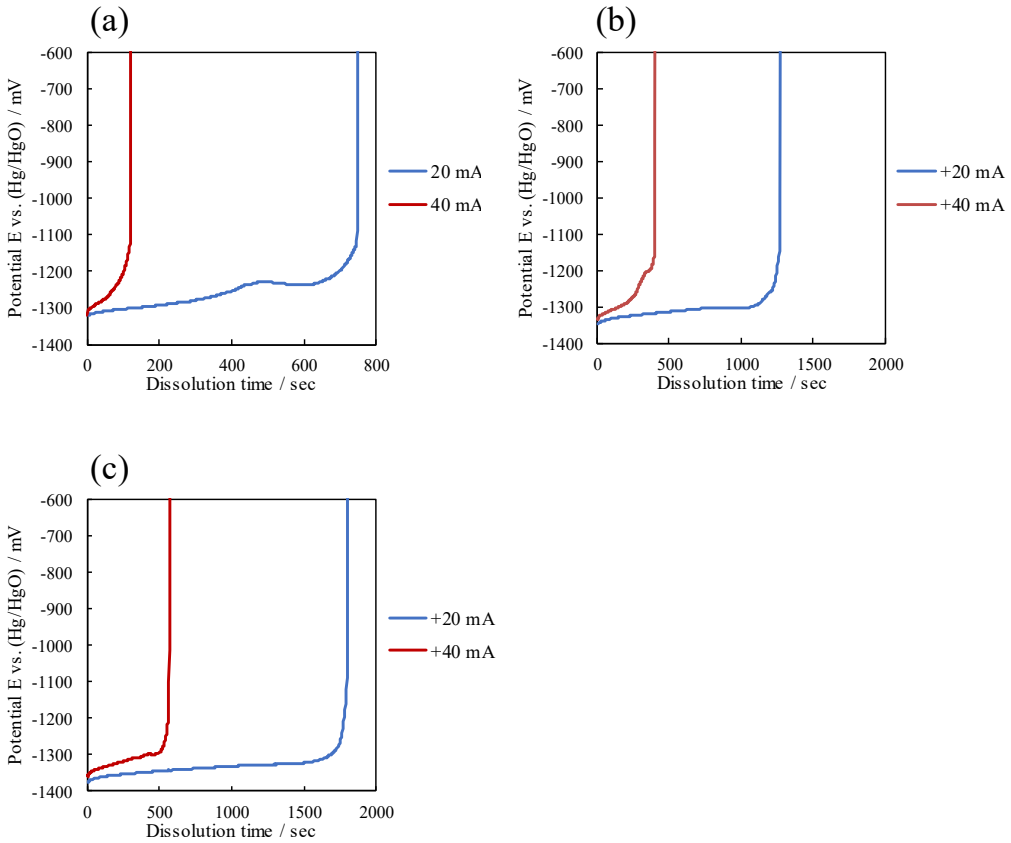

Fig 4.2 Potential profiles during anodic dissolution of Zn in (a) 2.0 mol dm^{-3}, (b) 4.0 mol dm^{-3}, and (c) 6.0 mol dm^{-3} KOH solutions at +20 mA cm^{-2} (blue line) and +40 mA cm^{-2} (red line).

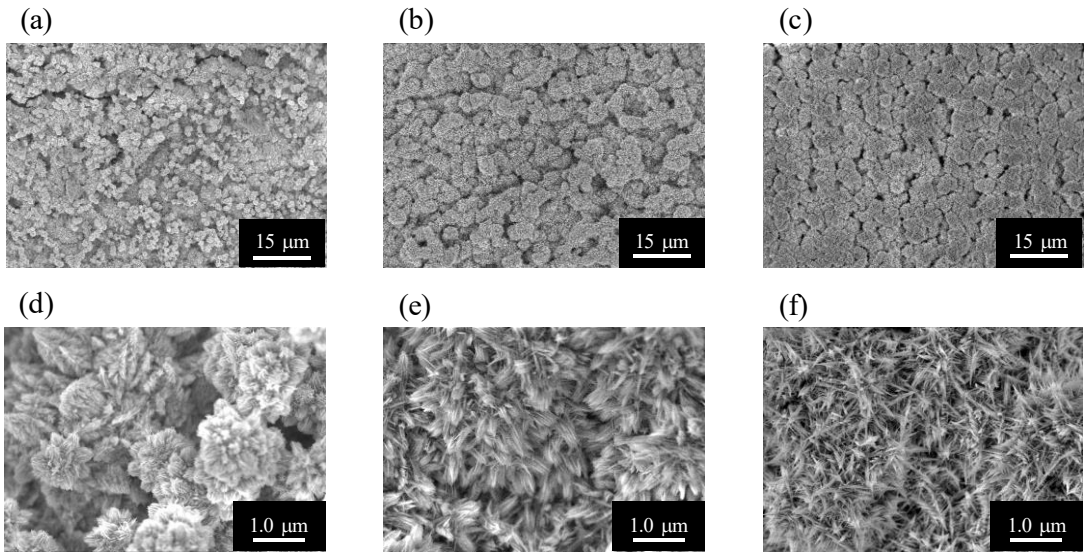

Fig 4.3 SEM images of Zn electrodes after discharge at +20 mA cm^{-2} in (a), (d) 2.0, (b), (e) 4.0 and (c), (f) 6.0 mol dm^{-3} KOH solutions. (d), (e), and (f) are higher magnification images of (a), (b), and (c) respectively.

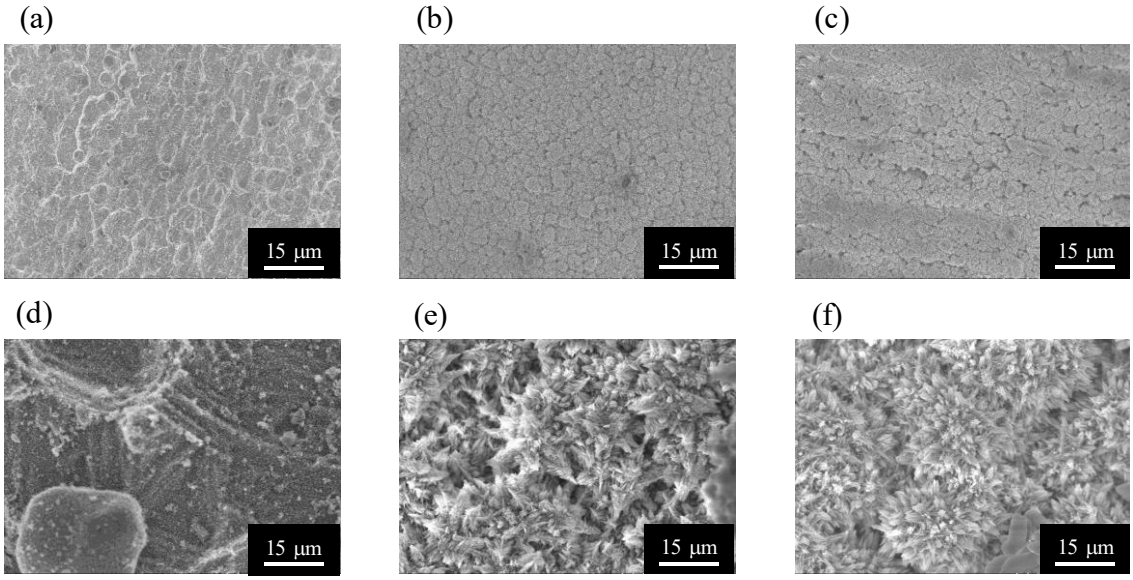

Fig 4.4 SEM images of Zn electrodes after discharge at +40 mA cm^{-2} in (a), (d) 2.0, (b), (e) 4.0 and (c), (f) 6.0 mol dm^{-3} KOH solutions. (d), (e), and (f) are higher magnification images of (a), (b), and (c), respectively.

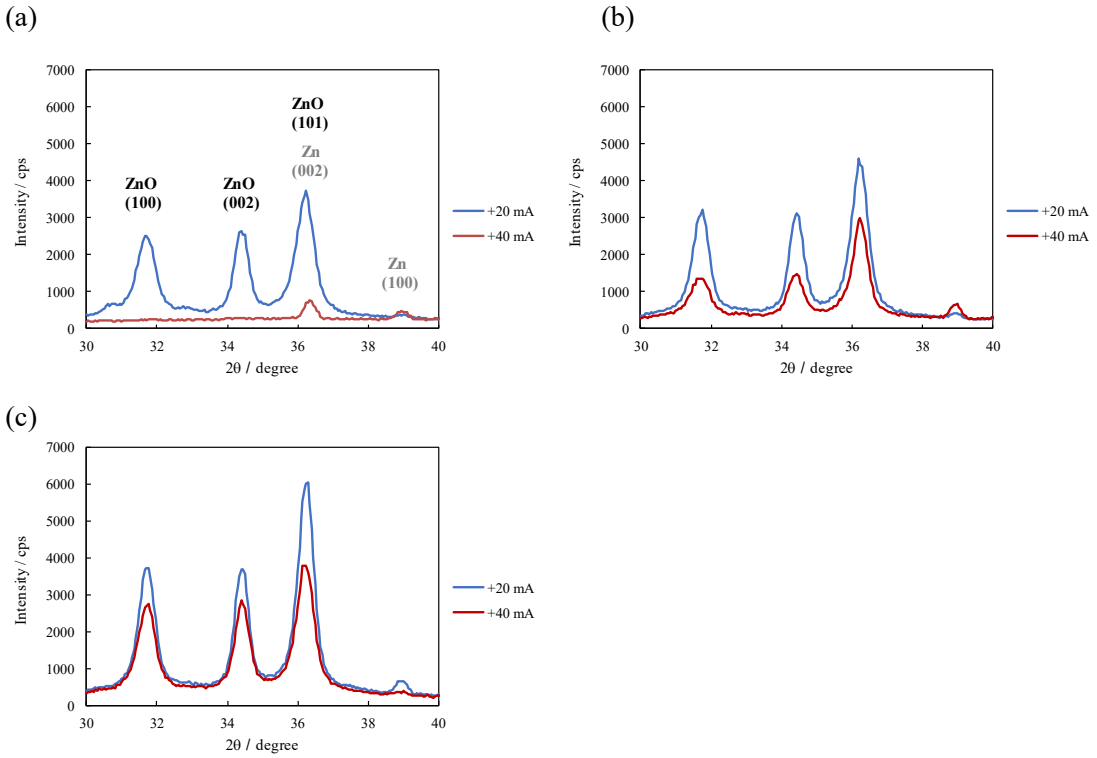

Fig 4.5 XRD patterns of the electrode after passivation in (a) 2.0 mol dm^{-3}, (b) 4.0 mol dm^{-3}, and (c) 6.0 mol dm^{-3} KOH solutions at +20 mA cm^{-2} (blue line) and +40 mA cm^{-2} (red line).

From Fig. 4.3, cluster-like structures of ZnO forms on the electrode at each condition. The density of the structures decreases at high KOH concentration or lower current density. This is caused by a lower driving force for ZnO nucleation; the degree of zincate supersaturation decreases at lower current density or higher KOH concentration (higher zincate solubility), and the amount of ZnO nuclei decreases [15, 16]. However, the size of each cluster-like structure increases by growth of the acicular crystals at higher KOH or lower current density. At these conditions, diffractions from ZnO becomes strong in XRD patterns, which indicates that the crystal growth of ZnO becomes dominant at higher KOH concentration and lower current density. Unlike the patterns obtained in electrodeposited Zn discussed in chapter 3, the ZnO patterns indicate no preferential growth direction of ZnO crystals on the electrode; no remarkable difference cannot be found in the pattern compared to peak intensities of each mirror index in the powder diffraction. This is because ZnO nucleation reaction itself is a homogeneous reaction (nucleation via supersaturation).

As the elementary steps for ZnO nucleation and growth in the hydrothermal growth in alkaline condition, it has been proposed that nucleation is initiated by the dehydration reactions between zincate species like (4.1) [17].

$$Zn(OH)_4^{2-} + Zn(OH)_4^{2-} \rightleftarrows Zn_2O(OH)_6^{4-} + H_2O \tag{4.1}$$

Each nucleus is grown by an incorporation of a growth unit (zincate ion) [13, 17, 18].

$$Zn_xO_y(OH)_z^{(z+2y-2x)-} + Zn(OH)_4^{2-} \rightleftarrows Zn_{x+1}O_{y+1}(OH)_{z+2}^{(z+2y-2x+2)-} + H_2O \tag{4.2}$$

During the anodic dissolution in higher KOH concentration or lower current density, an elementary step (4.1) is less dominant due to the lower degree of zincate supersaturation. However, each nucleus considerably grows possibly by an incorporation and decomposition of zincate to the surface. Actually, the acicular shapes of ZnO like Fig. 4.3 are often observed under the condition where elementary step (4.2) is dominant [18]. Furthermore, it was reported that the growth rate of (0001) face increased at higher OH^- concentration, which resulted in acicular and rod-like shapes of ZnO crystals [19]. Thus, although nucleation was governed by the solubility of zincate ion, the electrode was passivated by the crystal growth of each ZnO nucleus. An incorporation and decomposition of the growth unit (zincate) was thought to be a major elementary step for the ZnO growth.

Effects of initial zincate concentration

Morphological variations by initial zincate concentrations were also investigated. Zn plate was discharged at +20 mA cm^{-2} in 4.0 mol dm^{-3} KOH + 0.05 or 0.25 mol dm^{-3} zincate solution. Fig. 4.6 shows the potential profiles. Corresponding SEM images and XRD patterns are shown in Fig. 4.7 and Fig. 4.8, respectively.

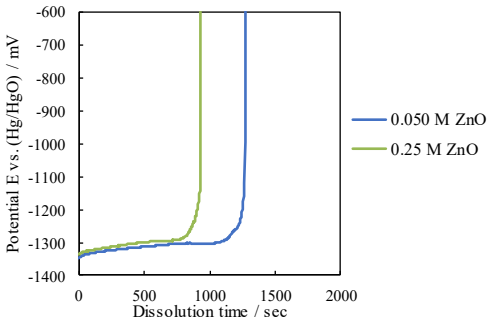

Fig 4.6 Potential profile during anodic dissolution of Zn in 4.0 mol dm^{-3} KOH + 0.050 or 0.25 mol dm^{-3} ZnO.

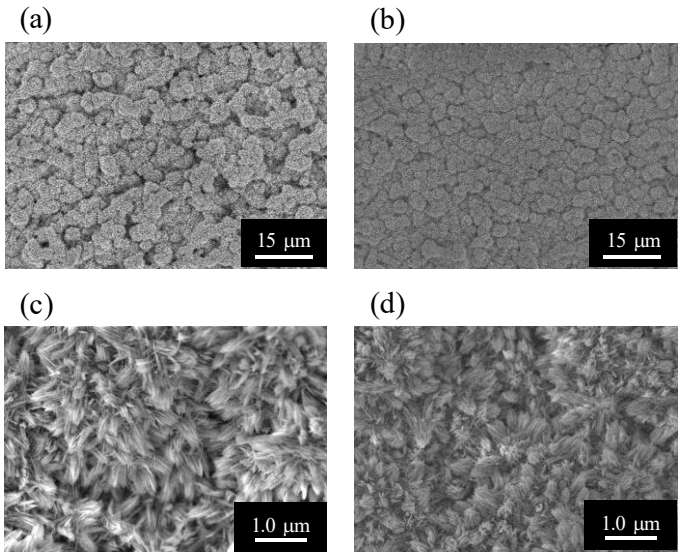

Fig 4.7 SEM images of Zn electrode after discharge in 4.0 mol dm^{-3} KOH + (a) 0.050 mol dm^{-3} and (b) 0.25 mol dm^{-3} zincate

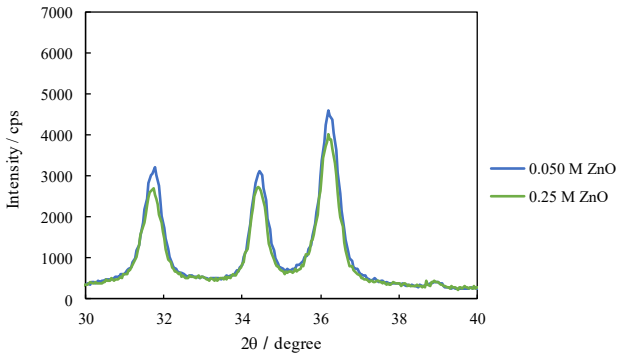

Fig 4.8 XRD patterns of the electrode after passivation in 4.0 mol dm^{-3} KOH + 0.050 mol dm^{-3} (blue) and 0.25 mol dm^{-3} zincate(green).

The ZnO formation behavior can be explained by a same scheme as is the case for the effects of KOH and current density; at higher initial zincate concentration (0.25 mol dm^{-3}), zincate concentration is quickly beyond the solubility limit. Then, ZnO nuclei dominantly forms. This results in shorter discharge time and the densely covered surface by the ZnO clusters. However, the crystal growth of ZnO is notable at lower initial zincate concentration (the lower degree of zincate supersaturation).

4.3.2 Changes in the ZnO growth behavior over dissolution time

Since the surface concentration of zincate continuously increases (the concentration of OH^- decreases), the driving force for the ZnO formation is dynamically changing during the dissolution process [11, 15]. To shed light on such a dynamic change, morphological variations and crystal structures were analyzed after stopping the dissolution at several times until passivation in 2.0 or 6.0 mol dm^{-3} KOH + 0.050 mol dm^{-3} zincate.

Figs. 4.9 and 4.10 represent SEM images of the electrode after discharging in 2.0 or 6.0 mol dm^{-3} KOH solution. Dissolution times were 200, 400, 600 and until passivation (740 s) in 2.0 mol dm^{-3} KOH solution, while 400, 1200, 1600 and until passivation (1800 s) in 6.0 mol dm^{-3} KOH . Corresponding XRD patterns are shown in Fig. 4.10.

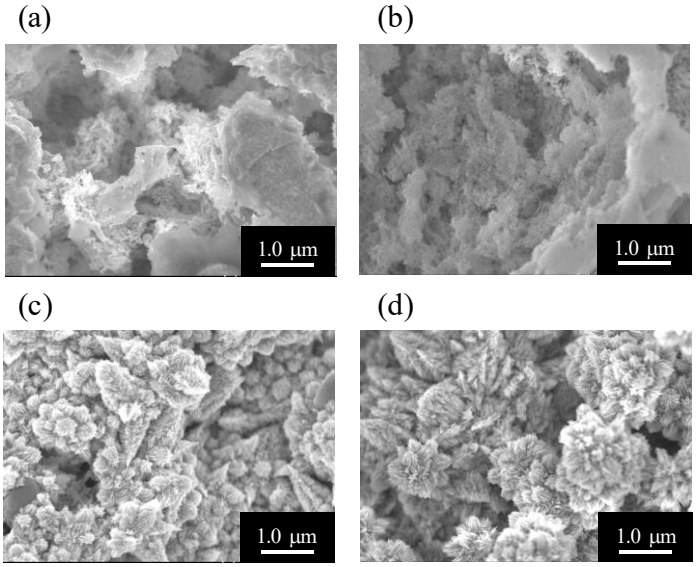

Fig. 4.9 SEM images of Zn electrodes after several dissolution times in 2.0 mol dm^{-3} KOH solution; (a) 200 s, (b) 400 s, (c) 600 s, and (d) passivation (740 s).

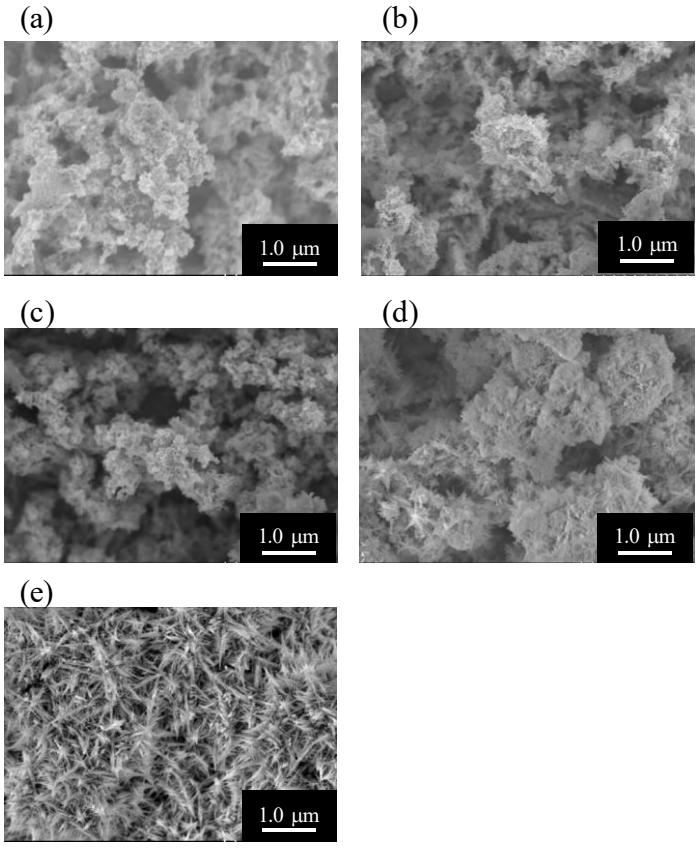

Fig. 4.10 SEM images of Zn electrodes after several dissolution times in 6.0 mol dm^{-3} KOH solution; (a) 400 s, (b) 800 s, (c) 1200 s, (b) 1600 s, and (h) passivation (1800 s).

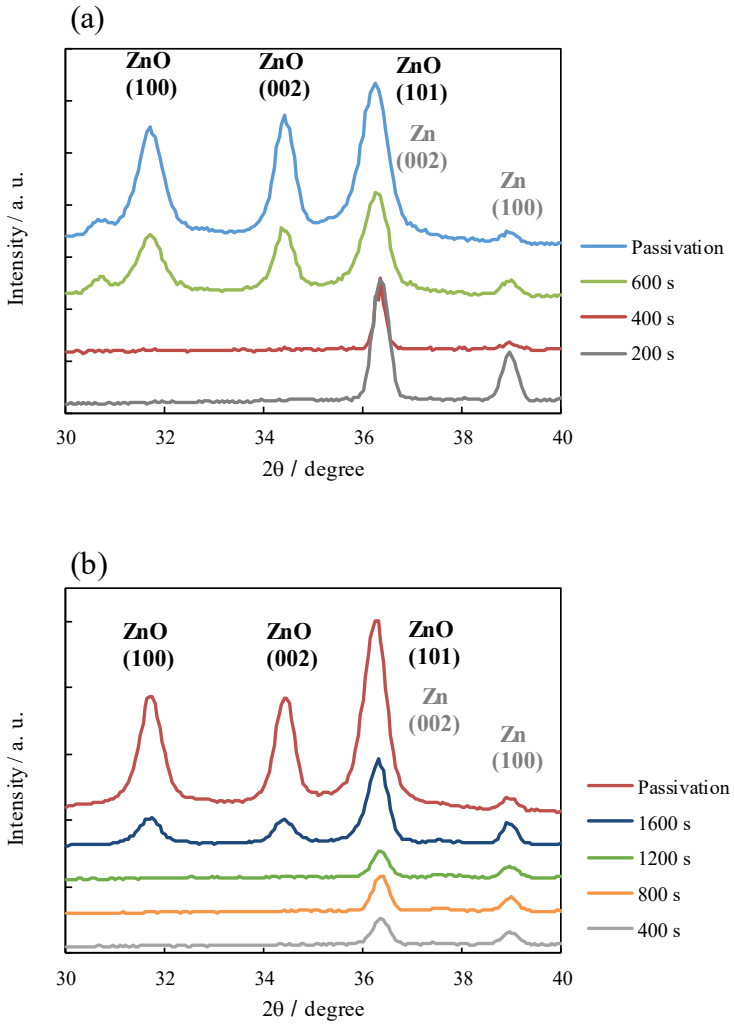

Fig. 4.11 XRD patterns of Zn electrode at several dissolution times in (a) 2.0 mol dm^{-3} KOH and (b) 6.0 mol dm^{-3} KOH solution.

At initial stages of the dissolution, there are no precipitates which have particular shapes of the ZnO crystals in SEM images. Although powder-like structures are observed, it was difficult to distinguish the precipitated ZnO and the underlying Zn. (This situation could be avoided by using electrodeposited Zn as a working electrode as discussed below.) In XRD patterns, no detectable diffraction was observed until 400 s (2.0 mol dm^{-3} KOH) or 1200 s (6.0 mol dm^{-3} KOH) though the diffractions from Zn substrate (Zn (002) and Zn (100)) slightly decreases. This indicates that the crystal growth of ZnO is dominant immediately before the passivation. Slight decrease in Zn diffraction at initial stages implies that ZnO with low crystallinity (amorphous) precipitated at the initial stage. Such a duplex character in the passivation films are discussed from early studies on Zn negative

electrodes [11, 20]. However, nucleation & growth process behind such a change is not fully understood. This aspect is further analyzed by *in situ* Raman analysis below.

4.3.3 I*n situ* Raman analysis on the discharge behavior of Zn negative electrode

Ex situ Raman analysis on the discharge products

SEM and XRD analysis shown above indicated changes in the ZnO growth behavior; the crystal growth of ZnO becomes dominant at later stages of dissolution. Raman scattering is another characterization technique often used for analyzing the structural changes of ZnO [21, 22]. Raman measurements were performed for the electrodes discharged in 2.0 mol dm^{-3} KOH + 0.050 mol dm^{-3} zincate (same samples which are characterized by SEM and XRD in Fig. 4.9 and 4.11 (a)). Fig. 4.12 shows Raman spectra of each electrode.

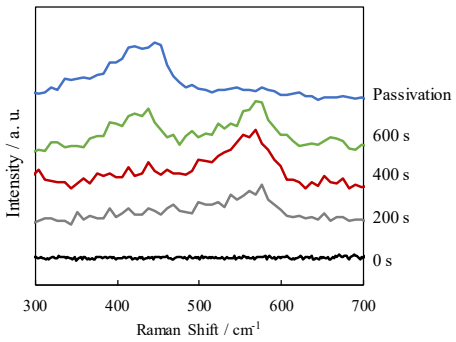

Fig 4.12 *Ex situ* Raman spectra of Zn electrode discharged for 200 s, 400 s, 600 s, and passivation.

At initial stages of dissolution (200 - 400 s), a peak evolved around 560 cm^{-1} which is assigned to E_1 longitudinal optical phonon (LO) mode of ZnO lattice. After dissolution proceeds, a peak at 440 cm^{-1} becomes dominant. This peak is E_2 mode of ZnO. E_1 (LO) mode originates from the crystal defects (Zn excess in the interstitial sites in the lattice), while E_2 mode is generally observed for the crystalline wurzite ZnO [23, 24]. Excess Zn in the interstitial sites of wurtzite structure forms new electronic states in the ZnO crystallite, which induces a resonant Raman scattering of E_1 (LO) mode [25]. Accordingly, Raman spectra also indicates the crystal growth of ZnO is dominant immediately before the passivation.

In situ Raman analysis during Zn dissolution reaction

However, it is difficult to discuss the structural changes only by *ex situ* analysis

because of the possible oxidation on Zn surface during air exposure. It is known that the native oxide layer on Zn also exhibits a scattering from E_1(LO) mode [26]. Therefore, Raman measurements were carried out to directly monitor the structural changes of ZnO during the discharge reactions; dissolution reaction was performed by using small sized electrode and the laser was irradiated every 100 s for 10 s after stating the discharge. Fig. 4.13 shows Raman spectra of Zn electrode every 400 s after starting the dissolution in 2.0 mol dm^{-3} KOH + 0.050 mol dm^{-3} zincate.

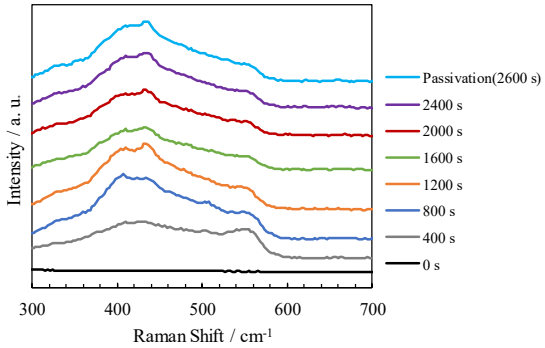

Fig 4.13 *In situ* Raman spectra of Zn electrode in 2.0 mol dm^{-3} KOH + 0.050 mol dm^{-3} zincate. Dissolution current was +100 mA cm^{-2} and diameter of electrode surface was 500 μmϕ (corresponding to the diameter of zinc wire).

Two peaks evolves during the dissolution; one is around 400-450 cm^{-1} which corresponds to E_2 mode and E_1 transverse optical phonon (TO) mode of ZnO, and the other is E_1 (LO) mode. Before 400 s (data not shown), there is no detectable peak and the precipitation of ZnO is thought to start around 400 s. At these initial stages of ZnO formation, E_1 (LO) mode is strong, and scatterings from E_2 and E_1 (TO) mode are relatively weak compared to later stages of dissolution. It means that ZnO formed at initial stages of dissolution contains the crystal defects as inferred in *ex situ* analysis. After dissolution proceeded, E_2 mode and E_1 (TO) mode became dominant, which is in accordance with the dominant crystal growth at later stages of dissolution (an increase in the peak intensities in XRD patterns and the evolution of acicular crystals in SEM observation). An increase in the intensity of E_2 mode at later stages of dissolution was previously observed for *in situ* Raman analysis during the potentiostatic dissolution of zinc electrode, too [27]. Thus, the crystallinity of the precipitated ZnO dynamically changes during the dissolution.

As a cause of the structural change, it is expected that elementary steps for nucleation & growth of ZnO varies during dissolution. At initial stages of dissolution where no ZnO is present near the electrode surface, ZnO is nucleated by dehydration

reactions between zincate species like (4.1). After dissolution proceeds, ZnO grows by an incorporation and decomposition of zincate on existing ZnO nuclei like (4.2). Zn excess may be introduced upon the former process at the condition where nucleation is favored. Correlations between favorable nucleation and the formation of Zn excess are inferred from former *in situ* Raman analysis, too; E_1 (LO) mode is dominant at low KOH concentration, and passivation at positive anodic potential [27, 28]. In both cases, nucleation is favored than the growth as discussed in 4.3.1.

Discussion: Nucleation & growth process of ZnO during anodic dissolution of Zn

From analysis above, nucleation & growth process of ZnO during anodic dissolution of Zn is rationalized as follows based on the dissolution-precipitation mechanism. First, only zinc dissolution and zincate formation occur before reaching the solubility limit of zincate (Fig. 4.14(a)). Then, after reaching the supersaturation condition, primary particles of ZnO are nucleated by the dehydration reactions between zincate species like (4.1). Upon this process, crystal defects (Zn excess in the interstitial sites) are likely to be introduced. Then, nuclei are grown by the reactions between polymetric species and incorporation of the growth unit (zincate) at the ZnO surface. Therefore, although nucleation process is governed by the supersaturation of zincate ions, the growth of each nuclei is thought to have remarkable influence on passivation and the cyclability of the electrode. This aspect is further discussed in Chapter 5.

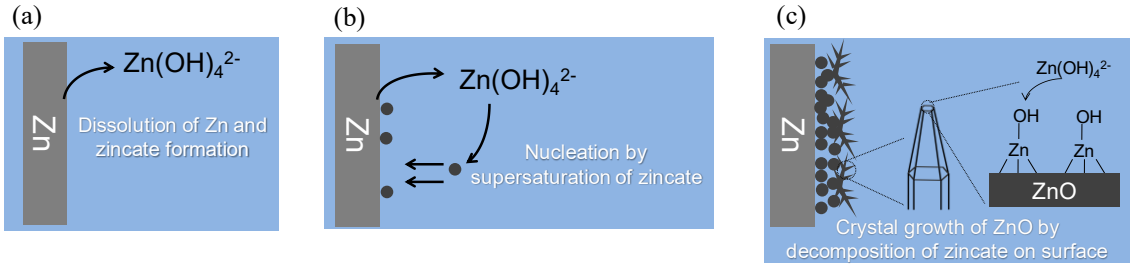

Fig. 4.14 Schematic images of the ZnO formation process during anodic dissolution of Zn; (a) before reaching supersaturation, (b) onset of nucleation of ZnO, (c) growth of ZnO and passivation.

4.3.4 Effects of surface morphologies of Zn negative electrode on the ZnO formation

Morphological variations of Zn and discharge products

In the analysis above, Zn plate was used as a working electrode. One of the issues to use Zn substrate was that it was difficult to distinguish the precipitated ZnO and the underlying Zn microstructures because residual Zn after dissolution had no particular morphologies (powder-like structures) in Figs. 4.9 and 4.10. Also, it is of practical interest to understand how Zn surface is involved in the ZnO formation process as mentioned in the introduction section. Based on these backgrounds, the effects of underlying Zn morphologies on the ZnO formation behavior were analyzed by using an electrodeposited Zn as a working electrode for anodic dissolution.

Zn electrodeposition was performed on a mirror-finished copper plate from 6.0 mol dm^{-3} KOH + 0.50 mol dm^{-3} zincate at −40 mA cm^{-2} for 1000 s. Also, electrodepositions in the solution containing 50 mmol dm^{-3} $K_2SnO_3 \cdot 3H_2O$ or 1.0 mmol dm^{-3} PbO was performed. Figure 4.15 compares morphological variations of Zn plate, electrodeposited Zn without additive, with Sn and with Pb.

After electrodepositions, several surface morphologies are obtained. When electrodeposition is performed without additive, layer-like structures (microsteps) exposing well-defined facets are formed. This facet is thought to be basal plane of hcp-Zn [29-31]. By adding Sn, Zn particles with more than 10 μm diameter are formed. Defined facet is not observed in each particle. When Pb is added, fine particles with several 100 nm diameter are deposited, which results in the lowest surface roughness among the electrodeposits. RMS roughness evaluated by laser scanning confocal microscope were 0.1 μm (Zn plate), 3.1 μm (electrodeposited Zn without additive), 3.7 μm (electrodeposited Zn with Sn) and 0.7 μm (electrodeposited Zn with Pb).

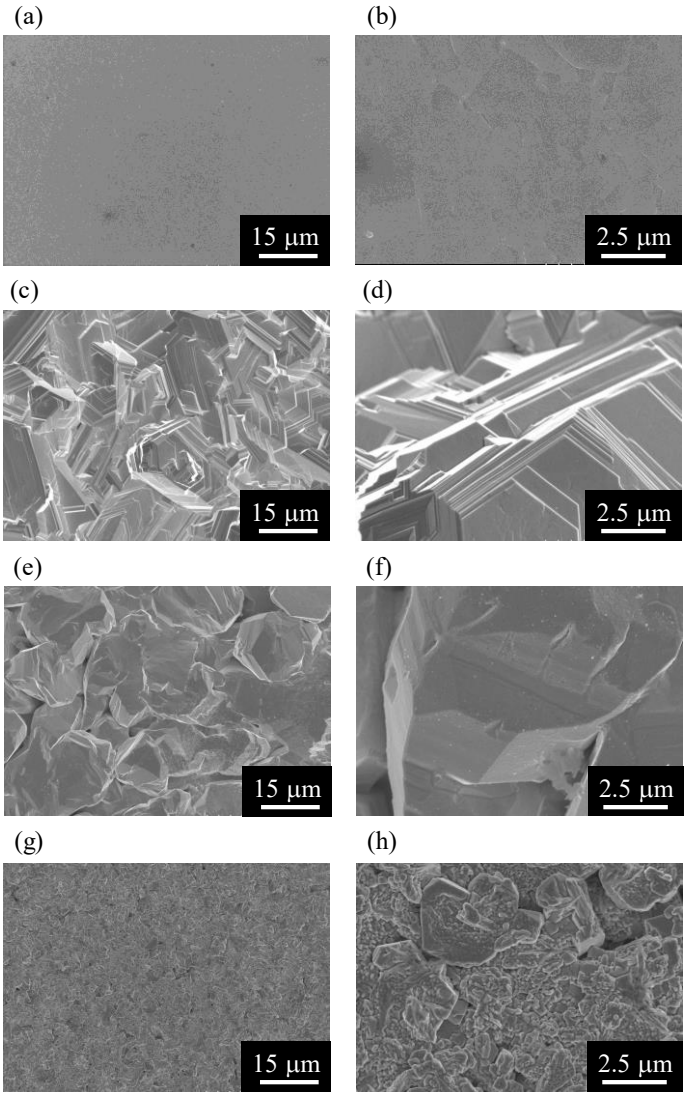

Fig 4.15 Morphological variations of Zn electrodes; (a), (b) mirror-finished Zn plate, (c), (d) electrodeposited Zn without additive, (e), (f) electrodeposited Zn with Sn, (g), (h) electrodeposited Zn with Pb. (b), (d), (f), and (h) are higher magnification images of (a), (c), (e), and (g), respectively.

These electrodes were discharged at +20 mA cm^{-2} until passivation. The potential profiles during dissolution is shown Fig. 4.16.

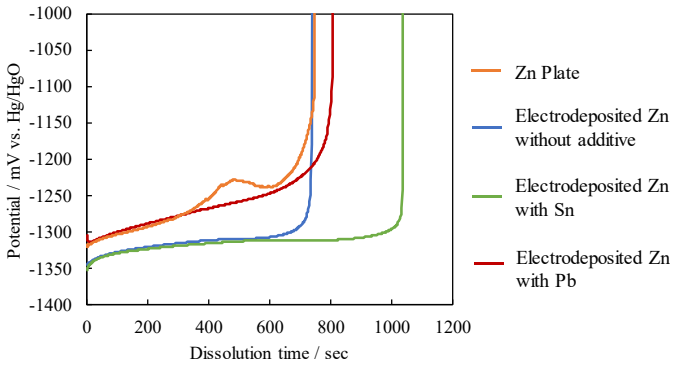

Fig 4.16 Potential profiles of Zn plates (orange), electrodeposited Zn without additive (blue), with Sn (green) and with Pb (red) during discharge at +20 mA cm^{-2}.

Despite the same discharge condition (current density and electrolyte) of each electrode, they exhibit different potential transients. First, the time of dissolution until passivation is altered by the underling Zn microstructures. The discharge time is extended by Sn and Pb addition. Especially, more than 200 s increase in the dissolution time is observed for electrodeposited Zn with Sn. Second, the potential value (overpotential for anodic dissolution of Zn) is considerably different in each case. Zn plate and electrodeposited Zn with Pb exhibit relatively large overpotential, and the potential continuously shifts to the positive value during the reaction. On the other hand, electrodeposited Zn without additive and with Sn show the stable potentials, and it suddenly increases to the cut-off potential at the passivation condition. As a cause of the potential change, several factors could be considered. First, the overpotential for the Zn dissolution reaction may increase at the presence of Pb in the deposits. In addition to the suppression effects of Pb on elementary steps for Zn electrodeposition (as discussed in Chapter 3), dissolution reaction (a reverse reaction of electrodeposition) is also likely to be suppressed by the presence of Pb [32, 33]. Second, substantial current density is varied due to the different surface roughness of each electrode. The current density for Zn plate and electrodeposits with Pb may be substantially larger than that for electrodeposits without additive and Sn because of the small surface roughness value. These variations may result in increase in the overpotential for dissolution. Furthermore, differences in the ZnO formation behavior induces variations in the overpotential and dissolution time as discussed below.

SEM images after passivation are shown in Fig 4.17.

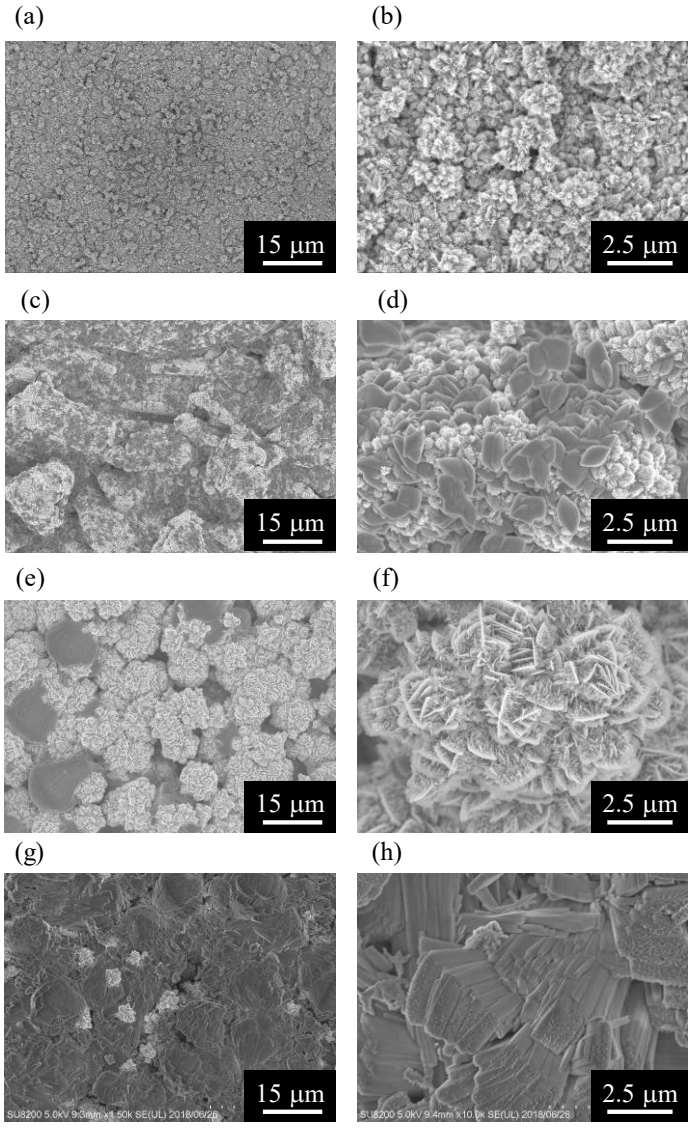

Fig 4.17 SEM images after passivation of (a), (b) mirror-finished Zn plate, (c), (d) electrodeposited Zn without additive, (e), (f) electrodeposited Zn with Sn, (g), (h) electrodeposited Zn with Pb. (b), (d), (f), and (h) are higher magnification images of (a), (c), (e), and (g), respectively.

Depending on the microstructures of Zn electrodeposits, various ZnO morphologies are obtained. In addition to the cluster-like structures comprising the acicular ZnO crystals, ellipsoidal structures are obtained on electrodeposited Zn without additive (Fig. 4.17 (c) and (d)). These structures appear in the dark contrast in SEM images. When electrodeposition is performed with Sn, majority of the precipitates are relatively large clusters having acicular shapes. In contrast, such cluster-like structures

are hardly observed on electrodeposits with Pb additive. Instead, plate-like aggregates are densely formed on the electrode. Crystal structures of the precipitates were analyzed by XRD (Fig. 4.18).

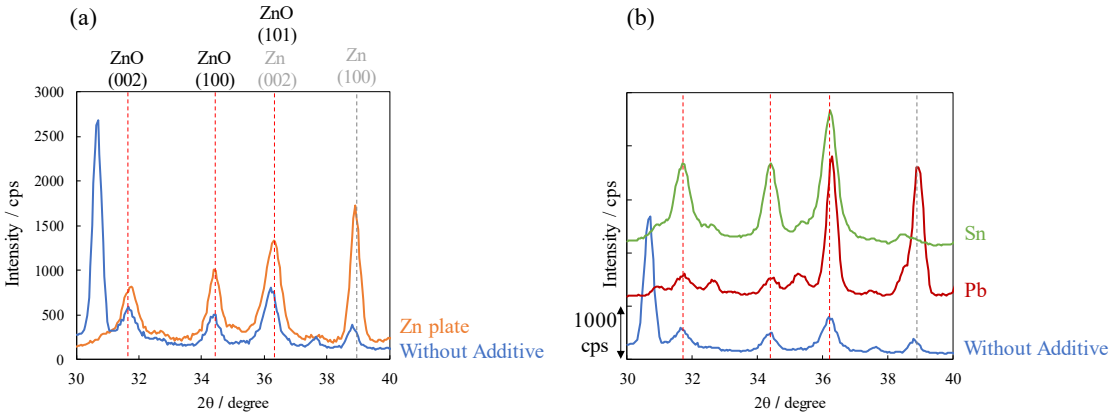

Fig 4.18 XRD patterns of Zn electrodes (Zn plate (orange), electrodeposited Zn without additive (blue), with Pb (red) and with Sn (green)) after discharge. (a) compares the patterns of discharge products on Zn plate and electrodeposited Zn without additive, and (b) shows patterns from electrodeposited Zn with and without additive species.

In Fig. 4.18(a), the precipitates on Zn plate exhibits the strong diffractions of wurtzite ZnO compared to that on electrodeposited Zn on Cu. In other words, the crystal growth of ZnO is suppressed upon the formation of the ellipsoidal structures shown in Fig 4.17(d). In Fig. 4.18(b), strong diffractions of ZnO appears on the electrodeposits with Sn additive. In contrast, peak intensities are weak in the Pb added electrodeposit. Furthermore, peaks which could not be assigned to wurtzite ZnO are observed in the case without additive (30.8 degree) and with Pb. These peaks may originate from different discharge products; *e.g.* $Zn(OH)_2$. For example, peaks at 31.0, 35.4, 37.6 and 38.6 degree are assigned to γ-$Zn(OH)_2$. Although majority of the discharge products in previously researches was ZnO, the formation of γ-$Zn(OH)_2$ was also reported especially in the case of dissolution in low KOH concentrations [8]. Since ZnO was formed by dehydration reaction of $Zn(OH)_2$, the electrode was passivated before converting $Zn(OH)_2$ to ZnO in these conditions [34-37]. For electrodeposited Zn without additive, a strong peak emerges at 30.8 degree. It is confirmed that this peak disappears after heating the electrode at 200˚C for 1 h (Fig. 4.19).

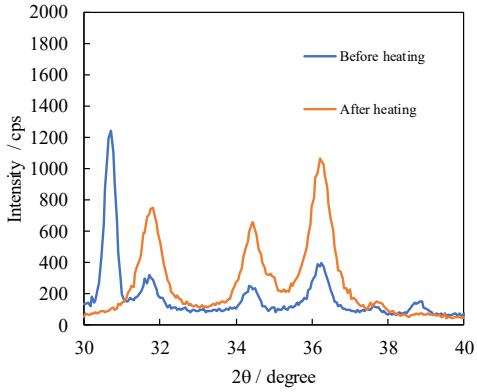

Fig 4.19 XRD patterns of discharge products on electrodeposited Zn without additive before heating (blue) and after heating (orange).

The presence of $Zn(OH)_2$ implies that the primary particles are formed as $Zn(OH)_2$, and its transformation to ZnO are suppressed in the case of electrodeposited without additive and with Pb. In short, we could find the correlations between morphologies and crystal structures; cluster-like structures comprising acicular crystals exhibit the strong diffraction of ZnO (Zn plate and Sn addition), while the crystal growth is not dominant in ellipsoidal and plate-like structures (the electrodeposit without additive and Pb addition).

The variations in ZnO morphologies and XRD patterns clearly suggest that the underlying Zn microstructure affect the ZnO formation process. In order to shed light on such an influence, the ZnO formation behavior is analyzed by time-resolved manner. Dissolution was stopped at certain dissolution time. Then, morphologies and crystal structures were analyzed by SEM and XRD. First, an analysis was performed on the electrodeposited Zn without additive. Fig. 4.20 shows morphological changes of the electrode over several dissolution times.

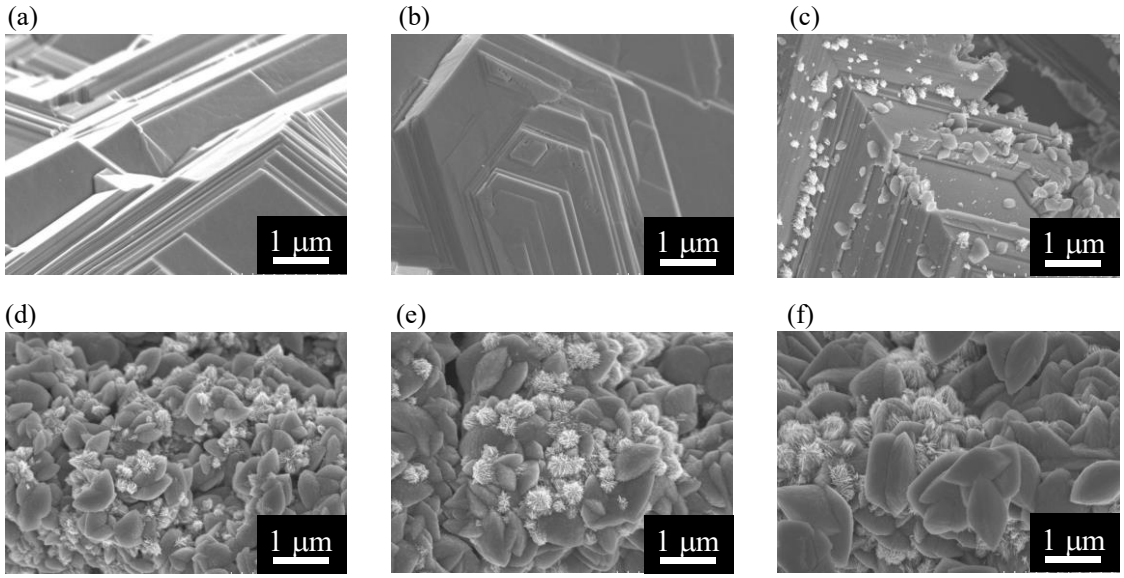

Fig. 4.20 Morphological variations during dissolution of electrodeposited Zn without additive at (a) 0 s (after electrodeposition), (b) 300 s, (c) 400 s, (d) 500 s, (e) 600 s, and (f) passivation.

At 300 s, no precipitates on Zn surface is observed and zincate ion may not reach the solubility limit. Zn surface after dissolution still exhibits the layer-like structures, which indicates that the dissolution reaction proceeds in a step-flow manner maintaining the underling Zn microstructures. From 400 s, the precipitates are visible on Zn surface. Then, the size of the precipitates increases until passivation. Especially, size of the ellipsoidal structures considerably increases compared to the cluster-like structures. XRD patterns of each electrode are shown in Fig. 4.21.

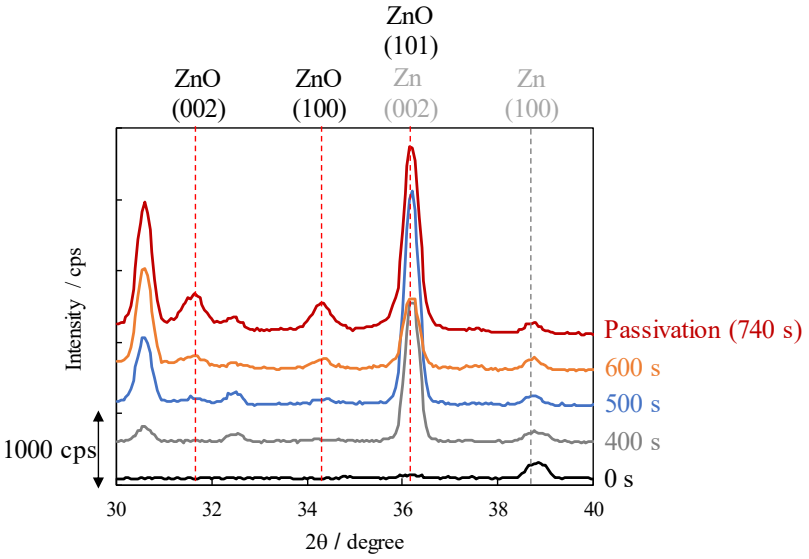

Fig. 4.21 XRD patterns of the discharge products on the electrodeposited Zn without additive at 0 s, 400 s, 500 s, 600 s, and passivation.

ZnO peaks appears around 500 s and it continuously increases until passivation. Also, a peak at 30.8 degree appears earlier (400 s). This implies that $Zn(OH)_2$ is the primary precipitate on electrodeposited Zn as inferred in Fig. 4.19. Morphological variations are analyzed for Sn and Pb addition case, too.

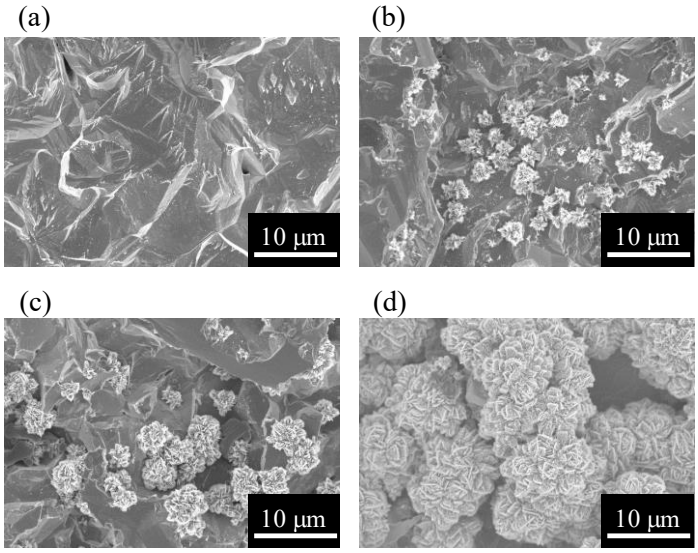

Fig. 4.22 Morphological variations of the electrodeposited Zn with Sn at (a) 300 s, (b) 500 s, (c) 600 s, and (d) passivation (1040 s).

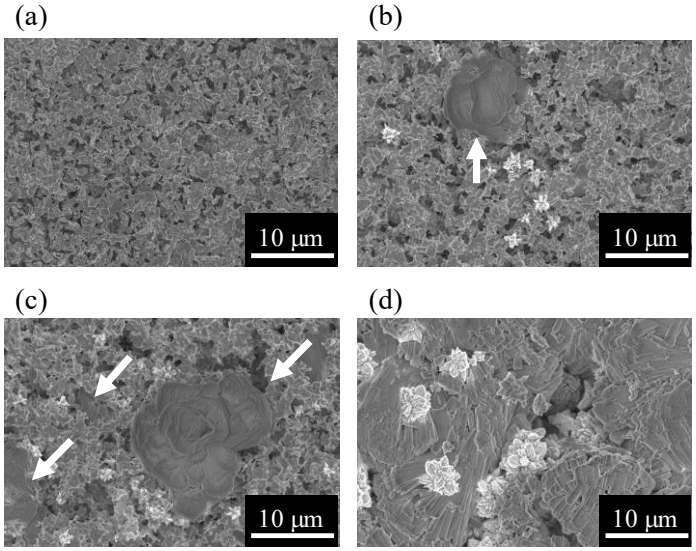

Fig. 4.23 Morphological variations of the electrodeposited Zn with Pb at (a) 300 s, (b) 500 s, (c) 600 s, and (d) passivation (830 s). White arrow shows the precipitates on the electrode.

In the case of Sn addition, small-sized clusters (several μm length) are dispersedly formed over the electrode surface. In contrast, relatively large aggregates forms from initial stages of dissolution in the case of Pb addition. A crystallinity of these structures is thought to be low compared to the cluster structures based on XRD analysis. Therefore, differences in the potential transients are caused by variations in the ZnO growh behavior as well; In the case of Pb, electrode surface is immediately covered by the precipitates, which results in a decrease in the active surface area and potential increase. On the other hand, Sn added electrodeposits exhibits a stable potential due to a gradual decrease in the active surface area.

Discussion: effects of surface morphologies on ZnO formation process

By using Zn electrodes with various morphologies, the discharge and ZnO formation behavior were considerably altered. Thus, Zn surface is involved in the dissolution-precipitation mechanisms. Qualitatively, there is a correlation between morphologies and intensity of diffraction from ZnO in XRD patterns; the diffraction of the cluster-like structures (formed on Zn plate and electrodeposit with Sn) is stronger than that from the ellipsoidal structures (formed on the electrodeposited Zn) and the plate-like structures (formed on the electrodeposited Zn with Pb). Thus, the crystal growth of ZnO is suppressed on the electrodeposited Zn and Pb addition case.

The cluster-like structures have been often observed even in the chemical

synthesis technique like a hydrothermal growth [13, 17, 18, 36]. It is considered that an incorporation and decomposition of the growth unit (zincate) at the ZnO surface results in such a morphology as discussed in 4.3.3. The formation of an ellipsoidal structure was also reported. From *in situ* SAXS and *ex situ* TEM analysis, such a structure was thought to be formed by an aggregation of primary ZnO nuclei [38-40]. Actually, the ellipsoidal structures formed on the electrodeposited Zn comprises much smaller particles as confirmed in Fig. 4.24.

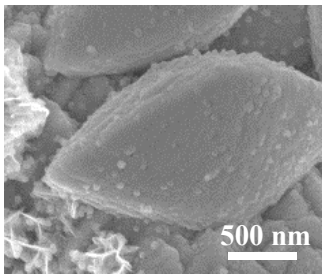

Fig 4.24 Enlarged SEM image of the ellipsoidal structure formed on the electrodeposited Zn without additive at +20 mA cm^{-2}.

Accordingly, the ellipsoidal structures and the plate-like structures formed on the electrodeposited Zn without additive and with Pb are possibly formed by an aggregation of primary particles, too. To further verify this assumption, dissolution was performed at +40 mA cm^{-2} and morphological changes were observed. At higher current density, nucleation is dominant than the growth process, which results in the larger number of primary nuclei. Fig. 4.25 compares the morphologies of electrodeposited Zn after discharge at +20 and +40 mA cm^{-2}.

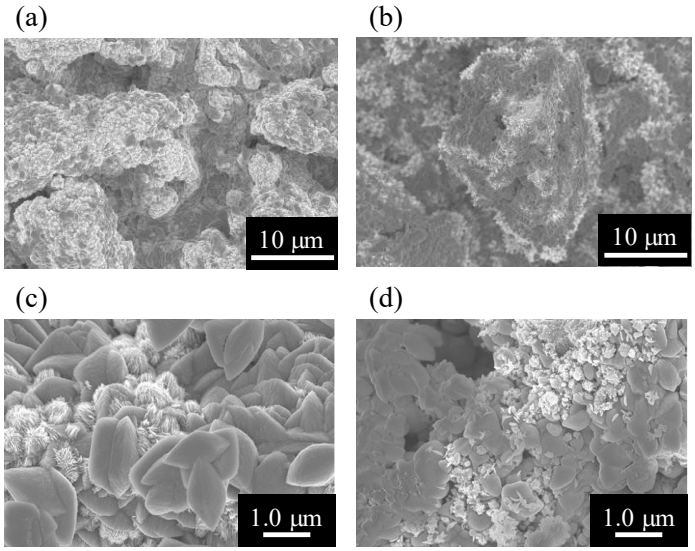

Fig 4.25 SEM images of the discharge products on the electrodeposited Zn without additive; (a), (c) + 20 mA cm^{-2} and (b), (d) +40 mA cm^{-2}. (c) and (d) are higher magnification images of (a) and (d), respectively.

As dissolution current increases, the portion of dark contrasted area increases in Fig 4.25 (b). It indicates that the number of the ellipsoidal structures (the shape was less defined than that at +20 mA cm^{-2}) increases at the higher degree of zincate supersaturation. Therefore, the formation of the ellipsoidal structures is reasonably explained by the aggregation of larger number of primary particles formed by the higher degree of supersaturation.

From these discussions, Zn surface is thought to be involved in the ZnO formation process as follows. When Zn surface has well defined facets (electrodeposited Zn without additive) or low surface roughness (electrodeposit with Pb), an aggregation of primary particles is promoted on the surface. This results in the formation of ellipsoidal or plate-like morphologies. On the other hand, when Zn surface doesn't have large terraces, the primary particles are less mobile on the surface. In this case, each nucleus is grown by the incorporation of the growth unit to ZnO, and the cluster-like structures form. Accordingly, it is possible to suppress the crystal growth of ZnO even at same dissolution condition by promoting an aggregation of primary particles.

Conclusion

The ZnO formation process during discharge was investigated to clarify the guiding principle for controlling the discharge reaction. First, Zn dissolution was performed in various conditions; *e.g.* different KOH, zincate concentrations and current density. As a result, the nucleation density of ZnO crystal were increased at the condition where the degree of zincate supersaturation was large. However, the crystal growth of ZnO was dominant even at higher KOH concentration or lower current density; the peak intensity of ZnO in XRD increased and the acicular ZnO crystals evolved under these conditions. This suggested that in addition to ZnO nucleation through the dehydration reactions between zincate species, the crystal growth of ZnO through zincate incorporation and decomposition on the crystal was important. *In situ* Raman measurements also revealed the structural changes of ZnO by different elementary steps for the ZnO formation; crystal defects (Zn excess in the interstitial sites) were introduced upon the nucleation process (dehydration reactions between zincate species) which was observed at initial stages of ZnO precipitation. In addition to the solution chemistry (*i.e.* OH^- activity and the degree of supersaturation), the microstructures of Zn electrode also had significant influence on the ZnO formation process. On Zn surface with well-defined facets or low surface roughness, an aggregation of primary ZnO nuclei was promoted. This made it possible to suppress the crystal growth of ZnO even at the same dissolution condition. Thus, the zincate decomposition on ZnO surface and an aggregation of nuclei on Zn surface had considerable influences on the morphologies and the crystal structures of ZnO precipitated during the discharge.

Reference

[1] M. Liu, G. M. Cook, N. P. Yao, Passivation of Zinc Anodes in KOH Electrolytes, *J. Electrochem. Soc*. **128** (1981) 1664.

[2] R. E. F. Einerhand, W. Vsscher, Zinc Electrode Shape Change, I. In Situ Monitoring, *J. Electrochem. Soc*. **138** (1991) 1.

[3] R. E. F. Einerhand, W. Vsscher, Zinc Electrode Shape Change, II. Process and Mechanism, *J. Electrochem. Soc.* **138** (1991) 7.

[4] H. -I. Kim, E. -J. Kim, S. -J. Kim, H. -C. Shin, Influence of ZnO precipitation on the cycling stability of rechargeable Zn-air batteries, *J. Appl. Electrochem.* **45** (2015) 335-342.

[5] A. Nakata, H. Murayama, K. Fukuda, T. Yamane, H. Arai, T. Hirai, Y. Uchimoto, J. Yamaki, Z. Ogumi, Transformation of Leaf-like Zinc Dendrite in Oxidation and Reduction Cycle, *Electrochim. Acta* **166** (2015) 82.

[6] A. Nakata, H. Arai, T. Yamane, T. Hirai, Z. Ogumi, Preserving Zinc Electrode Morphology in Aqueous Alkaline Electrolytes Mixed with Highly Concentrated Organic Solvent, *J. Electrochem. Soc.* **163** (2016) A50.

[7] M. Xu, D. G. Ivey, Z. Xie, W. Qu, Rechargeable Zn-air batteries: Progress in electrolyte development and cell configuration advancement, *J. Power Sources* **283** (2015) 358.

[8] M. Bockelmann, L. Reining, U. Kunz, T. Turek, Electrochemical characterization and mathematical modeling of zinc passivation in alkaline solutions; A review, *Electrochim. Acta* **237** (2017) 276.

[9] R. B. Peterson, C. L. Fields, B. A. Gregg, Epitaxial Chemical Deposition of ZnO Nanocolumns from NaOH Solutions, *Langmuir* **20** (2004) 5114.

[10] K. Ogata, K. Koike, S. Sasa, M. Inoue, M. Yano, ZnO nanorod arrays on n-type Si(111) substrates for pH measurements, *J. Vac. Sci. Technol. B,* **27** (2009) 1684.

[11] I. Arise, Y. Fukunaka, F. R. McLarnon, Ionic Mass Transfer Accompanying Anodic Dissolution of Zinc in Alkaline Solution, *J. Electrochem. Soc*. **153** (2006) A69.

[12] A.J. Bard, L.R. Faulkner, Electrochemical methods - Fundamentals and Applications, *John Wiley & Sons Inc.*, New York, 2000.

[13] S. Szpak, C. J. Gabriel, The Zn-KOH System: The Solution-Precipitation Path for Anodic ZnO Formation, *J. Electrochem. Soc*. **126** (1979) 1914.

[14] L. M. Bauch, A. R. Baikie, Passivation of zinc in concentrated alkaline solution – II. Role of various experimental factors and the distinction between the solid-state and dissolution-precipitation mechanisms, *Electrochim. Acta* **30** (1985) 1173.

[15] I. Arise, S. Kawai, Y. Fukunaka, F. R. McLarnon, Coupling Phenomena Between Zinc Surface Morphological Variations and Ionic Mass Transfer Rate in Alkaline Solution, *J. Electrochem. Soc.* **160**

(2013) D66-D74.

[16] C. Zhang, J. M. Wang, L. Zhang, J. Q. Zhang, C. N. Cao, The Behavior of the Amalgamated Zinc Electrode in Supersaturated Alkaline Zincate Solutions, *J. Electrochem. Soc.* **148** (2001) E310.

[17] W. -J. Li, E. -W. Shi, W. -Z. Zhong, Z. -W. Yin, Growth mechanism and growth habit of oxide crystals, *J. Cryst. Growth* **203** (1999) 186.

[18] N. Uekawa, R. Yamashita, Y. J. Wu, K. Kakegawa, Effect of alkali metal hydroxide on formation processes of zinc oxide crystallites from aqueous solutions containing $Zn(OH)_4^{2-}$ ions, *Phys. Chem. Chem. Phys*. **6** (2004) 442.

[19] L. N. Dem'yanets, D. V. Kostomarov, I. P. Kuz'mina, Chemistry and Kinetics of ZnO Growth from Alkaline Hydrothermal Solutions, *Inorg. Mater.* **38** (2002) 124.

[20] R. W. Powers, M. W. Breiter, The anodic dissolution and passivation of zinc in concentrated potassium hydroxide solutions, *J. Electrochem. Soc*. **116** (1969) 719.

[21] S. Youssef, C. Combette, J. Podlecki, R. A. Asmar, A. Foucaran, *Cryst. Growth Des.* **9** (2009) 1088.

[22] H. Matsuo, K. Yoshitoku, M. Saito, H. Takahashi, I. Terasaki, T. Homma, Fabrication of ZnO-Based Thermoelectric Micro-Devices by Electrodeposition, *J. Electrochem. Soc.* **165** (2018) D417.

[23] T. C. Damen, S. P. S. Porto, B. Tell, Raman Effect in Zinc Oxide, *Phys. Rev*. **142** (1966) 570.

[24] C. V. Manzano, O. Caballero-Calero, S. Hormeño, M. Penedo, M. Luna, M. S. Martín-González, ZnO morphology control by pulsed electrodeposition, *J. Phys. Chem. C* **117** (2013) 1502.

[25] J. M. Calleja, M. Cardona, Resonant Raman scattering in ZnO, *Phys. Rev. B* **16** (1977) 3753.

[26] A. H. Goff, S. Joiret, B. Saïdani, R. Wiart, In-situ Raman spectroscopy applied to the study of the deposition and passivation of zinc in alkaline electrolytes, *J. Electroanal. Chem*. **263** (1989) 127.

[27] Q. Shi, L. J. Rendek, W. -B. Cai, D. A. Scherson, In situ Raman spectroscopy of single particle microelectrodes: zinc passivation in alkaline electrolytes, *Electrochem. Solid-State Lett.* **6** (2003) E35.

[28] W. -B. Cai, D. A. Scherson, In situ Raman spectroscopy of zinc electrodes in alkaline solutions, *J. Electrochem. Soc.* **150** (2003) B217.

[29] J. O'M. Bockris, Z. Nagy, D. Drazic, On the Morphology of Zinc Electrodeposition from Alkaline Solutions, *J. Electrochem. Soc*. **120** (1973) 30.

[30] A. Tanaka, T. Nakamura, Y. Ueda, F. Noguchi, Observation of the Electrodeposition of Zinc from Sulfuric Acid Bath, *J. Jpn. Inst. Metals.* **44** (1980) 741.

[31] S. Itoh, N. Yamazoe, T. Seiyama, Electrocrystallization of various metals onto copper single crystal substrates, *Surf. Technol.* **5** (1977) 27.

[32] R. Ichino, C. Cachet, R. Wiart, Mechanism of zinc electrodeposition in acidic sulfate electrolytes containing Pb^{2+} ions, *Electrochim. Acta* **41** (1996) 1031.

[33] J. Bressan, R. Wiart, Use of impedance measurements for the control of the dendritic growth of zinc electrodeposits, *J. Appl. Electrochem.* **7** (1977) 505.

[34] F. Domoisson, R. Piolet, F. Bernard, Hydrothermal Synthesis of ZnO Crystals from $Zn(OH)_2$ Metastable Phases at Room to Supercritical Conditions, *Cryst. Growth Des.* **14** (2014) 5388.

[35] N. Uekawa, M. Kitamura, S. Ishii, T. Kojima, K. Kakegawa, Low-Temperatrure Synthesis of ZnO Nanoparticles by Heating of $Zn(OH)_2$ in a Neutral Mixed Solution of Ethanol and H_2O, *J. Ceramic Soc. Jpn*. **113** (2005) 439.

[36] M. Wang, Y. Zhou, Y. Zhang, S. H. Hahn, E. J. Kim, From $Zn(OH)_2$ to ZnO: a study on the mechanism of phase transformation, *Cryst. Eng. Comm.* **13** (2011) 6024.

[37] A. Moezzi, M. Cortie, A. McDonagh, Aqueous pathways for the formation of zinc oxide nanoparticles, *Dalton Trans*. **40** (2011) 4871.

[38] A. P. A. Oliveira, J. F. Hochepied, F. Grillon, M. H. Berger, Controlled Precipitation of Zinc Oxide Particles at Room Temperature, *Chem. Mater*. **15** (2003) 3202.

[39] J. Park, V. Privman, E. Matijević, Model of Formation of Monodispersed Colloids, *J. Phys. Chem. B* **105** (2001) 11630.

[40] M. Bitenc, P. Podbršček, P. Dubček, S. Bernstorff, G. Dražić, B. Orel, Z. C. Orel, The growth mechanism of zinc oxide and hydrozincite: a study using electron microscopies and *in situ* SAXS, *Cryst. Eng. Comm.* **14** (2012) 3080.

Chapter 5:

Controlling Zn Dissolution and ZnO Growth Process

5.1 Introduction

Towards achieving a high energy density and rapid charge discharge rates (*e.g.* for the application in Zn-air battery), the ZnO formation during discharge is inevitable. Therefore, in addition to suppressing the Zn dendrites and mossy structures during charging (Zn electrodeposition), the ZnO formation process needs to be controlled. Many researches in past reported the several controlling methods. Among them, the high solubility of zincate in alkaline solution is often considered as a cause of the shape change of the electrode (dendrite growth and redistribution of active materials) as discussed in the general introduction [1-3]. One of the methods to overcome these issues is to form insoluble discharge products on the surface. In this case, dendritic growth can be mitigated because the reactants are fixed on the surface and the diffusion limited condition is not established during Zn electrodeposition [3, 4]. Also, the redistributions of active materials are unlikely to occur because the accumulation of active materials is caused by variations in ionic concentration in the electrolyte. Therefore, many researchers tried not to form the soluble zincate species but to fix the discharge products (ZnO) on the surface. This was achieved by decreasing the solubility of zincate in the electrolyte by modifying the composition [5], introducing the additive species [6-8], preparing the ionomer with low permeability to zincate species [4].

Although these methods could improve the cyclability of the negative electrode, one of the major drawbacks lies in significant decrease in the discharge capacity [6, 7]. As demonstrated in chapter 4, the continuous discharge reaction becomes impossible after densely covering the electrode surface by ZnO. Thus, the acceleration of ZnO formation induces an earlier passivation and a decrease in the discharge capacity. Additionally, the battery failure (capacity fading and loss of the Coulombic efficiency) occurs even with these controlling methods, and many researchers have not described the exact cause of the failure [7]. Some researchers mentioned that it became difficult to reduce ZnO again to Zn upon charging when well-crystallized ZnO covered the surface because ZnO had an insulating or semiconductive property [9]. It was reported that the overpotential of ZnO for hydrogen evolution reaction (HER) was lower than that of metal Zn, which implied the Coulombic efficiencies might decrease when ZnO itself reacted [10, 11]. Actually, the study by electrochemical impedance spectroscopy (EIS) revealed that the

number of the capacitive semicircles changed from two to one when the electrode was oxidized at much positive potential [12]. At the presence of two semicircles, Zn beneath ZnO was thought to react (Zn was dissolved), but ZnO layer itself might react and oxygen was evolved on it when only one semicircle was observed.

Accordingly, in addition to fixing the discharge products on the surface, they are required to be reversibly reduced to Zn. To achieve this, one of the considerable methods is to suppress the crystal growth of ZnO. For example, sodium dodecyl benzene sulfonate (SDBS) was reported to be adsorb on ZnO surface and suppress the crystal growth of ZnO, which was beneficial for attaining the better cyclability and increase the discharge capacity [13, 14]. Similarly, Li^+ has been known to suppress the crystal growth in hydrothermal synthesis [15-17]. In the battery, Li^+ is sometimes added to the electrolyte, but their effects are discussed mainly with respect to cathodic (MnO_2 or $Ni(OH)_2$) reaction [18-22]. It is assumed that ZnO formation behavior is remarkably influenced by the presence of Li^+ during anodic dissolution of Zn as well. Therefore, in this section, effects of Li^+ on the discharge behavior and resultant influences on the following charging is investigated. Through this analysis, a rational reaction design for charge-discharge reactions is discussed.

5.2 Methodology

The effects of Li^+ addition on the discharge behavior were analyzed by performing Zn dissolution in Li^+ containing solutions. As is the case for metal additives effects investigated in chapter 3, $LiOH \cdot H_2O$ was used as lithium salt in order not to introduce the counter anion in the solution. Li^+ containing solution was prepared by dissolving $LiOH \cdot H_2O$ (reagent grade, Kanto chemical) in pure water, then it was mixed with KOH (UGR grade, Kanto chemical) to yield 1.5 – 5.5 mol dm^{-3} KOH + 0.50 mol dm^{-3} LiOH (0.50 mol dm^{-3} KOH in the solution used in chapter 4 was substituted by LiOH). Finally, 0.050 mol dm^{-3} ZnO (reagent grade, Kanto chemical) was dissolved in this solution. Galvanostatic dissolution was performed at +20 and +40 mA cm^{-2} in the electrochemical cell used in chapter 4. A working electrode was Zn plate or electrodeposited Zn on Cu plate. LSV was measured by sweeping the potential from REST potential to −0.60 V at scan rate at 20 mV s^{-1}. Characterizations on surface

morphologies and crystal structures of the precipitates were carried out as described in chapter 4. *In situ* Raman analysis of Zn electrode was performed in 1.5 mol dm^{-3} KOH + 0.050 mol dm^{-3} zincate + 0.50 mol dm^{-3} LiOH. Discharging and measurement conditions were same as those used in chapter 4.

The amount of the precipitated ZnO was analyzed by ICP-AES (5500x, Agilent). For this analysis, electrodeposited Zn on Cu plate was used for anodic dissolution. The electrode after passivation was dissolved in 5.0 mL nitric acids. Then, this solution was diluted to 100 mL, and used as an analyte for ICP-AES analysis. By measuring total amount of Zn species on the electrode, precipitated ZnO amount was evaluated by the following equation.

$$\begin{aligned}&\text{Amount of precipitated ZnO (C cm}^{-2}\text{)}\\&= \text{Total Zn Amount (measured value)} - \text{Theoretically remained amount}\\&\qquad\qquad (40\ \text{C cm}^{-2} - 0.020\ t\ \text{C cm}^{-2})\end{aligned} \tag{5.1}$$

When only dissolution reaction was considered, $40 - 0.020\ t$ C cm^{-2} of metal Zn remained on the electrode since $0.020\ t$ C cm^{-2} of Zn was dissolved as zincate. A difference between this value and the measured value corresponded to the amount of the precipitates.

In order to analyze the influence of the precipitated ZnO on the following charging behavior, morphological changes upon discharge to charge was analyzed by the *in situ* optical microscope observation as carried out in chapter 2; discharge of Zn was performed by using Zn wire (500 μmϕ) embedded in an epoxy resin. Zn wire was used as a counter and a quasi-reference electrode. The working electrode was horizontally upward faced to counter electrode by using the electrochemical cell shown in Fig. 2.3. Discharge was performed at +80 mA cm^{-2} until reaching the potential to +300 mV vs. Zn and charge was performed at −90 mA cm^{-2} for 2000 s.

5.3 Results and Discussion

5.3.1 Effects of Li^+ on Zn dissolution and ZnO growth

Changes in the polarization behavior of Zn and morphologies of ZnO

LSV of Zn plate was measured in 1.5 mol dm^{-3} KOH + 0.050 mol dm^{-3} zincate + 0.50 mol dm^{-3} LiOH and 2.0 mol dm^{-3} KOH + 0.050 mol dm^{-3} zincate. Figure 5.1 shows the profile at scan rate of 20 mV s^{-1}.

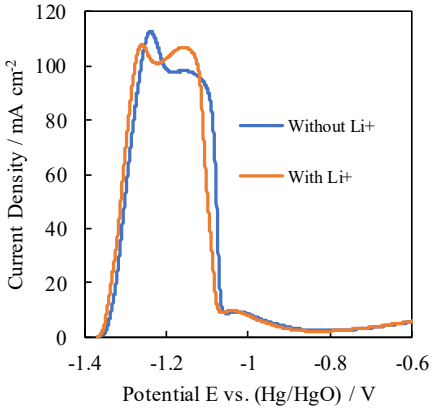

Fig. 5.1 LSV of Zn in 2.0 mol dm^{-3} KOH + 0.050 mol dm^{-3} zincate (blue line) and 1.5 mol dm^{-3} KOH + 0.050 mol dm^{-3} zincate + 0.50 mol dm^{-3} LiOH (orange line) at scan rate of 20 mV s^{-1}.

By sweeping the potential to positive value, there are two anodic peaks before dropping the current. These two peaks originate from the different coordination numbers of OH^- to Zn^{2+} ion; a negative peak corresponds to $Zn(OH)_4^{2-}$ and a latter peak is assigned to the $Zn(OH)_3^-$ formation [11, 23]. The formation of $Zn(OH)_3^-$ starts when sufficient OH^- is not available by increasing the Zn^{2+} concentrations. After these peaks, a current dropped by passivation of the electrode due to the ZnO formation. By adding Li^+, there are three notable differences in the polarization behavior. First, the current at active dissolution region (−1.4 V - −1.25 V) is increased by adding Li^+. For example, the current density at −1.3 V was 54 mA cm^{-2} in the solution without Li^+, but it increases to 71 mA cm^{-2} by adding Li^+. Secondly, the current at two peaks are changed. The peak currents in the solution without Li^+ are 113 and 98 mA cm^{-2}, while they are 108 and 107 mA cm^{-2} in the Li^+ containing solution. This means the formation of $Zn(OH)_4^{2-}$ is suppressed by the presence of Li^+, and $Zn(OH)_3^-$ is instead formed. Also, passivation occurs at more positive potential than in the solution without Li^+. These two differences originate from the decreased OH^- activity by Li^+. In previous studies, it was reported that the activity

coefficient of OH^- became small in the LiOH solution compared to KOH or NaOH solutions due to the largest charge density (smallest cation size) of Li^+ among alkali cations [24, 25]. Thus, the formation of $Zn(OH)_4^{2-}$ is suppressed and the ZnO formation is promoted by depletion of OH^-.

Galvanostatic dissolution of Zn plate was performed in 1.5 or 5.5 mol dm^{-3} KOH + 0.050 mol dm^{-3} zincate + 0.50 mol dm^{-3} LiOH at +20 mA cm^{-2}. Fig. 5.2 shows the potential changes during the discharge.

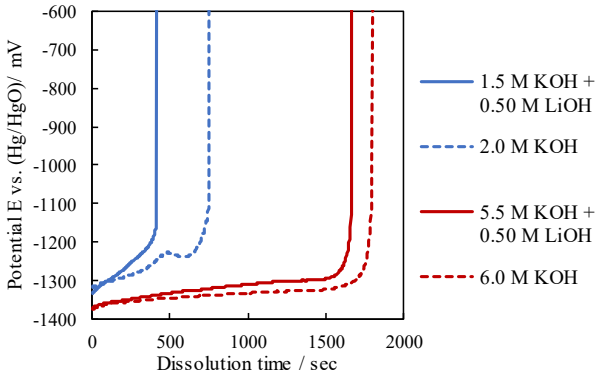

Fig. 5.2 Potential profiles during anodic dissolution of Zn in 1.5 mol dm^{-3} KOH (blue solid line) and 5.5 mol dm^{-3} KOH + 0.050 mol dm^{-3} zincate + 0.50 mol dm^{-3} LiOH at +20 mA cm^{-2}. Dashed line is the profile in the solution without Li^+ at relevant OH^- concentration shown in Fig. 4.2.

As is the case for LSV measurements, passivation occurs earlier by Li^+ than in the solution without Li^+ because of the decreased OH^- activity. However, the potential difference at initial stages of dissolution is small. In the case of 2.0 mol dm^{-3} OH^- solution, more negative potential is observed in Li^+ containing solution. This is in accordance with LSV results at active dissolution region; although concentration overpotential for OH^- is larger in the Li^+ containing solution, dissolution reaction itself is promoted by Li^+ at initial stages of dissolution. This trend is confirmed by the potentiostatic dissolution, too. Fig. 5.3 shows current profile during the potentiostatic dissolution at −1.3 V.

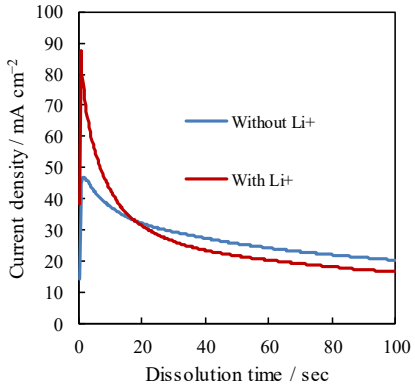

Fig. 5.3 Current profile during potentiostatic dissolution at −1.3 V.

At initial stages of dissolution, the profile in the Li^+ containing solution exhibits higher current density than that in the absence of Li^+. Thus, the active dissolution reaction of Zn is enhanced by the presence of Li^+. After the dissolution proceeds, the current becomes lower than that in the solution without Li^+. This decay may be caused by more pronounced decrease of OH^- by the presence of Li^+.

Figure 5.4 shows SEM images after passivation of Zn electrode in 1.5 mol dm^{-3} KOH and 5.5 mol dm^{-3} KOH + 0.050 mol dm^{-3} zincate + 0.50 mol dm^{-3} LiOH.

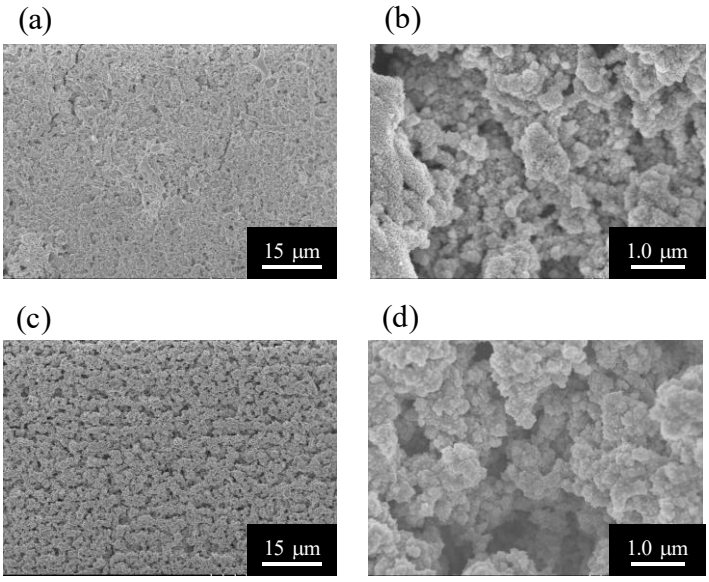

Fig 5.4 SEM images of Zn electrode after discharge at +20 mA cm^{-2} in (a), (c) 1.5 and (b), (d) 5.5 mol dm^{-3} KOH + 0.050 mol dm^{-3} zincate + 0.50 mol dm^{-3} LiOH solutions. (b) and (d) are higher magnification images of (a) and (c), respectively.

As is the case for the passivated film in the solution without Li^+, the cluster-like structures are formed by discharge. However, the acicular shapes crystals are no longer observed, and particulate particles are formed. XRD patterns at each condition are shown in Fig. 5.5.

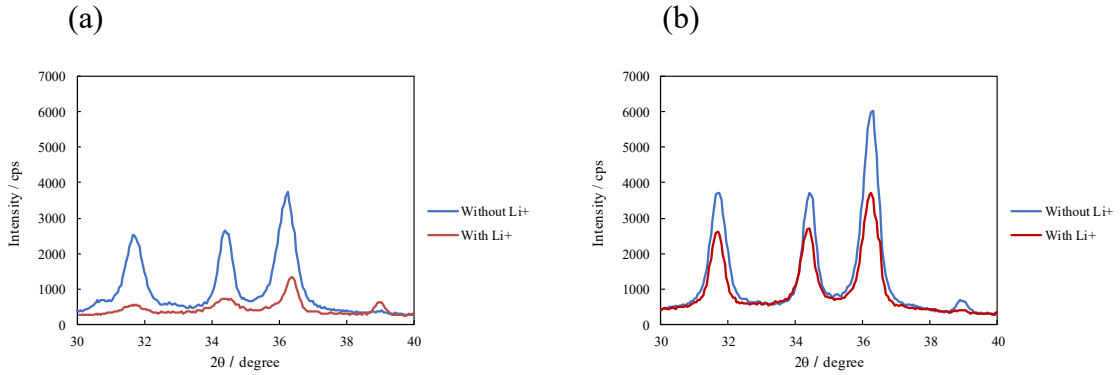

Fig 5.5 XRD patterns of the electrode after passivation in (a) 2.0 mol dm^{-3}, (b) 6.0 mol dm^{-3} OH^- solutions at +20 mA cm^{-2}; blue line shows the profile in the solution without Li^+ and red line shows those at the presence of Li^+.

At the presence of Li^+, the peak intensities of ZnO decrease. These results indicate that the crystal growth of ZnO is suppressed by the presence of Li^+. This suggests that the elementary steps for ZnO formation was changed by addition of Li^+ as previously suggested in the chemical synthesis technique [15, 16]; the zincate incorporation and decomposition at the surface of ZnO are suppressed, and nucleation (dehydration reactions between zincate species) are favored. Such a change was thought to be caused by Li^+ adsorption on the ZnO nuclei or incorporation of Li^+ in the Zn sites inside the ZnO lattice, which retarded the incorporation of negatively charged zincate intake at the surface. Such a Li^+ involvement in the ZnO formation process is further discussed from ICP-AES and *in situ* Raman analysis.

In addition to the changes in the ZnO crystal growth behavior, Zn dissolution behavior before forming ZnO is expected to be influenced by Li^+ addition as inferred in the polarization behavior and current profile during the potentiostatic measurement. To examine such a difference in a dissolution behavior, dissolution was stopped at 300 s before the ZnO formation in 2.0 mol dm^{-3} KOH + 0.050 mol dm^{-3} zincate and 1.5 mol dm^{-3} KOH + 0.050 mol dm^{-3} zincate + 0.50 mol dm^{-3} LiOH, and surface morphologies were analyzed by SEM. For this analysis, electrodeposited Zn was used as a working electrode to clarify the morphological changes from the layer-like structures.

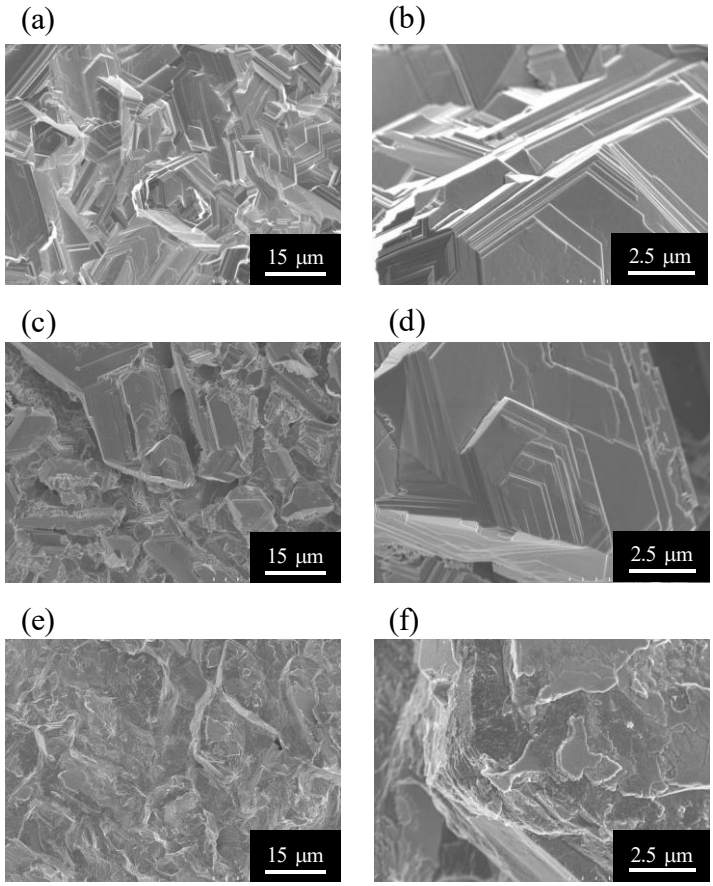

Fig. 5.6 SEM images of Zn electrodeposits after dissolution of (a), (b) 0 s (after electrodeposition), (c), (d) 300 s in the solution without Li^+, and (e), (f) 300 s in the solution with Li^+. (b), (d), and (f) are higher magnification images than (a), (c), and (e).

When dissolution is carried out without Li^+, microsteps are maintained even after dissolution. This suggests that dissolution proceeds in a step-flow manner. In contrast, well-defined microsteps are not observed at the presence of Li^+. which suggests that an entire Zn surface contributes to the dissolution reaction regardless of its microstructures. Changes in such a dissolution behavior has been often observed by the presence of specifically adsorbed anion and potential changes [26, 27]. Cations might also affect such a behavior by two possible ways. First, cation species forms an alloy with surface elements and modifying the surface properties (*e.g.* surface energy) [28]. Second, the stability of the reaction intermediates like $ZnOH_{ad}$ is influenced by cations in the outer Helmholtz plane, which promotes or suppresses the dissolution reaction. For example, the surface roughening during Pt oxidation is suppressed by the presence of Li^+ due to significant interactions of Li^+ with $PtOH_{ad}$ [29]. Latter explanation seems reasonable

because the surface alloying is unlikely due to much negative deposition potential of Li^+ than that of Zn. Since Li^+ has the largest charge density among alkali cations, Coulombic interactions between Li^+ and the surface is larger than that between K^+ and the surface.

RMS roughness of each electrode was evaluated by a laser scanning confocal microscope. After electrodeposition the roughness value is 3.1 μm. After anodic dissolution, this value increases to 6.0 μm at the absence of Li^+, and 4.2 μm at the presence of Li^+. In the case of solution without Li^+, relatively large Zn structures remains on the electrode surface after dissolution due to the dissolution like step-flow manner. On the other hand, less increase is observed in the case of Li^+ containing solution due to reactions from entire Zn surface. This effect may be beneficial for Zn negative electrode because the influence of Zn microstructures formed during charging (*i.e.* dendrites) can be mitigated by the presence of Li^+ upon discharging. It was previously reported that better cyclability of the negative electrode is attained by eliminating Zn dendrites upon discharging [3]. Actually, dissolution in the solution without Li^+ yields some protrusions on the surface, which are potentially initiation sites for Zn mossy structures in the following charging.

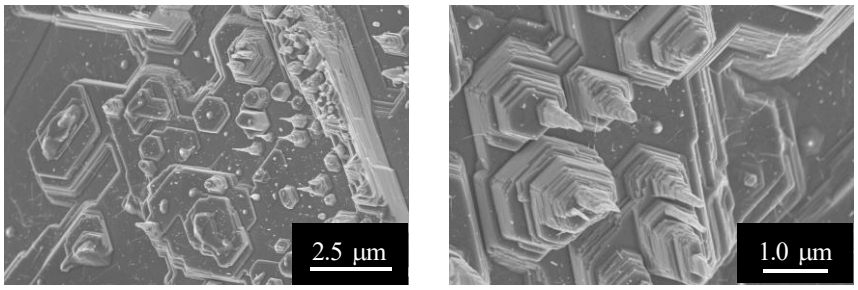

Fig. 5.7 Protrusion structures formed after dissolution in the solution without Li^+.

Analysis on precipitated amount of ZnO during discharge

In order to quantify the amount of the precipitated ZnO in the solution with and without Li^+, electrodeposited Zn was dissolved. Residual amount of Zn was measured by ICP-AES. From the procedure shown in the experimental section, the precipitated amount of ZnO was calculated. Fig. 5.8 shows SEM images of Zn electrodes after several dissolution times.

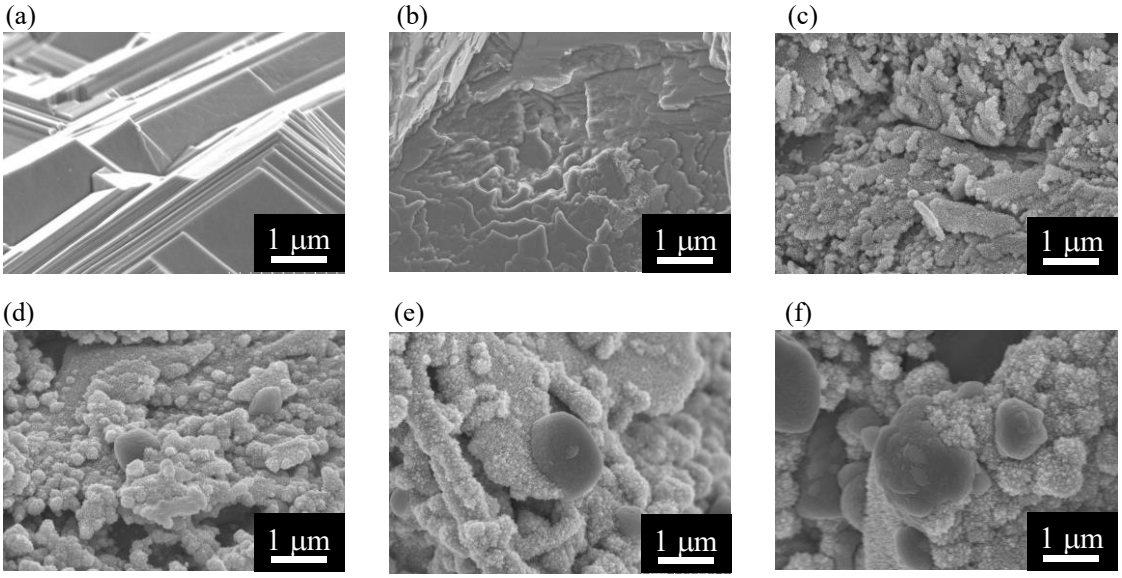

Fig. 5.8 Morphological variations during dissolution of electrodeposited Zn in 1.5 mol dm^{-3} KOH + 0.050 mol dm^{-3} zincate + 0.50 mol dm^{-3} LiOH at (a) 0 s (after electrodeposition), (b) 300 s, (c) 400 s, (d) 500 s, (e) 600 s, and (f) passivation.

The precipitated amount from 400 s until passivation calculated from the results of ICP-AES is plotted in Fig. 5.9.

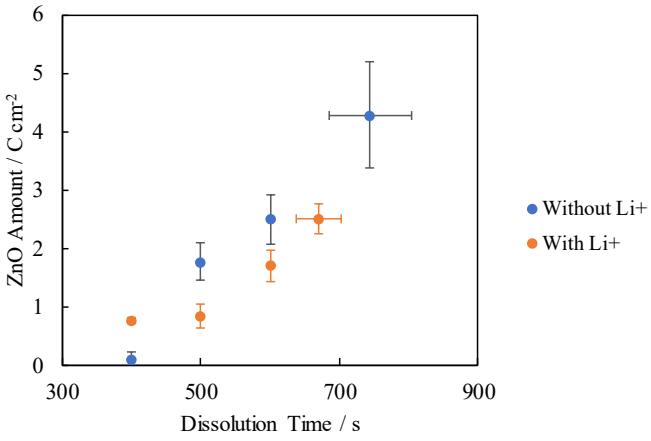

Fig. 5.9 Precipitated amount of ZnO in 2.0 mol dm^{-3} KOH + 0.050 mol dm^{-3} zincate and 1.5 mol dm^{-3} KOH + 0.050 mol dm^{-3} zincate + 0.50 mol dm^{-3} LiOH.

At initial stages of dissolution, the amount of ZnO is larger in Li^+ containing solution than in the solution without Li^+. This implies that onset of the ZnO precipitation becomes earlier by Li^+ addition due to lower OH^- activity, which induces a faster

nucleation. However, after 500 s, the amount rapidly increases in the solution without Li^+. Once ZnO is nucleated, it rapidly grows by an incorporation of zincate species to the nucleus. At the presence of Li^+, this process is retarded, and the precipitated amount decreases from 500 s. Eventually, the precipitated amount is lower in passivation condition at the presence of Li^+. This means the suppression on the crystal growth results in small number of the precipitated nuclei due to an insufficient increase in the cluster size for the precipitation. Cross-sectional SEM images shown in Fig. 5.10 also confirms the same trend; thickness of ZnO layer on electrodeposited Zn surface is thinner in the solution with Li^+ than at the absence of Li^+. In principle, such a retarded ZnO growth may be beneficial for improving the discharge capacity (extending passivation time), too [13, 14]. However, this is not the case for current study as shown in Fig. 5.2. This reason may be decreased OH^- activity surpasses the effect of compact ZnO formation; since passivation itself occurs by the depletion of OH^- at the surface (beneath ZnO layer), the decreased OH^- activity shortens the passivation time [30]. Extending discharge time may be possible through optimizing the Li^+ concentration in the solution as demonstrated in previous study [20].

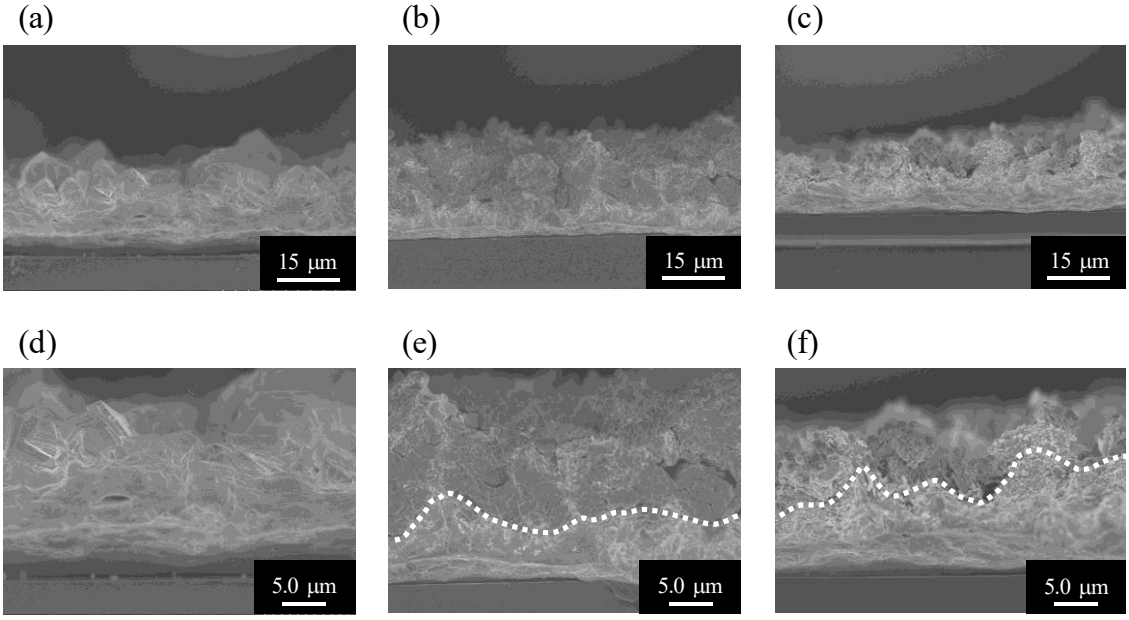

Fig. 5.10 Cross-sectional images of Zn electrode; (a), (d) before dissolution, (b), (e) passivation in the solution without Li^+, and (c), (f) passivation in the solution with Li^+. White dashed line denotes the interface between precipitated ZnO and underlying Zn.

Also, to confirm Li^+ adsorption or intake on ZnO, the emission intensity of 670.8 nm corresponding to Li was analyzed for various samples. The results are described in Table

5.1.

Table 5.1 Emission at 670.8 nm at various dissolution condition. Averaged value from 5 different measurements ± standard deviation.

	Emission at 670.8 nm / cps
(a) Passivation (without Li^+)	4083±53
(b) Passivation (with Li^+)	4683±28
(c) After 300 s (with Li^+)	3688±97
(d) After 300 s +300 s REST (with Li^+)	3732±84

Compared to the passivation film in the solution without Li^+ (condition (a) in the table), the intensity reasonably increases only in the case of passivation in Li^+ containing solution, (b). When dissolution is stopped before forming ZnO (c), the intensity decreases compared to that observed in condition (a). Same trend was observed even after holding an electrode in the Li^+ containing solution for another 300 s, (d). These results show interactions of Li^+ with ZnO (adsorption on ZnO surface or incorporation into the ZnO lattice) is more significant than that with Zn. A decrease in intensity in (c), (d) may originate from differences in the background intensity due to decreased Zn concentration by lack of ZnO layer. This result demonstrates that the interaction of ZnO with Li^+ is considerable, but it is still difficult to distinguish the adsorption and incorporation into the lattice due to very low detected amount (corresponding to less than 0.01 at% compared to the total amount of Zn and Li).

5.3.2 *In situ* Raman analysis of Zn electrodes in the solution containing Li^+

In order to further discuss the changes in nucleation & growth behavior of ZnO during discharging, *in situ* Raman analysis was performed as carried out in chapter 4. Fig. 5.11 shows the spectra in 1.5 mol dm^{-3} KOH + 0.050 mol dm^{-3} zincate + 0.50 mol dm^{-3} LiOH.

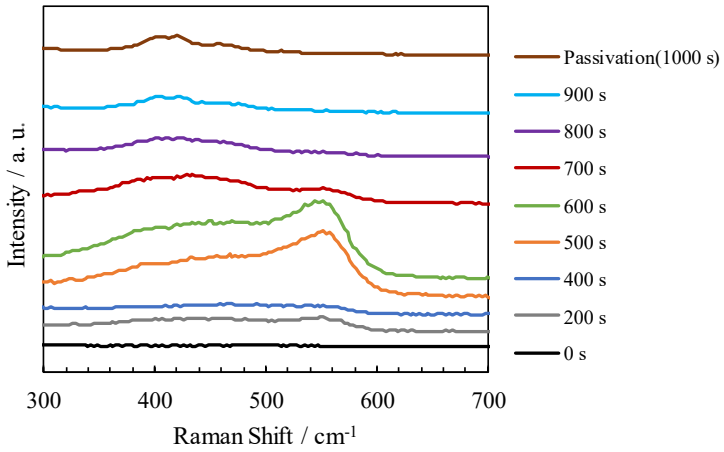

Fig. 5.11 *In situ* Raman spectra of Zn electrode in 1.5 mol dm^{-3} KOH + 0.050 mol dm^{-3} zincate + 0.50 mol dm^{-3} LiOH. Dissolution current is +100 mA cm^{-2} and diameter of the electrode is 500 μmϕ (corresponding to diameter of zinc wire).

A peak intensity of the E_2 mode corresponding to the crystalline wurtzite ZnO is weak even at passivation condition at the presence of Li^+. Also, the peak position is shifted to the lower wavenumber. Such a peak shift may occur when the lattice is distorted by incorporated Li^+. A dominant peak during dissolution is the E_1 (LO) mode. There are two possible reasons for the appearance of this peak. First, the E_1 (LO) mode may be induced by the incorporated Li^+ inside the lattice [31, 32]. However, the amount of Li^+ in the precipitates are much less than that in previous studies to explain the evolution of the E_1 (LO) mode. Another explanation is that excess Zn is formed by different nucleation & growth behavior of ZnO in the Li^+ containing solution. As discussed in chapter 4, this peak corresponds to excess Zn in interstitial sites of ZnO crystals. Also, there are qualitative correlations between the formation of Zn excess and the conditions favoring nucleation (dehydration reactions between zincate species). Therefore, suppressed E_2 mode as well as an appearance of E_1 (LO) mode are in accordance with the suppression in the crystal growth of ZnO inferred from SEM and XRD results.

In short, the Raman analysis shows the structural difference by the presence of Li^+ as follows. First, a peak shift in E_2 mode implies the distortion in the lattice possibly

due to an incorporation of Li^+ in the lattice. Second, the evolution of E_1 (LO) mode suggests the preferential nucleation than the growth by Li^+. This may be caused by the retarded zincate intake to the ZnO surface by Li^+ adsorption on the surface or incorporation into the lattice [15, 16].

5.3.3 Charging behavior after the formation of ZnO

As discussed above, Li^+ exhibited the suppression effects on the crystal growth of ZnO. One of the important issues in Zn negative electrode is maintaining the cyclability even after forming ZnO. In other words, precipitated ZnO should be reversibly reduced to metal Zn upon charging. In order to analyze how variations in the ZnO formation behaviors affect following charging behavior, morphological variations upon successive discharging to charging were analyzed in 4.0 mol dm^{-3} KOH + 0.25 mol dm^{-3} zincate and 3.5 mol dm^{-3} KOH + 0.25 mol dm^{-3} zincate + 0.50 mol dm^{-3} LiOH. Figs. 5.12 and 5.13 show the potential profiles during discharge at first step and charging in second step, respectively.

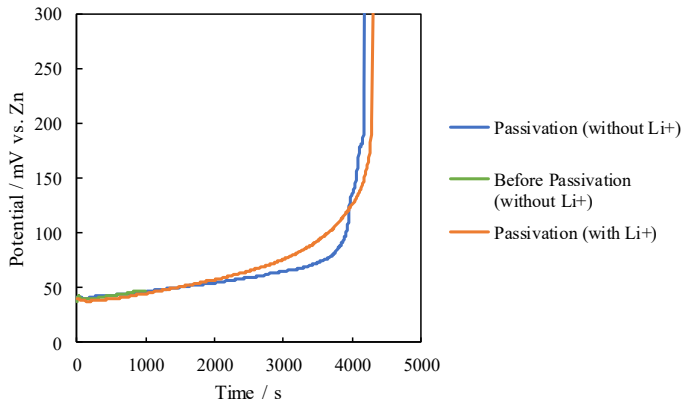

Fig. 5.12 Potential profile during discharging of Zn electrode (500 μmϕ embedded in epoxy resin). Current density is +80 mA cm^{-2} in the solution without Li^+ until passivation (blue line), for 1000 s (green line), and with Li^+ until passivation (orange line).

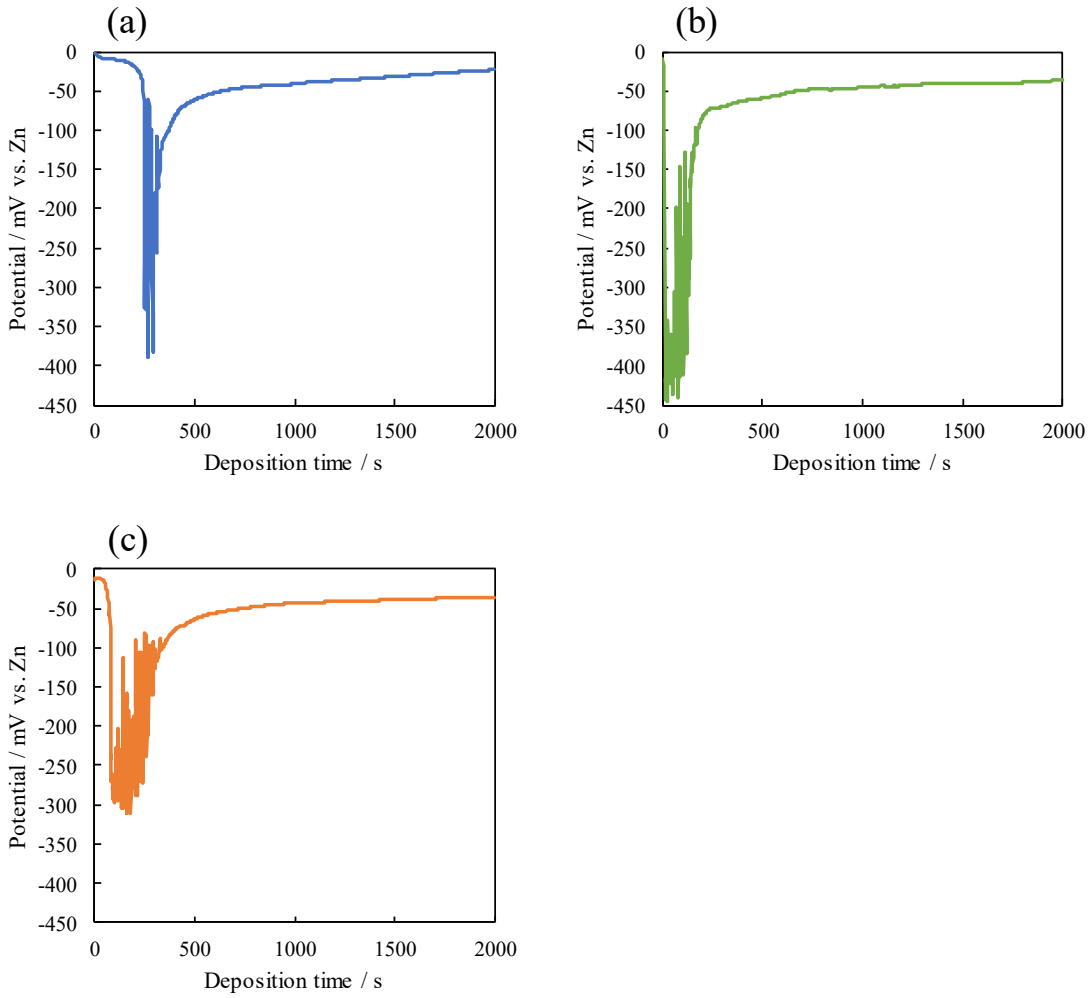

Fig. 5.13 Potential profile during charging of Zn electrode after performing discharge. Current density was −90 mA cm^{-2}. Deposition was performed after dissolution (a) without Li^+ until passivation, (b) without Li^+ for 1000 s, and (c) with Li^+ until passivation.

Morphological evolution during discharging and charging were *in situ* analyzed by an optical microscope. Fig. 5.14 represents the images in the solution without Li^+, and dissolution was performed until passivation. Fig. 5.15 shows the results obtained in same solution, but dissolution was stopped at 1000 s. In Fig. 5.16, the results of discharging in the Li^+ containing solution until passivation are shown.

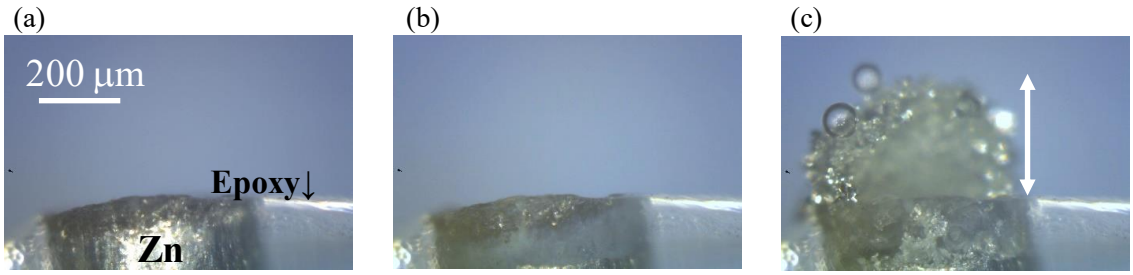

Fig. 5.14 CCD images of Zn electrode during discharging and charging in 4.0 mol dm^{-3} KOH + 0.25 mol dm^{-3} zincate. Discharge was performed until passivation. Images are taken at (a) 2100 s after discharge, (b) passivation (discharge for 4200 s) and (c) 500 s after starting the charge.

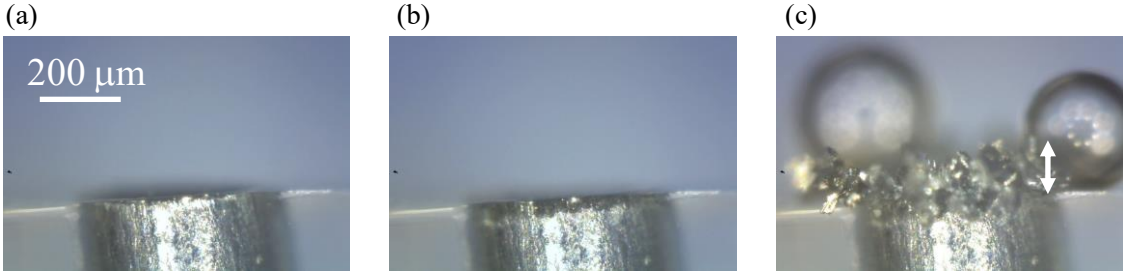

Fig. 5.15 CCD images of Zn electrode during discharging and charging in 4.0 mol dm^{-3} KOH + 0.25 mol dm^{-3} zincate. Discharge was performed for 1000 s. Images are taken at (a) 500 s after discharge, (b) 1000 s after discharge and (c) 500 s after starting the charge.

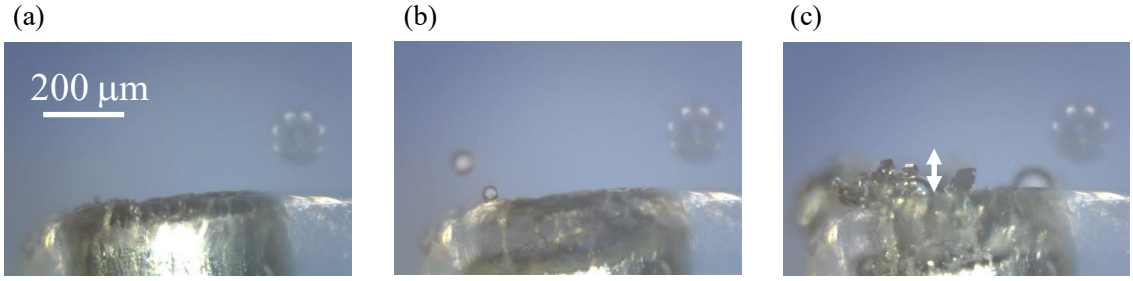

Fig. 5.16 CCD images of Zn electrode during discharging and charging in 3.5 mol dm^{-3} KOH + 0.25 mol dm^{-3} zincate + 0.50 mol dm^{-3} LiOH. Discharge was performed until passivation. Images are taken at (a) 2100 s after discharge, (b) passivation (discharge for 4300 s) and (c) 500 s after starting the charge.

In each charging condition, dendritic deposition is inferred from the oscillation of the potential profiles; dendritic growth is known to occur in a periodic manner possibly due

to Zn deposition and HER (When zincate ions is depleted by Zn electrodeposition, potential is shifted to HER, zincate concentration is recovered during this period.) [33]. At initial stages of deposition, there is a plateau region in the potential before potential drop (until 250 s in Fig. 5.13 (a) and until 80 s in Fig. 5.13 (b)). This behavior was ascribed to "Sand" behavior. After starting the electrodeposition, the concentration of zincate ions at the surface starts to decrease, when it goes down to zero, potential rapidly increases to the value corresponding to HER. Since this time is indicator for the onset of dendritic growth, it is expected that dendrite formation is delayed in passivated condition in the solution without Li^+ [34]. This may be caused by an increase in the surface area during dissolution; since the surface roughness tends to increase in the solution without Li^+ compared to the Li^+ containing solution, substantial current density is possibly decreased in this condition. This results in longer Sand time. After forming dendrites at the negative potential, surface roughness is further increased. This results in decrease in the local current density, which is reflected in the positive shift and stable potential value at the later stages of deposition. In addition to longer Sand time, the duration of the potential oscillation is shorter during the deposition after passivation in the solution without Li^+ than in the solution with Li^+. This also suggests dendritic growth is relatively suppressed in this condition.

From CCD images, however, very rough deposits evolve in Fig. 5.14 despite dendritic growth is expected to be suppressed in this condition. The length of the white arrows shown in each figure is 300, 130 and 110 μm, respectively. From CCD images immediately after starting the charge, this rough deposit evolves not by deposition on Zn surface but by the protuberance of the residual Zn after dissolution. It is notable that black parts remain after dissolution inside the epoxy resin at passivation condition in Fig. 5.14 (b), while transparent parts are seen in the Li^+ containing solution in Fig. 5.16 (b). Thus, non-uniform dissolution in the solution without Li^+ may result in the evolution of rough deposits upon following charge. A rapid recovery of deposition potential to positive value may originate from sudden increase in the surface area by this morphological change. Li^+ is effective to suppress such an irregular evolution of Zn deposits by uniformly dissolving Zn upon discharge as discussed in Fig. 5.6.

In order to further discuss microstructures and crystal structures during these morphological changes, successive discharge and charge were performed for a larger sized electrode in an electrode configuration shown in Fig. 4.1. Photographs taken by digital camera after charging and SEM images are shown in Fig. 5.17.

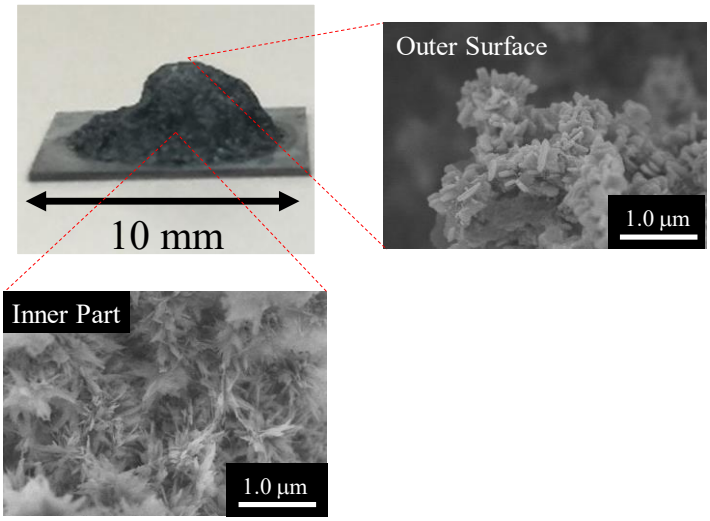

Fig. 5.17 Photographs of the rough deposits formed after charging and SEM images

Although it is difficult to distinguish Zn and ZnO from SEM images, acicular crystals are observed inside the rough deposits, which is similar to the structures observed after passivation. XRD patterns of this sample and the deposits formed after switching the potential before passivation are shown in Fig. 5.18.

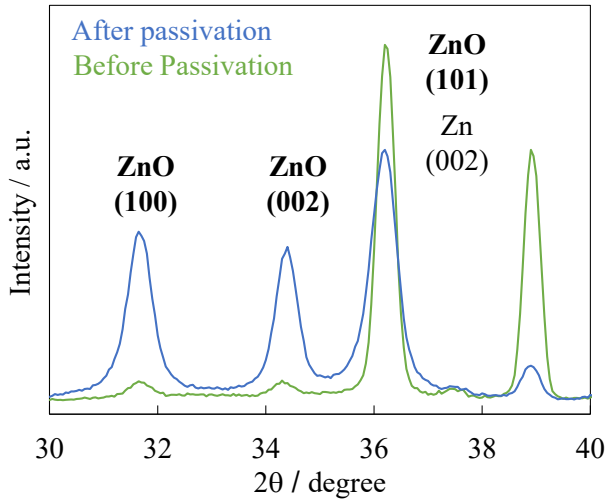

Fig. 5.18 XRD patterns of Zn deposits after charging. Prior to charging, discharge is performed at +20 mA cm^{-2} until passivation (blue line) and for 1100 s (green line).

When the potential was changed after passivation, intense ZnO peaks remains even after charging. This analysis indicates that ZnO formed during discharge is not fully reduced

upon following charging, and which induces a protuberance of residual Zn. Thus, in addition to a uniform dissolution of Zn by the presence of Li^+, the suppression on the protuberance of the rough Zn deposits can be ascribed to suppressed crystal growth of ZnO in Li^+ containing solution or shorter dissolution time.

Conclusion

As a controlling method for discharge behavior of Zn negative electrode, the effects of Li^+ addition on the discharge of Zn negative electrode were investigated. Li^+ had the effects both on dissolution of Zn and ZnO precipitation. During an anodic dissolution, Li^+ promoted the reaction by dissolving Zn regardless of the underlying microstructures; step-flow dissolution was changed to dissolution from an entire surface. This was beneficial for suppressing the surface roughening during discharging. When ZnO was precipitated in the solution with Li^+, the crystal growth of ZnO was suppressed. This was thought to be caused by alterations to the elementary steps for the ZnO formation by Li^+ incorporation into the ZnO lattice; an incorporation and a decomposition of zincate at ZnO surface was suppressed. Instead, ZnO was formed mainly by dehydration reactions between zincate species. Corresponding change in the crystal structure was revealed by *in situ* Raman analysis; excess Zn was formed during discharge in the Li^+ containing solution. Furthermore, by monitoring the morphological changes upon discharge to charge, these changes were beneficial for suppressing the protuberance of rough deposits during charging. This was ascribed to the uniform Zn dissolution and the suppressed ZnO growth during the discharge by Li^+. Thus, to maintain the electrode cyclability, it was important to eliminate the Zn microstructures by dissolution and mitigate the crystal growth of ZnO.

Reference

[1] R. E. F. Einerhand, W. Vsscher, Zinc Electrode Shape Change, I. In Situ Monitoring, *J. Electrochem. Soc*. **138** (1991) 1.

[2] R. E. F. Einerhand, W. Vsscher, Zinc Electrode Shape Change, II. Process and Mechanism, *J. Electrochem. Soc.* **138** (1991) 7.

[3] A. Nakata, H. Murayama, K. Fukuda, T. Yamane, H. Arai, T. Hirai, Y. Uchimoto, J. Yamaki, Z. Ogumi, Transformation of Leaf-like Zinc Dendrite in Oxidation and Reduction Cycle, *Electrochim. Acta* **166** (2015) 82.

[4] K. Miyazaki, 3. Zn-Air secondary batteries, *Electrochemistry* **82** (2014) 181.

[5] T. C. Adler, F. R. McLarnon, E. J. Cairns, Low-Zinc-Solubility Electrolytes for Use in Zinc/Nickel Oxide Cells, *J. Electrochem. Soc*. **140** (1993) 289.

[6] X-M. Zhu, H-X. Yang, X-P. Ai, J-X. Yu, Y -L. Cao, Structural and electrochemical characterization of mechanochemically synthesized calcium zincate as rechargeable anodic materials, *J. Appl. Electrochem.* **33** (2003) 607.

[7] A. Nakata, H. Arai, T. Yamane, T. Hirai, Z. Ogumi, Preserving Zinc Electrode Morphology in Aqueous Alkaline Electrolytes Mixed with Highly Concentrated Organic Solvent, *J. Electrochem. Soc.* **163** (2016) A50.

[8] D. Schröder, N. N. S. Borker, M. König, U. Krewer, Performance of zinc air batteries with added K_2CO_3 in the alkaline electrolyte, *J. Appl. Electrochem*. **42** (2015) 427.

[9] H. -I. Kim, E. -J. Kim, S. -J. Kim, H. -C. Shin, Influence of ZnO precipitation on the cycling stability of rechargeable Zn-air batteries, *J. Appl. Electrochem.* **45** (2015) 335-342.

[10] I. Sanghi, M. Fleishcmann, Some potentiostatic studies on zinc, *Electrochim. Acta* **1** (1959) 161.

[11] M. Bockelmann, L. Reining, U. Kunz, T. Turek, Electrochemical characterization and mathematical modeling of zinc passivation in alkaline solutions; A review, *Electrochim. Acta* **237** (2017) 276.

[12] M. Cai, S. -M. Park, Oxidation of zinc in alkaline solutions studied by electrochemical impedance spectroscopy, *J. Electrochem. Soc*. **143** (1996) 3895.

[13] H. Yang, Y. Cao, X. Ai, L. Xiao, Improved discharge capacity and suppressed surface passivation of zinc anode in dilute alkaline solution using surfactant additives, *J. Power Sources* **128** (2004) 97.

[14] R. K. Ghavami, Z. Rafiei, Performance improvements of alkaline batteries by studying the effects of different kinds of surfactant and different derivatives of benzene on the electrochemical properties of electrolytic zinc, *J. Power. Sources* **162** (2006) 893.

[15] N. Uekawa, R. Yamashita, Y. J. Wu, K. Kakegawa, Effect of alkali metal hydroxide on formation processes of zinc oxide crystallites from aqueous solutions containing $Zn(OH)_4^{2-}$ ions, *Phys. Chem. Chem. Phys*. **6** (2004) 442.

[16] L. N. Dem'yanets, D. V. Kostomarov, I. P. Kuz'mina, Chemistry and Kinetics of ZnO Growth from Alkaline Hydrothermal Solutions, *Inorg. Mater.* **38** (2002) 124.

[17] C. D. Chouvy, J. Vedel, Supersaturated zincate solutions: A study of the decomposition kinetics, *J. Electrochem. Soc.* **138** (1991) 2538.

[18] F. R. McLarnon, E. J. Cairns, The Secondary Alkaline Zinc Electrode, *J. Electrochem. Soc.* **138** (1991) 645.

[19] J. F. Parker, I. R. Pala, C. N. Chervin, J. W. Long, D. R. Rolison, Minimizing Shape Change at Zn Spongy Anodes in Rechargeable Ni-Zn Cells: Impact of Electrolyte Formulation, *J. Electrochem. Soc.* **163** (2016) A351.

[20] A. Marshall, N. A. Hampson, The discharge behavior of the zinc/air slurry cell, *Electroanal. Chem. Interfacial. Electrochem.* **59** (1975) 33.

[21] P. C. Foller, Effects of additives on the suspension of products of discharge of zinc in alkaline solution, *J. Appl. Electrochem.* **17** (1987) 1296.

[22] K. Bass, P. J. Mitchell, G. D. Wilcox, Methods for the reduction of shape change and dendritic growth in zinc-based secondary cells, *J. Power Sources* **35** (1991) 333.

[23] T. P. Dirkse, N. A. Hampson, The anodic behavior of zinc in aqueous KOH solution II. Passivation experiments using linear sweep voltammetry, *Electrochim. Acta* **17** (1972) 387.

[24] H. Corti, R. Crovetto, R. F. Prini, Aqueous solutions of lithium hydroxide at various temperatures: Conductivity and activity coefficients, *J. Solution Chem*. **8** (1979) 897.

[25] R. A. Noulty, D. G. Leaist, Activity coefficients and diffusion coefficients of dilute aqueous solutions of lithium, sodium, and potassium hydroxides, *J. Solution Chem*. **13** (1984) 767.

[26] O. M. Magnussen, M. R. Vogt, J. Scherer, R. J. Behm, Double-layer structure, corrosion and corrosion inhibition of copper in aqueous solution, *Appl. Phys. A* **66** (1998) S447.

[27] O. M. Magnussen, Ordered anion adlayer on metal electrode surfaces, *Chem. Rev.* **102** (2002) 679.

[28] M. R. Vogt, A. Lachwnwitzer, O. M. Magnussen, R. J. Behm, In-situ STM study of the initial stages of corrosion of Cu(100) electrodes in sulfuric and hydrochloric acid solution, *Surf. Sci.* **399** (1998) 46.

[29] M. Nakamura, Y. Nakajima, N. Hoshi, H. Tajiri, O. Sakata, Effect of non-specifically adsorbed ions on the surface oxidation of Pt (111), *Chem. Phys. Chem.* **14** (2013) 2426.

[30] M. B. Liu, G. M. Cook, N. P. Yao, Passivation of Zinc Anodes in KOH Electrolytes, *J. Electrochem Soc*. **128** (1981) 1663.

[31] Y. L. Du, Y. Deng, M. S. Zhang, Investigation of Li-induced structural disorder and phase transition in ZnO by Raman spectroscopy, *Solid State Commun*. **137** (2006) 78.

[32] M. Jiang, L. L. Liu, Z. Wang, Z. Q. Chen, Microstructure of ZnO-Li_2CO_3 compound studied by positron annihilation spectroscopy, *Phys. Status Solidi A* **211** (2014) 206.

[33] K. Fukami, S. Nakanishi, T. Tada, H. Yamasaki, S. Sakai, S. Fukushima, Y. Nakato, Self-Organized Periodic Growth of Stacked Hexeagonal Wafers in Synchronization with a Potential Oscillation in Zinc Electrodeposition, *J. Electrochem. Soc.* **152** (2004) C493.

[34] P. Bai, J. Li, F. R. Brushett, M. Z. Bazant, Transition of lithium growth mechanism in liquid electrolytes, *Energy Environ. Sci.* **9** (2016) 3221.

Chapter 6:

General Conclusion

The introduction of renewable energy to power distribution system motivates many researchers to develop rechargeable Zn batteries these days. However, despite long history from 19th century and successful commercialization in the primary batteries, the application of Zn negative electrodes in secondary batteries are still challenging in 21st century. Main reason lies in morphological changes of Zn negative electrodes; deposition of irregular shaped Zn electrodeposits and passivation of electrode by ZnO formation during discharge. Although there are knowledge accumulations about electrochemistry of Zn negative electrodes, fundamental principles for achieving the rechargeable Zn negative electrode are still missing. Many researches have reported several controlling methods for improving the cyclability of the electrode, but they were often trial-and-error approaches. This is caused by insufficient understandings on interfacial phenomena governing morphological variations of Zn negative electrode (*i.e.* electrodeposition of Zn, its anodic dissolution, and ZnO formation via supersaturation), and its connection to the controlling methods. For realizing the rechargeable Zn batteries, the guiding principle for controlling Zn electrode reactions is indispensable. The objective of this thesis is to establish such a principle based on profound understandings on Zn electrodes reactions.

In this chapter, major results obtained in this thesis are summarized. And its significance in controlling charge-discharge behavior of Zn negative electrodes is rationalized to establish strategies to realize the rechargeable Zn batteries.

In chapter 2, the electrodeposition behavior of Zn during charging operation was analyzed, and underlying mechanisms governing morphological variations were elucidated. Especially, the formation process of mossy structures which was major issues in large-scale energy storage system (flow-assisted Zn batteries) were discussed in detail.

From *in situ* optical microscope analysis on the growth behavior of mossy structures and its comparison with the dendrite formation, it was characterized by non-uniform deposition on the filamentous structure. At microscopic level, the evolution of microsteps was closely related with the mossy structures formation; deposition was localized on the terrace of microsteps at low deposition overpotential. Such a non-uniform deposition behavior was possibly caused by side-reactions during Zn electrodeposition (H_{ad} or oxide formation) because of decreased current efficiency during deposition.

Furthermore, the effects of cation indicated that the deposition process was influenced by an interaction between the non-specifically adsorbed cation and the reaction intermediates for Zn electrodeposition (*e.g.* electrode reactions were facilitated by K^+ or Li^+ compared to Cs^+), which determined the microstructures of Zn electrodeposits.

In chapter 3, metal additives effects were examined to suppress the formation of mossy structures in flow-assisted Zn battery. It was emphasized, (1) revealing the mechanisms behind compact Zn electrodeposition and (2) establishing a systematic basis enabling to control the flow-assisted battery.

From comparative analysis on the effects of Pb, Sn and In on the Zn electrodeposition process, it was pointed out that Sn and In can suppress the formation of mossy structures without increasing the deposition overpotential. By combining analysis on morphologies, crystal structures and composition, the process governing compact Zn electrodeposition was clarified; additive metals were codeposited with Zn and provided the surface enabling compact Zn electrodeposition through an aggregation at the surface of the deposits. This process was possible due to lower surface energy of codeposited metal than that of Zn, and no-alloy formation between additive metals and Zn. Charge-discharge reactions of Zn-Ni flow-assisted battery with Sn and In additives showed that In exhibited better performance in compact Zn electrodeposition and charge-discharge characteristics than that of Sn. This was achieved by (1) sufficient deposition amount during charging to enable compact Zn electrodeposition, (2) high overpotential of In for hydrogen evolution reaction (HER) to avoid decrease in the Coulombic efficiency, and (3) reversible dissolution of additives upon discharge to avoid the accumulation of inactive phase.

In chapter 4, the formation process of ZnO during discharge of the electrode was analyzed to clarify the guideline for controlling the discharge behavior. This process is important toward achieving high energy density and rapid charge-discharge cycles because ZnO precipitation affect the discharge capacity and the cyclability of the electrode.

By systematically investigating the effects of KOH, zincate concentrations, and current densities on the discharge behavior, it was confirmed that the nucleation density of ZnO was large under conditions where the degree of supersaturation was large. This was consistent with previous studies. However, XRD and SEM analysis showed that dominant crystal growth was observed after discharge at low current density and high KOH concentration. Furthermore, *in situ* Raman analysis revealed the dynamic changes in the growth behavior of ZnO during discharge. At initial stages of dissolution, precipitated ZnO contained crystal defects (excess Zn), while it changed to crystalline wurtzite ZnO at later stages. These changes suggested that Zn excess was introduced upon nucleation (dehydration reaction between zincate species), and the crystal growth was governed by decomposition of zincate on a primary nucleus. Thus, in addition to the solution chemistry governing nucleation of ZnO (*e.g.* OH^- and water activity) previously discussed, the surface reaction of zincate species in ZnO particles had considerable influences on morphologies and crystal structures of ZnO.

In chapter 5, the perspective for controlling the Zn dissolution and ZnO formation process was discussed based on the results obtained in chapter 4. Especially, the effects of Li^+ on the discharge process were investigated. Although Li^+ was known as additive to alter the ZnO crystal growth in the chemical synthesis and was sometimes used in an electrolyte for Zn batteries, their influences on charge-discharge reactions have not been rationalized.

The most notable difference by the presence of Li^+ was its suppression effects on the crystal growth of ZnO. *In situ* Raman analysis showed that the formation of crystalline wurtzite ZnO was suppressed, and the precipitates were highly defective ZnO. This means that the ZnO formation occurred mainly by the dehydration reactions between zincate species, and the crystal growth via decomposition of zincate on ZnO surface was suppressed. Furthermore, Li^+ affected the dissolution reaction of Zn, as well. At the presence of Li^+, Zn dissolution occurred regardless of underlying Zn microstructures due to an enhancement effect of Li^+ on the dissolution reaction, which was beneficial for mitigating the surface roughening upon dissolution. These two effects on the discharge process remarkably suppressed morphological changes upon following charging; at the

absence of Li^+, rough deposits were evolved from residual Zn remained during the discharge, but direct deposition on the dissolved front was observed in the case of Li^+ containing solution.

This thesis work focused on the interfacial processes governing electrochemical reactions of Zn and provided the guiding principles toward the controlling charge-discharge reactions of Zn negative electrodes for applications in the grid-scale energy storage systems. From profound understandings on interfacial phenomena governing electrodeposition of Zn, anodic dissolution and ZnO formation, the perspective toward achieving the rechargeable Zn batteries is clarified. Among phenomena occurring at μm to nm scale, the evolution of microsteps and the deposition of metals additives (including aggregation at the surface) influenced on determining microstructures of Zn electrodeposits. Atomic scale interaction of reaction intermediates and cations at the interface played an important role in non-uniform Zn electrodeposition/dissolution and the elementary steps for ZnO formation. These findings provide a basis to design rational interfacial reactions and realize the rechargeable Zn negative electrodes.

List of Achievements

1. Original Articles

"Morphological evolution of mossy structures during the electrodeposition of zinc from an alkaline zincate solution"
Tomohiro Otani, Masato Nagata, Yasuhiro Fukunaka, Takayuki Homma
Electrochimica Acta, **206**, 366-373 (2016).
(https://doi.org/10.1016/j.electacta.2016.04.124)

"Effect of lead and tin additives on surface morphology evolution of electrodeposited zinc"
Tomohiro Otani, Yasuhiro Fukunaka, Takayuki Homma
Electrochimica Acta, **242**, 364-372 (2017).
(http://dx.doi.org/10.1016/j.electacta.2017.04.130)

2. Presentations

[International Conference]

"Analysis on electrodeposition process of mossy shaped zinc"
Tomohiro. Otani, Masato Nagata, Yasuhiro Fukunaka, Takayuki Homma
11th International Symposium on Electrochemical Micro & Nanosystem Technologies (EMNT2016), Brussels, Belgium, 2016 August.

"Effects of Metal Additives on Morphological Evolution of Zinc Electrodeposition"
Tomohiro Otani, Yasuhiro Fukunaka, Takayuki Homma
Nucleation & Growth Research Conference, Kyoto, Japan, 2016 September.

"Growth Behavior of ZnO during Discharge of Zinc Negative Electrode"
Tomohiro Otani, Masato Nagata, Yasuhiro Fukunaka, Takayuki Homma
PRiME 2016, Honolulu, U.S.A., 2016 October.

"Analysis on Growth Process of Irregular Shaped Zn Electrodeposits and Roles of Metal Additives"
Tomohiro Otani, Yasuhiro Fukunaka, Takayuki Homma
68th Annual Meeting of the International Society of Electrochemistry, Providence, U.S.A., 2017 August.

"Effect of metal additives on morphological evolution of zinc electrodeposition"
Tomohiro Otani, Yasuhiro Fukunaka, Takayuki Homma
5th DGIST-Waseda Workshop on Electrochemistry 2017, Tokyo, Japan, 2017 December.

"Effect of electrolyte flow on the evolution of microsteps during zinc electrodeposition"
Yuta Masuda, Tomohiro Otani, Yasuhiro Fukunaka, Takayuki Homma
22nd Topical Meeting of the International Society of Electrochemistry, Tokyo, Japan, 2018 April.

"Influences of ZnO Formation on Morphological Evolution of Zn Negative Electrode"
Tomohiro Otani, Masato Nagata, Yasuhiro Fukunaka, Takayuki Homma
22nd Topical Meeting of the International Society of Electrochemistry, Tokyo, Japan, 2018 April.

"Analysis of ZnO Growth Process and Effect of Li^+ Additive on Zn Negative Electrode"
Tomohiro Otani, Masato Nagata, Yasuhiro Fukunaka, Takayuki Homma
14th International Fischer Symposium, Seeon, Germany, 2018 May.

[Domestic Conferences]

"Analysis on electrodeposition behavior of zinc focusing on early deposition stage"
Tomohiro Otani, Yasuhiro Fukunaka, Takayuki Homma
131st Meeting of the Surface Finishing Society of Japan, Kanagawa, Japan, 2015 March.

"Analysis on anodic reaction of Zn electrode focusing on precipitation process of ZnO"
Masato Nagata, Tomohiro Otani, Yasuhiro Fukunaka, Takayuki Homma
133rd Meeting of the Surface Finishing Society of Japan, Tokyo, Japan, 2016 March.

"Analysis on electrodeposition behavior of spongy shaped zinc"
Tomohiro Otani, Masato Nagata, Yasuhiro Fukunaka, Takayuki Homma
83th Meeting of the Electrochemical Society of Japan, Osaka, Japan 2016 March.

"Analysis on electrodeposition process of zinc mossy structure focused on the effect of metal additives"
Yuta Masuda, Tomohiro Otani, Yasuhiro Fukunaka, Takayuki Homma
84th Meeting of the Electrochemical Society of Japan, Tokyo, Japan, 2017 March.

"Analysis on formation process of ZnO and charge-discharge reactions of Zn negative electrode"
Masato Nagata, Tomohiro Otani, Yasuhiro Fukunaka, Takayuki Homma
7th CSJ Chemistry Festa, Tokyo, Japan, 2017 October.

"Analysis on ZnO formation process during anodic dissolution of Zn by *in situ* Raman spectroscopy"
Tetsuya Yasuda, Tomohiro Otani, Masahiro Kunimoto, Masahiro Yanagisawa, Takayuki Homma
138th Meeting of the Surface Finishing Society of Japan, Hokkaido, Japan, 2018 September.

"Analysis on Surface Morphological Evolution of ZnO during Anodic Dissolution of Zn Negative Electrode"
Tomohiro Otani, Ryosuke Kudo, Yasuhiro Fukunaka, Takayuki Homma
2018 Fall Meeting of Electrochemical Society of Japan, Ishikawa, Japan, 2018 September.

3. Others

[Academic Papers]

"Fabrication of ultra-high density nanodot arrays with high coercivity based on analysis of initial deposition process"
Hiroki Hagiwara, Siggi Wodarz, Tomohiro Otani, Daiki Nishiie, Giovanni Zangari, Takayuki Homma
IEEE technical report, **114**, 7-10 (2014).

"Fabrication of FePt and CoPt Magnetic Nanodot Arrays by Electrodeposition Process", Takayuki Homma, Siggi Wodarz, Daiki Nishiie, Tomohiro Otani, Siyuan Ge, Giovanni Zangari
Electrochemical Society Transaction, **64(31)**, 1-9 (2015).

"Characterization of Electrodeposited Co-Pt Nanodot Array at Initial Deposition Stage", Siggi Wodarz, Tomohiro Otani, Hiroki Hagiwara, Takayuki Homma
Electrochemical Society Transaction, **64(45)**, 99-105 (2015),

"Thickness Control of 3-Dimensional Mesoporous Silica Ultrathin Films by Wet-Etching",
Maho Kobayashi, Kyoka Susuki, Tomohiro Otani, Shinpei Enomoto, Haruo Otsuji, Yoshiyuki Kuroda, Hiroaki Wada, Atsushi Shimojima, Takayuki Homma, Kazuyuki Kuroda
Nanoscale, **9**, 8321-8329 (2017).

[International Conferences]

"Fabrication of FePt and CoPt Magnetic Nanodot Arrays by Electrodeposition Process", Takayuki Homma, Siggi Wodarz, Daiki Nishiie, Tomohiro Otani, Siyuan Ge, Giovanni Zangari
2014 ECS & SMEQ Joint International Meeting, Cancun, Mexico, 2014 October.

"Characterization of Electrodeposited Co-Pt Nano-Dot Array at Initial Deposition Stage", Siggi Wodarz, Tomohiro Otani, Hiroki Hagiwara, Takayuki Homma
2014 ECS & SMEQ Joint International Meeting, Cancun, Mexico, 2014 October.

"Analysis of the Initial Stage of Co-Pt Electrodeposition Process at Nanopatterned Substrate"
Siggi Wodarz, Tomohiro Otani, Hiroki Hagiwara, Takayuki Homma
10th International Symposium on Electrochemical Micro & Nanosystem Technology (EMNT2014), Okinawa, Japan, 2014 November.

"Connecting Anodic Gas Evolution in Aqueous and High Temperature Molten Electrolyte Systems Via the Current Interrupt Technique"
Brian Chmielowiec, Tatsuki Fujimura, Tomohiro Otani, Keigo Aoyama, Toshiyuki Nohira, Takayuki Homma, Antoine Allanore
68th Annual Meeting of the International Society of Electrochemistry, Providence, U.S.A., 2017 August.

"Surface Reactivity of a Tin Electrode in Organic Carbonate Electrolytes"
Ivana Hassa, Tomohiro Otani, Takayuki Homma, Philip N. Ross, Robert Kostecki
232nd ECS Meeting, National Harbor, U.S.A., 2017 October.

[Domestic Conferences]

"Fabrication of ultra-high density nanodot arrays with high coercivity based on analysis of initial deposition process"
Hiroki Hagiwara, Siggi Wodarz, Tomohiro Otani, Daiki Nishiie, Giovanni Zangari, Takayuki Homma
IEICE-MR, Tokyo, Japan, July 2014.

4. Awards

Best Originality Award, 2016 TECO Green Tech Contest, 2016 August.

Excellent Poster Presentation Award, 5th DGIST-Waseda Workshop on Electrochemistry, 2017 December.

Acknowledgement

First, I would like to express appreciation to Prof. Takayuki Homma. Since I joined the laboratory activity in 2013, he has taught me a lot of skills regarding how to organize the scientific research, profound knowledge about electrochemistry and how to present/write scientific findings. These instructions formed my fundamental abilities as researchers. Furthermore, I learned an attitude towards researches and process of thinking. He gave me a lot of opportunities like international conference meetings and research activities abroad. Through these experiences, I gained basic skills to survive the globalized word as researchers or engineers. I hope further expansion and deepening of the research activities of the group in future.

I would like to express my appreciation to Prof. Kenichi Oyaizu, Prof. Toshiyuki Momma, and Dr. Kenichi Uemura (Nippon Steel & Sumitomo Metal Co.) for reviewing this thesis. Their comments and suggestions are very valuable for deepening the discussion and rising the scientific value of the thesis work.

I want to thank Prof. Yasuhiro Fukunaka for his advice and encouragement during Ph. D course. I have been always surprised to see his enthusiasm for research activities. I learned a lot from such an attitude as a scientist. I hope great success in the ISS-FS project in future. I also thank Prof. Masahiro Yanagisawa, Prof. Mikiko Saito and Dr. Morten Bertz for suggestions and comments about my experiments.

Dr. Masahiro Kunimoto often gives me valuable insight and advice in a wide variety of scientific fields. Discussion with him was really enjoyable and widened my viewpoints for chemistry.

I am grateful to Prof. Hiroyuki Nishide and Prof. Toru Asahi, and all professors contributing to the Leading Graduate Course for Science and Engineering, Waseda University. Activities of the course really widened my viewpoints for science, industry and society. The interactions with academic researchers and collaboration with industries gave me valuable opportunities and relationships. Through this course, I gained a confidence to work in the industry in the globalized world.

The results about Zn-Ni flow-assisted battery described in Chapter 3 are achieved in the collaboration work in the Central Research Laboratory, Kyocera. I appreciate the internship opportunity, and kind supports from Mr. Takeshi Okuma and Dr. Shoji Yamashita. I recognized that understandings on interfacial phenomena of Zn was

essential to realize the rechargeable Zn batteries from their R&D activities, which motivated me a lot for this thesis works.

I would like to thank Dr. Robert Kostecki for accepting me for an internship work in Lawrance Berkeley National Laboratory in the U.S.A. The professional working environment in the laboratory and the frontier researches impressed me a lot. I would like to thank Dr. Ivana Hasa and colleagues for their supports and advice during my internship.

I would like to thank Dr. Siggi Wodarz for his instruction in the Lab. I learned fundamental skills of electrochemistry and characterization techniques from him. I also thank Dr. Yasuhiro Tsuyuki for his encouragement and advice in the Lab. and the Leading Graduate Course. Discussions and collaborations with other Ph. D. candidates, Mr. Yelchur Venkata Akash and Mr. Tatsuki Fujimura was meaningful and valuable for deepening research activities in the Lab.

I want to thank Mr. Masato Nagata, Mr. Yuta Masuda, Mr. Tetsuya Yasuda, and Mr. Ryosuke Kudo for their contribution to the researches on Zn negative electrodes. Their findings often give me new insight and motivated me for advancing to new research fields.

Lastly, I would like to express appreciation to my family for their patience and supports during my 5-year Ph. D. course. Without their understandings and supports, this work would not be achieved.

February 2019
Tomohiro Otani